HARVARD UNIVERSITY

Graduate School of Arts and Sciences

DISSERTATION ACCEPTANCE CERTIFICATE

The undersigned, appointed by the

Harvard John A. Paulson School of Engineering and Applied Sciences
have examined a dissertation entitled:

"Functionality through multistability: from deployable structures to soft robots"

presented by: David Melancon

Signature Katia Bertoldi

Typed name: Professor K. Bertoldi

Signature Chris H. Rycroft

Typed name: Professor C. Rycroft

Signature

Typed name: Professor C. Hoberman

December 7, 2021

Functionality through multistability: from deployable structures to soft robots

A DISSERTATION PRESENTED

BY

DAVID MELANCON

TO

THE SCHOOL OF ENGINEERING AND APPLIED SCIENCES

IN PARTIAL FULFILLMENT OF THE REQUIREMENTS

FOR THE DEGREE OF

DOCTOR OF PHILOSOPHY

IN THE SUBJECT OF

APPLIED MATHEMATICS

HARVARD UNIVERSITY

CAMBRIDGE, MASSACHUSETTS

DECEMBER 2021

Dissertation Advisor: Prof. Katia Bertoldi
Co-advisor: Chuck Hoberman

David Melancon

Functionality through multistability: from deployable structures to soft robots

Inflating a rubber balloon leads to a dramatic shape change: a property that is exploited in the design of deployable structures and soft robots. On the one hand, inflation can be used to transform seemingly flat shapes into shelters, field hospitals, and space modules. On the other hand, fluid-driven actuators capable of complex motion can power highly adaptive and inherently safe soft robots. In both cases, just like the simple balloon, only one input is required to achieve the desired deformation. This simplicity, however, brings strict limitations: deployable structures need continuous supply of pressure to remain upright and soft actuators are restricted to uni-modal and slow deformation.

In this dissertation, I embrace multistability as a paradigm to improve the functionality of inflatable systems. In particular, I take inspiration from elastic instabilities arising from simple geometric principles—such as folding a 2D sheet of paper or snapping a curved cap to its inverse shape—to design balloons engineered to have a multi-welled energy landscape.

In the first part of this dissertation, I draw inspiration from origami to design multistable and inflatable structures at the meter scale. First, I propose a systematic way of building bistable origami shapes with two compatible and closed configurations. Then, using experiments and numerical analyses, I demonstrate that under certain conditions, pneumatic inflation can be used to navigate between the stable states. Finally, I combine the simple shapes to build large-scale functional structures such as shelters and archways. Because these deployable systems are multistable, pressure can be disconnected when they are fully expanded.

In the second part, I again use origami as a platform to create soft actuators capable of multimodal and arbitrary deformations based on a single pressure input. I start by focusing on the classic Kresling origami: a pattern that once folded, takes on the shape of a faceted cylinder that simply extends, contracts, and twists upon inflation and deflation. By modifying one of the facets, I show that the module can become bistable, i.e. the modified facet snaps at a certain pressure threshold. This snap-through instability breaks the rotational symmetry and unlocks bending as a deformation mode upon subsequent deflation. By combining multiple of these modified Kresling cylinders—each one snapping at different pressure levels—I then build actuators that deform along vastly different trajectories from one single source of pressure. Guided by experiments and numerical analyses, I inverse design actuators with prescribed deformation modes to demonstrate their potential for robotic applications.

Finally, I exploit snapping instabilities to decouple the input signal from the output deformation in soft actuators. In particular, I design a soft machine capable of jumping based on the snapping of spherical shells. As this instability is accompanied with the sudden release of energy at constant volume, i.e. no influx of fluid is needed to trigger the large deformation, the robot jumps upon an arbitrarily slow volume input. Using experiment and numerical simulations, I optimize the actuator's release of energy and jumping height.

Contents

Listing of figures

To *Flo* who made me love hard puzzles.

Acknowledgments

Acknowledging all the people that helped me through my graduate studies is not an easy task. Unsurprisingly, a doctorate is not limited to time spent in the lab doing research. For me, a Ph.D. is about engaging with people with vastly different ideas and backgrounds to (try to) solve beautiful problems. I was unbelievably lucky to meet brilliant scholars from all around the world, each of whom influenced and shaped the researcher I have become.

I would like to give a special thank to my supervisor Katia Bertoldi who gave me the opportunity to join her research group at Harvard University. From the very first day, Katia gave me freedom to pursue my own ideas and provided invaluable guidance so that these ideas could flourish into meaningful scientific contributions. I am sure our professional and personal relationship will continue to grow in the years to come.

I also have to express my deep gratitude to my co-advisor Chuck Hoberman, who has been an incredible source of inspiration during my doctorate. Under his keen mentorship, I learned to embrace art and design as powerful tools for scientific development.

Further, I would like to thank my committee member Chris Rycroft for his suggestions and comments on my research during my doctorate. Chris is by a landslide the best teacher I have had at Harvard and I feel many technical skills showcased in this dissertation were developed through taking his applied mathematics courses.

I also have to acknowledge the support of my dear colleagues from the Bertoldi group. In particular, Benjamin Gorissen, Antonio Elia Forte, Ahmad Zareei, and Eder Medina, all of whom have been real research mentors and have become true friends.

Finally, I cannot forget my family and friends for their unrelenting support. Preserving a healthy work-life balance is the dream of every graduate student and they undoubtedly made this dream a reality.

1 Introduction

"This is going to be fun and easy." – A first year grad student

1.1 Multistability as a paradigm for functionality

Balloons are among the most simple engineering systems. Yet this very simplicity—large deformation upon the application of internal pressure—makes them an ideal platform for a wide range of applications, particularly in the fields of *deployable structures* and *soft robots*. In the former, the objective is to transform rapidly and reliably a compact object to a functional shape while maximizing the expansion ratio along the process[1–4]. In the latter, flexibility of each of the robot's components is required to ensure adaptability to unstructured environments and safer human-robot interactions[5–7]. This explains why highly sophisticated balloons have been recently used to deploy space modules[8] and field hospitals[9] as well as to design pneumatic actuators that make soft robots bend[10], grip[11,12], crawl[13,14], swim[15,16], and jump[17,18] (see Figure 1.1).

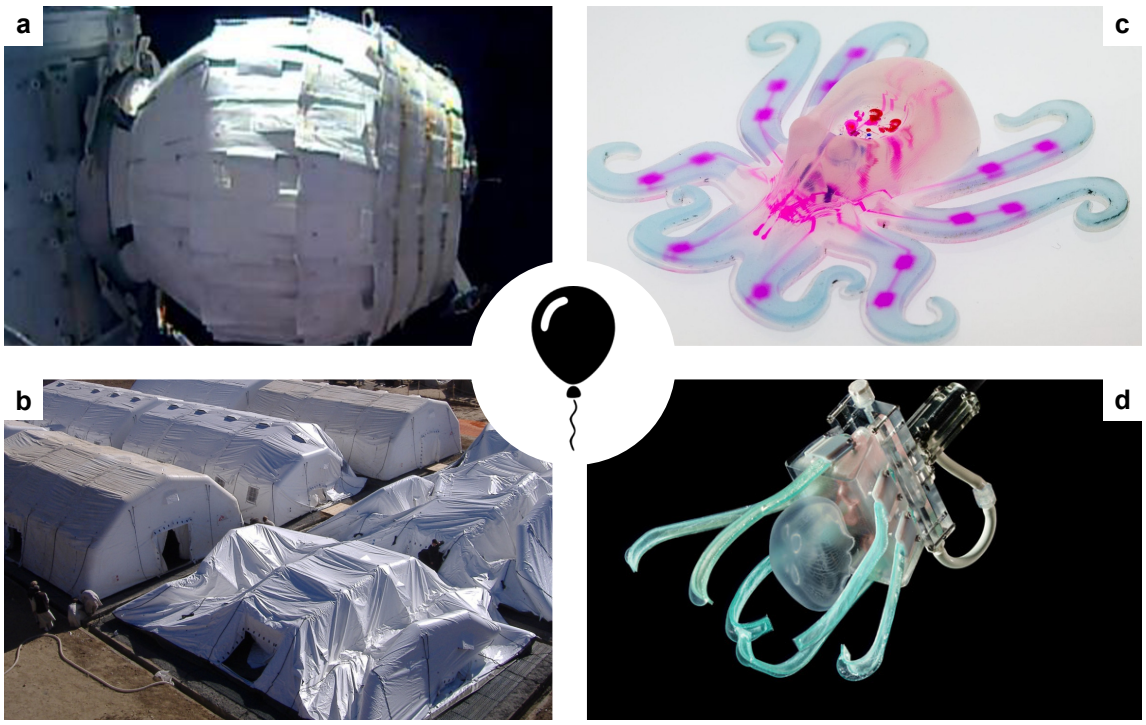

Figure 1.1: Engineered balloons. (a) A deployable space module[8]. **(b)** Inflatable field hospitals[9]. **(c)** A microfluidic 3D-printed soft robot[19]. **(d)** A soft robotic gripper capable of ultragentle manipulation[12].

While these systems are highly complex, their overall response can be essentially captured by analyzing the pressure-volume relation of a simple spherical balloon where, during inflation, the internal pressure increases with respect to the input volume* (see blue curve in the top panel of Figure 1.2a). This monotonic response makes it easy to deploy an inflatable structure or actuate a

*The pressure-volume response shown in Figure 1.2a assumes a Gent material model with stretch-limiting behavior[20].

soft robot, however, it also severely limits their functionality. These limitations can be highlighted by plotting the energy landscape associated with a monotonic pressure-volume curve (see red curve in the bottom panel of Figure 1.2a), which can be calculated as

$$E = \int p \mathrm{d}\Delta V, \tag{1.1}$$

where E is the elastic energy, p the internal pressure, and ΔV the volume change. Clearly, because the energy landscape is monostable—i.e. there exists only a single stable state at $\Delta V = 0$—a first limitation is that typical inflatable structures require a *continuous supply of pressure to remain deployed*. Any sudden release of pressure results in unavoidable collapse. Additionally, inflatable actuators with near linear energy landscapes show a strong coupling between the input signal (e.g. pressure or volume) and the output deformation, resulting in *uni-modal deformation* and *slow response*.

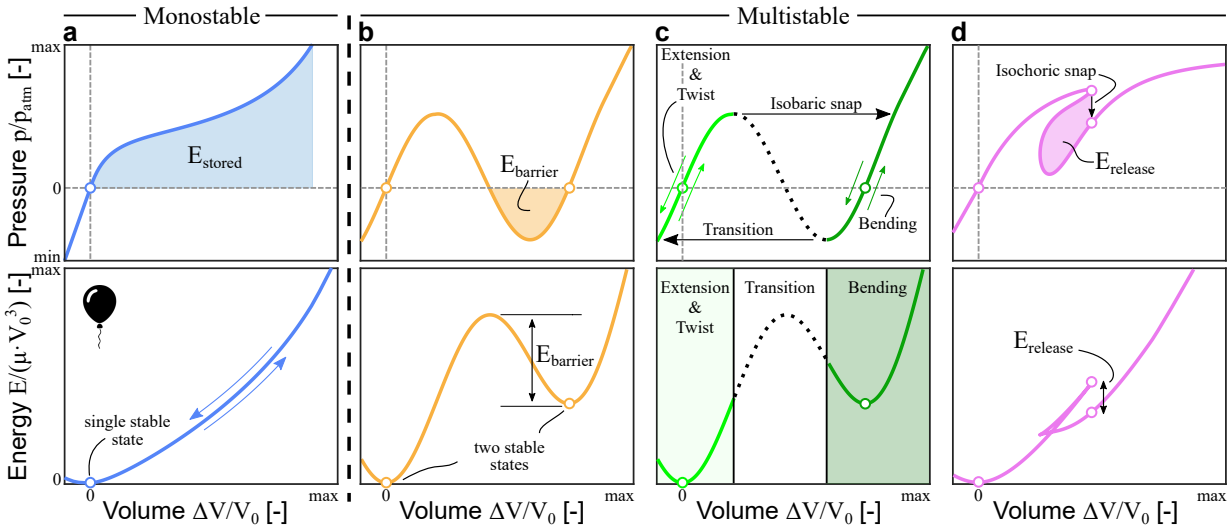

Figure 1.2: Advantages of multistable energy landscapes in inflatable systems. Pressure-volume relations normalized by atmospheric pressure p_{atm} and initial volume V_0 (top) and integrated energy landscapes normalized by shear modulus μ (bottom) of monostable and multistable balloons. **(a)** Inflating a monostable spherical balloon stores elastic energy E_{stored}. **(b)** A multistable inflatable system could be deployed to a second stable state in which an energy barrier $E_{barrier}$ would prevent collapse. **(c)** A multistable inflatable system driven by pressure could undergo isobaric snap-through instabilities to switch between different deformation modes such as extension, twist, and bending. **(d)** A multistable inflatable system driven by volume could undergo isochoric snap-through instabilities to trigger energy release and fast deformation upon an arbitrary slow volume input.

These limitations could be overcome by designing inflatable systems with *multi-welled energy landscapes*—i.e. multiple stable states where the energy is locally minimized. First, leveraging bistability (i.e. two stable states) could lead to the design of pressure-deployable structures that lock in place after deploying from a flat to an expanded configuration. In this case, the internal pressure (instead of simply rising with volume) would eventually become negative upon inflation

with the enclosed area bellow the x-axis on the pressure-volume curve representing the energy barrier $E_{barrier}$ in the deployed state preventing collapse upon a sudden release of pressure (see Figure 1.2b). Naturally, by providing enough energy through vacuum, i.e. $E_{vacuum} > E_{barrier}$, the bistable system could also be brought back to the initial compact state.

Second, a fluidic actuator with a multistable energy landscape could be inflated to undergo non-reversible snap-through and snap-back instabilities to decouple the input signal from the output deformation (see Figures 1.2c-d). In Figure 1.2c, pressure is used as the signal to trigger snap-through transitions and switch between arbitrary modes of deformation such as extension, twisting, and bending. In Figure 1.2d, the actuator snaps under constant volume, triggering the fast release of elastic energy upon an arbitrary slow input of volume.

1.2 Objectives

Motivated by these opportunities, this dissertation's overarching goal is to provide functionality through multistability with a particular focus on the following objectives:

Objective 1: Design inflatable structures with compact and expanded stable states
Objective 2: Enable multimodal deformation in soft robots based on a single input signal
Objective 3: Enable fast deformation in soft robots based on an arbitrary slow input signal

1.3 Approach

To meet the dissertation's goal, we leverage simple geometry in inflatable structures and actuators to tune their energy landscape. In particular, to accomplish the first two objectives, we take inspiration from origami, the ancient art form of paper-folding, to realize multistable deployable structures and multimodal actuators. In the last decade, origami has emerged as a new design paradigm in architecture and robotics because of its functional properties such as shape morphing[21–24], high expansion ratio[25], and easy actuation through self-folding[26,27] or inflation[28–30] (see examples of origami devices leveraging deployability and multistability in Figure 1.3). More importantly, the geometry of the crease pattern can be rationally designed to support a multi-welled energy landscape[31–38]. This dissertation brings together the *deployability* and *multistability* of origami-inspired devices to enable the design of multistable and inflatable structures and fluidic soft actuators capable of multimodal deformation based on a single input.

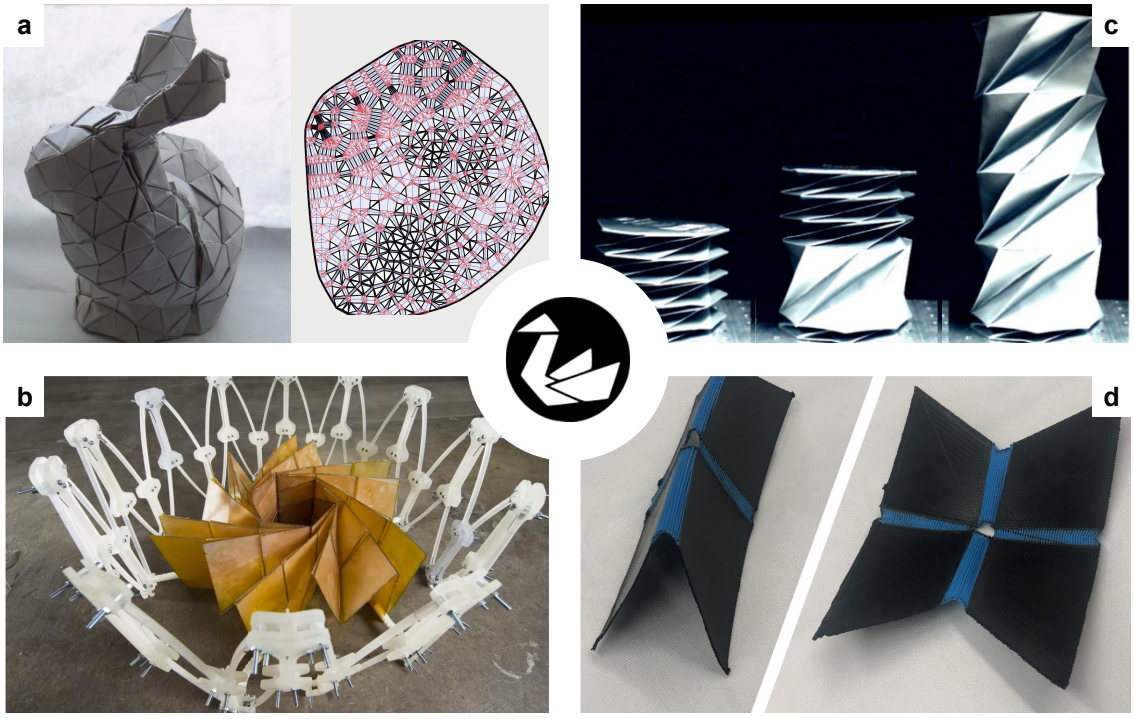

Figure 1.3: Deployability and multistability of origami patterns. **(a)** 3D Stanford bunny (left) folded out of a 2D creased sheet of paper (right)[24]. **(b)** Deployable solar panel inspired by origami[39]. **(c)** The different stable states of the multistable Kresling pattern[40]. **(d)** The two stable states of an origami degree-four vertex[38].

Finally, to realize the third objective of enabling fast deformation in soft robots, we take inspiration from snapping instabilities as they can decouple the slow input signal from the output deformation and triggers rapid events[41–45]. Examples of such instabilites are reported in Figure 1.4. In particular, we focused on the snapping of pressurized spherical shells. Importantly, this fully elastic instability—if the shell is made of a soft material—triggers the sudden release of energy at constant volume. In this dissertation, we harness this isochoric snap-through transition as a powerful nonlinear mechanism to decouple the slow input single from the output deformation and spark rapid events.

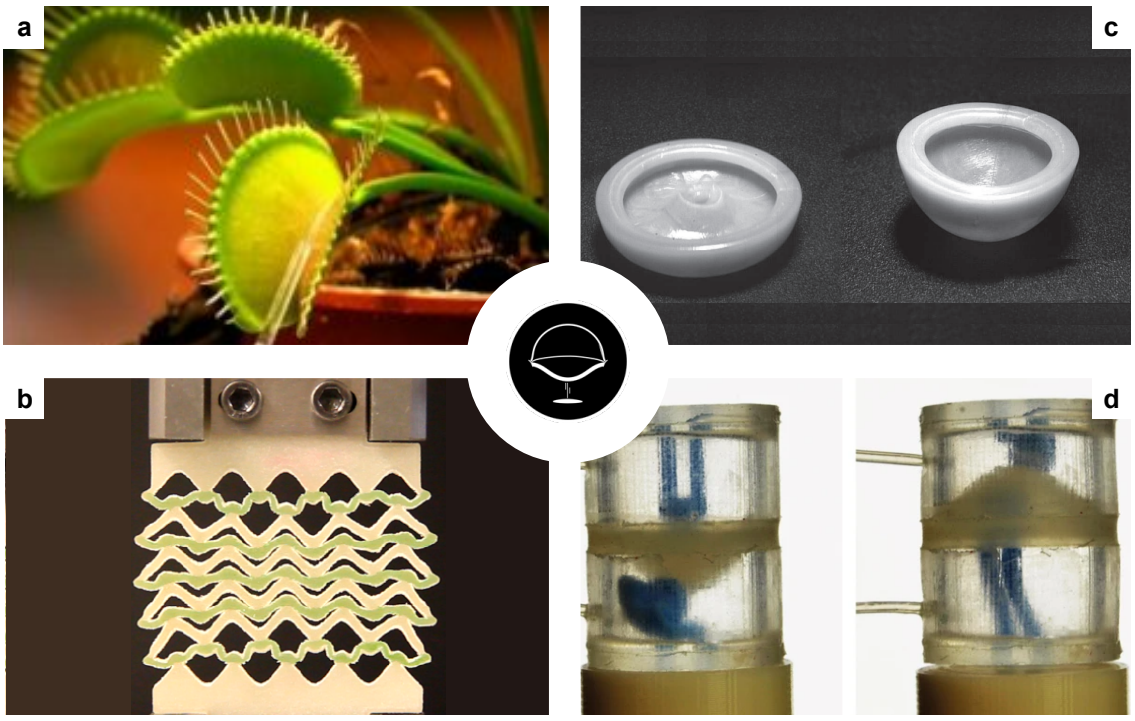

Figure 1.4: Snapping instabilities. (a) The snapping of the Venus flytrap[43]. **(b)** A metamaterial made of snapping beams[46]. **(c)** A jumping popper[44]. **(d)** A soft bistable valve[42].

1.4 Dissertation overview

Chapters 2 to 4 constitute the core of this dissertation, with each chapter based on a first-author article published in or submitted to a peer reviewed journal.

Chapter 2 introduces the concept of rigid-walled deployable structures inspired from origami that are at the same time inflatable and multistable. Guided by simple geometric principles and experiments, we first show that a polyhedron comprised of rigid triangular facets connected by elastic hinges can have multiple stable configurations. We then present a library of simple origami shapes that can be inflated and deflated between stable states. Finally, we combine these units to build functional structures at the meter-scale. The result is a comprehensive, scale independent platform to design and analyze complex deployable structures that can be actuated by simple air pressure. Because they have multiple stable states, these structures can remain deployed at atmospheric pressure and retracted by applying vacuum.

Still using origami as an inspiration, chapter 3 focuses on fluidic actuators capable of arbitrary deformation modes based on a single pressure input. The building block of our multimodal actuators are based on the Kresling pattern that simply extends when inflated and contracts and twists when deflated. To enable additional deformation modes, we modify the pattern's geometry by adding two valley creases in one of the panels to make it bistable. During inflation the module

transitions to a second stable state where the panel is snapped outward. In that state, the breakage of rotational symmetry gives rise to bending upon deflation up until a critical negative pressure is reached and the module resets to its initial stable state. We then couple multiple of these building blocks—each having different pressure thresholds at which the modified panel snaps—to create inflatable actuators capable of complex and multimodal deformation. Finally, guided by a combination of experiments and numerical analyses, we inverse design the actuators' deformation and show their potential as smart robotic systems.

In chapter 4, we embrace structural instabilities to enable the fast actuation in fluidic soft actuators. In particular, we draw inspiration from the snapping of elastic shells—an instability that suddenly releases energy—to design a simple soft machine capable of jumping. As this snap-through instability happens at constant volume, there is no influx of fluid needed to trigger the energy release, resulting in a quasi-instantaneous and large deformation. Furthermore, using finite element modelling, we optimize the design of our jumpers to maximize the released energy and, consequently, jumping height. We also demonstrate the actuator's ability to be reset to the initial, undeformed state, enabling cyclic jumping.

Finally, the Outlook in chapter 5 provides a condensed summary of the results and contributions as well as a description of future directions. A complete list of my publications can be found at the end of this dissertation.

2

Multistable inflatable origami structures at the meter scale

By: David Melancon, Benjamin Gorissen, Carlos-José Garcia-Mora, Chuck Hoberman, and Katia Bertoldi.
Published in *Nature* on April 21st, 2021. **doi:10.1038/s41586-021-03407-4**

2.1 Abstract

From stadium covers to solar sails, we rely on deployability for the design of large-scale structures that can quickly compress to a fraction of their size[1–4]. Historically, two main strategies have been pursued to design deployable systems. The first and most common approach involves mechanisms comprising interconnected bar elements, which can synchronously expand and retract[47–49], occasionally locking in place through bistable elements[50,51]. The second strategy instead, makes use of inflatable membranes that morph into target shapes by means of a single pressure input[52–54]. Neither strategy however, can be readily used to provide an enclosed domain able to lock in place after deployment: the integration of protective covering in linkage-based constructions is challenging and pneumatic systems require a constant applied pressure to keep their expanded shape[55–57]. Here, we draw inspiration from origami, the Japanese art of paper folding, to design rigid-walled deployable structures that are multistable and inflatable. Guided by geometric analyses and experiments, we create a library of bistable origami shapes that can be deployed through a single fluidic pressure input. We then combine these units to build functional structures at the meter-scale, such as arches and emergency shelters, providing a direct pathway for a new generation of large-scale inflatable systems that lock in place after deployment and offer a robust enclosure through their stiff faces.

2.2 Introduction

Large, deployable structures should ideally (*i*) occupy the minimum possible volume when folded; (*ii*) be autonomous when deploying; (*iii*) lock in place after deployment; and (*iv*) provide a structurally robust shell (if they are designed to define a closed environment). To satisfy all these requirements, we here present a novel approach with roots in the Japanese art of paper folding: origami. Extensively used in robotics[58–62], metamaterials[21,25,63–65] and structures[66–69], origami principles have potential to lead to efficient large-scale deployable structures as they offer (*i*) a versatile crease-based approach to shape design[22–24]; (*ii*) an easy actuation through inflation, if enclosed[28–30]; (*iii*) self-locking capabilities when designed to support multiple energy wells[31–38]; and (*iv*) the possibility to create a protective environment through their faces. While previous origami systems have explored inflatability and multistability separately[28–38], here we show that these two properties can coexist, unlocking an unprecedented design space of meter-scale inflatable structures that harness multistability to maintain their deployed shape without the need for continuous actuation (see schematics in Figure 2.1a).

2.3 Triangular facets as a platform for bistable and inflatable structures

To create inflatable and bistable origami structures, we start by considering a triangular building block ABC and denote with α and β the internal angles enclosed by the edges AB-AC and AB-BC, respectively (see Figure 2.1b). The triangle initially lies in the xy-plane and is subsequently deployed through a rotation around its edge BC. As shown in Figure 2.1b, this deployment results in the displacement w_A of vertex A along the z-direction as well as in a volume V_{ABC} under the triangle

$$V_{ABC} = \frac{w_A ||AB||^2}{6} \frac{\sin\alpha}{\sin(\alpha+\beta)} \sqrt{\sin^2\beta - \frac{w_A^2}{||AB||^2}}, \tag{2.1}$$

where $||AB||$ indicates the length of AB. By focusing on the xy-plane, through simple geometrical considerations, one can see that if $\beta \in [\pi/4 - \alpha/2, \pi/2 - \alpha]$, the projection of vertex A during the deployment intersects the circle circumscribed to the initial configuration (see Figure 2.1b) when

$$w_A = w_A^c = ||AB|| \sqrt{1 - \frac{\cos^2\beta}{\sin^2(\alpha+\beta)}}. \tag{2.2}$$

It follows from the inscribed angle theorem[70] that for $w_A = w_A^c$ the angle α is recovered on the xy-plane (see the Supplementary Materials, Section A.1 for details). As such, if triangles of this type are used as building blocks to form origami polyhedra, the assembled systems will have two distinct compatible configurations: one flat (identified by $w_A = 0$) and one expanded (identified by $w_A = w_A^c$). By contrast, any configuration with $0 < w_A < w_A^c$ will be geometrically frustrated, with incompatibility, Δ_{ABC}, that can be estimated as

$$\Delta_{ABC} = ||AC_{xy}|| \cdot \sin(\alpha_{xy} - \alpha), \tag{2.3}$$

where AC_{xy} and α_{xy} are the projection on the xy-plane of edge AC and angle α, respectively (note that $\alpha_{xy} = \alpha$ only for $w_A = 0$ and w_A^c — see the inset in Figure 2.1c).

Therefore, to accommodate geometric frustration and realize closed origami shapes (i.e. shapes forming a closed inflatable cavity) capable of switching between two compatible configurations, we connect stiff triangular building blocks to stretchable hinges. Importantly, whereas polyhedra comprised of rigid triangular faces connected by perfect rotational hinges are known to be either rigid[71] or volume-invariant during deployment[72,73], we anticipate our closed origami with stiff facets and flexible hinges to be bistable. Indeed, for hinges with low enough bending stiffness, we expect the energy profile of the closed origami to exhibit two local minima in correspondence of the flat and expanded compatible states (where the energy in the system can only be attributed to hinge bending), separated by an energy barrier caused by the deformation of the facets and the

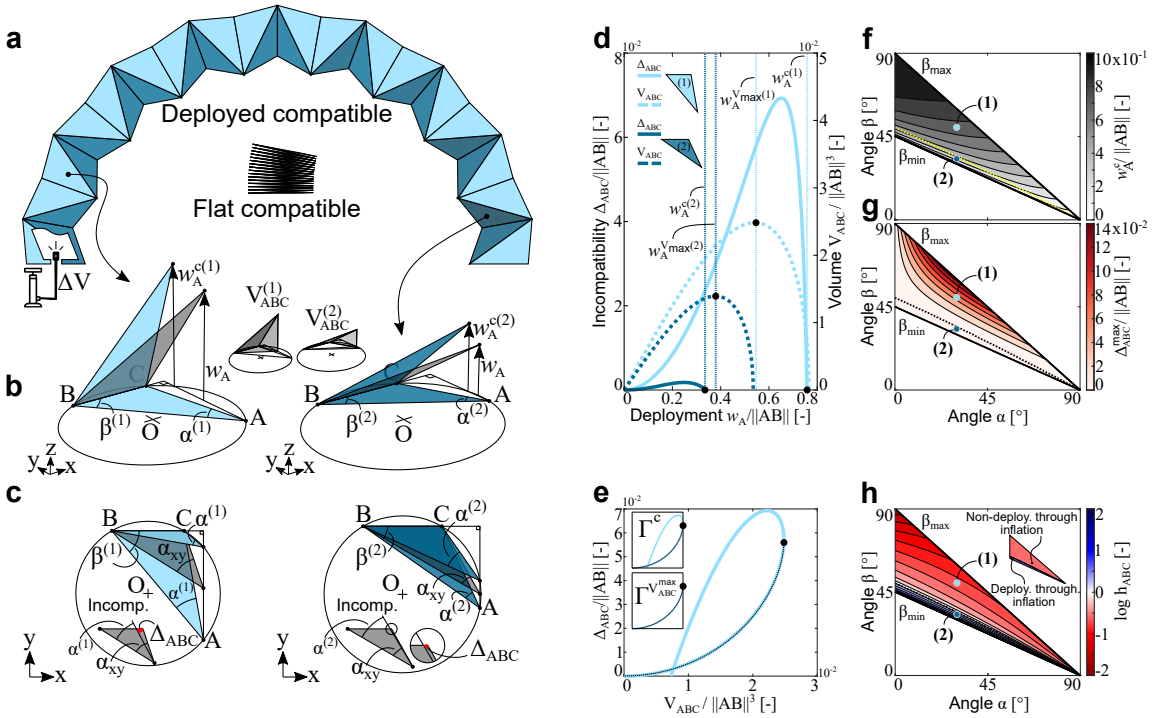

Figure 2.1: Triangular facets as building blocks for large-scale inflatable and bistable origami structures. **(a)** Schematics illustrating the deployment via inflation of a large-scale origami structure comprising triangular facets. **(b)** Deployment of two triangular building blocks with angles ($\alpha^{(1)}$, $\beta^{(1)}$) and ($\alpha^{(2)}$, $\beta^{(2)}$). **(c)** Projected view of the deployment. **(d)** Evolution of incompatibility, Δ_{ABC}, and underlying volume, V_{ABC}, as a function of the deployment height, w_A. **(e)** Evolution of incompatibility, Δ_{ABC}, as a function of the underlying volume, V_{ABC}. **(f-h)** Contour maps of the compatible deployment height, w_A^c, maximum incompatibility, Δ_{ABC}^{max}, and inflation constraint, h_{ABC}.

hinges required to accommodate geometric incompatibility.

To gain more insights into the behavior of our building blocks, we focus on the deployment of two triangles with ($\alpha^{(1)}$, $\beta^{(1)}$) = (30°, 50°) and ($\alpha^{(2)}$, $\beta^{(2)}$) = (30°, 33°). In Figure 2.1d, we report the evolution of the incompatibility, Δ_{ABC}, and the underlying volume, V_{ABC}, as a function of the deployment height, w_A, for both triangles. We find that the triangle with $\beta^{(1)} = 50°$ is characterized by both larger w_A^c and maximum incompatibility, $\Delta_{ABC}^{max} = \max(\Delta_{ABC})$. However, for this triangle the expanded compatible state is located after the configuration corresponding to the maximum underlying volume ($w_A^{c(1)} > w_A^{V_{ABC}^{max}(1)}$) and, therefore, cannot be reached when V_{ABC} is controlled. As such, whereas we expect a closed origami structure realized using these triangles to have two stable states with very different internal volume, we cannot use inflation to switch between the two of them. By contrast, the triangle with $\beta^{(2)} = 33°$ exhibits much smaller Δ_{ABC}^{max} and w_A^c, but can be deployed when controlling the volume since $w_A^{c(2)} < w_A^{V_{ABC}^{max}(2)}$. This suggests that closed origami realized using this triangle can be deployed using inflation, but have an expanded configuration very similar to the flat one. Further, we expect such structures to be only marginally bistable, as small perturbations are enough to overcome the energy barrier associated to the small $\Delta_{ABC}^{max(2)}$.

While in Figures 2.1b-d we focus on two geometries, we next consider all deployable triangles (i.e. triangles with $\pi/4-\alpha/2 \leq \beta \leq \pi/2-\alpha$) and seek for those that can potentially lead to deployable structures that are simultaneously bistable and inflatable. Towards this end, we use w_A^c to estimate the change in shape between the compatible states and Δ_{ABC}^{max} to evaluate bistability (i.e. to estimate the energy required to snap back from the expanded to the flat state). Further, we introduce an inflation constraint

$$h_{ABC} = \frac{\Gamma^{V_{ABC}^{max}}}{\Gamma^c}, \tag{2.4}$$

where $\Gamma^{V_{ABC}^{max}}$ and Γ^c are the arc lengths measured on the Δ_{ABC}-V_{ABC} curve between the flat stable state and the state of maximum volume and between the flat and expanded stable configurations, respectively (see Figure 2.1e). It follows from Eq. 2.4 that only geometries with $\log h_{ABC} \geq 0$ can be deployed through fluidic actuation as those are the only ones for which the expanded compatible configuration is reached before the one with maximum volume during inflation (note that $\log h_{ABC} = -1.46$ and 0.322 for the two triangles considered in Figures 2.1b-c).

In Figures 2.1f-h, we report w_A^c, Δ_{ABC}^{max}, and h_{ABC} for all deployable triangles. We find that both w_A^c and Δ_{ABC}^{max} are maximized in the region close to the upper boundary of the domain (i.e. when $\beta \to \pi/2-\alpha$). By contrast, the triangles deployable through inflation (for which $\log h_{ABC} \geq 0$) are all close to the lower boundary of the domain (i.e. when $\beta \to \pi/4-\alpha/2$) and exhibit small values of w_A^c and Δ_{ABC}^{max}. As such, these results indicate that we cannot realize closed origami structures that are at the same time bistable and inflatable using a single triangle building block.

2.4 Extending the design space to enable deployment via inflation

In an attempt to realize inflatable closed origami structures with stable flat and expanded configurations, we turn our focus to systems realized by assembling two different triangles with internal angles $(\alpha^{(1)}, \beta^{(1)})$ and $(\alpha^{(2)}, \beta^{(2)})$. To begin with, we arrange $2n$ triangles of each type to form two identical layers with n-fold symmetry and connect them at their outer boundaries (see Figures 2.2a and c). The resulting star-like structures (reminiscent of an origami waterbomb base[32,74]) define an internal volume $V = 2n(V_{ABC}^{(1)} + V_{ABC}^{(2)})$, exhibit geometric incompatibility $\Delta = 2n(\Delta_{ABC}^{(1)} + \Delta_{ABC}^{(2)})$ and are inflatable only if $\log h = \log(\Gamma^{V^{max}}/\Gamma^c) \geq 0$, where $\Gamma^{V^{max}}$ and Γ^c are the arc lengths measured on the Δ-V curve between the states with $V = 0$ and $V = V^{max} = \max(V)$ and between the two stable configurations, respectively. However, it is important to note that to realize these star-like structures the pair of triangles cannot be arbitrarily chosen. This is because geometric compatibility is guaranteed only if the two triangles have (*i*) identical deployed compatible height (i.e. $w_A^{c\,(1)} = w_A^{c\,(2)}$); (*ii*) connecting deployed edges (either AB or AC) of equal length; and (*iii*) angles that satisfy $\alpha^{(1)} + \alpha^{(2)} = \pi/n$.

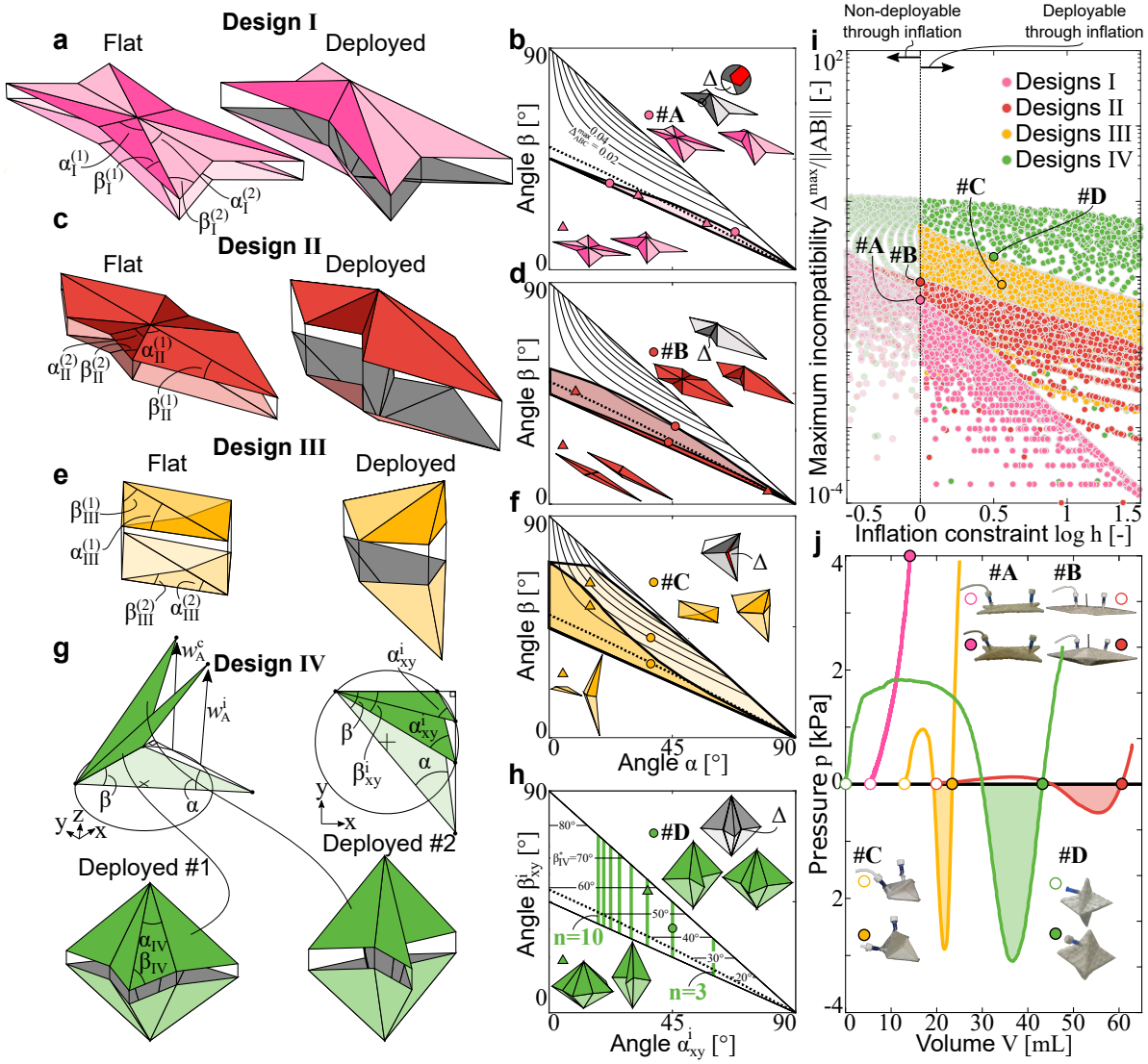

Figure 2.2: Bistable and inflatable origami shapes. **(a-f)** Examples of (a-b) Designs I, (c-d) Design II, and (e-f) Design III geometries in both the flat and deployed stable configurations along with the regions in the $\alpha - \beta$ space leading to inflatable structures. Note that the bright and dark shaded regions in the plots represent the triangles with angles $(\alpha^{(1)}, \beta^{(1)})$ and $(\alpha^{(2)}, \beta^{(2)})$, respectively. Further, the contour lines represent the maximum incompatibility of the triangular building blocks, Δ^{max}_{ABC}. **(g)** Deployment of a triangular building block that has been initially rotated around its edge BC to have a height w^i_A. **(h)** Contour map of angle β^*_{IV} required to obtain Designs IV that are both inflatable and bistable. **(i)** Maximum incompatibility, Δ^{max}, versus the inflation constraint, h, for $500,000$ random geometries of Designs I-IV. **(j)** Pressure-volume curves recorded when testing our centimeter-scale prototypes. See Supplementary Information in Section A.1 for rationale behind geometry and material selection.

As shown in Figure 2.2a, we first connect the two triangles via their longest edge ($||AB^{(1)}|| = ||AB^{(2)}||$) and refer to these structures as Designs I. We identify all possible geometries by enforcing requirements (*i*)-(*iii*) and find that designs deployable through inflation (for which $\log h \geq 0$) not only have a deployed shape almost indistinguishable from the initial flat one (see insets of structures in Figure 2.2b), but are also made of two triangles with very low Δ^{max}_{ABC} (see area highlighted in magenta in Figure 2.2b). As such, the inflatable Designs I exhibit very low maximum incompatibility $\Delta^{max} = \max(\Delta)$ (see magenta markers in Figure 2.2i for $500,000$ randomly chosen geometries). To investigate the performance of these inflatable designs, we fabricate and test the geometry with $\log h \geq 0$ and the highest Δ^{max} (Design I-A with $(\alpha^{(1)}_{\text{I-A}}, \beta^{(1)}_{\text{I-A}}) = (22°, 35°)$ and $(\alpha^{(2)}_{\text{I-A}}, \beta^{(2)}_{\text{I-A}}) = (68°, 14°)$ for which $\Delta^{max}/||AB|| = 2.67 \times 10^{-2}$— see magenta circular marker in Figure 2.2i). A centimeter-scale prototype with $||AB^{(1)}|| = ||AB^{(2)}|| = 60$ mm is constructed by connecting 3D-printed stiff triangular facets with compliant hinges made of thin polyester sheets and an inflatable cavity is formed by coating it with a 0.5 mm-thick layer of silicone rubber (see insets in Figure 2.2j and the Supplementary Materials, Section A.2 for details). The sample is then deployed by supplying water at a constant rate of 10 mL/min with a syringe pump (Pump 33DS, Harvard Apparatus), while monitoring the pressure with a pressure-sensor (MPXV7025DP — see the Supplementary Materials, Section A.3 for details). We find that the pressure, p, increases monotonically with V until the maximum volume for the cavity is reached (see Figure 2.2j). As such, our test reveals that the Δ^{max} of this design is not large enough to make the fabricated structure bistable.

Next, with the goal of increasing the geometric incompatibility of the inflatable designs, we investigate the response of star-like structures in which the longest edge of one triangle, $AB^{(1)}$, is connected to the shortest edge of the other one, $AC^{(2)}$ (we refer to these designs as Designs II—see Figure 2.2c). Again, we impose requirements (*i*)-(*iii*) to identify all possible geometries and find that those deployable through inflation comprise two very distinct triangles: a first one with low Δ^{max}_{ABC} but $\log h^{(1)}_{ABC} > 0$ (see area highlighted in dark red in Figure 2.2d) and a second one with substantially larger Δ^{max}_{ABC} but $\log h^{(2)}_{ABC} < 0$ (see area highlighted in bright red in Figure 2.2d). Remarkably, we find that the combination of these different triangles results in inflatable designs with higher maximum incompatibility compared to Designs I (see red markers in Figure 2.2i for $500,000$ randomly chosen geometries). As a result, when we fabricate and test the inflatable geometry that maximizes Δ^{max} (Design II-B with $(\alpha^{(1)}_{\text{II-B}}, \beta^{(1)}_{\text{II-B}}) = (43.6°, 25.2°)$ and $(\alpha^{(2)}_{\text{II-B}}, \beta^{(2)}_{\text{II-B}}) = (46.4°, 33.5°)$ for which $\Delta^{max}/||AB|| = 8.58 \times 10^{-2}$—see red marker in Figure 2.2i) we observe a negative pressure region (see red curve in Figure 2.2j). This confirms the presence of an expanded stable configuration that can be reached through fluidic actuation (see Figure A.23 for details) and indicate the existence of a threshold value of $\Delta^{max}/||AB||$ (dependent on materials and fabrication process) that marks the transition from monostable to bistable behavior.

Whereas the connection of two different triangles side by side enables us to design inflatable and bistable structures, it limits us to star-like shapes. To expand the range of shapes, we next

arrange the two triangles on top of each other in the flat configuration and mirror them twice to form an inflatable cavity (we refer to these structures as Design III—see Figure 2.2e). This leads to geometries comprising eight triangles that are initially flat and transform into wedge-like shapes upon deployment. As for Designs I and II, geometric compatibility for Designs III requires a pair of triangles with $w_A^{c\,(1)} = w_A^{c\,(2)}$ and $||AB^{(1)}|| = ||AC^{(2)}||$, but the closure of the cavity is only possible if $\alpha_{\text{III}}^{(1)} = \alpha_{\text{III}}^{(2)}$. By imposing these constraints and $\log h \geq 0$, we find that inflatable Designs III can be realized by combining two triangles with $\log h_{ABC} < 0$ and, therefore, substantially larger Δ_{max}^{ABC} (see areas highlighted in yellow in Figure 2.2f). This is because the internal volume of Designs III is defined by the difference between $V_{ABC}^{(1)}$ and $V_{ABC}^{(2)}$ (i.e. $V = 4(V_{ABC}^{(1)} - V_{ABC}^{(2)})$) instead of their sum as for Designs I-II. Importantly, by plotting Δ^{max} vs. h for $500,000$ randomly chosen Designs III, we find that these geometries are characterized by much larger maximum incompatibility in the inflatable domain. As a result, when we fabricate and test Design III-C with $(\alpha_{\text{III-C}}^{(1)}, \beta_{\text{III-C}}^{(1)}) = (37.1°, 30.0°)$ and $(\alpha_{\text{III-C}}^{(2)}, \beta_{\text{III-C}}^{(2)}) = (37.1°, 40.6°)$, (for which $\Delta^{max}/||AB|| = 9.93 \times 10^{-2}$), we record even larger values of negative pressure (i.e. larger energy barrier preventing the snap back) compared to the previous bistable Design II-B (see Figure 2.2j).

So far, all identified designs (i.e. Designs I-III) have been realized by assembling triangles that initially lie in the xy-plane and recover their angle α on such plane for $w_A = w_A^c$. However, the triangle in the xy-plane can also be seen as the projection of a triangle with internal angles α and β that has been initially rotated around its edge BC to have a height w_A^i and projected angles α_{xy}^i and β_{xy}^i (see Figure 2.2g). In this case, if $\beta_{xy}^i \in [\pi/4 - \alpha_{xy}^i/2, \pi/2 - \alpha_{xy}^i]$, the angle α_{xy}^i is preserved for two distinct deployment heights, w_A^i and w_A^c (see inset in Figure 2.2g and Supplementary Materials, Section A.1 for details). As such, we can use these triangles as building blocks to realize star-like origami shapes with two expanded stable configurations in correspondence of w_A^i and w_A^c. An interesting feature of this family of structures (which we refer to as Designs IV) is that, if we select $\alpha_{xy}^i = \pi/n$ $(n = 3\,, 4\,, \ldots)$ and

$$\beta_{IV} \geq \beta_{IV}^* = \tan^{-1}\left(\sqrt{2}\tan\beta_{xy}^i\right), \tag{2.5}$$

the resulting origami are bistable and inflatable even if made out of a single triangular building block (see Supplementary Materials, Section A.1 for details). This is because, for $\beta_{IV} \geq \beta_{IV}^*$, V_{ABC} monotonically decreases when deploying the triangle from w_A^i to w_A^c, so the compatible state corresponding to w_A^c can always be reached by deflation. To demonstrate the concept, in Figure 2.2i, we consider $500,000$ different geometries of Design IV for which $\alpha_{xy}^i = \pi/4, \beta_{xy}^i \in [\pi/4 - \alpha_{IV}/2, \pi/2 - \alpha_{IV}]$, and $\beta_{IV} \in [\beta_{xy}^i, \pi/2[$ and find that all geometries with $\beta_{IV} \geq \beta_{IV}^*$ are inflatable. Further, since β_{IV}^* is not affected by α_{xy}^i (see map of β_{IV}^* in Figure 2.2h), inflatable origami structure can be realized by assembling highly incompatible triangles lying near the upper bound of their design space. This results in inflatable designs exhibiting a maximum incompatibility, Δ^{max}, much higher than Designs I-III and with a flat stable state in the xz-plane (since for $\beta = \pi/2 - \alpha$ the compatible deployment height is such that the deployed triangle lies in the orthogonal xz-plane with $w_A^c = ||AC||$— see

Supplementary Materials, Section A.1 for details). In full agreement with these findings, when we fabricate and test Design IV-D with $(\alpha_{\text{IV-D}}, \beta_{\text{IV-D}}) = (29°, 56°)$ and $(\alpha^i_{xy}, \beta^i_{xy}) = (45°, 33°)$, (for which $\Delta^{max}/||AB|| = 2.05 \times 10^{-1}$), we record the largest negative pressure and energy barrier in the deployed stable state (see green curve in Figure 2.2j).

2.5 Meter-scale functional structures

As a next step, we use the simple geometries presented in Figure 2.2 as basis to design functional and easily deployable structures for real-world applications and build them at the meter scale.

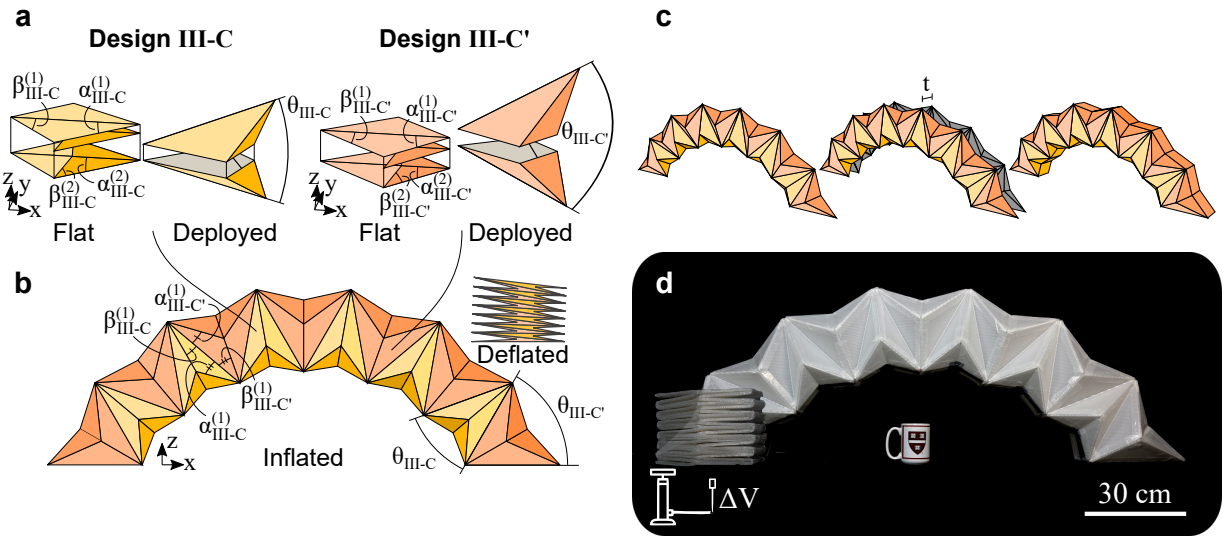

Figure 2.3: Meter-scale inflatable archway. **(a)** The two Design III units used to construct the arch. **(b)** Schematics illustrating an inflatable archway comprising six Design III-C and seven Design III-C′ units. **(c)** To facilitate inflation, we create a single cavity by cutting all units through their xz mirror plane, separating the two resulting parts by a distance t, and connecting them with rectangular facets. **(d)** Fabricated meter-scale inflatable arch in its flat and deployed stable configurations.

To begin with, we use the expanded wedge-like shapes of Designs III as building blocks to realize an inflatable archway. Focusing on Design III-C, we find that in the expanded stable state it has an opening angle $\theta_{\text{III-C}} = 40°$ (see Figure 2.3a). To design a deployable arch, we couple this unit with a different geometry of the same design family (which we referred to as Design III-C′) that (*i*) is bistable and deployable through inflation; (*ii*) has an edge AB of equal length; (*iii*) has an opening angle $\theta_{\text{III-C}'}$ such that, when we alternate $m+1$ units of Designs III-C′ with m units of Designs III-C, we span an angle of 180° in the expanded configuration; and (*iv*) has the larger triangle (referred to as triangle 1 in Figure 2.2) identical to that of Design III-C but mirrored (i.e. $\alpha^{(1)}_{\text{III-C}} = \beta^{(1)}_{\text{III-C}'}$ and $\beta^{(1)}_{\text{III-C}} = \alpha^{(1)}_{\text{III-C}'}$—see Figure 2.3b) to ensure compactness in the flat state. By inspecting the database of Figure 2.2j, we find that for $m = 6$ all above requirements

are satisfied when Design III-C' is characterized by ($\alpha^{(1)}_{\text{III-C}'}$, $\beta^{(1)}_{\text{III-C}'}$, $\alpha^{(2)}_{\text{III-C}'}$, $\beta^{(2)}_{\text{III-C}'}$) = (30°, 37°, 30°, and 51°). However, since the resulting archway comprises 13 inflatable cavities, multiple pressure inputs would be needed to inflate it. To simplify the deployment process, we modify the structure by cutting it through the xz mirror plane, separating the two resulting parts by a distance t, and connecting them with rectangular facets (see insets in Figure 2.3c). Since this procedure does not affect the geometric deployment of the triangles, we expect the additional facets to have negligible impact on the structure's multistability, but to facilitate its inflatability by creating a single cavity. In Figure 2.3d, we show a meter-scale version of this archway with $||AB|| = 30$ cm and $t = 10$ cm constructed out of corrugated plastic sheets (clear 8 ft × 4 ft, 4-mm thick sheets from Corrugated Plastics). To build this structure, we use a digital cutting system (G3 cutter from Zünd) to cut two parts (each comprising both triangular building blocks and rectangular facets— see Figure A.20) and pattern the hinges by scoring the sheets to locally reduce the thickness of the material. We then connect the two digitally cut parts using adhesive tape to form an airtight cavity (see Supplementary Materials, Section A.2 for details). In the folded configuration, the structure has a height of 20 cm and a width of 30 cm. Upon pressurization, it inflates into a 60 cm tall and 150 cm wide archway that, because of its multistability, preserves its shape even when the pressure is suddenly released. Finally, it can be folded back to the initial flat state by applying vacuum to overcome the energy barrier.

Another strategy to realize functional shapes is to merge components of different design families together to form a single cavity. As an example, we can create an inflatable tent-like geometry by combining one layer of a Design I with another one of a Design IV (see Figure 2.4a). To ensure successful merging, the two layers must have (*i*) outer edges BC of equal length, and (*ii*) the same xy-projection in the two compatible states (i.e. $\alpha^{(1)}_{\text{I}} = \alpha^{(2)}_{\text{I}} = \alpha^{i}_{xy}$ and $\beta^{(1)}_{\text{I}} = \beta^{(2)}_{\text{I}} = \beta^{i}_{xy}$). Further, to realize structures with a fully flat compatible state, we choose the triangles to lie on the upper boundary of the deployable domain (i.e. triangles with $\beta^{(1)}_{\text{I}} = \pi/2 - \alpha^{(1)}_{\text{I}}$ and $\beta^{(2)}_{\text{I}} = \pi/2 - \alpha^{(2)}_{\text{I}}$). By imposing these constraints, we can design tent-like structures that can be folded flat and expanded via inflation (see Figure A.24 for a centimeter-scale version), but their compactness is limited by the long AB edge of the Design IV. To further decrease the occupied volume in the compact state, we truncate the triangular building blocks of the Design IV layer into quadrilaterals and add additional layers of Design IV, some of which can be folded inwardly. As shown in Figure 2.4b, these operations do not only reduce the initial volume, but also result in a more livable sheltered space in the deployed state. To demonstrate this strategy, we fabricate the structure shown in Figure 2.4b at the meter-scale applying the same construction process used for the inflatable archway (see Supplementary Materials, Section A.2 for details). As shown in Figures 2.4c and d, the structure can be folded completely flat (with the ceiling folded inward) to occupy a space of 1 × 2 × 0.25 m. When an input pressure is provided, the structure first expands to a stable configuration with the roof folded inward. Upon further pressurization the roof snaps outward and the final deployed shape of

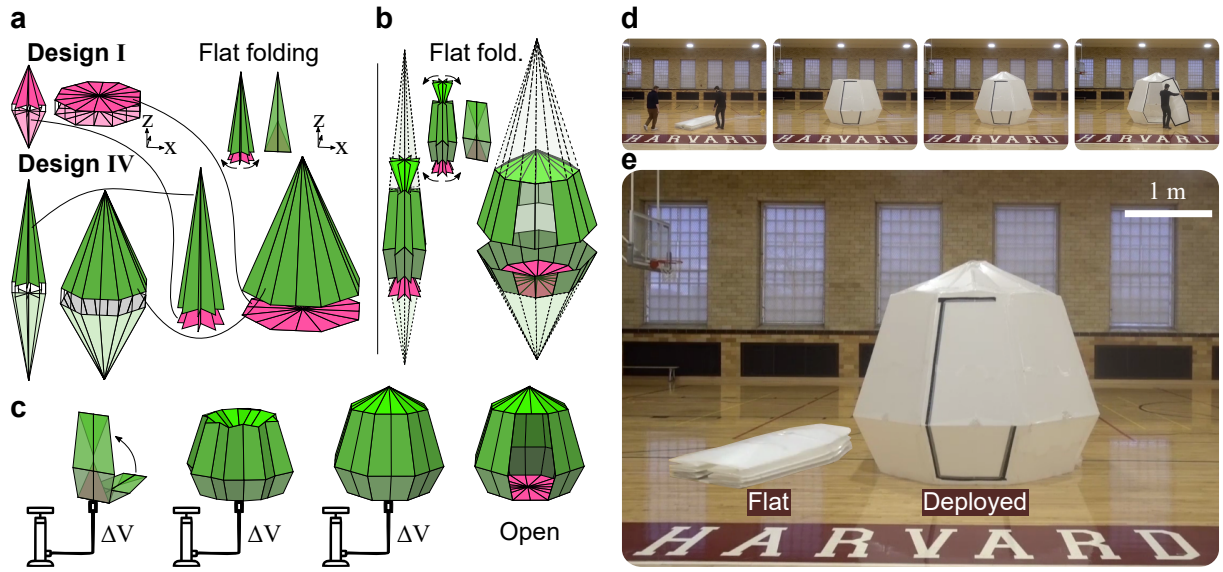

Figure 2.4: Meter-scale inflatable shelter. **(a)** A tent-like design can be created by merging one layer of a Design I with another one of a Design IV. Note in that the initial, zero-volume configuration of the tent, both layers are in their compatible expanded state, whereas in the final inflated configuration of the tent, both layers are in their initial state (flat for Design I and initially rotated for Design IV). **(b)** The initial volume can be further decreased by truncating the triangular facets into quadrilaterals and arranging successive layers of Design IV. **(c)** Schematics illustrating the deployment process. **(d-e)** The fabricated meter-scale inflatable shelter can be inflated from a compact state to a fully deployed state. Because of multistability, the door can be opened and make the internal space accessible.

$2.5 \times 2.6 \times 2.6$ m is reached. Importantly, because of the multistability, at this point the door can be opened without impacting structural integrity, making the internal space accessible. Finally, using vacuum, the shelter can be folded back to the flat configuration.

2.6 Conclusion

In summary, we demonstrated how geometry can be efficiently exploited to realize inflatable origami structures characterized by two stable configurations—one compact and one expanded. The design methodology presented in this work could be extended both to larger and smaller scales if properly accounting for loading conditions and fabrication challenges[4,52,53,62]. Since our functional structures are multistable, they can also be designed to achieve target deployment sequences (Figure A.25). In addition, by introducing building blocks comprising more than two different facets, we expect to further expand the range of achievable shapes (Figure A.26). To that end, complementary to our geometric model and experiments, a mechanical model capable of predicting the full energy landscape[33,75] could provide a useful tool to guide such exploration. Finally, building on our results, deployable structures able to switch between targeted stable states

could be efficiently identified by generalizing our design rules to arbitrary origami polyhedra and, combining them with stochastic optimization algorithms, solve the inverse design problem.

2.7 Methods

Details of the design, materials, and fabrication methods are summarized in Supplementary Materials, Sections A.1 and A.2. The experimental procedure of the inflation with water to measure the pressure-volume curve is described in Supplementary Materials, Section A.3. Finally, additional information about extending our methodology to more complex designs is provided in Supplementary Materials, Section A.4.

3

MuA-Ori: Multimodal Actuated Origami

By: Antonio Elia Forte*, David Melancon*, Leon M. Kamp, Benjamin Gorissen, and Katia Bertoldi.
MuA-Ori: Multimodal Actuated Origami. arXiv:2112.01366.

3.1 Abstract

Recently, inflatable elements integrated in robotics systems have enabled complex motions as a result of simple inputs. However, these fluidic actuators typically exhibit unimodal deformation upon inflation. Here, we present a new design concept for modular, fluidic actuators that can switch between deformation modes as a response to an input threshold. Our system comprises bistable origami modules in which snapping breaks rotational symmetry, giving access to a bending deformation. By tuning geometry, the modules can be designed to snap at different pressure thresholds, rotate clockwise or counterclockwise when actuated, and bend in different planes. Due to their ability to assume multiple deformation modes as response to a single pressure input we call our system MuA-Ori, or Multimodal Actuated Origami. MuA-Ori provides an ideal platform to design actuators that can switch between different configurations, reach multiple, pre-defined targets in space, and move along complex trajectories.

3.2 Introduction

Deformable and inflatable components have increasingly been integrated into robotic systems, as they provide complex deformations[76,77], the ability to morph into target shapes[55,57,78–80], and inherent compliance, which in turn enables safe interactions[81–83]. These, however, suffer from a common drawback: an intrinsic one-to-one relationship between input pressure and output deformation. Upon inflation in fact, fluidic actuators exhibit unimodal deformation, which accentuates as pressure increases[10]. In order to overcome this and create complex functionality, multiple actuators can be assembled and carefully sequenced[13,84–87], or multiple chambers of a single actuator can be pressurized independently[88,89]. As an alternative route, bidirectional bending has been achieved by harnessing material inextensibility[90] and non-linearity[91,92]. However, a design strategy that enables arbitrary deformation modes with a single pressure input is still absent.

In an effort to design novel robotic systems, engineers and scientists have recently explored origami principles to create machines that are self-foldable[26,27,58] and realizable in a variety of materials using both planar and 3D fabrication techniques[93–95]. The functionality of such origami robots can be further expanded if the crease pattern supports a non-convex energy landscape, which enables multiple stable states[31,32,34–37,96–98]. For example, self-locking grippers[38] and energy-absorbing components for drones[99] were designed out of multistable origami sheets based on the tiling of the degree-four vertex; bistable mechanical bits and logic elements were created by introducing multistability in the classic waterbomb origami pattern[32,100,101] and, finally, bistable configurations of the Kresling pattern[96,102] were exploited to generate locomotion via peristaltic motion[103] or differential friction[104], create flexible joints for robotic manipulation[105], and store mechanical memory[97,106]. All together, these examples show that multistable origami are a

promising platform to realize fluidic actuators capable of supporting arbitrary deformation modes when actuated with a single input.

Inspired by the potential of the Kresling pattern in the design of robotic systems, here we employ this classic origami fold as a building block to realize multi-output, but single-input actuators. As part of our strategy, we start with a monostable Kresling pattern and make it bistable by introducing two additional valley creases in one of its panels (see Figures 3.1a-b). During inflation, this panel unfolds and snaps outward, breaking the rotational symmetry of the module. Importantly, upon vacuum such asymmetry gives rise to bending in the opposite direction to the bistable panel up until a critical negative pressure is reached: at this point the panel snaps inward, resetting the module to its initial state. We use a combinatorial approach to couple multiple modules and create actuators with prescribed and complex deformation states that can be reached by controlling a single pressure input. Given that they output multiple deformation modes with a single input, we call our devices Multi-modal Actuated Origami, or MuA-Ori. MuA-Ori offers new opportunities for the design of robotic systems capable of performing complex tasks despite the simple actuation scheme, as demonstrated by the design of a land rowing robot.

3.3 The MuA-Ori building blocks based on Kresling pattern

To realize our nonlinear and reconfigurable MuA-Ori, we use origami building blocks comprising one layer of the classic Kresling pattern (also known as nejiri ori)[102]. More specifically, in its initial, undeformed state, the single module consists of two hexagonal caps with edges of length $l = 30$ mm, separated by a distance $h = 24$ mm, and rotated by an angle $\alpha = 30°$ with respect to each other (see Figure 3.1a). The hexagons are connected at each side by a panel comprising a pair of triangular facets coupled by alternating mountain (i.e. edges $A'B$ and AB') and valley (i.e. edge BB') creases. Since the Kresling pattern is not rigid foldable[96], any change in its internal volume will lead to an incompatible configuration. To accommodate the resulting geometrical frustration, we 3D-print 1-mm thick triangular facets out of a compliant material (TPU95A from Ultimaker with Young's modulus $E = 26$ MPa) and reduce the thickness locally to 0.4 mm to create the hinges (see prototype in Figure 3.1a). Further, to facilitate coupling between different modules, we 3D-print the hexagonal caps out of a stiffer material (PLA from Ultimaker with Young's modulus $E = 2.3$ GPa) and, to form an inflatable cavity, we coat the origami unit with a thin layer of polydimethylsiloxane (PDMS) (see Supplementary Materials, Section B.1 for fabrication details). Finally, it is worth noticing that the chosen values of the parameters (h, l, α) yield a monostable origami module (i.e. the Kresling pattern is only stable in its initial, undeformed state).

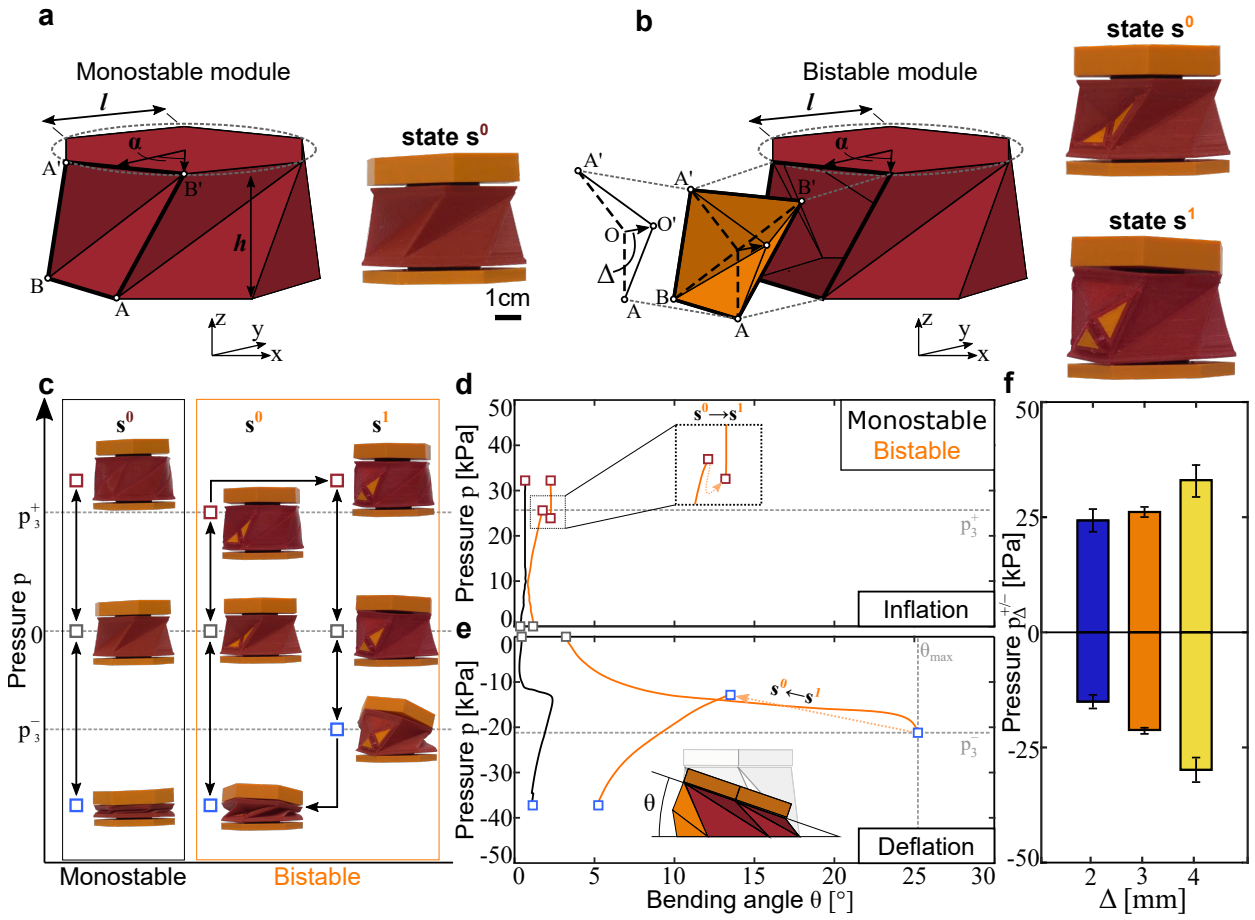

Figure 3.1: Bistable origami modules as building blocks for multi-output, single input inflatable actuators. (a) Schematics of a monostable module based on the hexagonal-base Kresling origami pattern, along with a 3D-printed prototype. The panels of the monostable modules remain always folded inward. We refer to this state of deformation as state s^0. **(b)** Bistable module with a modified panel (highlighted in orange) made of four triangular facets $A'BO'$, $AO'B'$, $AO'B$, and $A'B'O'$ and characterized by a depth Δ from vertex O to O', along with a 3D-printed prototype displayed in its two stable states: state s^0 for which all panels (including the modified panel) are folded inward; and state s^1 for which the modified panel is popped outward (while all other panels are still folded inward). **(c)** State diagram of the pressurized origami modules. **(d-e)** Pressure vs. bending angle curves for the monostable and bistable origami modules during inflation and deflation. At the onset of deflation for the bistable unit, θ is slightly larger than in the monostable module due to the geometrical incompatibility that arises in the structure when the modified panel is in the outward configuration. **(f)** Experimental positive and negative pressure thresholds, p_Δ^+ and p_Δ^-, as a function of the modified panel's depth, Δ.

To investigate the response of a single module, we inflate it with water while submerged in water (to eliminate the effects of gravity - see Supplementary Materials, Section B.2 for details). As expected[96], the Kresling unit extends and contracts (while twisting at the same time) upon inflation and deflation (Figure 3.1c) and returns to its undeformed state as soon as the pressure is removed. This state of deformation, in which all panels are folded inward, is named s^0. When in this state the bending angle, θ, remains close to zero (Figures 3.1d-e).

Aiming at unlocking different deformation modes with one single pressure input, we then take inspiration from bistability in degree-four vertices[35,101,107] and modify one of the original Kresling panels by introducing two additional valley creases (i.e. AO and $A'O$ with O being the midpoint of crease BB', see Figure 3.1b). While this effectively creates a degree-four vertex, it results in a monostable origami unit, as no snap-through instability is recorded upon inflation (see Supplementary Materials, Section B.2 for details). To increase the geometric incompatibility during deployment and achieve bistability in the unit, we then move the degree-four vertex inward by Δ (see Figure 3.1b where Δ is the norm of vector $\overline{OO'}$ perpendicular to vectors $\overline{AA'}$ and $\overline{BB'}$). Choosing $\Delta = 3$ mm, for example, we can fabricate an origami unit that can easily transition between two stable states: state s^0 for which all panels are folded inward, and state s^1 for which the modified panel is popped outward (while all other panels are still folded inward). Similar to the unit based on the classic Kresling pattern, upon inflation this modified module simply extends with all panels bent inward if $p < 26.1 \pm 0.9$ kPa. However, at $p_3^+ = 26.1 \pm 0.9$ kPa (where the subscript refers to $\Delta = 3$ mm and the superscript refers to positive pressure), the unit snaps from state s^0 with the modified panel folded inward to state s^1 where it is popped outward (Figure 3.1c)—a transition which is accompanied by a discontinuity of the bending angle θ (see zoom-in in Figure 3.1d). Finally, a further increase in pressure causes the unit to elongate until the maximum structural limit is reached. Afterward, when the input pressure is removed, the modified panel remains popped outward (see Figure 3.1c) because of bistability. As such, when we apply negative pressure the unit not only contracts, but also bends (see Figures 3.1c and e), exhibiting a behaviour that radically differs from that of the Kresling module. Specifically, we find that at first θ monotonically increases until the two hexagonal caps come into physical contact effectively clipping the available range of bending deformation to $\theta_{max} = 21.7 \pm 0.3\,^\circ$. As previously mentioned, this bending deformation is caused by the modified panel, which remains in the popped outward configuration (while the other panels fold under increasing negative pressure) and breaks the radial symmetry. Finally, when the negative pressure passes the threshold $p_3^- = -21.2 \pm 0.7$ kPa (where the superscript refers to negative pressure), the modified panel snaps back to the inward position (see snapping transition from state s^1 to state s^0 in Figure 3.1c) and θ suddenly decreases (dashed orange arrow in Figure 3.1e). If one continues to apply negative pressure to the module, the unit folds (almost) flat, as clearly shown by the decreasing trend of θ.

Next, we investigate the effect of the depth Δ of our degree-four vertex panel on the positive and negative pressure thresholds, p_Δ^+ and p_Δ^-, as well as the deformed configurations reached upon snapping. The experimental results reported in Figure 3.1f for $\Delta = 2$, 3, and 4 mm indicate that the absolute value of the pressure thresholds increases with Δ within the considered range. Differently, we find that the bending angle, the axial displacement of the end caps and their relative twist remain almost constant with Δ. In fact, the first reaches an upper limit when the caps get in contact with each other and the other two are dominated by the geometric characteristics of the Kresling pattern

(see Figure B.7). Note that for $\Delta < 2$ mm, the modules are found to be monostable. This means that negligible bending is recorded upon application of negative pressure, since the degree-four vertex panel snaps back immediately. Differently, for $\Delta \geq 4$ mm, the positive pressure required to snap the modified panel outward is so high that the module fails (see Figure B.6).

3.4 Extending the design space for complex outputs

After demonstrating that our bistable module can transition between different stable states with distinct deformation modes (i.e. extension, twisting, and bending), we next combine these units to form actuators able to achieve complex outputs: the MuA-Ori. By combining n modules, we can construct $(3 \times 2 \times 6 + 1 \times 2)^n = 38^n$ different actuators since for each module k we can select (*i*) either a regular Kresling module or a unit comprising a modified, degree-four vertex panel with depth $\Delta^k \in \{2, 3, 4\}$ mm; (*ii*) the upper cap to be rotated clockwise or anticlockwise with respect to the bottom one, $c^k \in \{//, \backslash\backslash\}$, and (*iii*) the side on which the modified panel is located, $f^k \in \{1, \ldots, 6\}$ (see Figure 3.2a). Note that the domain of all constraints is discrete since we choose a limited set of values for Δ and all end plates to have their sides aligned.

To navigate the vast design space systematically and efficiently, we develop a simple algorithm that predicts all stable states and snapping transitions for actuators comprising n modules upon inflation and deflation. First, we extract key geometric features from the experiments conducted on single units, i.e. height, twisting, and bending angle of the top cap associated to all stable states and snapping transitions (see Figures B.6-B.7). When assuming pressure continuity, these data allow the prediction of all configurations for the stable states and snapping transitions of any n-units actuator (see Supplementary Materials, Section B.3 for details on the algorithm). Note that we also assume perfect coupling between units, so that the pressure thresholds, $p_\Delta^{+/-}$, found in the experimental characterization of Figure 3.1f, remain unchanged and identical for units with the same geometrical parameters.

As an example, in Figure 3.2a, we consider an actuator comprising $n = 2$ modules characterized by $[\Delta^1 c^1 f^1; \Delta^2 c^2 f^2] = [2//3; 4//6]$, where we assume the first unit to be the one at the bottom. As expected, this MuA-Ori has four stable states at atmospheric pressure, s^{ij} (where the subscripts $i,j = 0, 1$, refer to the state of the modified panels, with $\Delta = 2$ and 4 mm, respectively), and six snapping transitions that can be triggered by varying the internal pressure (Fig 3.2b). Whereas the stable states s^{10} and s^{11} can be readily obtained by simply increasing pressure, a more complex pressure path is required to achieve state s^{01}, as one has to (*i*) increase pressure above p_4^+ and then (*ii*) decrease it below p_2^-. To validate the model, we then conduct experiments on units connected via 3D-printed screws (see Figure B.2 for details) and find that they closely match the predictions (see Fig 3.2b).

Since our final goal is to build actuators with programmed deformation modes, we further quantify the deployment of our actuator by recording the vector connecting the caps' centroids, $\mathbf{d}$, at each stable state and snapping transition. In Figure 3.2c we report the norm of $\mathbf{d}$ normalized by the height of a single module, $||\mathbf{d}||/h$, and the angle between each $\mathbf{d}$ and the z-axis, θ_{act}, for all 12 configurations supported by the actuator characterized by $[\Delta^1 c^1 f^1; \Delta^2 c^2 f^2] = [2//3; 4//6]$. We find that in the positive pressure regime the achievable deformation is limited to simple extension, resulting in configurations all clustered in a portion of the design space characterized by $\theta_{act} \sim 5°$ and $||\mathbf{d}||/h \sim 2$ (gray and red triangles). By contrast, behaviors characterized by large bending angles ($\theta_{act} \sim 20°$) unfold under negative pressure (blue triangles). Importantly, such bending provides opportunities for the design of actuators that can reach a wider range of configurations. This becomes even clearer when expanding the range of possible configurations by varying the parameters Δ^k, c^k, and f^k and considering not only $n = 2$ but also $n = 3$ building blocks (triangles and circles in Figure 3.2d, respectively). Once again, we notice that all configurations under positive

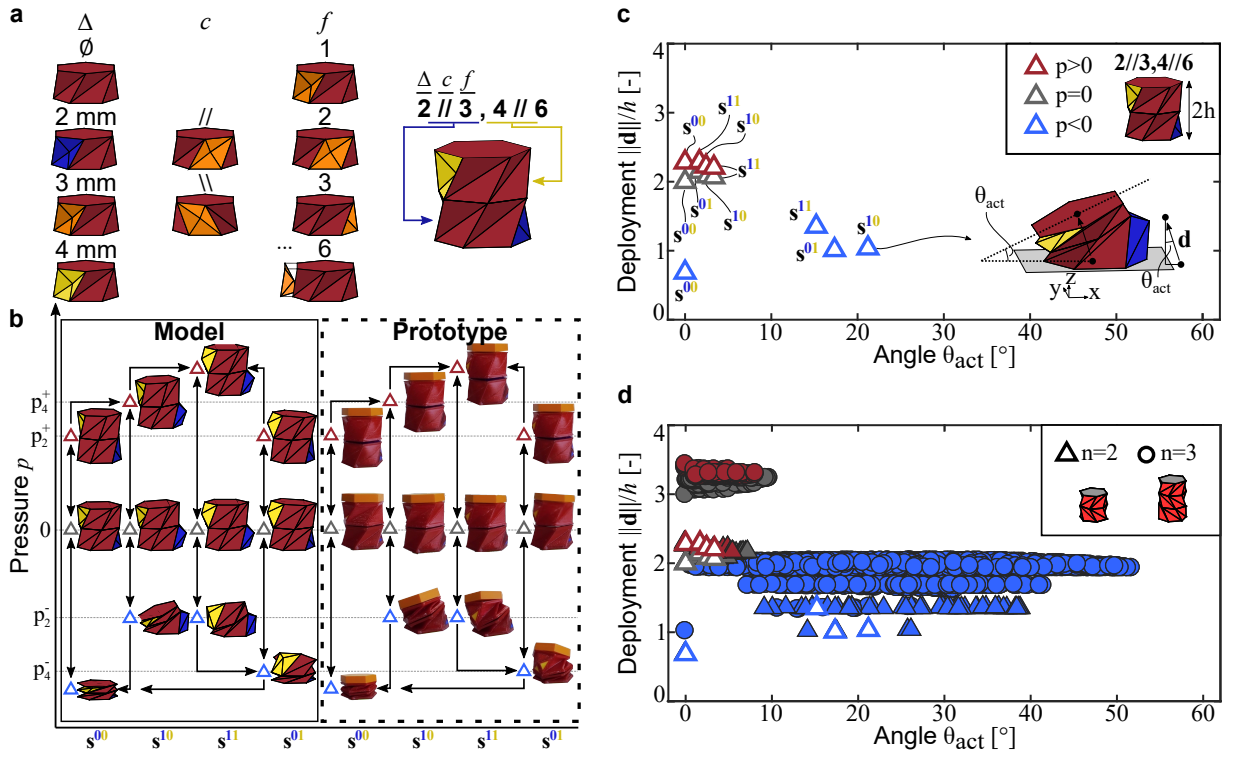

Figure 3.2: Extending the design space. **(a)** For each k module we define 3 geometrical parameters: Δ^k, c^k, and f^k. Note that, for simplicity, we also assign f^1, but only the location of the modified panel relative to its neighbor is important. **(b)** State diagram for a 2-units actuator characterized by $[\Delta^1 c^1 f^1; \Delta^2 c^2 f^2] = [2//3; 4//6]$: geometrical model prediction on the left, experimental snapshots on the right. **(c)** Normalized deployment $||\mathbf{d}||/h$ and angle θ_{act} for every stable state of the 2-units actuator characterized by $[\Delta^1 c^1 f^1; \Delta^2 c^2 f^2] = [2//3; 4//6]$. **(d)** Normalized deployment $||\mathbf{d}||/h$ and angle θ_{act} for every stable state of any possible 2-units (triangles) and 3-units (circles) actuator in the design space.

and atmospheric pressure cluster on low values of bending angle and a normalized deployment that is roughly equal to the number of building blocks considered. Differently, in the negative pressure regime a rich set of deformations unfolds, characterized by a wide range of achievable θ_{act} (the maximum values of θ_{act} increases from 40° to 50° from $n = 2$ to $n = 3$) at near-constant normalized deployment ($||\mathbf{d}||/h$ increases slightly from about 1.5 to 2 from $n = 2$ to $n = 3$). These results indicate that by stacking our origami modules to form arrays, we can realize actuators capable of supporting a variety of deformation modes, which can be selected by varying the level of applied pressure.

3.5 Inverse design to reach multiple targets

Motivated by the results in Figure 3.2, we then investigate the behavior of arrays with a larger number of units. Our goal is to build actuators capable of switching between target deformation modes when inflated with a single pressure source. However, since the use of n modules leads to 38^n possible actuator designs (i.e. $54,872$ for $n = 3$ and $2,085,136$ for $n = 4$), it is crucial to use a robust algorithm to efficiently scan the range of responses that can be achieved and identify configurations leading to the target deformation modes. Toward this end, given the discrete nature of our design variables, we use a greedy algorithm based on the best-first search method[108,109]—a progressive local search algorithm that, at each iteration, minimizes the cost function by looking at a set of available solutions (see Figure 3.3). Although there exists many algorithms to solve this type of discrete optimization problems[110,111], we find that the greedy algorithm provides the best trade-off between accuracy and computational cost (see Supplementary Information, Section B.4 for details and comparison of the different algorithms). Specifically, our greedy algorithm identifies MuA-Ori comprising n units built out of n_s super-cells each with n_u modules (so that $n = n_u \cdot n_s$) whose tip can reach a desired set of targets arbitrarily positioned in the surrounding space. At the first iteration, the algorithm starts by selecting the actuator super-cell design that minimizes

$$\Psi = \frac{1}{n_{targets} \cdot h} \sum_{m=1}^{n_{targets}} \min ||\mathbf{d} - \mathbf{T}_m||, \tag{3.1}$$

where $n_{targets}$ is the number of targets, and $\mathbf{T}_m$ is the vector connecting the m-th target with the origin. Once the first super-cell is chosen, the algorithm stores it in memory and starts a second iteration. This comes to an end when the algorithm identifies a second super-cell that, connected to the first, one minimizes Eq. 3.1. The first two super-cells are then stored in memory and the algorithm advances to the next one. Note that in this study, to balance the number of available designs and computational cost, we set the greedy algorithm to consider super-cells made of 3 units (i.e. $n_u = 3$) (see Figures B.15 and B.18 for a comparison across super-cells made with different n_u) and, to avoid

fabricating excessively long actuators whose response could be affected by gravity, terminate the algorithm after stacking 5 super-cells.

To demonstrate our approach, we select two distinct sets of targets within the reachable space (see black and red circular markers in Figure 3.3a and Supplementary Materials Figures B.15-B.19 for additional targets). For the first set of black targets $(T1, T2)$ with small height and radius of action, we find that the objective function Ψ is minimized for an actuator with $n_s = 1$ and $[\Delta^1 c^1 f^1; \Delta^2 c^2 f^2; \Delta^3 c^3 f^3] = [4\backslash\backslash 2; 3//6; 4\backslash\backslash 2]$ (see Figure 3.3b). As this 3-unit actuator only comprises modules with $\Delta = 3$ and 4 mm, its state diagram (shown in Figure 3.3d) is qualitatively similar to the one reported in Figure 3.2b. To reach the target $T1$, the internal pressure must first be raised above p_4^+ and then lowered to p_3^- (see shaded gray line in Figure 3.3c). Successively, the target $T2$ is reached by further lowering the pressure to p_4^-. It is worth noticing that, in this example, increasing the pressure above p_4^+, decreasing it below p_4- and finally bringing it back to zero

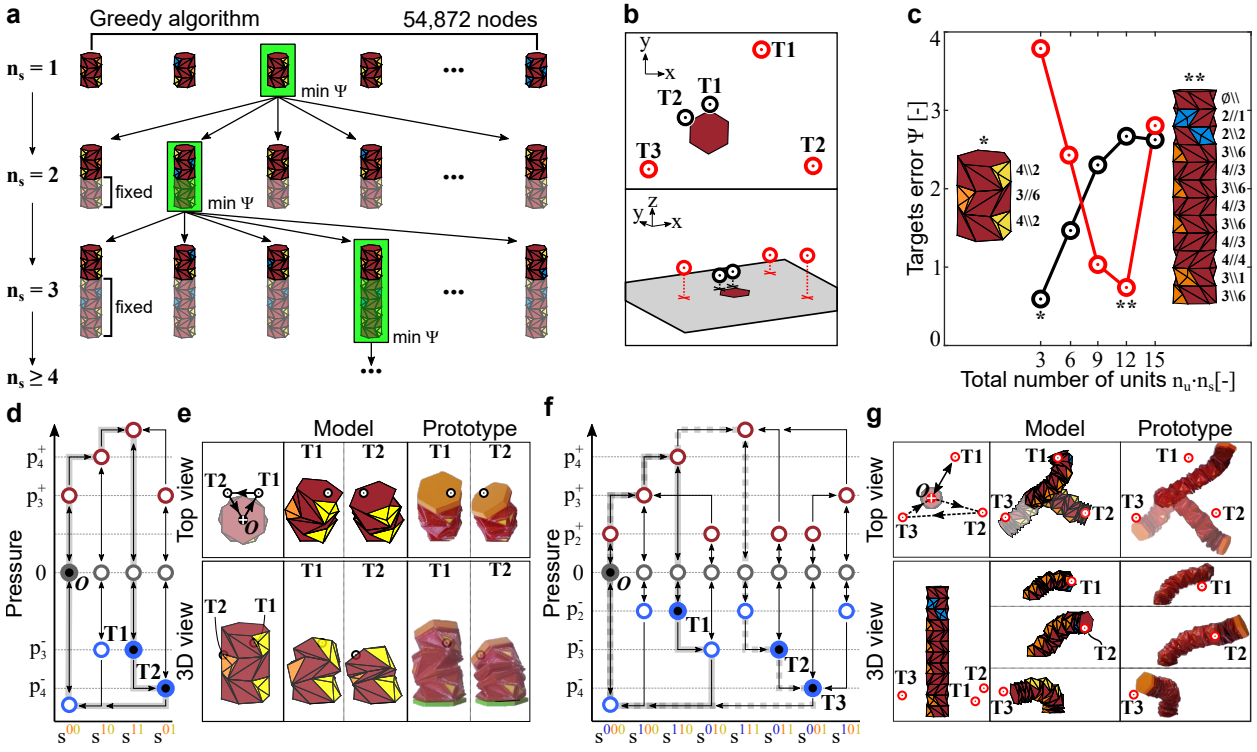

Figure 3.3: Inverse design to reach multiple targets. We employ the greedy algorithm to inverse design actuators able to reach a set of targets with a single pressure source. **(a)** Two distinct set of targets (black and red), top and 3D view. **(b)** Targets error Ψ as a function of total number of units: the optimal actuators produced by the algorithm for both set of targets are reported as $(*)$ and $(**)$, along with the respective parameters for each module. **(c)** State diagram for the 3-units actuator $(*)$ with targets $T1$ and $T2$ highlighted. **(d)** Top and 3D view of the model and the experimental prototype for the 3-units actuator reaching the black targets. **(e)** State diagram for the 12-units actuator $(**)$ with targets $T1$, $T2$ and $T3$ highlighted. **(f)** Top and 3D view of the model and the experimental prototype for the 12-units actuator reaching the red targets.

results in a triangular path for the centroid of the top plate, which is spanned in a counterclockwise direction (Figure 3.3d). Importantly, when we apply this pressure history to a physical sample, the actuator's tip follows the predicted trajectory and approaches the two targets very closely (see Figure 3.3d), confirming the validity of our design strategy. As predicted by our model, the actuator starts straight, bends toward $T1$, bends toward $T2$ and finally returns to the straight configuration O after reset.

For the second set of red targets $(T1, T2, T3)$, the larger height and radius of action of the targets lead to an optimal actuator comprising $n_s = 4$ super-cells (note that the convex shape of Ψ is due to a correlation between the optimal number of units and the average distance of the targets from the origin—see Supplementary Materials Figure B.19). As shown in Figure 3.3b, this 12-unit actuator comprises the classic Kresling module as well as bistable units with $\Delta = 2$, 3, and 4 mm. This results in 8 stable states, 14 snapping transitions, and a more complex state diagram in which not all targets are reached consecutively by continuously decreasing pressure (Figure 3.3e). More specifically, to move from $T1$ to $T2$, this actuator has to be reset by decreasing the pressure below p_3^- before increasing above p_4^+ and then lowering it to p_3^-. As such, in this case the centroid of the top plate of the actuator passes through the straight configuration O when moving from $T1$ to $T2$ and its trajectory comprises two disconnected loops, $O-T1$ and $O-T2-T3$ (Figure 3.3f). Note that we can add additional constraints to our greedy algorithm to make sure the targets fall within the same closed loop on the state diagram. This obviously leads to a different design and may increase the targets error (see Supplementary Materials Figure B.17 for details). However, the ability to fully control the actuator's sequential trajectory makes the platform ideal for robotic applications.

3.6 MuA-Ori for robotic applications

To show the potential of the MuA-Ori for robotic applications we take inspiration from the closed trajectory of a rowing stroke, and use the closed triangular loop of the 3-unit actuator in Figure 3.3e to propel a land rowing robot (Figure 3.4a). The robot comprises two symmetric arms (corresponding to the 3-unit MuA-Ori in Figure 3.3) connected through a single fluidic line and mounted on a wheeled chassis. Further, to harnesses the cyclic motion of the actuator and generate positive mechanical work with the ground, we connect two rigid rods to the outer caps that serve as stroke amplifiers and attach silicon patches at their ends to increase friction with the ground. When increasing the pressure above p_4^+ and then lowering it to p_3^- the two actuators reach $T1$. At this point the rigid rods touch the ground. Then, when we further decrease the pressure, the rigid rods move backward to T2 creating a forward thrust and eventually lift off from the ground, completing the stroke. Finally, lowering the pressure below p_4^- resets the locomotion cycle (see Figures 3.4c and d). As shown in the experimental snapshots in Figure 3.4e we can harness this particular trajectory instructed by the model to create locomotion: the robot advances of about 16 cm in 20 cycles. Note

that, differently from other robotic platforms with similar performance but requiring one or more actuators per leg with dedicated pressure sources[13,87], our robots operate with a single pressure input, which largely simplifies its control.

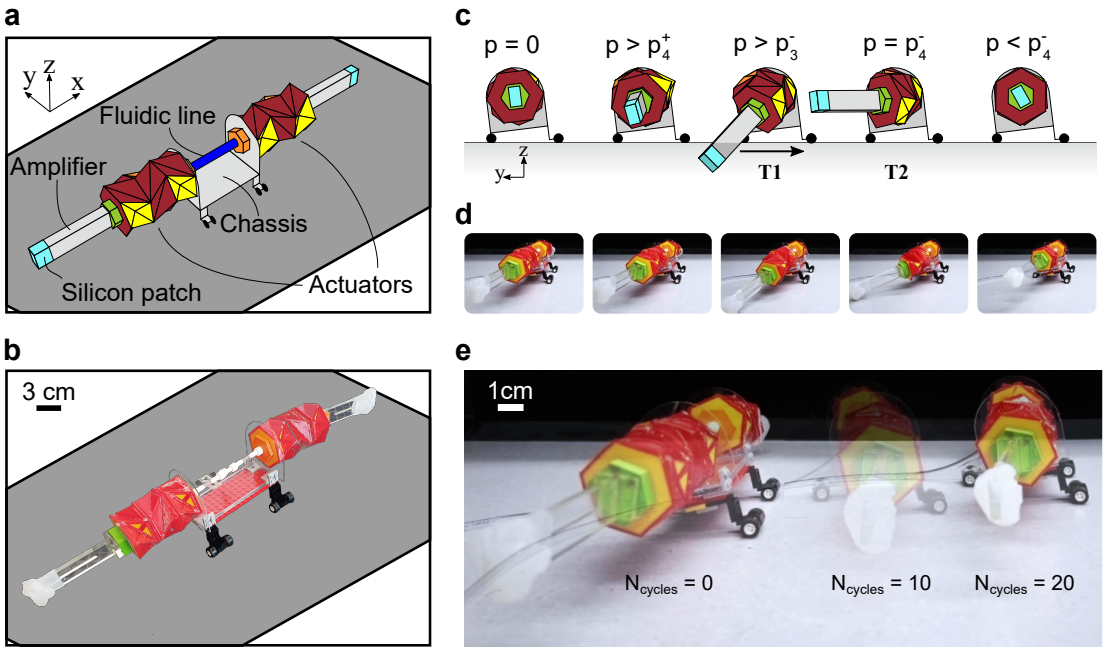

Figure 3.4: Land rowing robot. **(a)** Schematics of the robot. **(b)** Robot prototype. **(c)-(d)** Trajectory followed by the robot's arms upon inflation and deflation, as predicted by the model (c) and observed in experiments (d). **(e)** Experimental snapshots of the robot in the initial configuration and after 10 and 20 cycles.

3.7 Conclusion

To summarize, in this work we have presented a platform to design fluidic origami robots that can switch between a range of different configurations using only one pressurized input: the MuA-Ori. The key characteristics of our platform is an origami building block with a degree-four vertex panel, which can be geometrically programmed to snap at a certain input threshold, inducing bending. This, together with the position of the modified panel in the origami module and their direction of rotation, constitute the parameters of a rich design space that we can efficiently scan with a custom greedy algorithm. Therefore, instructed by this model, we are able to automatically design and build optimal robotic arms that can reach a set of defined targets, and actuators capable of tracing spacial trajectories in a programmed sequence, enabling mechanical tasks and functions. While in this study we have used a simple geometric model to identify optimal designs, a fully mechanical model may be needed in order to extend the proposed approach to larger designs for which the effect of gravity is not negligible. In addition, the current design space could be further expanded

through investigating the effect of other geometrical parameters (e.g. l, h, and α) on the resulting deformation of the modules, as well as expanding the range of the considered values of Δ. While this could lead to more complex deformation modes and enhanced functionality, a drawback is a more complex state diagram. This means that a given actuator might have to go through a longer loading history to reach some prescribed targets, increasing the operational time-span. A potential solution to this is to measure the volume at which the module snaps inward and outward, assume constant flow rate, and derive the time associated to each snapping transition. This time span could then be included as variable in the optimization algorithm, in order to find a design that reaches the target in the shortest possible time. To conclude, we envisage that the MuA-Ori concept hereby presented will serve as future strategy for the design of fluidic origami robots able to overcome the unimodal deformation constraint, despite the simple actuation.

3.8 Methods

Details of the design, materials, and fabrication methods are summarized in Supplementary Materials, Section B.1. The experimental procedure of the inflation with water to measure the pressure-volume curve is described in Supplementary Materials, Section B.2, along with additional experimental data. Details on the numerical mode are provided in Supplementary Materials, Section B.3. Finally, the optimization algorithms used in this study are described in detail in Supplementary Materials, Section B.4, along with additional data.

4

Inflatable soft jumper inspired by shell snapping

By: Benjamin Gorissen*, David Melancon*, Nikolaos Vasios, Mehdi Torbati, and Katia Bertoldi.
Published in *Science Robotics* on May 20th, 2020. **doi:10.1126/scirobotics.abb1967**

4.1 Abstract

Fluidic soft actuators are enlarging the robotics toolbox by providing flexible elements that can display highly complex deformations. While these actuators are adaptable and inherently safe, their actuation speed is typically slow as the influx of fluid is limited by viscous forces. To overcome this limitation and realize soft actuators capable of rapid movements, we focus on spherical caps that exhibit isochoric snapping when pressurized under volume-controlled conditions. First, we note that this snap-through instability leads to both a sudden release of energy and a fast cap displacement. Inspired by these findings, we investigate the response of actuators that comprise such spherical caps as building blocks and observe the same isochoric snapping mechanism upon inflation. Finally, we demonstrate that this instability can be exploited to make these actuators jump even when inflated at a slow rate. As such, our study provides the foundation for the design of a new class of fluidic soft devices that can convert a slow input signal into a fast output deformation.

4.2 Introduction

Inflatable soft actuators have emerged as an ideal platform to realize active structures capable of safe interactions with unstructured environments[5–7]. Their compliance and ability to achieve complex deformations has enabled the design of flexible machines for a wide spectrum of applications[112], ranging from minimally invasive surgical tools[81] and exoskeletons[82] to warehouse grippers[113] and add-ons for video games[83]. However, existing fluidic soft actuators are typically slow, since a significant amount of fluid has to be supplied for their operation, the influx of which is restricted by viscous forces in tubes and valves. To overcome this limitation, it has been shown that fast actuation can be achieved either by modifying the geometry to reduce the amount of fluid needed for inflation[10] or by using chemical reactions to generate explosive bursts of pressure[17]. Alternatively, snapping instabilities can also provide a powerful nonlinear mechanism that decouples the slow input signal from the output deformation and triggers rapid events[41–45].

Inspired by recent progress using snapping instabilities to increase the speed of actuation[41,114], we investigate the snapping of spherical caps as a mechanism to realize fluidic soft actuators capable of rapid movements. We first show that the snapping of elastomeric spherical caps upon pressurization results in a sudden release of energy, the amount of which can be controlled by tuning the caps' geometry, material stiffness, and boundary conditions at the edges. We then realize fluidic soft actuators by combining two spherical caps (see Figure 4.1A) and find that the energy released upon snapping of the inner cap leads to a rapid inversion of its pole that ultimately enables jumping. Finally, we identify geometric and material parameters that result in significant energy release and jump height, providing a rich design domain for fluidic soft actuators capable of extremely fast movements regardless of inflation rate.

4.3 Snapping of spherical caps as a platform for fast fluidic soft robots

To create fast inflatable soft actuators, we start by conducting Finite Element (FE) analyses to investigate the response upon pressurization of elastomeric spherical caps with radius, R, thickness, t, and polar angle, θ (see Figure 4.1B). In our simulations (which are conducted using the commercial package ABAQUS 2018/Standard), we assume the deformation to be axisymmetric, discretize the models with 4-node bilinear axisymmetric solid elements, and use an incompressible Gent material model with initial shear modulus, μ[20]. We pressurize the caps by supplying incompressible fluid to a cavity above them (highlighted in gray in the inset in Figure 4.1B) and simulate the quasi-static pressure-volume curve via the modified Riks algorithm[115,116]. In Figure 4.1B, we consider a thin cap with polar angle $\theta = 60°$, normalized radius $\eta = R/t = 30$, and clamped boundary conditions at the base. We find that the pressure-volume curve of this cap is qualitatively identical to those

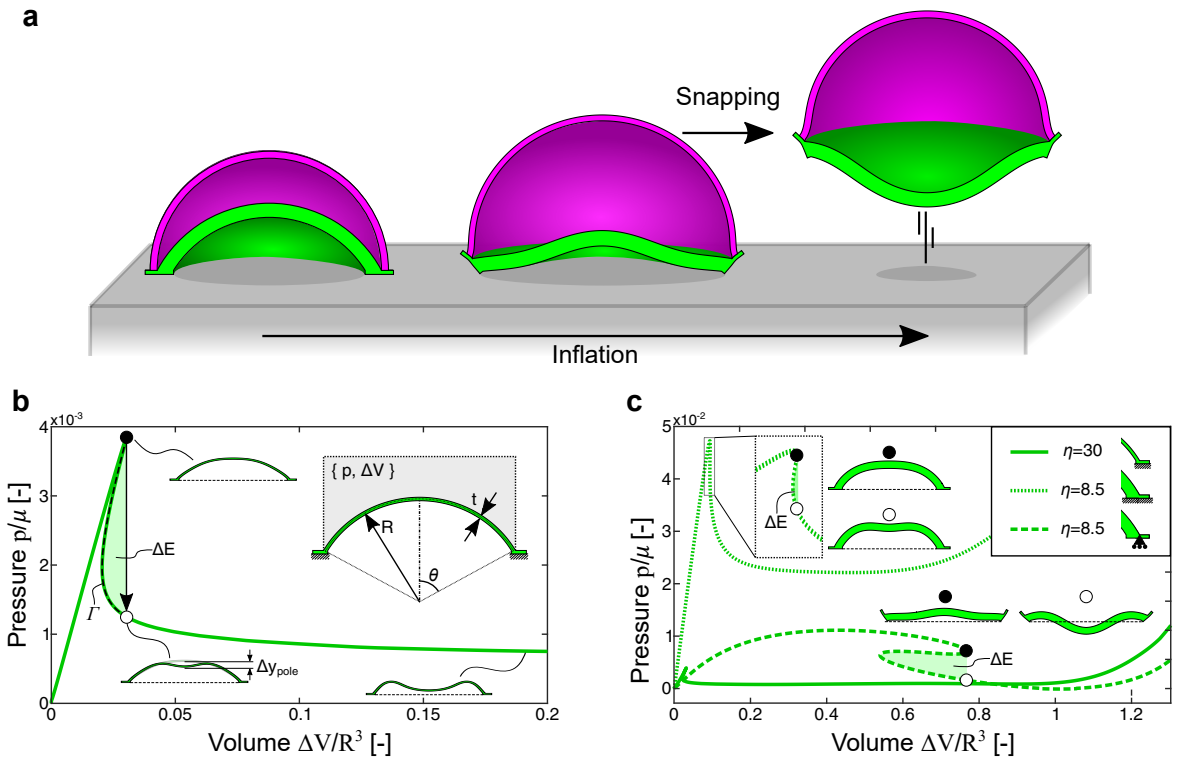

Figure 4.1: Snapping of spherical caps for fast fluidic soft robots. **A.** Our soft fluidic actuators comprise two spherical caps connected at their base. Upon inflation the inner cap snaps and enables our simple device to take off. **B.** The pressure-volume curve, normalized by initial shear modulus μ and radius R, of a given pressurized spherical cap is characterized by a limit point when inflating under volume-controlled conditions. This volume limit point causes an isochoric snapping instability, which leads to a sudden release of energy, ΔE (highlighted in green), and the inversion of the inner cap (which we characterize by quantifying the distance travelled be the cap's pole, Δy_{pole}). **C.** Comparison between the pressure-volume curves of thin (solid green line) and thick spherical caps with both clamped (dotted green line) and roller (dashed green line) boundary conditions. Note that the normalized radius η is defined as the ratio of cap radius over cap thickness (i.e. $\eta = R/t$).

recently reported for pressurized spherical shells[117–119] and is characterized by a limit point when inflating under volume-controlled conditions (indicated by a black circular marker in Figure 4.1B). This volume limit causes an instability leading the system to snap to a point of lower pressure (white circular marker in Figure 4.1B). This occurs while conserving the volume in the cavity and results in a partial inversion of the cap, which we characterize by quantifying the distance traveled by the pole during the instability, Δy_{pole} (see insets in Figure 4.1B). Further, we note that the isochoric snapping of the cap is accompanied by a sudden release of energy, ΔE, that graphically corresponds to the green highlighted area in Figure 4.1B and can be obtained as

$$\Delta E = \int_{\Gamma} p \, d\Delta V, \tag{4.1}$$

where Γ is the equilibrium path that connects the limit point in volume and the corresponding isochoric point on the lower branch (highlighted by a dashed black line in Figure 4.1B). For the considered cap, we find $\Delta E = 1.50 \times 10^{-5} \mu R^3$ and $\Delta y_{pole} = 1.31 \times 10^{-1} R$.

Next, to investigate the effect of geometry on ΔE and Δy_{pole}, we compare the response of the thin spherical cap to that of a thicker one with $\eta = 8.5$ and both with clamped and roller boundary conditions at the base. The results reported in Figure 4.1C indicate that the boundary conditions play a major role on the snapping behavior. The clamped thick cap is characterized by a very large maximum pressure, but a very small energy release and pole displacement upon snapping ($\Delta E = 4.78 \times 10^{-6} \mu R^3$ and $\Delta y_{pole} = 6.30 \times 10^{-2} R$). On the other hand, roller boundary conditions lower the maximum pressure, but lead to a much higher energy release and pole displacement ($\Delta E = 8.00 \times 10^{-4} \mu R^3$ and $\Delta y_{pole} = 2.67 \times 10^{-1} R$). As a result, our simulations indicate not only that isochoric snapping of spherical caps provides opportunities to realize systems capable of suddenly releasing a significant amount of energy through their inversion, but also that by tuning geometry and boundary conditions we can control and maximize the response of these systems.

4.4 Inflatable soft actuators inspired by shell snapping

Having demonstrated numerically that snapping of a spherical cap results in a sudden energy release and pole displacement, we now investigate the mechanical response of fully soft actuators comprising two spherical caps connected at their base to form a cavity that we inflate with an incompressible fluid (see Figure 4.1A). We begin by considering three actuators with inner caps identical to those introduced in Figure 4.1C (with $R_i = 30$ mm) with outer caps characterized by $\theta_o = 90°$ and $\eta_o = 16.5$ (note that here and in the following the subscripts o and i are used to indicate properties of the outer and inner caps, respectively). Specifically, Design A has a thin inner cap with $\theta_i = 60°$ and $\eta_i = 30$, while Designs B and C have a thick cap with $\theta_i = 60°$ and $\eta_i = 8.5$. Further, while we assume that both caps of Designs A and B are made of the same elastomeric

material (i.e. $\mu_i/\mu_o = 1$), for Design C we consider an outer cap made of a softer rubber, resulting in $\mu_i/\mu_o = 5.8$. The numerically obtained pressure-volume curves for the three actuators (shown in Figure 4.2A as blue lines) share many features with those reported in Figure 4.1C for the individual pressurized caps and are all characterized by a limit point near to the maximum pressure when considering volume-controlled conditions. As such, our actuators also exhibit isochoric snapping upon inflation and this again results in a sudden release of elastic energy and the inversion of the inner cap. By comparing the responses of the three actuators, we find that Design C exhibits the largest energy release and displacement of the inner cap's pole ($\Delta E = 0.875$ mJ, 5.67 mJ, and 31.4 mJ for Designs A, B and C, respectively, whereas $\Delta y_{pole} = 7.68$ mm, 7.55 mm, and 20.89 mm for Designs A, B, and C, respectively). These results agree with the trends observed for the individual pres-

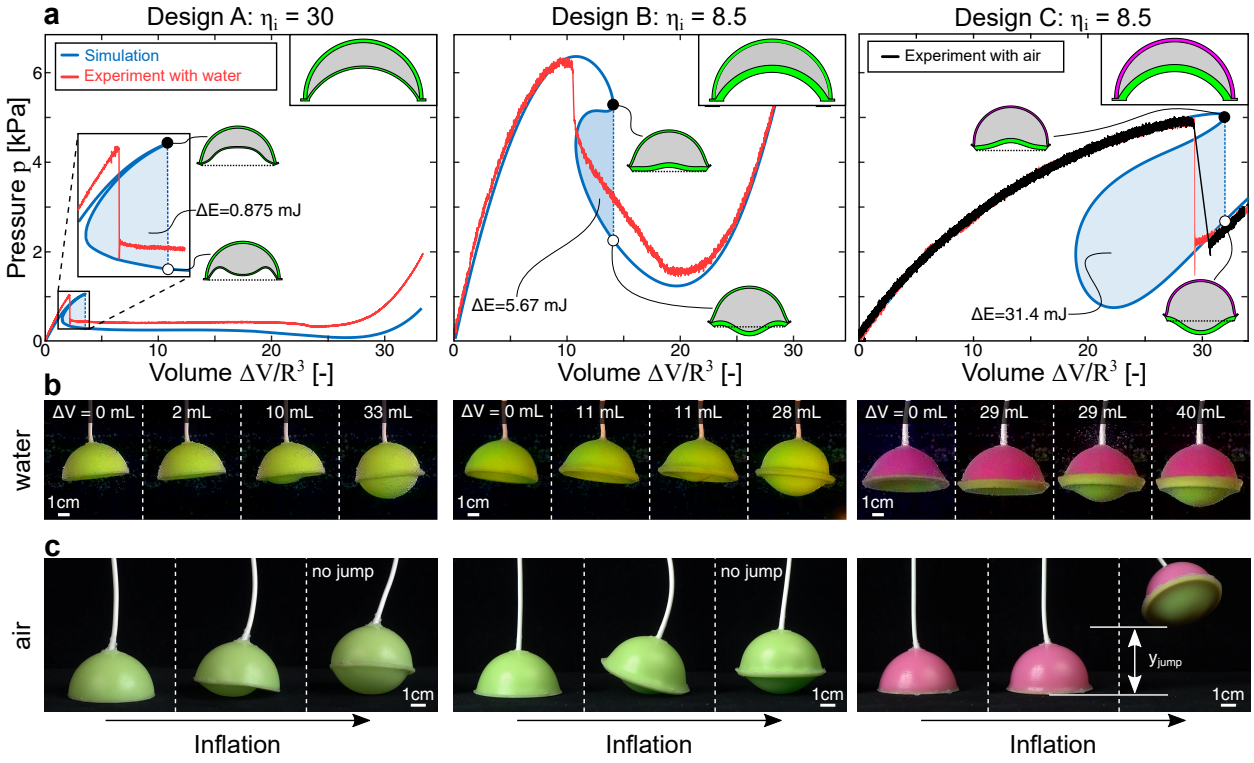

Figure 4.2: Our inflatable soft actuators. **A** Experimental (red) and numerical (blue) pressure-volume curves for the inflation with water of three actuators (all with inner cap radius $R_i = 30$ mm) characterized by normalized radii, polar angles, and ratio of shear moduli (η_i, θ_i, η_o, θ_o, μ_i/μ_o)=(30, 60°, 16.5, 90°, 1) (Design A), (8.5, 60°, 16.5, 90°, 1) (Design B), and (16.5, 60°, 16.5, 90°, 5.8) (Design C). The energy released upon snapping, ΔE, is highlighted by the shaded blue region. The volume limit point upon inflation is identified with a black circular marker, while its corresponding isochoric point on the lower branch is identified with a white circular marker. For Design C, we also report the experimental pressure-volume curve obtained when inflating the actuator with air (black line). **B** Experimental snapshots of the three design during inflation with water at different amounts of supplied fluid. **C** Experimental snapshots of the three designs during inflation with air. The isochoric snapping makes Design C jump and reach a maximum height denoted y_{jump}.

surized caps (see Figure 4.1C), as both ΔE and Δy_{pole} increase for thicker caps that are allowed to rotate at their base (note that in our actuators such boundary conditions are not directly controlled, but rather determined by the outer cap – see Figure C.12). Furthermore, the results highlight the important role of the outer caps and indicate that both ΔE and Δy_{pole} can be enhanced by increasing their compliance. This is because compliant outer caps can sustain more deformation prior to snapping (see insets in Figure 4.2A) and, therefore, enable the actuator to store more elastic energy that can be potentially released upon instability.

Next, to experimentally validate our analyses, we fabricate the three actuators using molds and inflate them with water while submerged in water to eliminate the effects of gravity (see Supplementary Materials for details). In this experimental analysis, all caps are fabricated out of Zhermack Elite Double 32 (with green color and initial shear modulus $\mu = 0.35$ MPa), except for the outer cap of Design C where we use Zhermack Elite Double 8 (with purple color and initial shear modulus $\mu = 0.06$ MPa). Note that these values are obtained by minimizing the error between experiments and simulations for Design C and are within the range previously reported in the literature[118,120–122]. In Figure 4.2A, we compare the numerical (blue lines) and experimental (red lines) pressure-volume curves for the three actuators, while in Figure 4.2B we display snapshots that are taken during the tests. We find good agreement between simulations and experiments, with pressure measurements that show a sudden drop near the numerically predicted limit point. The small discrepancies between experiments and simulations can be attributed to unavoidable imperfections introduced during fabrication, visco-elasticity of the rubber, and slight asymmetric buckling of the inner cap. Furthermore, in all of our tests, as observed in the simulations, snapping is also accompanied by the sudden inversion of the inner cap. While Δy_{pole} for Design A is such that the inner cap's pole remains above the base plane of the actuator upon snapping, for Designs B and C the large value of Δy_{pole} allows for their inner cap's pole to cross it (see Figure 4.2B).

Motivated by these results, we investigate how snapping can be exploited to enhance the functionality of our simple robots and make them jump even when inflated at a slow rate. To this end, we position our actuators on a flat surface and slowly inflate them with air (see Supplementary Materials for details). The snapshots reported in Figure 4.2C reveal that, despite the slow rate of inflation (10 mL/min with a syringe pump), the isochoric snapping makes Design C jump and reach a maximum height of $y_{jump} = 42.9$ mm. On the other hand, even though the inner cap of Designs A and B snaps upon inflation, their ΔE and Δy_{pole} are not large enough to enable them to take off. Although this last set of test was conducted using a compressible fluid (air), the effect of fluid compressibility on the response of the system energy release is negligible and only leads to a slight increase of volume during snap-through (see Figure 4.2A and Supplementary Materials for details). As such, the experiments and analyses conducted using an incompressible fluid can be also used to understand and improve the performance of our air-inflated jumpers.

4.5 Improving the actuators' response

Thus far we have shown that the geometry and material properties of the caps strongly affect the snapping behavior and that by tuning ΔE and Δy_{pole} we can harness the instability to make our actuators jump. Motivated by these findings, we proceed by systematically exploring the parameter space to identify designs that can jump higher than Design C. Figure 4.2C indicates that jumping requires large enough ΔE and Δy_{pole} and Figure 4.2A that ΔE and Δy_{pole} can be enhanced by combining an inner cap that releases a large amount of energy upon snapping with an outer cap that stores a large amount of energy prior to snapping. Therefore, we start by considering the two caps separately and use axisymmetric FE analyses to investigate their behavior for a wide range of geometric parameters (i.e. $40° \leq \theta_i \leq 80°$, $5 \leq \eta_i \leq 12.5$, $40° \leq \theta_o \leq 90°$, $5 \leq \eta_o \leq 20$).

Focusing on the inner cap, we find that by varying θ_i and η_i its response undergoes several transitions (see Figure 4.3A-B). For low values of θ_i and η_i (i.e. for thick and shallow caps), the inner cap does not exhibit isochoric snapping (see light gray region in Figure 4.3A-B). By increasing θ_i at constant η_i, snapping is eventually triggered upon inflation. Within this domain both the energy released by the inner cap, ΔE_i, and its pole displacement, Δy_{pole}, increase monotonically as a function of θ_i, suggesting that the response of our actuators can be enhanced by considering deep and sufficiently thick inner caps. Finally, for high values of θ_i and η_i (i.e. for thin and deep caps) the pressure-volume curves become self-crossing (see dark gray region in Figure 4.3A-B), which is an indication of the existence of a more favorable asymmetric deformation path with low ΔE_i and Δy_{pole} (see Figure C.15).

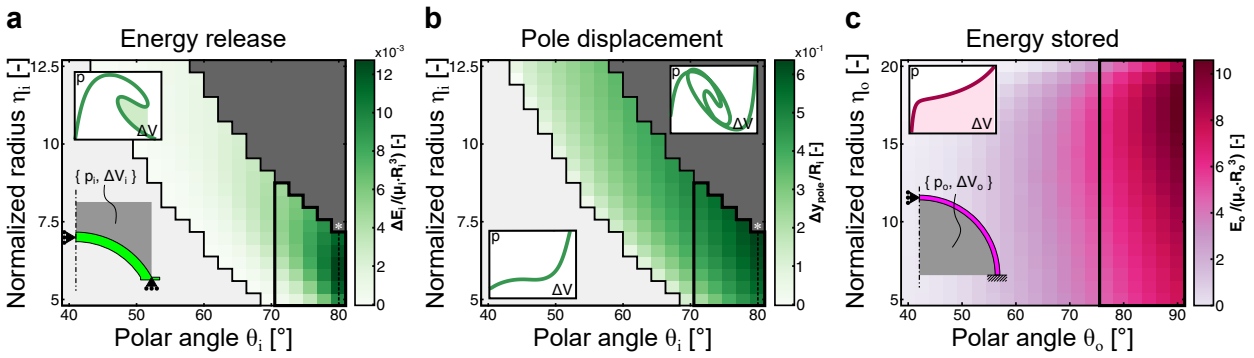

Figure 4.3: Mechanical response of the inner and outer caps upon inflation. **(a)-(b)** Evolution of the inner cap's normalized (a) energy release, $\Delta E_i/(\mu_i R_i^3)$, and (b) pole displacement, $\Delta y_{pole}/R_i$, upon snapping as a function of the normalized radius, η_i, and the polar angle, θ_i. **(c)** Evolution of the outer cap's normalized stored energy at $p/\mu_o = 0.5$, $E_o/(\mu_o R_o^3)$, as a function of the normalized radius, η_o, and the polar angle, θ_o.

Next, we turn our attention to the outer cap and find that its response is less rich and resembles that of an inflated thin spherical balloon[123,124]. Since the outer cap in our actuators acts as an energy reservoir, in Figure 4.3C, we report the evolution of the stored energy in the outer cap, E_o, at a normalized pressure of $p/\mu_o = 0.5$, as a function of the polar angle θ_o and the normalized

radius η_o. The results indicate that E_o increases monotonically with θ_o (almost irrespective of η_o), therefore suggesting that the response of our actuators can be enhanced by focusing on deep outer caps.

While the results of Figure 4.3 enable us to identify promising regions of the design space (i.e. inner caps with $\theta_i \geq 70°$ and $\eta_i \leq 8$ and outer ones with $\theta_o \geq 76°$), they cannot be directly used to realize the best possible jumper as they neglect the coupling between the two caps. Therefore, as next step, we use axisymmetric FE analyses to simulate the response of 4800 actuators constructed by combining inner and outer caps within the identified promising regions (highlighted by black contours in Figure 4.3). In Figure 4.4A, we report ΔE and Δy_{pole} for all simulated actuators with both $\mu_i/\mu_o = 1$ (green markers) and 5.8 (purple markers). Four key features emerge from the plot. First, by comparing the results with those obtained for the three actuators considered in Figure 4.2 (indicated by square markers in Figure 4.4A) we find that both ΔE and Δy_{pole} can be greatly increased when the geometry is properly tuned. Second, the results show that, on one hand, there is

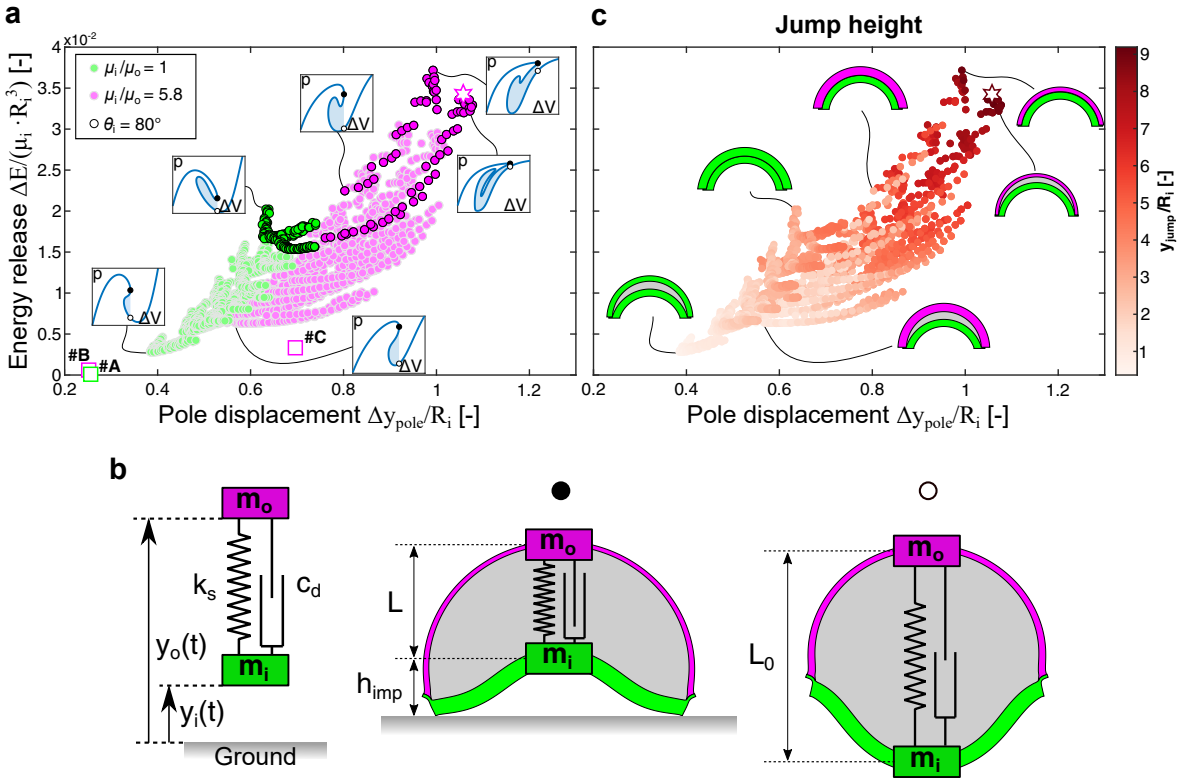

Figure 4.4: Improving the response of the actuators. **(a)** Normalized energy release, $\Delta E/(\mu_i R_i^3)$, vs. normalized pole displacement, $\Delta y_{pole}/R_i$, for actuators with inner polar angle $\theta_i \geq 70°$, normalized inner radius $\eta_i \leq 8$, and normalized outer radius $\theta_o \geq 76°$. **(b)** Reduced order mass-spring model used to predict jump height based on the numerical results reported in (a). The model comprises two masses m_i and m_o connected via a spring with stiffness k_s and a dashpot with damping coefficient c_d. **(c)** Normalized jump height, y_{jump}/R_i as a function of energy release and pole displacement for the 4800 actuators considered in (a).

a strong correlation between ΔE and Δy_{pole} and, on the other hand, there is a disconnection between them and the drop in pressure associated with the snapping instability. Specifically, by inspecting the pressure-volume curves for the actuators (shown as insets in Figure 4.4A) we find that for the designs with large ΔE and Δy_{pole} the drop in pressure is small, while the area enclosed by the pressure-volume curve between the limit point and the corresponding isochoric point on the lower branch is large. Third, the results confirm the importance of a flexible outer cap as both ΔE and Δy_{pole} are significantly larger for the actuators with $\mu_i/\mu_o = 5.8$. Fourth, we find that the inner cap plays a crucial role and that by choosing $\theta_i = 80°$ to optimize its response we significantly improve the performance of the actuators (see black contour markers in Figure 4.4A). At the same time, however, the results also highlight that for actuators with $\mu_i/\mu_o = 5.8$ the outer cap geometry is important, as some design choices lead to noticeably lower ΔE and Δy_{pole}.

Our quasi-static FE simulations allow us to efficiently explore the design space and calculate ΔE and Δy_{pole} for a large number of designs. However, since they do not account for dynamic effects, they cannot be used to directly characterize the ability of the actuators to jump. To overcome this limitation, we establish a simple mass-spring model that takes the FE results of Figure 4.4A as input and predicts the jump height, y_{jump}. This reduced order model comprises two concentrated masses, m_i and m_o, connected by a spring with stiffness k_s and rest length L_0 (Figure 4.4B). We choose m_i and m_o to be equal to the mass of the inner and outer cap, respectively, and to be located at their corresponding poles. We then focus on the numerically predicted configurations immediately before and after snapping and assume that the mechanical system stores an amount of energy equal to ΔE in the former and is stress-free in the latter. It follows that L_0 is equal to the distance between the poles immediately before snapping and that (see Figure 4.4B)

$$k_s = \frac{2\Delta E}{\left(\Delta y_{pole}\right)^2}. \tag{4.2}$$

Finally, we consider the spring to be initially pre-compressed by Δy_{pole} and m_i to be positioned at a distance h_{imp} from the ground (h_{imp} being the numerically predicted distance of the inner cap's pole from the ground immediately before snapping). At time $t = 0$, we release the system and analytically determine the position of the two masses, $y_i(t)$ and $y_o(t)$, as a function of time while accounting for contact with a rigid surface.

To verify the validity of our simplified mass-spring model, we first focus on three designs with $(\eta_i, \theta_i, \eta_o, \theta_o, \mu_i/\mu_o)$= (8.5, 60°, 16.5, 90°, 5.8) (Design C), (5.4, 80°, 15.3, 87°, 5.8), and (5.8, 80°, 10.5, 85°, 5.8) and compare the experimentally measured jump heights (h_{jump} = 42.9 mm, 160 mm, and 209 mm, respectively) to the predicted ones. When choosing a coefficient of restitution $\alpha = 0.5$ and approximating the effect of dissipation with a linear dashpot with damping coefficient c_d = 0.4 kg/s, we find excellent agreement between the two sets of data, with the model predicting $y_{jump} = \max\left(y_i(t)\right)$ = 41.4 mm, 175 mm, and 226 mm (see Supplementary Materials for details). As

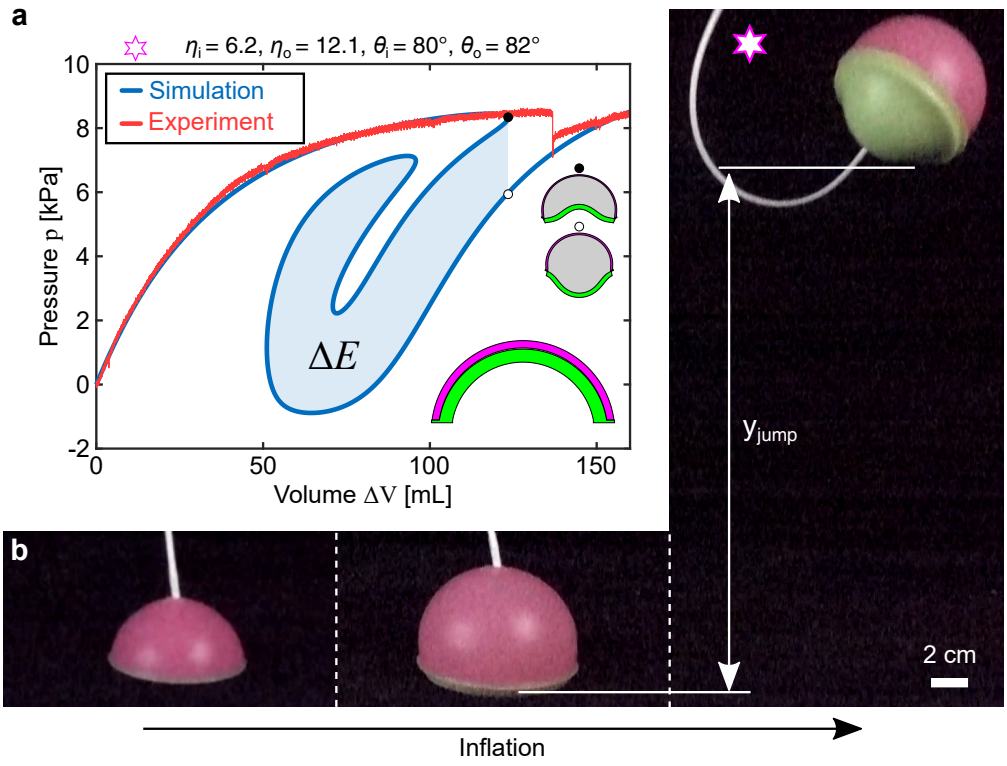

Figure 4.5: Actuator with highest jump height. **(a)** Numerical (blue line) and experimental (red line) pressure-volume for the actuator with normalized radii, polar angles, and ratio of shear moduli (η_i, θ_i, η_o, θ_o, μ_i/μ_o)=(6.2, 80°, 12.1, 82°, 5.8) and inner cap radius R_i= 30 mm. **(b)** Experimental snapshots of the actuator upon inflation with air.

such, these results indicate that our simple mass-spring model, despite the fact that it cannot capture the complex dynamic behavior typical of shells[44,125,126], can accurately predict the jump height of our soft jumpers. Having confirmed the validity of our model, we then use it to calculate y_{jump} for all the 4800 actuators considered in Figure 4.4A. The results reported in Figure 4.4C clearly indicate that a high jump requires both ΔE and Δy_{pole} to be large. Specifically, we find that the jump height is highest for an actuator with (η_i, θ_i, η_o, θ_o, μ_i/μ_o)= (6.2, 80°, 12.1, 82°, 5.8) for which ΔE=324 mJ and Δy_{pole}=31.7 mm. For such an actuator, our model predicts $y_{jump} = 275$ mm, a jump height that is one order of magnitude larger than that previously recorded for Design C. Remarkably, our experimental results fully confirm the numerical predictions for this design for both the pressure-volume curve (see Figure 4.5A) and the jump height $y_{jump} = 283$ mm (see Figure 4.5B), further reinforcing the validity and efficiency of our numerical scheme to identify actuators with improved performance.

4.6 Conclusion

In summary, we have introduced a new family of inflatable soft actuators that harness isochoric snapping to move rapidly and even jump when inflated slowly. This remarkable behavior is encoded in their pressure-volume relationship, which exhibits two limit points in volume. While fluidic actuators are typically characterized by a monotonic pressure-volume curve[10,85], it has been recently shown that limit points in pressure can be exploited to enhance their functionality and enable sequencing[84,127,128]. Here, we show that by introducing limit points in volume we can realize soft robots capable of suddenly releasing a given amount of energy. Since the instability occurs at constant volume and does not involve transfer of fluid, the release of energy is extremely fast and enables us to convert the slow input signal into exceptionally rapid events such as jumps. Finally, our actuators can be simply reset and brought back to the initial configuration through vacuum and, therefore, can take off repetitively.

Although in this study we have demonstrated the concept for spherical caps at the centimeter-scale, our approach can be extended to any shape and does not depend on size. Remarkably, since both ΔE and the gravitational potential energy are proportional to the mass, the jump height is independent of size[129]. As such, we expect the relative jump, y_{jump}/R_i, to monotonically increase as the actuators are scaled down. On the other hand, on-board actuation and control may be embedded in larger jumpers (as the mass of these additional elements become negligible compared to that of the actuators) and open up the way to real-world applications requiring untethered soft robots[14,130]. Finally, while in this study we have focused on the response of spherical caps under inflation, similar highly non-linear behavior (i.e. force-displacement curves characterized by limit points in displacement) has been reported for the indentation of shallow arches[131] and shells with curved creases[132]. Since structural elements with limit points in force have already been used to realize mechanical metamaterials with novel properties[46,133–136], we believe that by integrating these new building blocks into their design we can further expand their modes of functionality.

4.7 Methods

Details of the design, materials, and fabrication methods are summarized in Supplementary Materials, Sections C.1 and C.2. The experimental procedures, including the inflation with water to measure the pressure-volume curve and the inflation with air to measure jump height are described in Supplementary Materials, Section C.3. FEA procedures and jumper mass-spring model are detailed in Supplementary Materials, Sections C.4 and C.5. Validation of the FEA model and jumper mass-spring model is reported in Supplementary Materials C.6.

5
Outlook

"We have learned much. There still remains much to learn. We are not going in circles, we are going upwards. The path is a spiral; we already climbed many steps."
– H. Hesse, *Siddhartha*

5.1 Summary and contributions

In this dissertation, I demonstrated how geometry can be leveraged to tune the energy landscape of inflatable systems and lead to enhanced functionality. First, in chapters 2 and 3, I focused on the geometric principles at play when folding origami patterns to realize multistable devices. In chapter 2, I proposed a systematic way of designing closed origami shapes that can be inflated and deflated between different stable configurations. I then extended this methodology to realize meter-scale functional structures, including inflatable archways and shelters. Following from this work, in chapter 3, I showed that multistable origami patterns can be utilized to decouple the input signal from the output deformation in soft actuators. This led to the design of fluidic actuators capable of arbitrary and programmable deformation modes from one single pressure source. Finally, in chapter 4, I exploited elastic instabilities in pressurized shells to trigger fast deformations in soft robots, regardless of their actuation speed. In particular, I designed and fabricated a soft robot made of spherical cap that suddenly releases energy and jumps upon arbitrarily slow inflation. The contributions of this dissertation are illustrated in Figure 5.1.

Figure 5.1: Contributions. **(a)** Meter-scale inflatable and multistable structures **(b)** Multimodal soft actuators. **(c)** Fast soft robotic jumper.

5.2 Future directions

The research projects presented within this dissertation show that geometry (rather than chemical composition) can play a key role in determining the physics of a material or structure. Advanced numerical methods and data-driven approaches are readily available to tailor the micro-architecture of materials for targeted properties[137–139]. Instead of avoiding instabilities, we seek them out to obtain transformable structures than can morph into prescribed and distinct stable shapes[140,141]. We also rely on nonlinearities arising from geometry to simplify actuation and embed intelligence in soft robots that adapt to their environment and interact safely with humans[5]. However, the design of these systems still mostly relies on intuition, experience, and proof-of-concept demonstrations, resulting in limited industrial exploitation. Future studies should seek to unite these recent scientific achievements and focus on multistability to automatize the design and fabrication process across all scales of materials and structures that are multi-form, multi-functional and multi-purpose. In particular, I envision opportunities to:

- **Direction 1 Automated design**: Solving the inverse design process to find geometries giving rise to prescribed responses at distinct stable states
- **Direction 2 Multi-Scale fabrication**: Designing and fabricating across all-scales materials that can switch their properties on demand
- **Direction 3 Applications**: Building transformable structures that address real-world problems

5.2.1 Direction 1: Automated Design

The biggest challenge in building the next generation of smart materials and structures is to automatize the design process to get a prescribed *nonlinear* and *time-varying* response. This involves solving the forward problem to understand and model the effect of geometry as well as the inverse problem to systematically find the required geometrical features needed for targeted properties. More efficient materials and structures could be designed by prescribing a nonlinear response at distinct stable states. Towards this end, data-driven approach based on evolutionary algorithms and artificial neural networks coupled with finite element and reduced-order models could be used to automatically generate geometries that lead to (i) *Prescribed snap-through instabilities*, (ii) *Targeted deformations and stable shapes*, (iii) *Pre-determined response history*.

Focusing on the buckling of spherical shells (Figure 5.2a), by simply modifying the geometry, i.e. the thickness or polar angle of the shell, it is possible to switch from a monotonic relation between pressure and volume to a response where we have both pressure and volume snap-through instabilities. In order to get *prescribed snap-through instabilities*, one could focus on shell structures of arbitrary geometry, develop a library of geometry-driven instabilities using the finite element method, and use optimization tools such as evolutionary algorithms and machine learning to solve the inverse design problem. In order to get *targeted deformation and stable states*, one could harness cylindrical buckling in soft actuators (Figure 5.2b). By modifying the geometry of the void and subjecting a soft cylinder to vacuum, it is possible to transition between a mode of deformation characterized by twisting to a mode characterized by bending. While here the void geometry is fixed, adaptive void geometry in soft actuators could help to switch from one deformation state to the other. Finally, for the more challenging task of designing materials and structures with *pre-determined response history*, one could extend the work that I have conducted on multimodal and multistable soft actuators[142]. The complex state diagram of such actuators is shown in Figure 5.2c. By setting a specific pressure history, the actuator can switch between different stable states of deformation. One could expand this concept to design materials and structures that change their stable states and properties passively (from time-varying environmental stimuli) and actively (from sudden external inputs).

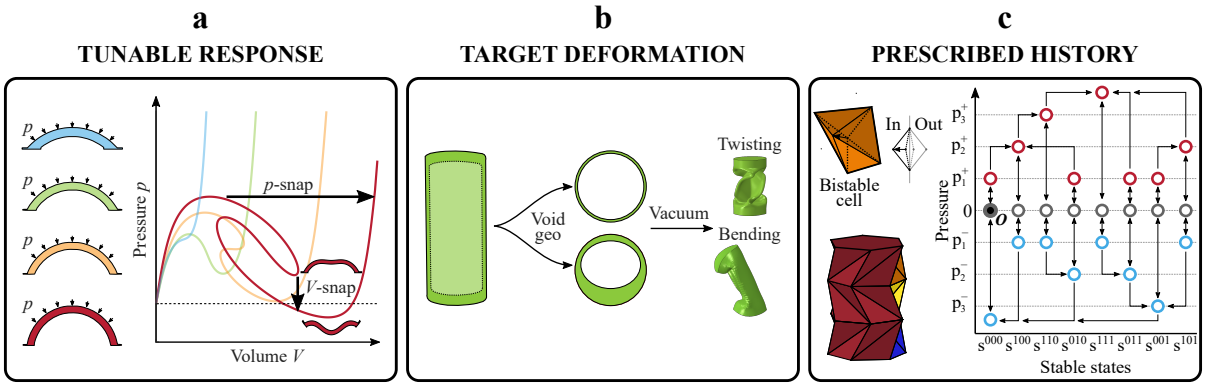

Figure 5.2: Direction 1: Automated design. **(a)** Designing the *response* through geometry: example of how the geometry of a pressurized spherical shell impacts its pressure-volume response, from a monotonic behavior to a curve exhibiting both isobaric and isochoric snap-through instabilities. **(b)** Designing the *deformation* through geometry: example of how the void shape of a soft cylinder can lead to twisting or bending when vacuum is applied. **(c)** Designing the *history* through geometry: example of a 3-unit inflatable actuator inspired by origami that can transition to and from 8 different stable states (with the cell popped inward or outward) depending on the applied pressure history.

5.2.2 Direction 2: Multi-Scale Fabrication of Multistable Materials and Structures

In parallel to the fundamental research of *Direction 1 Automated Design*, it is essential to design and fabricate materials and structures, across all scales, that can switch their properties on demand. This would involve transferring the complex geometries and instabilities found in *Direction 1 Automated Design* to real, manufacturable samples. In particular, the goal would be to fabricate:

- Multistable materials that can *switch their topology*
- Multistable structures capable of *shape and volume morphing*

It is well-known that the morphological parameters of architected materials (e.g. nodal connectivity, relative density, etc.) influence their mechanical response[143]. Indeed, if the nodal connectivity is low, the material is said to be bending-dominated and its stiffness, E, and strength, σ_{cr}, scale with relative density, ρ, as $E \propto \rho^2$ and $\sigma_{cr} \propto \rho^{1.5}$. Instead, if the nodal connectivity is high, the architected material is stretching-dominated and the stiffness and strength scaling is linear. Materials that could switch between the two topologies could be used for multi-purposes as they would offer robust load-bearing functionality in the stretching-dominated state and enhanced energy absorption in the bending-dominated state. As an example, in Figure 5.3a, I demonstrate that snapping beams in a hexagonal unit cells could trigger the transition from a bending-dominated state to a stretching-dominated state. These topology-switching materials could be fabricated via multi-material additive manufacturing technologies.

Furthermore, structures that can change shape and volume on demand could be applied in the fabrication of transformable acoustic panels made of adaptive Helmholtz resonator unit cells. Traditionally, a Helmholtz resonator is made of a closed cavity with an opening through a narrow neck. Depending on the cavity volume and neck geometry, the resonator can excite and damp specific frequencies[144]. By utilizing the design tools developed in *Direction 1 Automated Design*, one could fabricate acoustic panels made of Helmholtz resonators that can change shape and volume to display targeted acoustic properties. In Figure 5.3c, I report initial work on an origami-inspired multistable Helmholtz resonator. By tessellating the multistable unit, the panels can snap into specific internal volumes to damp out selected frequencies. This research could lead to acoustic panels that can transform to adapt to different settings and be utilized in various fields including aerospace and the recording industry.

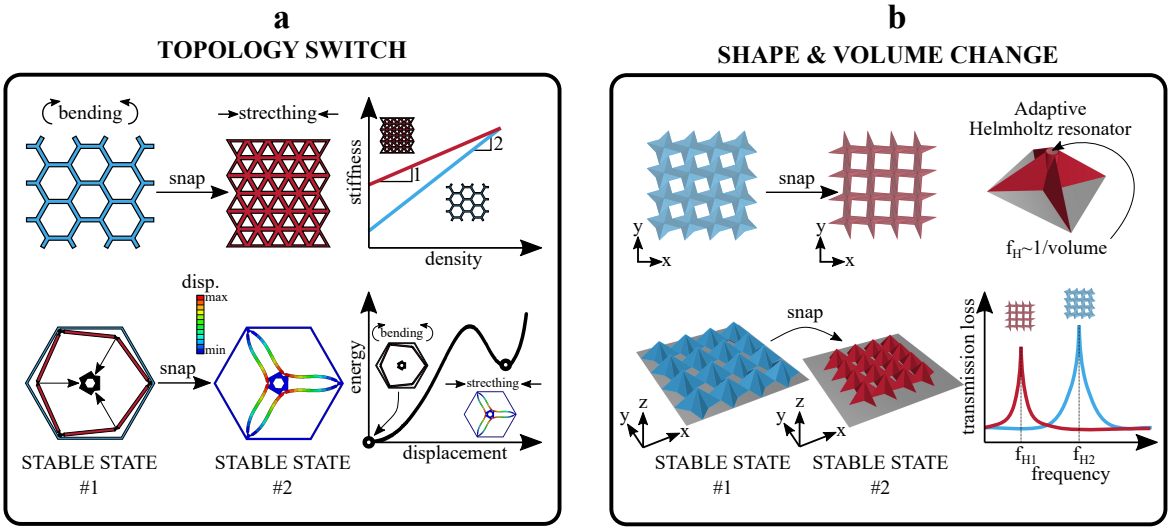

Figure 5.3: Direction 2: Multi-scale fabrication of multistable materials and structures. **(a)** Topology-switching lattices: example of an architected material that harnesses beam buckling and multistability to switch from a bending-dominated to a stretching-dominated topology. **(b)** Shape and volume morphing structures: example of an origami-inspired structure that can modulate its acoustic response through multistability to damp out prescribed frequencies.

5.2.3 Direction 3: Applications of Transformable Structures

We rely heavily on transformable, deployable structures for the most basic tasks (e.g. folding a packaging box), for immensely complex feats of engineering (e.g. deploying solar sails for spacecraft propulsion) as well as in emergency situations (e.g. quickly creating sheltered space in disaster areas). Therefore, robust and autonomous deployment as well as resilience and adaptability to unexpected disruptions need to be included in the design of transformable systems. One could apply the results of the research conducted in the previous Directions of *Automated Design* and *Multi-Scale Fabrication* to build adaptive and transformable structures that exhibit the following properties:

- Transform from a compact stable state to pre-determined, stable, and expanded states
- Deploy robustly and autonomously to reduce setup times
- Consist of rigid walls to provide physical, acoustic, and thermal barriers
- Made of cost-efficient, environmental-friendly, and reusable material
- Proven to support extreme loading conditions both numerically and experimentally

To start, one could extend the initial work I have done on building a pressure-deployable and multistable emergency shelter (Figure 5.4a and[145]). This would include using the design tools

developed in the first research direction *Automated Design* to generalize the deployed shapes and focus on other applications such as deployable space structures, field hospitals, and flood barriers. In addition, development of rigorous numerical and experimental tools is needed to confirm these structures can be used in the harshest of environments. Finally, to increase the impact and use of these structures—particularly in disaster areas and to provide temporary sheltering to alleviate homelessness—it is important to focus on easy fabrication techniques as well as cost-efficient, reusable, and degradable materials.

Figure 5.4: Direction 3: Applications. **(a)** Concept of a large-scale pressure-deployable shelter. Once inflated, because of the multistability, the pressure supply can be removed to make the internal space accessible. **(b)** The shelter made of stiff faces connected by flexible hinges provides physical, acoustic, and thermal barriers and could be used for emergency response in disaster zones or as a transformable habitat for deep space exploration.

A

Supplementary Information: Multistable inflatable origami structures at the meter scale

By: David Melancon, Benjamin Gorissen, Carlos-José Garcia-Mora, Chuck Hoberman, and Katia Bertoldi
Published in *Nature* on April 21th, 2021. **doi:10.1038/s41586-021-03407-4**

A.1 Design

Our origami-inspired deployable structures are made out of stiff triangular facets connected by compliant hinges. In this section, we first show that the inscribed angle theorem can be utilized to design triangular building blocks with two compatible states. Next, we demonstrate that assembling these building blocks in rational ways leads to a library of inflatable and bistable origami shapes.

A.1.1 Deployment of an initially flat triangular building block

We start by considering a triangular building block ABC with internal angle $\alpha \equiv \angle BAC$ and $\beta \equiv \angle ABC$. The triangle is initially flat (i.e. it lies in the xy-plane) and is deployed through a rotation about its edge BC, which leads to a displacement w_A of vertex A along the z-direction and a volume under the triangle, V_{ABC}, that can be calculated as

$$V_{ABC} = \frac{1}{6} AB \cdot \left(AC \times AA_{xy}\right) = \frac{w_A ||AB||^2}{6} \frac{\sin\alpha}{\sin\left(\alpha+\beta\right)} \sqrt{\sin^2\beta - \frac{w_A^2}{||AB||^2}}, \tag{A.1}$$

where AA_{xy} is the segment formed by connecting vertex A to its projection on the xy-plane, $||AB||$ is the length of edge AB, and $w_A = ||AA_{xy}||$ (see Figure A.1a). Focusing on the xy-plane (see Figures A.1b–c), we see that, if

$$\alpha \in \left]\alpha_{min}, \alpha_{max}\right[= \left]0, \frac{\pi}{2}\right[, \quad \text{and} \quad \beta \in \left[\beta_{min}, \beta_{max}\right] = \left[\frac{\pi}{4} - \frac{\alpha}{2}, \frac{\pi}{2} - \alpha\right], \tag{A.2}$$

the projection of the triangle intersects a circle circumscribed to the initial configuration at a displacement, w_A^c, and volume, V_{ABC}^c. The displacement w_A^c can be obtained as

$$w_A^c = \sqrt{||AC||^2 - ||AC_{xy}^c||^2} = ||AB|| \sqrt{1 - \frac{\cos^2\beta}{\sin^2(\alpha+\beta)}}, \tag{A.3}$$

where $||AC||$ is the length of edge AC and AC_{xy}^c is the edge AC projected on the xy-plane at the intersection with the circle, whose length is given by

$$||AC_{xy}^c|| = ||AB|| \cot(\alpha+\beta). \tag{A.4}$$

Further, by substituting Eq. A.3 in Eq. A.1, we get

$$V_{ABC}^c = \frac{||AB||^3}{6} \sin\alpha \sin\beta \cos\beta \csc(\alpha+\beta) \cot(\alpha+\beta) \sqrt{1 - \cot^2\beta \cot^2(\alpha+\beta)}. \tag{A.5}$$

It follows from the inscribed angle theorem (which states that, since the angle α inscribed in a circle is half of the central angle that subtends the same arc, α does not change as its vertex is moved

on the circle—see Figures A.1d-e) that for $w_A = w_A^c$ and $V_{ABC} = V_{ABC}^c$, the angle α is recovered on the projected plane. As such, the triangle ABC possesses two states—one flat and one deployed—for which $\alpha = \alpha_{xy}$ separated by states for which $\alpha_{xy} \neq \alpha$ (see gray triangle is Figures A.1a-b). Using simple geometry, we can determine α_{xy} as a function of w_A as

$$\alpha_{xy} = \arccos\left(\frac{AB_{xy} \cdot AC_{xy}}{||AB_{xy}|| \cdot ||AC_{xy}||}\right) = \arccos\left(\frac{1 - 2\frac{w_A^2}{||AB||^2} - \frac{\sin(\alpha-\beta)}{\sin(\alpha+\beta)}}{2\sqrt{1 - \frac{w_A^2}{||AB||^2}}\sqrt{\left(\frac{\sin\beta}{\sin(\alpha+\beta)}\right)^2 - \frac{w_A^2}{||AB||^2}}}\right), \tag{A.6}$$

where AB_{xy} and AC_{xy} are the edges AB and AC projected on the xy-plane, which have length

$$||AB_{xy}|| = \sqrt{1 - \frac{w_A^2}{||AB||^2}}, \tag{A.7}$$

and

$$||AC_{xy}|| = ||AB||\sqrt{\frac{\sin^2\beta}{\sin^2(\alpha+\beta)} - \frac{w_A^2}{||AB||^2}}. \tag{A.8}$$

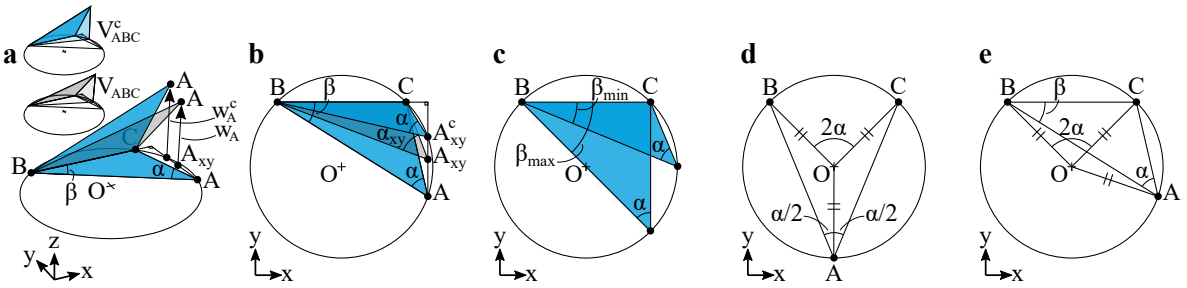

Figure A.1: Deployment of an initially flat triangular building block. **(a-b)** Isometric and projected views of a triangular building block ABC that recovers its projected angle α during deployment leading to two distinct compatible states. **(c)** Initially flat triangular building block ABC in the limit cases where $\beta = \beta_{min}$ and $\beta = \beta_{max}$. **(d)** According to the inscribed angle theorem, the angle $\angle BAC$ is half the central angle $\angle BOC$. **(e)** Moving the vertex A on the circle below the edge BC does not change the angle $\angle BAC$.

In Figure A.2a, we show the evolution of the projected angle variation, i.e. $\Delta\alpha \equiv \alpha_{xy} - \alpha$, as a function of w_A for a triangular building block with $\alpha = 45°$ and $\beta = 32°$. We find a highly non-linear relation characterized by a local maximum

$$\Delta\alpha_{max} \equiv \max(\Delta\alpha) = \arccos\left(\frac{2\cot(\alpha+\beta)\sin 2\beta}{\sqrt{\csc^4(\alpha+\beta)\sin 2\beta \sin(2(\alpha+\beta))\sin^2(\alpha+2\beta)}}\right), \tag{A.9}$$

at a deployment height

$$w_A^{\Delta\alpha_{max}} = ||AB||\sin\beta\sqrt{1 - \cot\beta\cot(\alpha+\beta)}. \tag{A.10}$$

and two points ($w_A = 0$ and $w_A = w_A^c$) at which $\Delta\alpha = 0$.

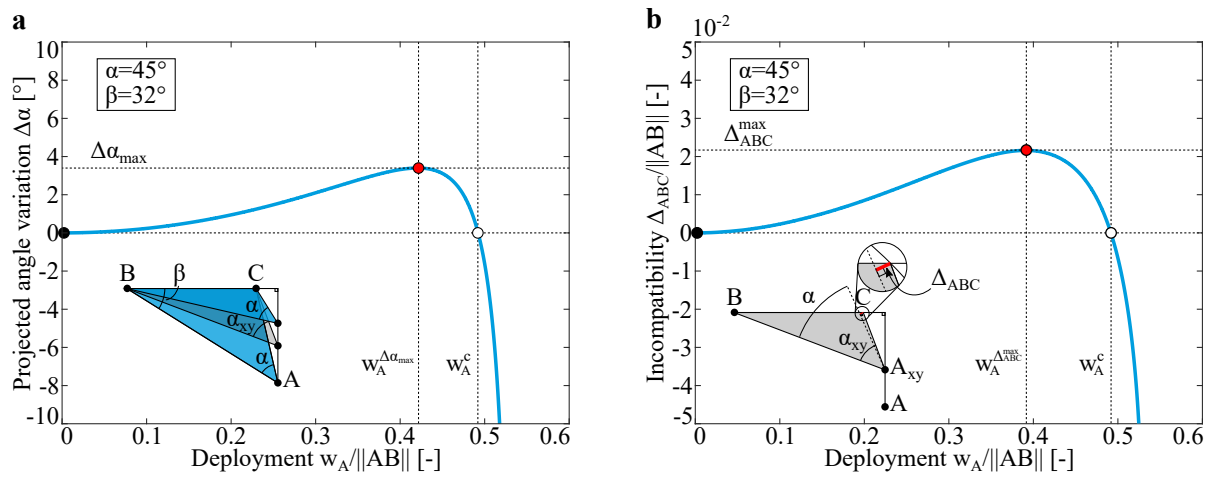

Figure A.2: Evolution of $\Delta\alpha$ and Δ_{ABC} during deployment. (a-b) Evolution of $\Delta\alpha$ and Δ_{ABC} as a function of the deployment of vertex A, w_A, for a triangle with $\alpha = 45°$ and $\beta = 32°$.

Further, the difference between α_{xy} and α can also be quantified by introducing the distance

$$\Delta_{ABC} = ||AC_{xy}|| \cdot \sin\Delta\alpha = ||AC_{xy}|| \cdot \sin(\alpha_{xy} - \alpha), \tag{A.11}$$

that we will later use to characterize the geometric incompatibility of the resulting origami structures for $0 < w_A < w_A^c$ and, therefore, estimate the energy required for them to snap back from the expanded to the flat state. In Figure A.2b, we show the evolution of Δ_{ABC} as a function of w_A for a triangle with $\alpha = 45°$ and $\beta = 32°$. As expected, we find a similar behavior to that reported in Figure A.2a for $\Delta\alpha$, with a local maximum $\Delta_{ABC}^{max} \equiv \max(\Delta_{ABC})$ at a deployed height $w_A^{\Delta_{ABC}^{max}}$ and two points ($w_A = 0$ and w_A^c) at which $\Delta_{ABC} = 0$.

Next, in Figure A.3 we show the effect of α and β on Δ_{ABC}. First, in Figure A.3a we investigate how β affects the Δ_{ABC} vs. w_A curve when choosing $\alpha = 45°$. We find that

- for $\beta \to \beta_{min} = \pi/4 - \alpha/2$

$$w_A^c \to 0, \quad \text{and} \quad \Delta_{ABC}^{max} = \max(\Delta_{ABC}) \to 0. \tag{A.12}$$

- for $\beta \to \beta_{max} = \pi/2 - \alpha$, Δ_{ABC}^{max} largely increases and

$$w_A^c \to w_A^{\Delta_{ABC}^{max}}. \tag{A.13}$$

As shown in Figure A.3b, similar trends are found when increasing the angle α for a fixed value of β (here we choose $\beta = 45°$). It is also interesting to note that for $\alpha = 60°$ Δ_{ABC} monotonically increases and the triangle does not have a deployed compatible state. This is because for $\alpha = 60°$, $\beta = 45° > \beta_{max} = \pi/2 - \alpha$.

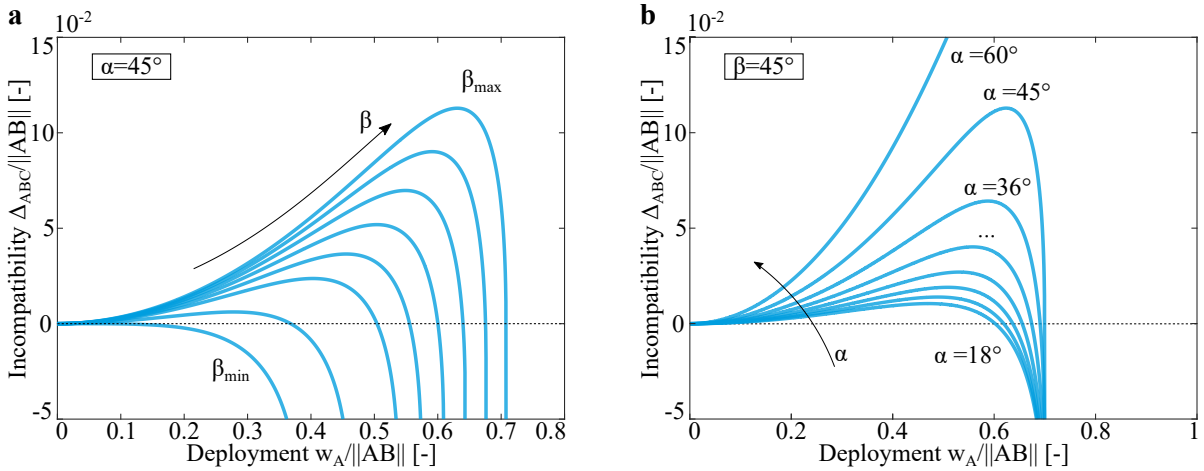

Figure A.3: Effect of α and β on the Δ_{ABC}-w_A curve. (a) Effect of varying β for triangles with $\alpha = 45°$. **(b)** Effect of varying α for triangles with $\beta = 45°$

To identify triangles that can potentially lead to deployable structures that are inflatable, we then plot the evolution of Δ_{ABC} as a function of V_{ABC}. In Figure A.4a we report such curves for triangles with $\alpha = 45°$ and $\beta \in [22.5°, 45°]$ and highlight two important volume configurations: the volume at the deployed compatible state , V^c_{ABC} (white circular marker), and the maximum volume, V^{max}_{ABC} (green circular marker), that can be expressed as

$$V^{max}_{ABC} = \frac{||AB||^3}{12} \frac{\sin\alpha \sin^2\beta}{\sin(\alpha+\beta)}. \tag{A.14}$$

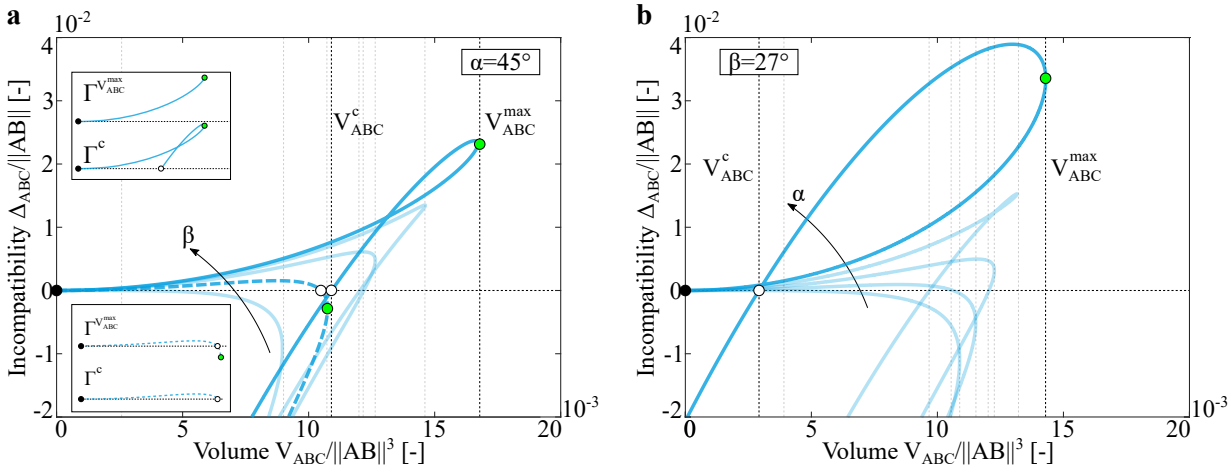

Figure A.4: Effect of α and β on the Δ_{ABC}-V_{ABC} curve. (a) Effect of varying β for triangles with $\alpha = 45°$. The compatible, V^c_{ABC}, and maximum, V^{max}_{ABC}, volume states are highlighted for $\beta = 45°$.**(b)** Effect of varying α for triangles with $\beta = 27°$. The compatible, V^c_{ABC}, and maximum, V^{max}_{ABC}, volume states are highlighted for $\alpha = 60°$.

We find that for low values of β the deployed compatible state with corresponding volume, V^c_{ABC}, is reached before the state of maximum volume, V^{max}_{ABC}, enabling actuation through inflation (see inset on the lower left corner of Figure A.4a). Differently, for large values of β the configuration of maximum volume is reached before the deployed compatible state and, therefore, that state cannot be reached through inflation (see inset on the upper left corner of Figure A.4a). Note that these trends are also found when considering a triangle with $\beta = 27°$ and $\alpha \in [36°, 60°]$ (see Figure A.4b). Guided by these results, we then introduce the inflation constraint

$$h_{ABC} = \frac{\Gamma^{V^{max}_{ABC}}}{\Gamma^c}, \tag{A.15}$$

where $\Gamma^{V^{max}_{ABC}}$ and Γ^c are the arc lengths measured on the Δ_{ABC}-V_{ABC} curve between the flat compatible state and the state of maximum volume and between the flat and expanded compatible configurations, respectively (see Figure A.4a). It follows from Eq. A.15 that only triangles with $\log h_{ABC} \geq 0$ can be deployed through fluidic actuation as those are the only ones for which the expanded compatible configuration is reached before the one with maximum volume during inflation.

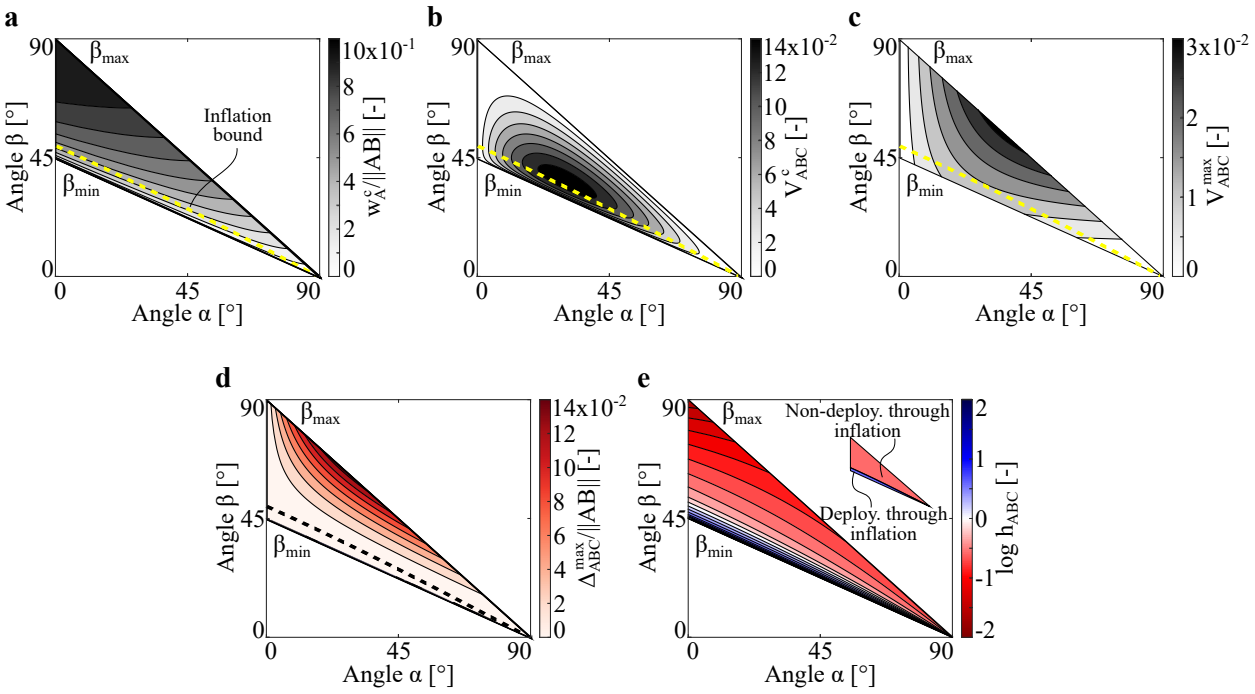

Figure A.5: Deployment of an initially flat triangular building block: summary of derived results. (a-e) Contour maps of (a) the compatible deployment height, w^c_A, (b) the volume at the deployed compatible state, V^c_{ABC}, (c) the maximum volume, V^{max}_{ABC}, (d) the maximum incompatibility during deployment, Δ^{max}_{ABC}, and (e) the inflation constraint, $\log h_{ABC}$, as a function of the angles α and β.

Finally, in Figure A.5 we summarize the results derived here by reporting contour maps of the compatible deployment height, w_A^c, the compatible deployment volume, V_{ABC}^c, the maximum volume, V_{ABC}^{max}, the maximum geometric incompatibility, Δ_{ABC}^{max}, and the inflation constraint, $\log h_{ABC}$.

A.1.2 Deployment of an initially rotated triangular building block

So far, we have focused on triangular building blocks defined by internal angles α and β that initially lie in the xy-plane and recover their projected angle α in a deployed state on such plane for $w_A = w_A^c$ and $V_{ABC} = V_{ABC}^c$. However, the triangle in the xy-plane can also be seen as the projection of a triangle with internal angles α and β that has been initially rotated around its edge BC to have a deployment height w_A^i, volume under the triangle V_{ABC}^i, and projected angles α_{xy}^i and β_{xy}^i (see Figure A.6). Note that such initially rotated building block is fully defined by the projected angles α_{xy}^i and β_{xy}^i and the internal angle β and that its other geometric parameters, α and w_A^i, can be derived from simple geometric considerations as

$$\alpha = \pi - \arccos\left(\frac{\sqrt{2}\left(\cos 2\beta - \frac{\sin\left(\alpha_{xy}^i + 2\beta_{xy}^i\right)}{\sin\alpha_{xy}^i}\right)}{\sqrt{-\frac{\frac{\cos 2\alpha_{xy}^i + \cos\left(2\alpha_{xy}^i + 4\beta_{xy}^i\right) - 2}{\sin\alpha_{xy}^i} + 4\cos 2\beta \sin\left(\alpha_{xy}^i + 2\beta_{xy}^i\right)}{\sin\alpha_{xy}^i}}}\right), \tag{A.16}$$

and

$$w_A^i = \sqrt{||AC||^2 - ||AC_{xy}^i||^2} = ||AB||\sin\beta\sqrt{1 - \frac{\tan^2\beta_{xy}^i}{\tan^2\beta}}, \tag{A.17}$$

where AC_{xy}^i is the edge AC projected on the xy-plane at the first intersection with the circle, whose length is given by

$$||AC_{xy}^i|| = ||AB||\frac{\cos\beta\tan\beta_{xy}^i}{\sin(\alpha_{xy}^i + \beta_{xy}^i)}. \tag{A.18}$$

Further, by substituting Eq. A.17 into Eq. A.1, we find that the volume initially under the triangle is

$$V_{ABC}^i = \frac{||AB||^3}{6}\frac{\cos^2\beta\,\sin\alpha_{xy}^i\,\sin\beta\,\tan\beta_{xy}^i}{\sin\left(\alpha_{xy}^i + \beta_{xy}^i\right)\cos\beta_{xy}^i}\sqrt{1 - \frac{\tan^2\beta_{xy}^i}{\tan^2\beta}}. \tag{A.19}$$

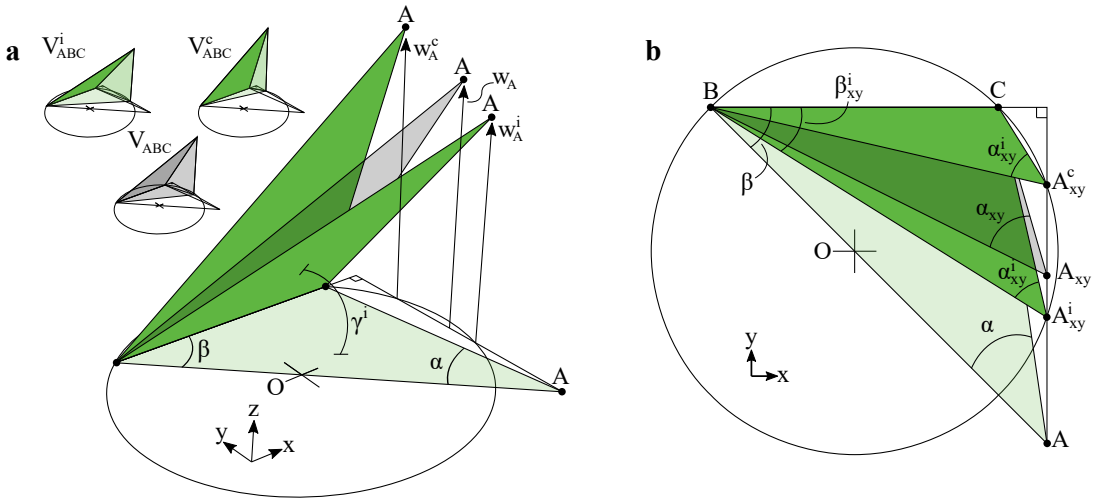

Figure A.6: Deployment of an initially rotated triangular building block. (a-b) Isometric and projected views of a triangular building block ABC that recovers its projected angle α^i_{xy} during deployment leading to two distinct compatible states.

Focusing on the xy-plane (see Figure A.6b), we see that, if

$$\begin{aligned}
\alpha^i_{xy} &\in \left]\left(\alpha^i_{xy}\right)_{min}, \left(\alpha^i_{xy}\right)_{max}\right[= \left]0, \frac{\pi}{2}\right[, \\
\beta^i_{xy} &\in \left[\left(\beta^i_{xy}\right)_{min}, \left(\beta^i_{xy}\right)_{max}\right] = \left[\frac{\pi}{4} - \frac{\alpha^i_{xy}}{2}, \frac{\pi}{2} - \alpha^i_{xy}\right], \\
\beta &\in [\beta_{min}, \beta_{max}[= \left[\beta^i_{xy}, \frac{\pi}{2}\right[,
\end{aligned} \tag{A.20}$$

upon further rotation the projection of the triangle intersects a circle circumscribed to the initial configuration also at a displacement, w^c_A, and volume, V^c_{ABC}. The displacement w^c_A can be obtained as

$$w^c_A = \sqrt{||AC||^2 - ||AC^c_{xy}||^2} = ||AB|| \sin\beta \sqrt{1 - \cot^2(\alpha^i_{xy} + \beta^i_{xy}) \cot^2\beta}, \tag{A.21}$$

where AC^c_{xy} is the edge AC projected on the xy-plane at the second intersection with the circle, whose length is given by

$$||AC^c_{xy}|| = ||AB|| \frac{\cos\beta \cot\left(\alpha^i_{xy} + \beta^i_{xy}\right)}{\cos\beta^i_{xy}}. \tag{A.22}$$

Further, by substituting Eq. A.21 in Eq. A.1, we get

$$V^c_{ABC} = \frac{||AB||^3}{6} \frac{\cos^2\beta \, \sin(\alpha^i_{xy}) \, \sin\beta}{\sin\left(\alpha^i_{xy}+\beta^i_{xy}\right) \, \tan\left(\alpha^i_{xy}+\beta^i_{xy}\right) \, \cos\left(\beta^i_{xy}\right)} \sqrt{1-\cot^2\left(\alpha^i_{xy}+\beta^i_{xy}\right)\cot^2\beta}. \tag{A.23}$$

It follows from the inscribed angle theorem that for $w_A = w^c_A$ and $V_{ABC} = V^c_{ABC}$, the projected angle α^i_{xy} is recovered on the projected plane. As such, the triangle ABC possesses two states – identified by w^i_A and w^c_A – for which $\alpha^i_{xy} = \alpha_{xy}$ separated by states for which $\alpha^i_{xy} \neq \alpha_{xy}$, where α_{xy} is still given by Eq. A.6.

In Figure A.7a we show the evolution of the projected angle variation, $\Delta\alpha \equiv \alpha_{xy} - \alpha^i_{xy}$, as a function of w_A for a triangular building block with $\beta = 45°$, $\alpha^i_{xy} = 45°$, and $\beta^i_{xy} = 32°$ (for which $\alpha = 36.8°$ according to Eq. A.16). We find a non-linear relationship similar to that obtained for the initially flat building blocks, characterized by a local maximum

$$\Delta\alpha_{max} \equiv \max(\Delta\alpha) = \arccos\left(\frac{2\cot(\alpha^i_{xy}+\beta^i_{xy})\sin 2\beta^i_{xy}}{\sqrt{\csc^4(\alpha^i_{xy}+\beta^i_{xy})\sin 2\beta^i_{xy}\sin(2(\alpha^i_{xy}+\beta^i_{xy}))\sin^2(\alpha^i_{xy}+2\beta^i_{xy})}}\right), \tag{A.24}$$

at

$$w^{\Delta\alpha_{max}}_A = ||AB||\sin\beta\sqrt{1-\tan\beta^i_{xy}\cot^2\beta\cot(\alpha^i_{xy}+\beta^i_{xy})}. \tag{A.25}$$

and two points ($w_A = w^i_A$ and $w_A = w^c_A$) at which $\Delta\alpha = 0$.

As for the initially flat building blocks, also in this case we can quantify the difference between α_{xy} and α^i_{xy} by introducing the distance

$$\Delta_{ABC} = ||AC_{xy}|| \cdot \sin(\alpha_{xy} - \alpha^i_{xy}), \tag{A.26}$$

where $||AC_{xy}||$ is given in Eq. A.8. In Figure A.7b we show the evolution of Δ_{ABC} as a function of w_A for a triangular building block with $\beta = 45°$, $\alpha^i_{xy} = 45°$, and $\beta^i_{xy} = 32°$. Again, we find a behavior similar to that observed for the initially flat building blocks, with a local maximum $\Delta^{max}_{ABC} \equiv \max(\Delta_{ABC})$ at $w^{\Delta^{max}_{ABC}}_A$ and two points ($w_A = w^i_A$ and w^c_A) at which $\Delta_{ABC} = 0$.

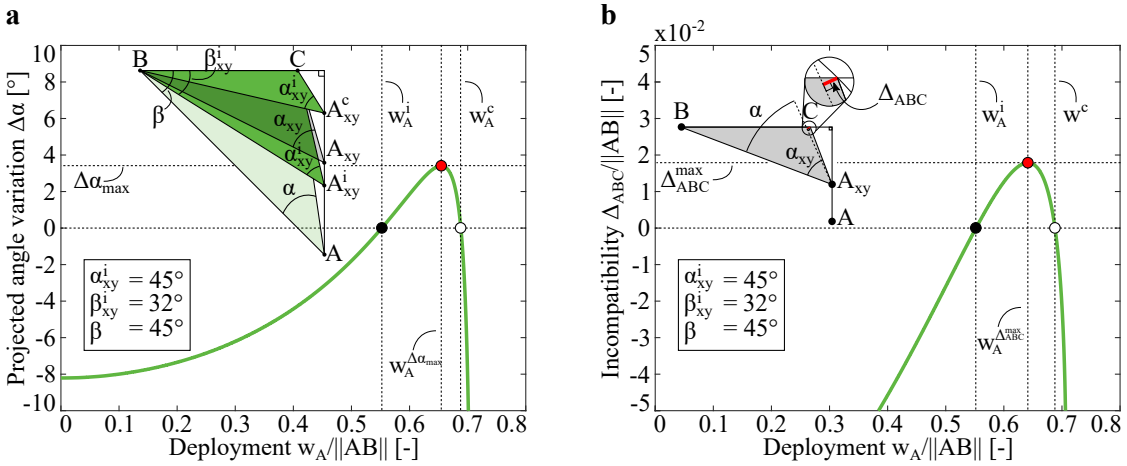

Figure A.7: Evolution of $\Delta\alpha$ and Δ_{ABC} during deployment. (a-b) Evolution of (a) $\Delta\alpha$ and (b) Δ_{ABC} as a function of the deployment of vertex A, w_A, for a triangle with $\alpha^i_{xy} = 45°$, $\beta^i_{xy} = 32°$ and $\beta = 45°$. The red circular marker indicates the local maximum, whereas the black and white circular markers indicate the two compatible configurations.

Next, in Figure A.8 we explore the effect of α^i_{xy}, β^i_{xy}, and β on Δ_{ABC}. First, in Figure A.8a we investigate how β^i_{xy} affects the Δ_{ABC} vs. w_A curve when choosing $\alpha^i_{xy} = 45°$ and $\beta = 45°$. We find that

- for $\beta^i_{xy} \to \left(\beta^i_{xy}\right)_{min} = \pi/4 - \alpha^i_{xy}/2$

$$w^i_A \to w^c_A, \quad \text{and} \quad \Delta^{max}_{ABC} = \max\left(\Delta_{ABC}\right) \to 0. \tag{A.27}$$

- for $\beta^i_{xy} \to \left(\beta^i_{xy}\right)_{max} = \pi/2 - \alpha^i_{xy}$, Δ^{max}_{ABC} largely increases and

$$w^i_A \to 0, \quad \text{and} \quad w^c_A \to w_A^{\Delta^{max}_{ABC}}. \tag{A.28}$$

As shown in Figure A.8b, we find similar trends when increasing the angle α_{xy}, while keeping $\beta^i_{xy} = 32°$ and $\beta = 45°$. However, as expected from Eq. A.17, in this case the initial deployment height, w^i_A, is constant and not affected by α^i_{xy}. Finally, in Figure A.8c we investigate how β affects the Δ_{ABC} vs. w_A curve for triangles with $\alpha^i_{xy} = 45°$ and $\beta^i_{xy} = 45°$. By varying β over the range $[\beta^i_{xy}, \pi/2[$, we find that

- for $\beta \to \beta^i_{xy}$ we recover the case of the initially flat triangular building block and

$$w^i_A \to 0 \tag{A.29}$$

- for $\beta \to \pi/2$, Δ^{max}_{ABC} slightly decreases and

$$w^i_A \to w^c_A. \tag{A.30}$$

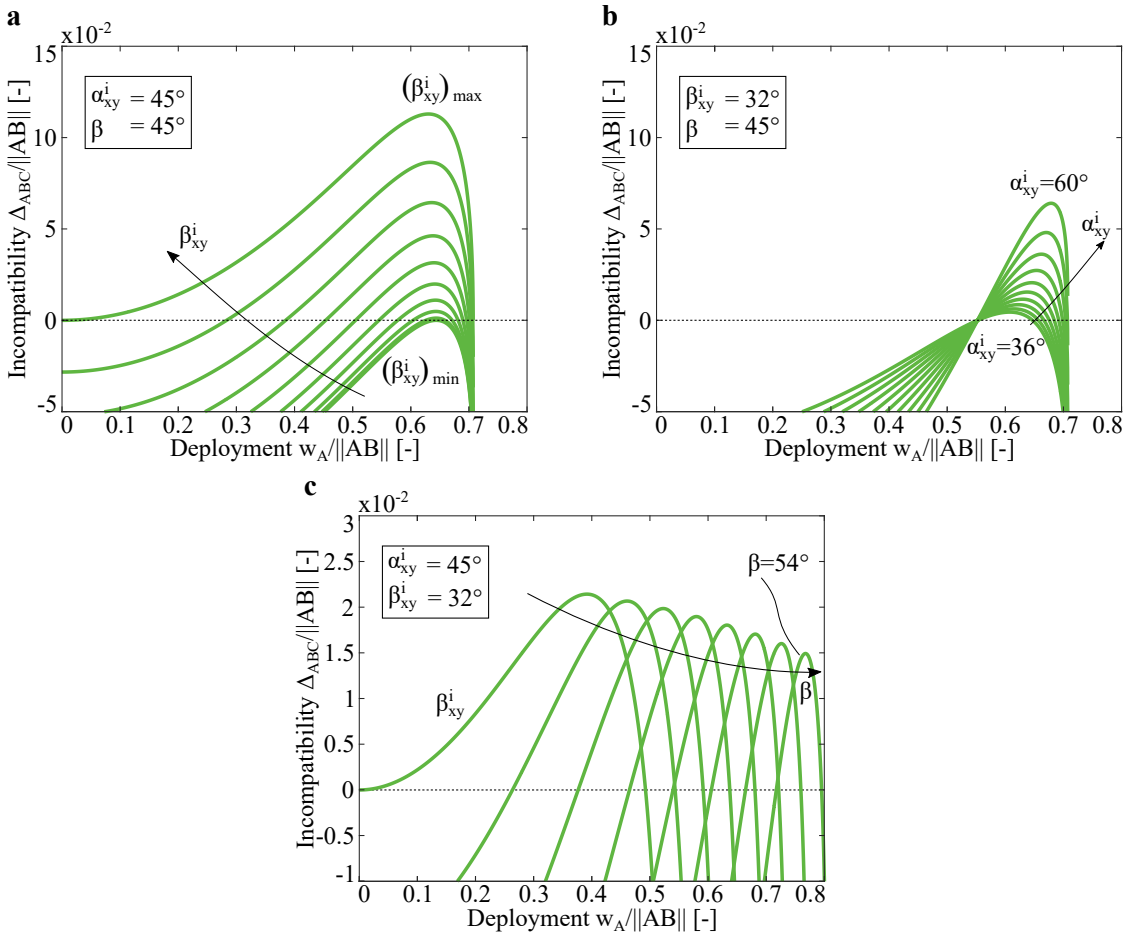

Figure A.8: Effect of β, α^i_{xy}, and β^i_{xy} on the Δ_{ABC}-w_A curve. **(a)** Effect of varying β^i_{xy} for triangles with $\alpha^i_{xy} = 45°$ and $\beta = 45°$. **(b)** Effect of varying α^i_{xy} for triangles with $\beta^i_{xy} = 32°$ and $\beta = 45°$. **(c)** Effect of varying β for triangles with $\alpha^i_{xy} = 45°$ and $\beta^i_{xy} = 32°$.

To identify triangles that can potentially lead to deployable structures that are inflatable, we then plot the evolution of Δ_{ABC} as a function of V_{ABC}. In Figure A.9a we report such curves for triangles with $\alpha^i_{xy} = 45°$, $\beta = 45°$ and $\beta^i_{xy} \in [22.5°, 45°]$ and highlight two important volume configurations: the volume at the deployed compatible state , V^c_{ABC} (white circular marker), and the maximum volume, V^{max}_{ABC} (green circular marker), that can be calculated from Eq. A.14. We find that for low values of β^i_{xy}, both deployed compatible state with corresponding volumes, V^i_{ABC} and V^c_{ABC} are reached before the state of maximum volume V^{max}_{ABC}, enabling actuation through inflation (see green dashed line in Figure A.9a). Differently, for large values of β the configuration of maximum volume is reached before the deployed compatible state with corresponding volume V^i_{ABC} and, therefore, that state cannot be reached through inflation (see green solid line in Figure A.9a). Note that similar trends are also found when considering a triangle with $\beta^i_{xy} = 32°$ and $\beta = 45°$ and $\alpha^i_{xy} \in [36°, 60°]$ (see Figure A.9b), although the effect of increasing α^i_{xy} is substantially smaller than β_{xy} on inflatability.

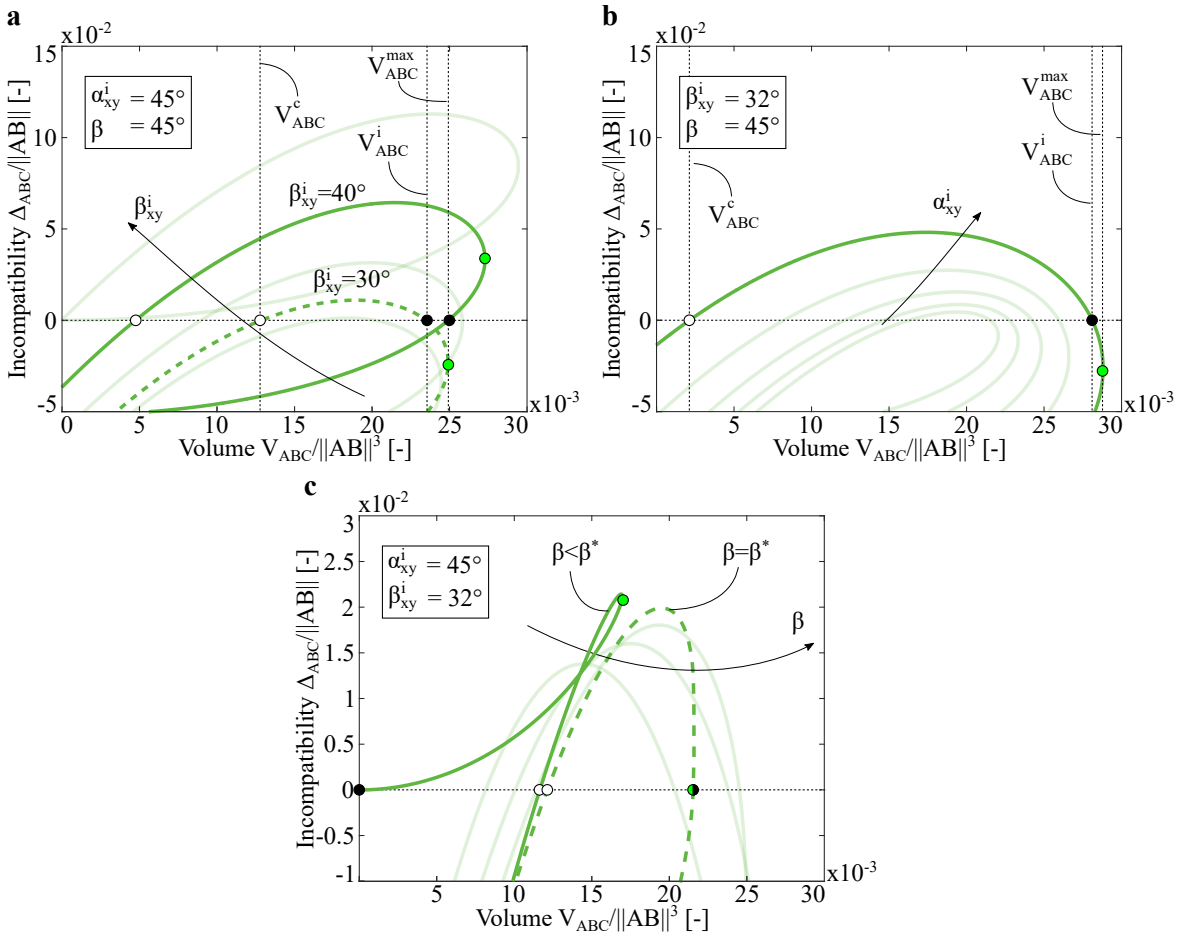

Figure A.9: Effect of β, α^i_{xy}, and β^i_{xy} on the Δ_{ABC}-V_{ABC} curve. **(a)** Effect of varying β^i_{xy} for triangles with $\alpha^i_{xy} = 45°$ and $\beta = 45°$. **(b)** Effect of varying α^i_{xy} for triangles with $\beta^i_{xy} = 32°$ and $\beta = 45°$. **(c)** Effect of varying β for triangles with $\alpha^i_{xy} = 45°$ and $\beta^i_{xy} = 32°$.

To identify initially rotated triangles that can deployed through fluidic actuation, we then use the inflation constraint defined in Eq. A.15. An interesting feature of the initially rotated building block is that for any combination of α^i_{xy} and β^i_{xy} (within the bounds defined in Eq. A.20), we can always select β such that $\log h_{ABC} \geq 0$. This is because we can set $\beta = \beta^*$, where β^* is the angle resulting in an initial rotated state defined by the deployment w^i_A that maximizes the volume under the triangle, i.e. $V^i_{ABC} = V^{max}_{ABC}$ (see Figure A.9c where for $\beta = \beta^*$ the black and green markers coincide). To determine β^*, we first determine the deployment angle, γ_i, by finding the dihedral angle (see Figure A.6a) between the planes of the flat and deployed triangles ABC

$$\gamma_i = \arccos\left(\frac{n_0 \cdot n_{w^i_A}}{||n_0|| \cdot ||n_{w^i_A}||}\right) = \arccos\left(\sqrt{\left(1 - \frac{w^2_A}{||AB||^2 \sin^2\beta}\right)}\right), \tag{A.31}$$

where n_0 and n_{w_A} are the normals of the planes defined by the flat and deployed triangles. Noting that a triangle maximizes its volume when the deployment angle is $\gamma_i = \pi/4$ and replacing w_A in Eq. A.31 by the expression of w_A^i in Eq. A.17, we find

$$\beta^* = \tan^{-1}\left(\sqrt{2}\tan\beta_{xy}^i\right). \tag{A.32}$$

Importantly, we expect an origami structure made out of initially rotated triangles with $\beta \geq \beta^*$ to be bistable and inflatable even if made out of a single building block.

Finally, in Figure A.10 we summarize the results derived here by reporting contour maps of the maximum geometric incompatibility, Δ_{ABC}^{max}, the inflation constraint, $\log h_{ABC}$, the compatible deployment heights, w_A^i and w_A^c, the compatible deployment volumes, V_{ABC}^i and V_{ABC}^c, and the maximum volume, V_{ABC}^{max} for three different values of β, i.e. $\beta = 30°$, $45°$, and $60°$.

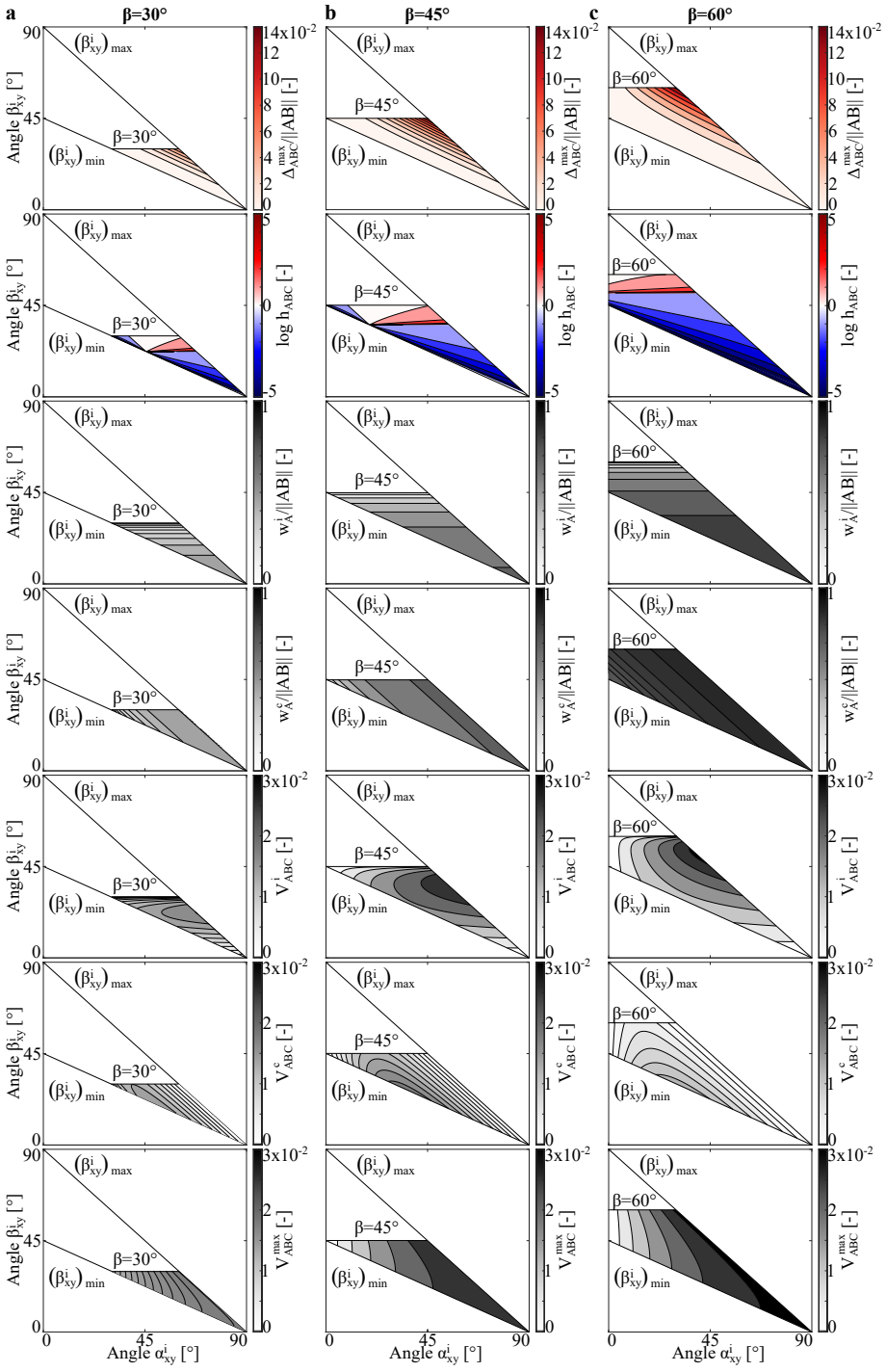

Figure A.10: Deployment of an initially rotated triangular building block: summary of derived results. (a-c) Contour maps of the maximum geometric incompatibility, Δ^{max}_{ABC}, the inflation constraint, $\log h_{ABC}$, the compatible deployment heights, w^i_A and w^c_A, the compatible deployment volumes, V^i_{ABC} and V^c_{ABC}, and the maximum volume, V^{max}_{ABC} for three different values of β, i.e. (a) $\beta = 30°$, (b) 45°, and (c) 60°.

A.1.3 Inflatable and bistable origami shapes

To realize inflatable origami structures with multiple stable states, we assemble the triangular building blocks discussed above. In this work, we present four different ways of connecting the building blocks to obtain a library of origami shapes. For three of them (which will be referred to as Design I, Design II, and Design III) we utilize initially flat building blocks, whereas for the fourth one (which will be referred to as Design IV) we utilize initially rotated building blocks.

Design I

To realize Design I, we arrange $2n$ initially flat triangles with angles $(\alpha^{(1)},\beta^{(1)})$ with $2n$ initially flat triangles with angles $(\alpha^{(2)},\beta^{(2)})$ to form two identical layers with n-fold symmetry and connect them at their outer boundaries (see Figure A.11). The resulting star-like structures define an internal volume

$$V = 2n(V^{(1)}_{ABC} + V^{(2)}_{ABC}), \tag{A.33}$$

exhibit geometric incompatibility

$$\Delta = 2n(\Delta^{(1)}_{ABC} + \Delta^{(2)}_{ABC}) \tag{A.34}$$

and are inflatable only if

$$\log h = \log\left(\frac{\Gamma^{V^{max}}}{\Gamma^{c}}\right) \geq 0, \tag{A.35}$$

where $\Gamma^{V^{max}}$ and Γ^{c} are the arc lengths measured on the Δ-V curve between the states with $V = 0$ and $V = V^{max} = \max(V)$ and between the two stable configurations, respectively. Note that to ensure structural integrity, the two triangular building blocks must have

(*i*) identical compatible deployment heights, i.e. $w^{c(1)}_{A} = w^{c(2)}_{A}$;

(*ii*) connecting deployed edges AB of equal length, i.e $||AB^{(1)}|| = ||AB^{(2)}||$;

(*iii*) angles that satisfy $\alpha^{(1)} + \alpha^{(2)} = \pi/n$.

Therefore, to realize a Design I structure, we first select the number of symmetric folds, n, and the angles of the first triangular building blocks $\alpha^{(1)}$ and $\beta^{(1)}$. It follows from requirements (*i*-*iii*) that the second triangular building block must have its internal angles equal to

$$\begin{aligned} \alpha^{(2)} &= \pi/n - \alpha^{(1)}, \\ \beta^{(2)} &= \arctan\left(\frac{\sin(\alpha^{(1)} + \beta^{(1)})}{\cos\beta^{(1)}\cos\alpha^{(2)}} - \tan\alpha^{(2)}\right). \end{aligned} \tag{A.36}$$

In Figures A.11a-c, we show an example of a Design I geometry (referred to as Design I-A), with $(\alpha^{(1)}_{\text{I-A}}, \beta^{(1)}_{\text{I-A}}) = (22°, 35°)$ and $(\alpha^{(2)}_{\text{I-A}}, \beta^{(2)}_{\text{I-A}}) = (68°, 14°)$ for which $\Delta^{max}/||AB|| = 2.67 \times 10^{-2}$ and $\log h = 0$. Finally, in Figure A.11d, we plot the evolution of the maximum incompatibility, $\Delta^{max} \equiv \max(\Delta)$, as a function of the inflation constraint, $\log h$, for $500,000$ different geometries with $n \in [2, 5]$, $\alpha \in]0, \pi/n[$, and $\beta \in [\pi/4 - \alpha/2, \pi/2 - \alpha]$ (note that the increase in brightness of the data points in Figure A.11d indicates an increase in number of symmetry folds, n, of the origami geometry).

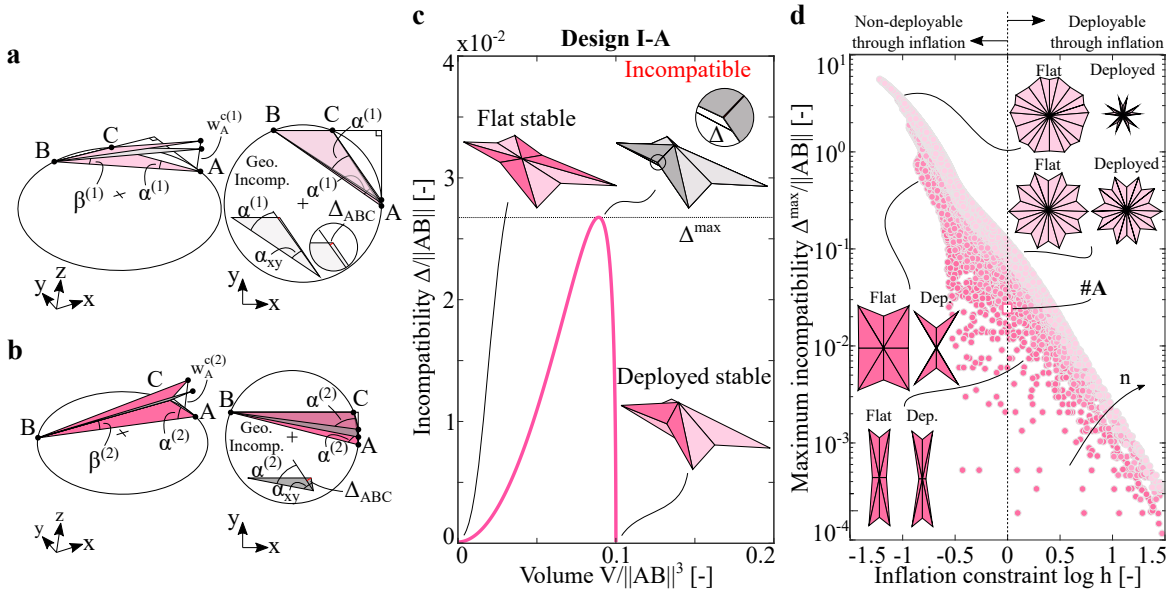

Figure A.11: Design I. (a-b) Isometric and projected views of the two building blocks used to create Design I-A. **(c)** Evolution of the incompatibility, Δ, as a function of the internal volume, V, for Design I-A. **(d)** Maximum incompatibility, Δ^{max} vs. inflation constraint, $\log h$ for $500,000$ different Design I geometries for increasing value of symmetry fold, n.

Design II

With the goal of increasing the geometric incompatibility of the inflatable designs, we investigate the response of star-like structures in which the longest edge of one triangle, $AB^{(1)}$, is connected to the shortest edge of the other one, $AC^{(2)}$. These geometries must satisfy the same requirements (*i-iii*) as Design I, except that we impose $||AB^{(1)}|| = ||AC^{(2)}||$ instead of $||AB^{(1)}|| = ||AB^{(2)}||$. Also in this case, to realize a Design II structure, we first select the number of symmetric folds, n, and the angles of the first triangular building block $\alpha^{(1)}$ and $\beta^{(1)}$. It then follows from requirements (*i-iii*) that the second triangular building block must have its internal angles equal to

$$\begin{aligned} \alpha^{(2)} &= \pi/n - \alpha^{(1)}, \\ \beta^{(2)} &= \arctan\left(\frac{\sin\beta^{(1)}}{\cos(\alpha^{(1)}+\beta^{(1)})\cos\alpha^{(2)}} - \tan\alpha^{(2)}\right). \end{aligned} \tag{A.37}$$

In Figures A.12a-c, we show an example of a Design II geometry (referred to as Design II-B), with $(\alpha^{(1)}_{\text{II-B}}, \beta^{(1)}_{\text{II-B}}) = (43.6°, 25.2°)$ and $(\alpha^{(2)}_{\text{II-B}}, \beta^{(2)}_{\text{II-B}}) = (46.4°, 33.5°)$ for which $\Delta^{max}/||AB|| = 8.58 \times 10^{-2}$ and $\log h = 0$. Finally, in Figure A.12d, we plot the evolution of the maximum incompatibility, Δ^{max}, as a function of the inflation constraint, $\log h$, for $500,000$ different geometries with $n \in [2,5]$, $\alpha \in]0, \pi/n[$, and $\beta \in [\pi/4 - \alpha/2, \pi/2 - \alpha]$.

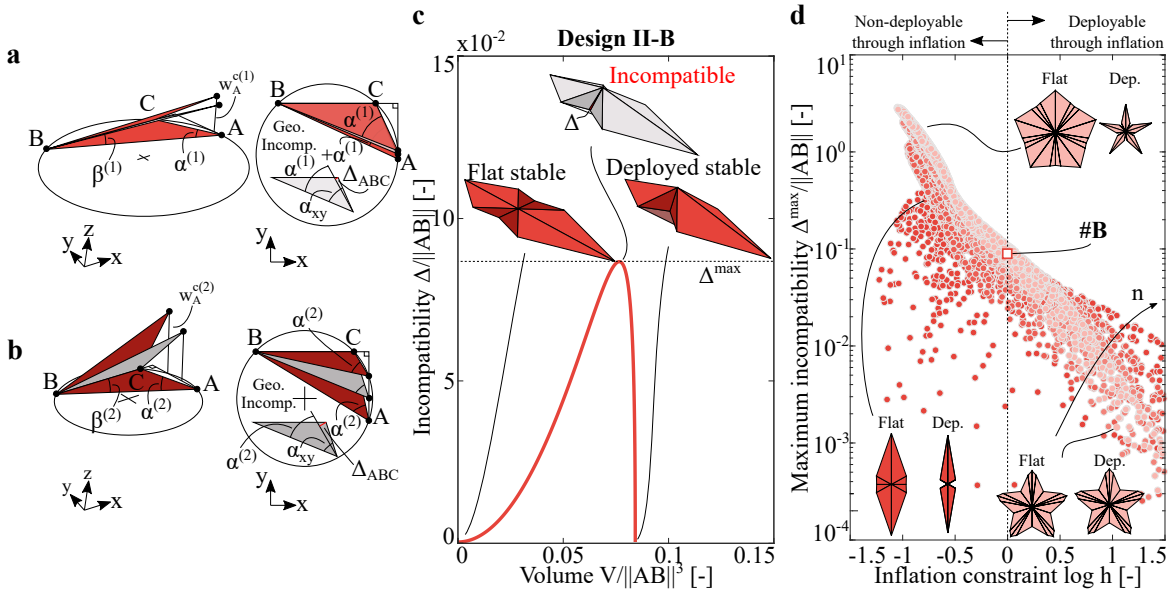

Figure A.12: Design II. (a-b) Isometric and projected views of the two building blocks used to create Design II-B. **(c)** Evolution of the incompatibility, Δ, as a function of the internal volume, V, for Design II-B. **(d)** Maximum incompatibility, Δ^{max} vs. inflation constraint, $\log h$ for $500,000$ different Design II geometries for increasing value of symmetry fold, n.

Design III

Whereas the connection of two different initially flat triangles side by side enables us to design inflatable and bistable structures, it limits us to star-like shapes. To expand the range of shapes, we next arrange the two triangles on top of each other in the flat configuration and mirror them twice to form an inflatable cavity (see Figure A.13). This leads to geometries comprising eight triangles that are initially flat and transformed into wedge-like shapes upon deployment. These geometries define an internal volume

$$V = 4\left(V^{(1)}_{ABC} - V^{(2)}_{ABC}\right), \tag{A.38}$$

exhibit geometric incompatibility

$$\Delta = 4\left(\Delta^{(1)}_{ABC} + \Delta^{(2)}_{ABC}\right) \tag{A.39}$$

and are inflatable only if the constraint given in Eq. A.35 is satisfied. Note that to ensure structural integrity, the two triangular building blocks must have

(*i*) identical compatible deployment heights, i.e. $w_A^{c(1)} = w_A^{c(2)}$;

(*ii*) connecting deployed edges of equal length, i.e $||AB^{(1)}|| = ||AC^{(2)}||$;

(*iii*) angles that satisfy $\alpha^{(1)} = \alpha^{(2)}$.

Therefore, to realize a Design III structure, we first select the angle of the first triangular building block $\alpha^{(1)}$ and $\beta^{(1)}$. It then follows from requirements (*i*-*iii*) that the second triangular building blocks must have its internal angles equal to

$$\begin{aligned} \alpha^{(2)} &= \alpha^{(1)}, \\ \beta^{(2)} &= \arctan\left(\frac{\sin\beta^{(1)}}{\cos(\alpha^{(1)}+\beta^{(1)})\cos\alpha^{(2)}} - \tan\alpha^{(2)}\right). \end{aligned} \tag{A.40}$$

In Figures A.13a-c, we show an example of a Design III geometry (referred to as Design III-C), with $(\alpha^{(1)}_{\text{III-C}}, \beta^{(1)}_{\text{III-C}}) = (37.1°, 30.0°)$ and $(\alpha^{(2)}_{\text{III-C}}, \beta^{(2)}_{\text{III-C}}) = (37.1°, 40.6°)$ for which $\Delta^{max}/||AB|| = 9.93 \times 10^{-2}$ and $\log h = 0.544$. Finally, in Figure A.13d, we plot the evolution of the maximum incompatibility, Δ^{max}, as a function of the inflation constraint, $\log h$, for $500,000$ different geometries with $\alpha \in]0, \pi/2[$, and $\beta \in [\pi/4 - \alpha/2, \pi/2 - \alpha]$.

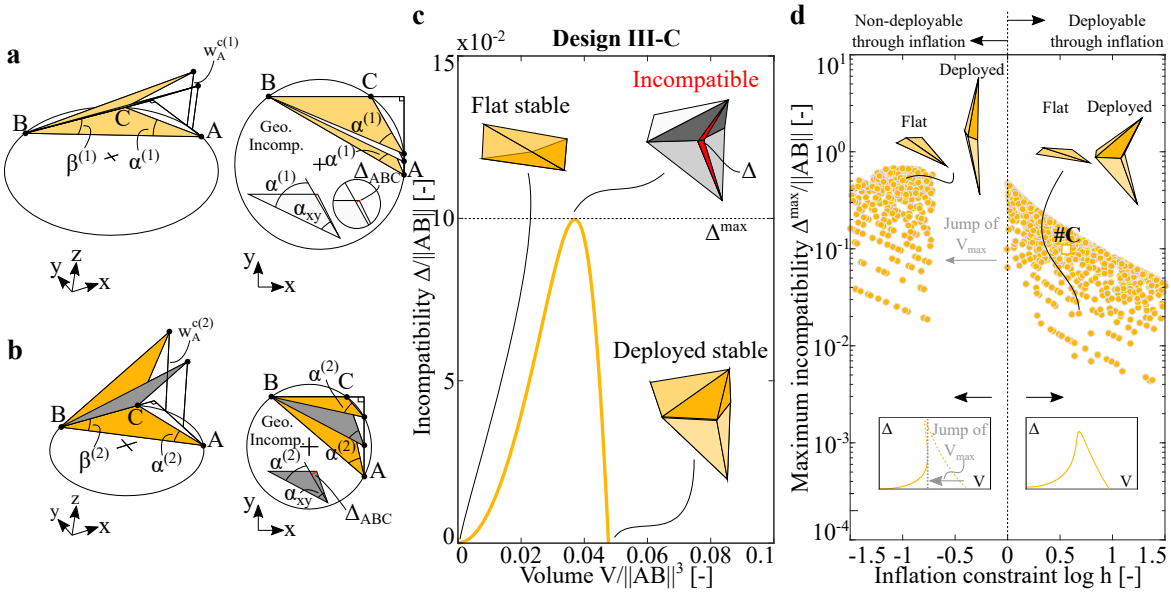

Figure A.13: Design III. (a-b) Isometric and projected views of the two building blocks used to create Design III-C. **(c)** Evolution of the incompatibility, Δ, as a function of the internal volume, V, for Design III-C. **(d)** Maximum incompatibility, Δ^{max} vs. inflation constraint, $\log h$ for $500,000$ different Design III geometries.

Design IV

To realize Design IV, we arrange $4n$ initially deployed triangles with angles α and β to form two identical layers with n-fold symmetry and connect them at their outer boundaries (see Figure A.14). Note that in this case, since we can choose $\beta > \beta^*$, we can use only one triangular building block to make bistable and inflatable structures. The resulting star-like structures define an internal volume

$$V = 4nV_{ABC}, \tag{A.41}$$

exhibit geometric incompatibility

$$\Delta = 4n\Delta_{ABC}, \tag{A.42}$$

and are inflatable only if

$$\log h = \log\left(\frac{\Gamma^{V^{max}}}{\Gamma^{c}}\right) \geq 0, \tag{A.43}$$

where $\Gamma^{V^{max}}$ and Γ^{c} are the arc lengths measured on the Δ-V curve between the states with $V = 4nV^{i}_{ABC}$ and $V = V^{max} = \max(V)$ and between the two stable configurations, respectively. Note that to ensure structural integrity, the triangular building blocks must have

(i) projected angle $\alpha^{i}_{xy} = \pi/n$;

(ii) projected angle $\beta^{i}_{xy} \in [\pi/4 - \alpha^{i}_{xy}/2, \pi/2 - \alpha^{i}_{xy}]$;

(*iii*) interior angle $\beta \in [\beta^i_{xy}, \pi/2[$.

Therefore, to realize a Design IV structure, we first select the number of symmetric folds, n, the projected angle β^i_{xy} and the interior angle β. Then, we use Eq. A.16 to determine α. Note that to make the structure deployable through inflation (i.e. $\log h \geq 0$) we have to select $\beta \geq \beta^*$.

In Figures A.14a-c, we show an example of a Design IV geometry (referred to as Design IV-D), with $(\alpha_{\text{IV-D}}, \beta_{\text{IV-D}}) = (29°, 56°)$ and $(\alpha^i_{xy}, \beta^i_{xy}) = (45°, 33°)$ for which $\Delta^{max}/||AB|| = 2.05 \times 10^{-1}$ and $\log h = 0.508$. Finally, in Figure A.14d, we plot the evolution of the maximum incompatibility, Δ^{max}, as a function of the inflation constraint, $\log h$, for $500,000$ different geometries with $n \in [3, 5]$, $\beta^i_{xy} \in [\pi/4 - \alpha/2, \pi/2 - \alpha]$, and $\beta \in [\beta^i_{xy}, \pi/2[$.

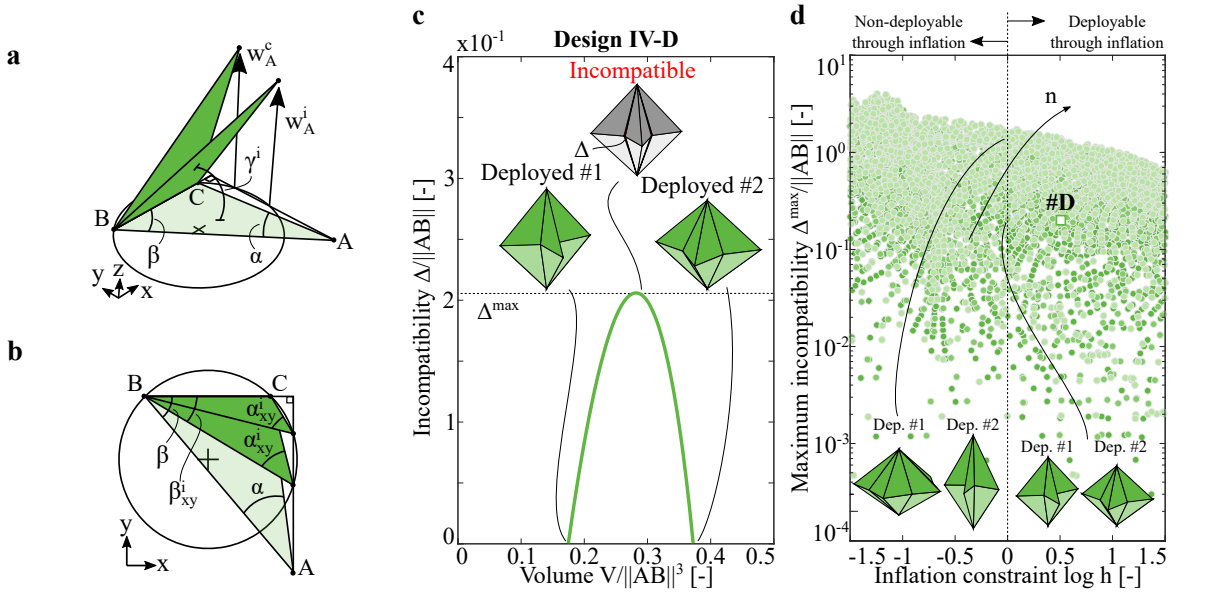

Figure A.14: Design IV. (a-b) Isometric and projected views of the triangular building block used to create Design IV-D. **(c)** Evolution of the incompatibility, Δ, as a function of the internal volume, V, for Design IV-D. **(d)** Maximum incompatibility, Δ^{max} vs. inflation constraint, $\log h$ for $500,000$ different Design IV geometries for increasing value of symmetry fold, n.

A.2 Fabrication

In this study, we fabricate both centimeter-scale and meter-scale origami structures. This section gives details of the fabrication methodology used for the two considered scales.

A.2.1 Geometry and material selection

The main structures built in this study include four simple centimeter-scale origami designs, i.e. Designs I-A, II-B, III-C, and III-D, as well as two meter-scale functional designs, i.e. the archway and the shelter. Designs I-A and II-B are both chosen because they maximize the geometric incompatibility of their respective class while still being inflatable to their expanded stable state, i.e. $\log h = 0$. Design III-C is chosen with incompatibility higher than that of Design II-B—to ensure bistability—and geometry suitable for the realization of the inflatable archway (Design III-C is one of the units of our arch—see Figure2.3a). Finally, we select Design IV-D to have incompatibility higher than that of Design II-B (as well as that of Design III-C) and to have two non-zero volume stable states (a property that cannot be achieved with Designs I-III).

To provide a robust and protective environment as well as to accommodate geometric frustration during deployment and minimize bending energy in the hinges, we build our origami structures out of stiff faces and compliant hinges. To realize centimeter-scale structures, inspired by recent works[64,65], we use two different methods based on cardboard and 3D-printed faces. In the first method, we connect laser-cut cardboard faces with a double-sided adhesive sheet to form the hinges. The cardboard structures can be fabricated quickly and inexpensively to validate the compatible shapes coming from our design methodology. However, they do not provide an airtight cavity to perform experimental testing. To realize inflatable prototypes, in the second method, we assemble centimeter-scale structures by connecting faces 3D-printed out of a standard rigid material (polyactic acid) with flexible polyester laser-cut sheets to form the hinges. For the meter-scale model, we use corrugated plastic sheets for the faces as they are available in large format (8 ft $\times$ 4 ft, 4-mm thick) and have high bending stiffness to weight ratio because of the corrugation. To form the compliant hinges, we reduce the thickness of the material locally by scoring the plastic sheet (see archway pattern in Figure A.20). In the case of the shelter, we also engrave the sheets (reducing the thickness on an area rather than a single line) to further increase the compliance compliance to the hinges to allow geometric frustration during the deployment (see shelter pattern in Figure A.20). Details on each fabrication technique are provided below.

A.2.2 Centimeter-scale structures

Structures with cardboard faces

In the first method, we assemble laser-cut cardboard facets with double-sided adhesive tape to form the hinges (see Figure A.15). Below are the eight steps needed to fabricate a cardboard sample (see Figure A.16):

- **Step 1:** we cut the different components of the origami structure out of 0.25-mm thick cardboard sheets (Bristol pad from Blick) with a 150 W laser-cutter (PLS6.150D from Universal Laser Systems), using both lasers at 30% power, 30% speed, and 1000 pulses per inch (**Step 1a**). **Step 1b:** we obtain a first sheet with trapezoidal shapes cut out to later accommodate for connection tabs (see **Step 3**). **Step 1c:** we obtain another sheet with trapezoidal shapes both cut out and patterned to later accommodate for connection pockets and tabs (see **Step 3**). Note that the circular holes are for alignment purposes (see **Steps 2** and **3**).
- **Step 2:** we insert the cut sheet obtained in **Step 1b** on an alignment platform and place double-sided adhesive tape (0.05-mm thick sheet from Graphix) on the origami parts.
- **Step 3:** we overlay the sheet obtained in **Step 1c** on top of the sheet with adhesive to create two layers of triangular facets connected by adhesive tape to form the hinges. Note the tabs and pockets now have exposed adhesive for connection.
- **Step 4:** we place the two assembled sheets in the laser cutter at the same location using the alignment circular holes.
- **Step 5:** we cut out the perimeter of the origami patterns on the sheets with the laser-cutter and obtain two hinged triangular facet layers with tabs and pockets for connection.
- **Step 6:** we align the two layers and fold the tabs on the corresponding pockets to create a closed origami structure.
- **Step 7:** we insert inlets (for fluidic supply) on two of the faces (designed with an additional hole to accommodate it).
- **Step 8:** we deploy the origami structure from the flat stable state to the expanded stable state.

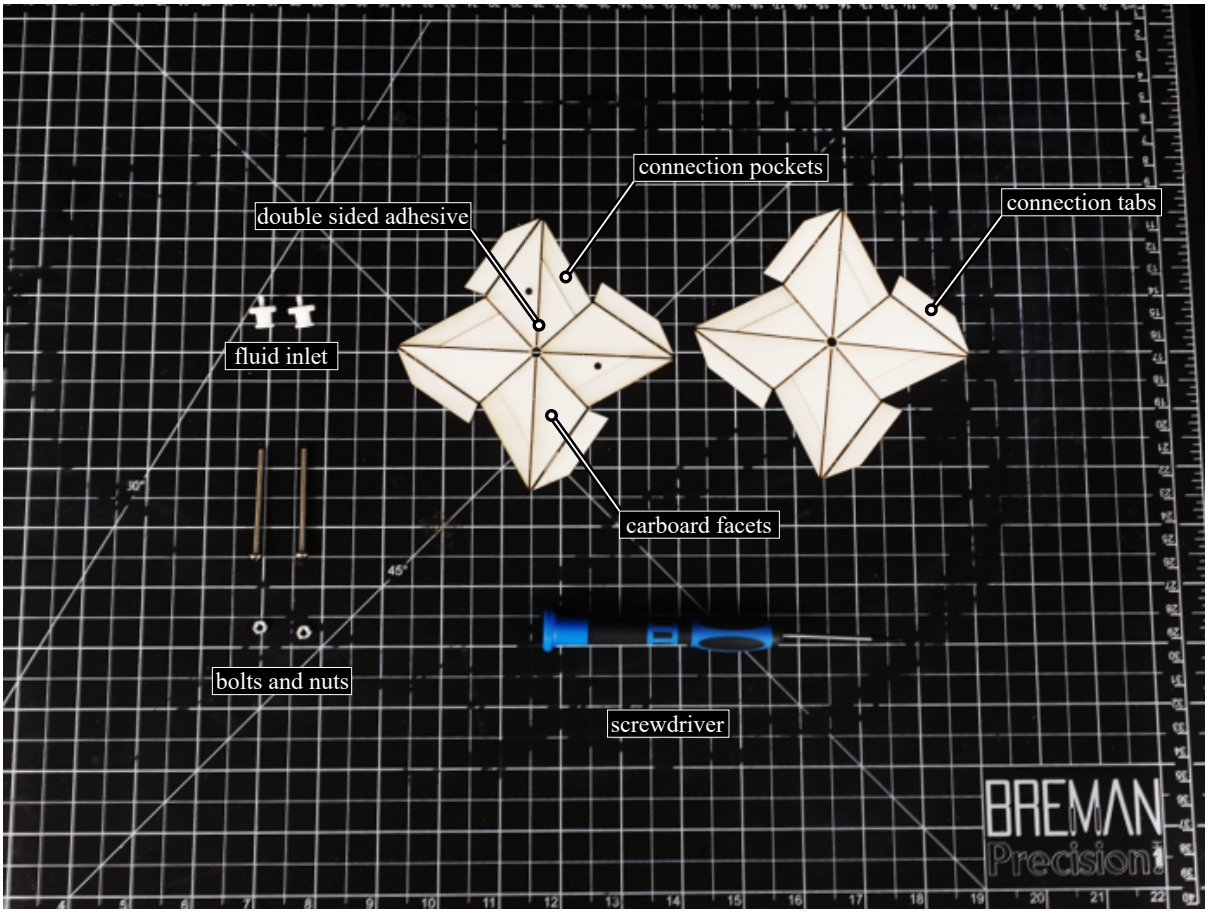

Figure A.15: Toolkit of the centimeter-scale origami structures with cardboard facets. The tools required to build the centimeter-scale origami structures out of cardboard facets and double-sided adhesive tape hinges.

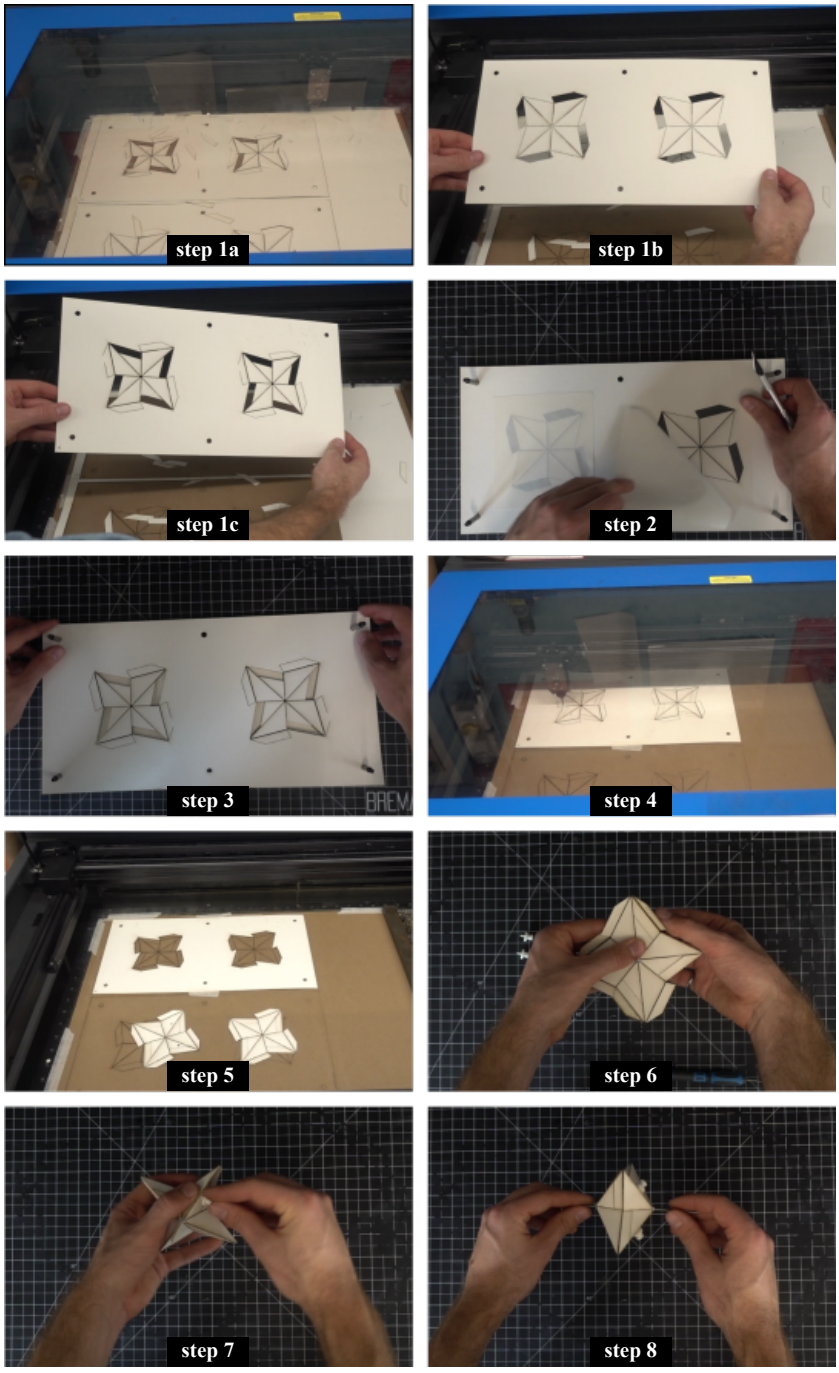

Figure A.16: Centimeter-scale fabrication with cardboard facets. Snapshots of the eight steps required to fabricate the centimeter-scale origami structures with cardboard facets.

Structures with 3D-printed faces

To realize inflatable prototypes, we assemble centimeter-scale structures by connecting 3D-printed faces with flexible laser-cut sheets to form the hinges (see Figure A.17).

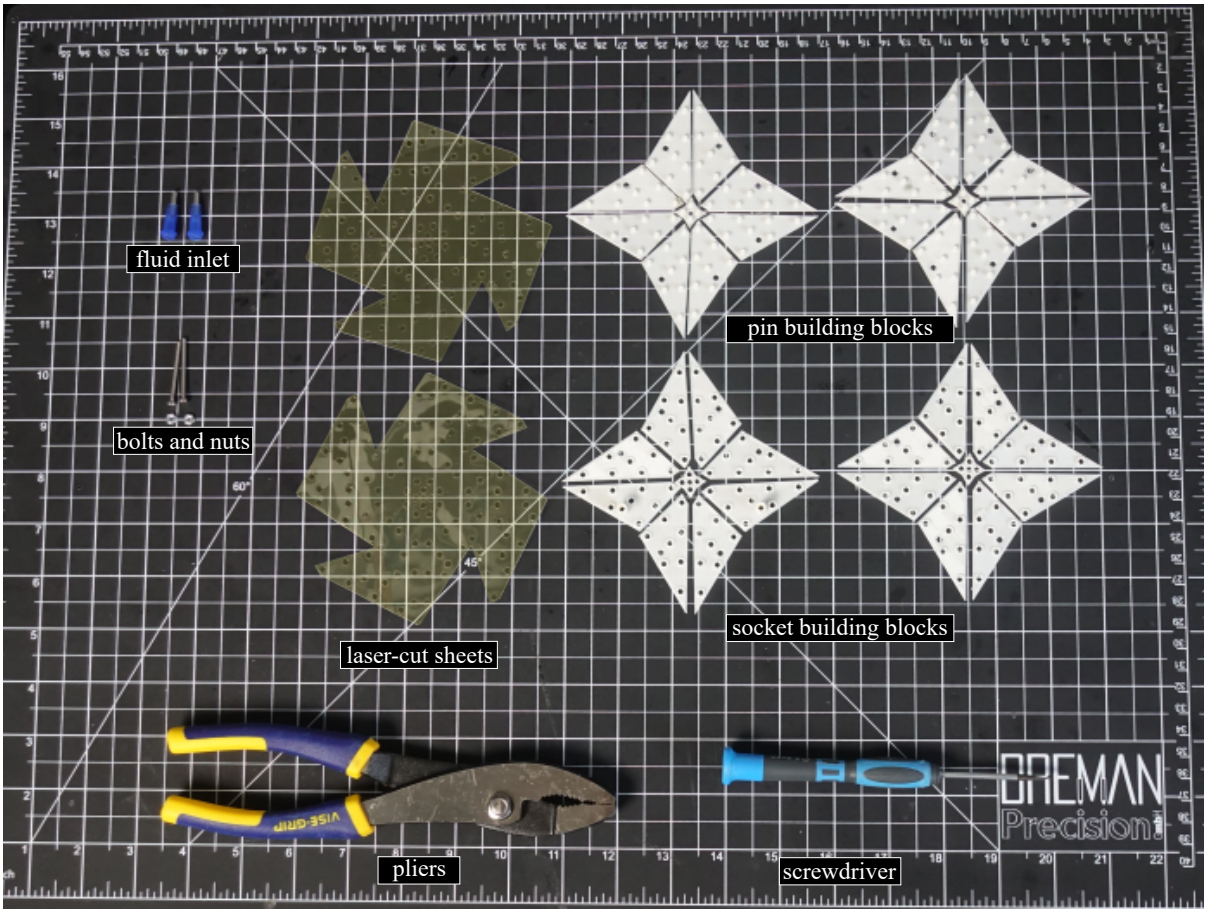

Figure A.17: Toolkit of the centimeter-scale origami structures with 3D-printed facets. The tools required to build the centimeter-scale origami structures with 3D-printed facets.

For each face of the structure, we 3D-print two 0.5-mm thick layers (3D Universe 2.85 mm white PLA filament bundle) using an Ultimaker 3 with a 0.25 mm print core with slight modifications to the *fine* default settings (travel acceleration lowered to 2000 mm/s^2). Note that to facilitate assembly one layer has a set of pins printed on one of its surfaces, whereas the other has sockets. The polyester sheets (0.002-in thick polyester film from McMaster-Carr) are cut with a 150 W laser-cutter (PLS6.150D from Universal Laser Systems), using both lasers at 8% power, 30 % speed, and 1000 pulses per inch. To connect faces together and form a complete origami structure, we snap the pin and socket connections on the 3D-printed parts together using pliers. Note that to obtain

optimal bonding between the faces we use pins with height and diameter equal to 1.5 mm and 2.65 mm, respectively, and ring sockets with height, internal, and external diameters equal to 0.5 mm, 2.8 mm, 4.3 mm, respectively. Finally, to seal the origami structure, we coat it in the deployed state with a 0.5 mm-thick layer of silicone rubber (Ecoflex 00-30 from Smooth-On). Below are the eight steps needed to fabricate a sample (see Figure A.18):

- **Step 1:** we 3D-print 0.5-mm thick faces with pins and sockets out of polyactic acid (3D Universe 2.85 mm white PLA filament bundle) using a Ultimaker 3.
- **Step 2:** we laser-cut 0.002-in thick polyester sheets with a 150 W laser-cutter (PLS6.150D from Universal Laser Systems). Note that holes to allow for the pin-socket connections are embedded into the sheets.
- **Step 3:** we insert an inlet (for fluidic supply) on one of the faces (designed with an additional socket to accommodate it) and snap the corresponding face with pins, while lying the laser-cut sheet in the middle.
- **Step 4:** we arrange on the two laser-cut sheets half of the faces (all oriented in the same direction as the face with the inlet in **Step 3**) and snap them together.
- **Step 5:** we insert another inlet (for pressure measurement) on a face designed with an additional socket to accommodate it. Note that this face is symmetric to the previous ones already snapped.
- **Step 6:** we arrange on the two laser-cut sheets the remaining half of the faces (all oriented in the same direction as the face with the inlet in **Step 5**) and snap them together to form the closed origami structure in the flat stable state.
- **Step 7:** we manually deploy the origami to its expanded stable state.
- **Step 8:** we coat the origami structure with a thin layer of silicone rubber (Ecoflex 00-30 from Smooth-On), hang it, and let it cure for three hours at room temperature. Note that we repeat the coating process twice and apply two layers.

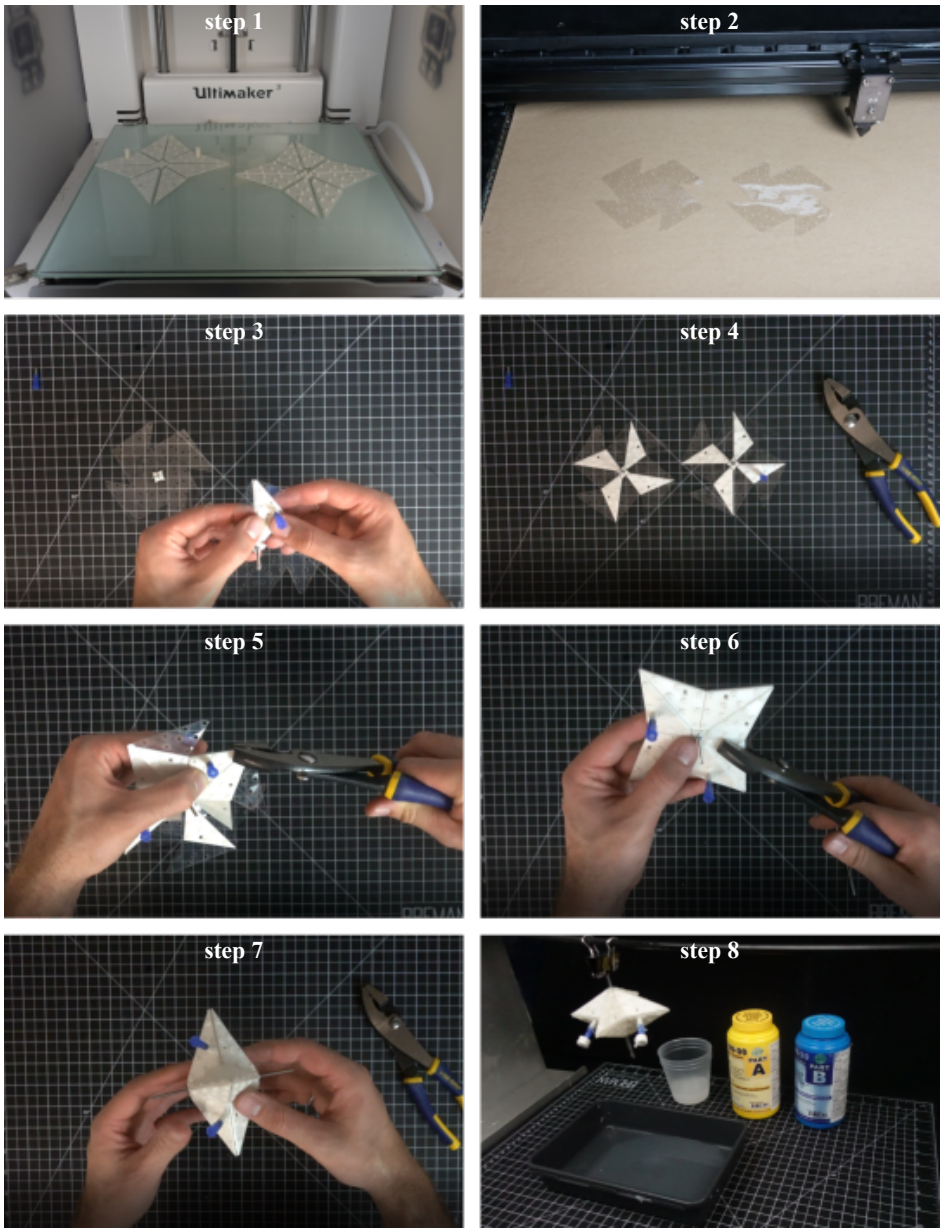

Figure A.18: Centimeter-scale fabrication with the 3D-printed facets. Snapshots of the eight steps required to fabricate the centimeter-scale origami structures with the 3D-printed facets.

In Section A.1, we demonstrated that we can design bistable and inflatable origami shapes with flat and expanded stable states. However, our prototypes have a non-zero rest angle in the initial stable state due to bending energy introduced in the hinges during fabrication. This rotation of the faces in the initial state is largely determined by the manufacturing technique used to realize the samples. To emphasize this point, in Figure A.19, we report the initial and expanded stable configurations for Design II-B (characterized by $(\alpha^{(1)}_{\text{II-B}}, \beta^{(1)}_{\text{II-B}}) = (43.6^\circ, 25.2^\circ)$ and $(\alpha^{(2)}_{\text{II-B}}, \beta^{(2)}_{\text{II-B}}) =$

$(46.4°, 33.5°)$) with cardboard and 3D-printed faces. While both samples show identical deployed stable configurations, their initial state is quite different. The cardboard structure is initially almost flat, but is not airtight (and therefore not inflatable). Differently, the silicone rubber layer that makes the sample with 3D-printed faces airtight (and therefore inflatable) leads to a more pronounced rotation of the faces in the initial state.

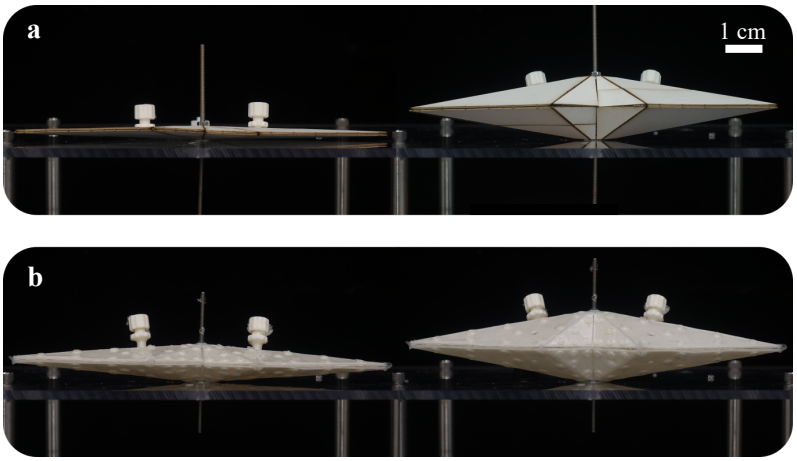

Figure A.19: Initial state for our sample. One of the stable states of our origami shapes can be designed to be geometrically flat. However, the fabricated structures exhibit a rest angle in the flat state due to the bending energy introduced in the hinges during fabrication as well as the finite thickness of the facets. Here, we show the stable flat state and deployed state of Design II-B (characterized by $(\alpha^{(1)}_{\text{II-B}}, \beta^{(1)}_{\text{II-B}}) = (43.6°, 25.2°)$ and $(\alpha^{(2)}_{\text{II-B}}, \beta^{(2)}_{\text{II-B}}) = (46.4°, 33.5°)$) fabricated with cardboard (**a**) and 3D-printed facets (**b**). While both samples show identical deployed stable configurations, their initial state is quite different. The cardboard structure is initially almost flat, but is not airtight (and therefore not inflatable). Differently, the Ecoflex layer that makes the sample with 3D-printed faces airtight (and therefore inflatable) leads to a more pronounced rotation of the faces in the initial state.

A.2.3 Meter-scale structures

All meter-scale structures tested in this study are made out of corrugated plastic sheets (clear 8 ft $\times$ 4 ft, 4-mm thick corrugated plastic sheets from Corrugated Plastics). The origami patterns are formed on the sheets using a digital cutting system (G3 cutter from Zünd). Note that for the inflatable arch we use a scoring operation (cutting through 75% of the material along a single line) to create compliant hinges that allow for the geometric incompatibility during deployment. However, to account for the larger amount of incompatibility in the shelter design, in addition to scoring, we engrave the sheets (removing 75% of the material on a localized zone with an engraver) to create hinges with extra compliance. The cutting patterns for the inflatable archway and emergency shelter are shown in Figure A.20.

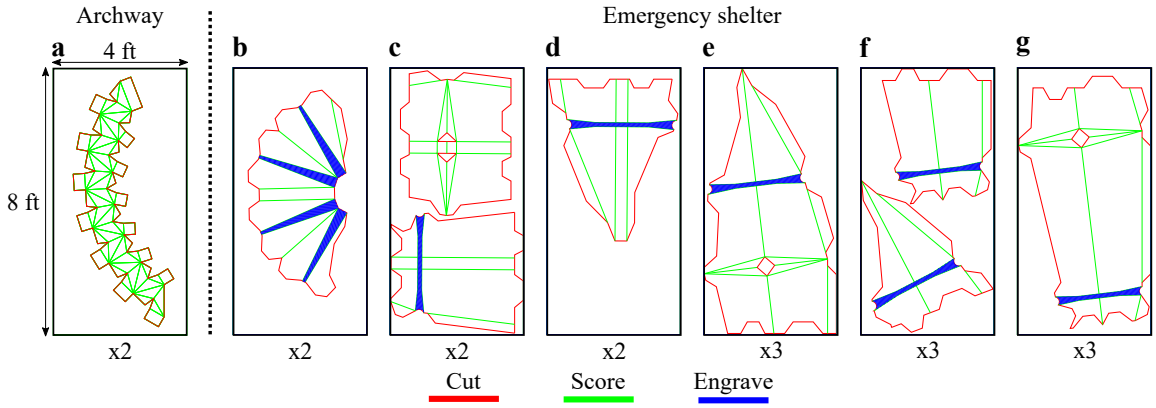

Figure A.20: Digital cutting patterns of the meter-scale archway and emergency shelter. **(a)** The archway is fabricated out of two identical cutting patterns where the red and green lines represent through cuts to release the parts and scoring operations to make the hinges, respectively. **(b-g)** The emergency shelter is assembled from six different cutting patterns that make the roof, walls, and floor of the structure. Here the red, green, and blue lines represent cutting, scoring, and engraving operations, respectively. Note that the latter give additional compliance to the hinges to allow geometric frustration during the deployment.

Once the sheets are cut, we assemble them using adhesive tape (transparent duct tape from 3M) to form an airtight cavity. As an example, our meter-scale origami shelter is fabricated using the following 20 steps (see Figure A.21):

- **Step 1:** we cut and score the corrugated plastic sheet using a digital cutting system (G3 cutter from Zünd).
- **Step 2:** we lay down the eight main panels of the meter-scale shelter assembled out of the cutting patterns in Figures A.20c-g.
- **Step 3:** we apply adhesive tape to the scored hinges to seal the main panels.
- **Step 4:** we assemble the sheets together to form the eight main panels of the meter-scale shelter.
- **Step 5:** we combine two of the main panels together by applying adhesive tape in the flat position.
- **Step 6:** we deploy these two main panels to finish assembling them.
- **Step 7:** we repeat Steps **5** and **6** on the next two panels.
- **Step 8:** we assemble the first four panels to form half of the structure.
- **Step 9:** we repeat Steps **5**-**8** to form the second half of the structure
- **Step 10:** we combine the two halves.
- **Step 11:** we apply adhesive tape to the scored hinges to seal the two panels forming the roof of the structure (assembled out of the cutting pattern in Figure A.21b).

- **Step 12:** we attach the roof to the rest of the structure with adhesive tape to form the complete closed shelter.
- **Step 13:** we cut through one of the main panels using a guide to create the door of the shelter.
- **Step 14:** we cut a hole in the bottom part of the shelter and fix a plastic tube for fluid supply.
- **Step 15:** we connect the shelter to a vacuum pump.
- **Step 16:** we deflate the shelter to the flat stable state.
- **Step 17:** we fold the shelter flat.
- **Step 18:** we bring the shelter back up and connect it to a pressure pump.
- **Step 19:** we inflate the shelter to the deployed stable state.
- **Step 20:** we disconnect the pressure supply and the shelter remains deployed.

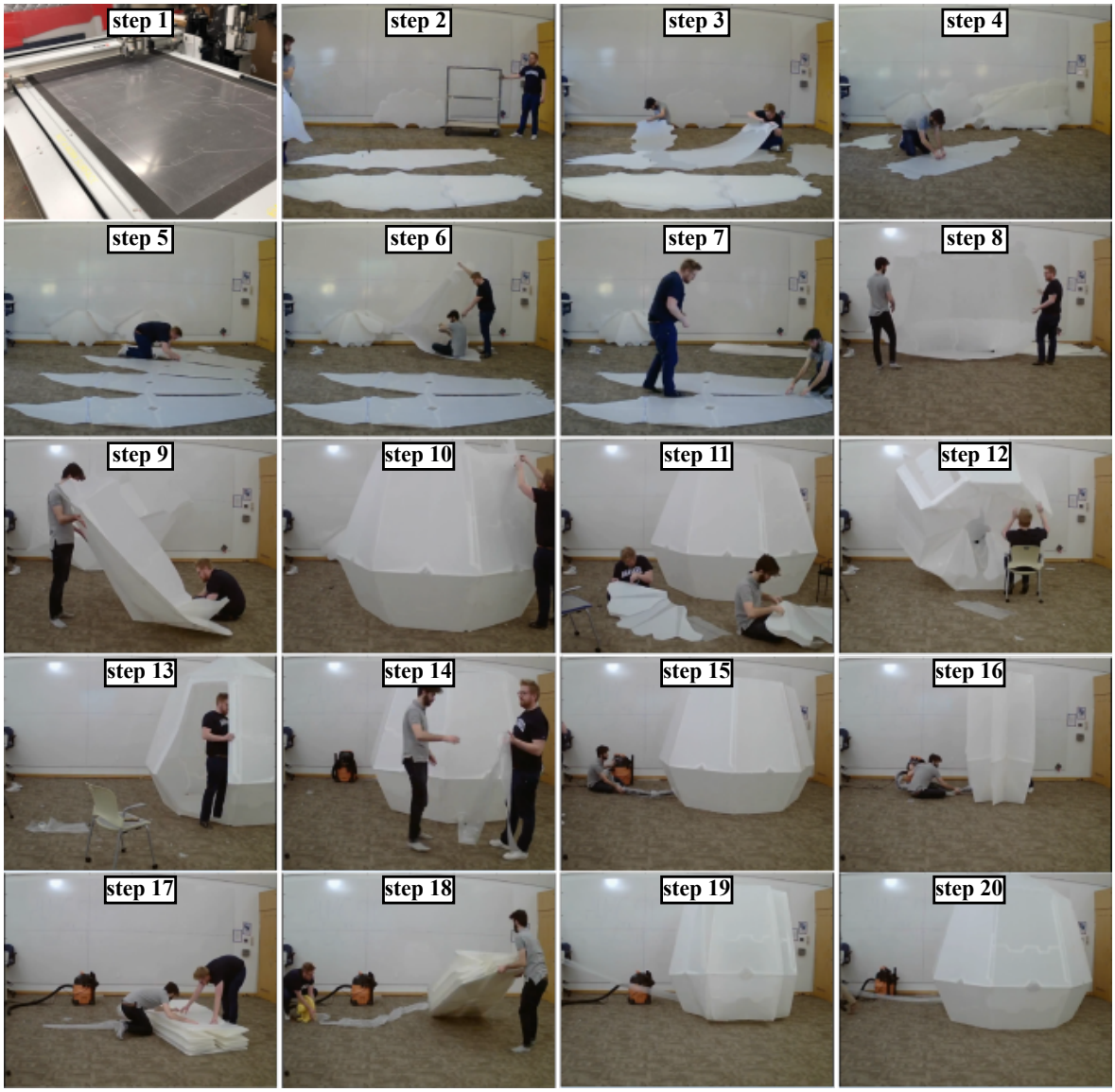

Figure A.21: Meter-scale fabrication. Snapshots of the 20 steps required to fabricate the meter-scale origami shelter.

A.3 Testing

To characterize the response of the fabricated centimeter-scale origami structures, we inflate them with water— to eliminate the influence of air compressibility— and measure their pressure-volume relation. As shown in Figure A.22, we use a syringe pump (Pump 33DS, Harvard Apparatus) to displace water into the origami structure at 10 mL/min and measure the pressure using a pressure sensor (MPXV7002DP with a measurement range of ± 2 kPa and MPXV7025DP with a measurement range of ± 25 kPa, both by NXP USA). Note that we submerge the entire structure in a water tank to eliminate the influence of gravity while eliminating air from all supply tubes and calibrating the pressure to atmospheric pressure before each measurement cycle.

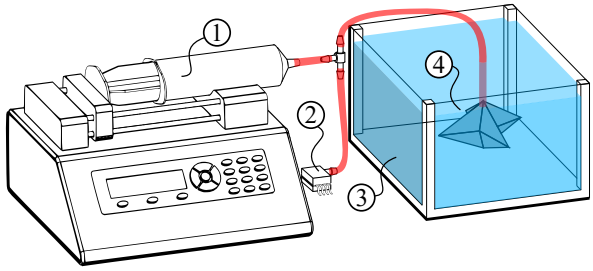

Figure A.22: Experimental setup of the inflation with water. Schematic of the test setup used to characterize the pressure-volume curve of the origami structures with (1) syringe pump, (2) pressure sensor, (3) water tank, and (4) origami structure.

In Figure A.23, we report the experimentally measured pressure-volume curves for Designs I-A, II-B, III-C, and IV-D. To validate repeatability, we test for each design three specimens and report the mean (solid lines) and standard deviation (shaded region). In addition to the pressure-volume curves, we also report the energy-landscape of each structure (dashed lines), obtained by integrating numerically the pressure-volume curves as

$$\mathcal{E} = \int \bar{p} \mathrm{d}\bar{V}, \tag{A.44}$$

where $\bar{p}$ and $\bar{V}$ are the average pressure and volume measured during our tests. We find that for Design I-A (Figure A.23a), the energy landscape is convex with a single minimum at $V = 0$ (identifying a monostasble structure). All other three designs are bistable as they exhibit brief period of negative pressure and an energy landscape with two local minima. Note that the energy profile of bistable structures is characterized by two energy barriers: the first one describes the energy cost for a structure to reach the stable expanded configuration and the second one the energy cost to snap back to its initial state.

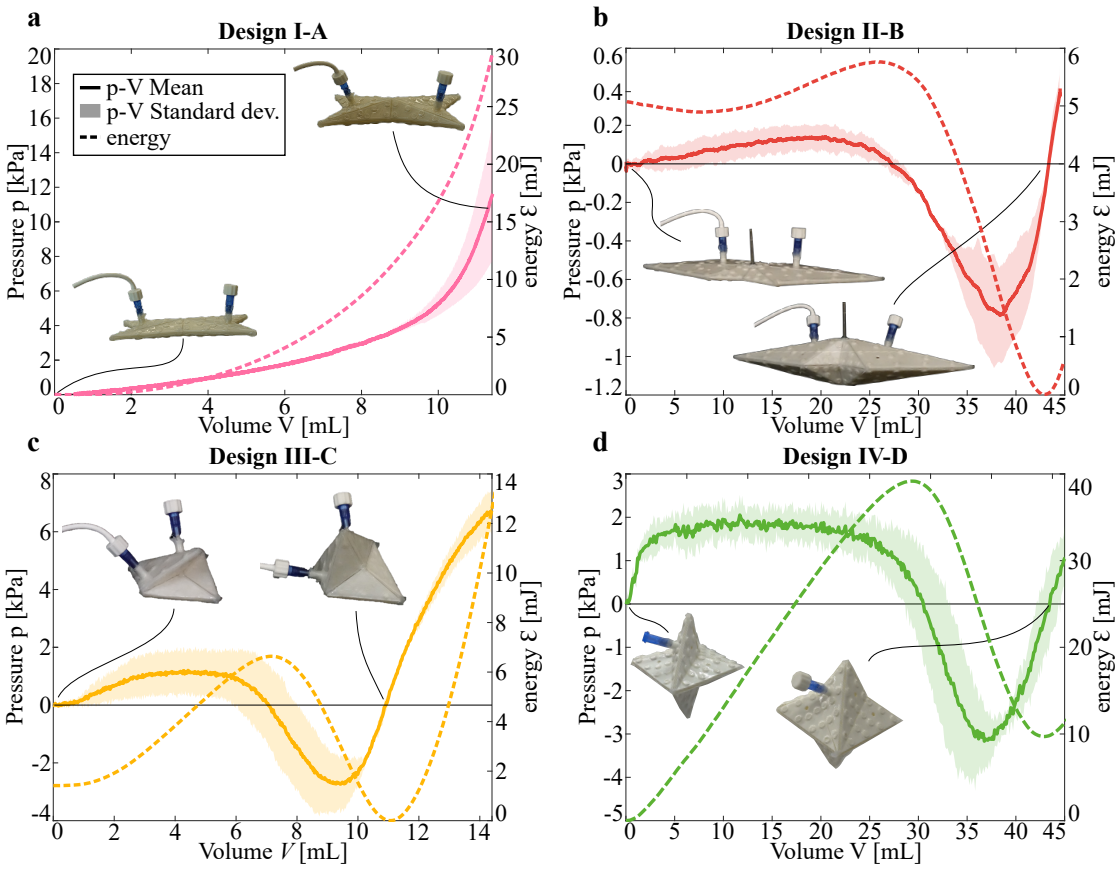

Figure A.23: Experimental pressure-volume curves of our origami structures. (a-d) Measured pressure vs. volume relationships and numerically integrated energy vs. volume curves for Designs I-A, II-B, III-C, and IV-D. We test for each design three specimens and report the mean pressure-volume curve (solid lines) with its standard deviation (shaded region) as well as the energy-volume curve (dashed lines) numerically integrated from the mean pressure-volume curve. Note that the initial non-zero pressure peak of Design II-B is coming from noise filtering of the pressure signal.

A.4 Additional results

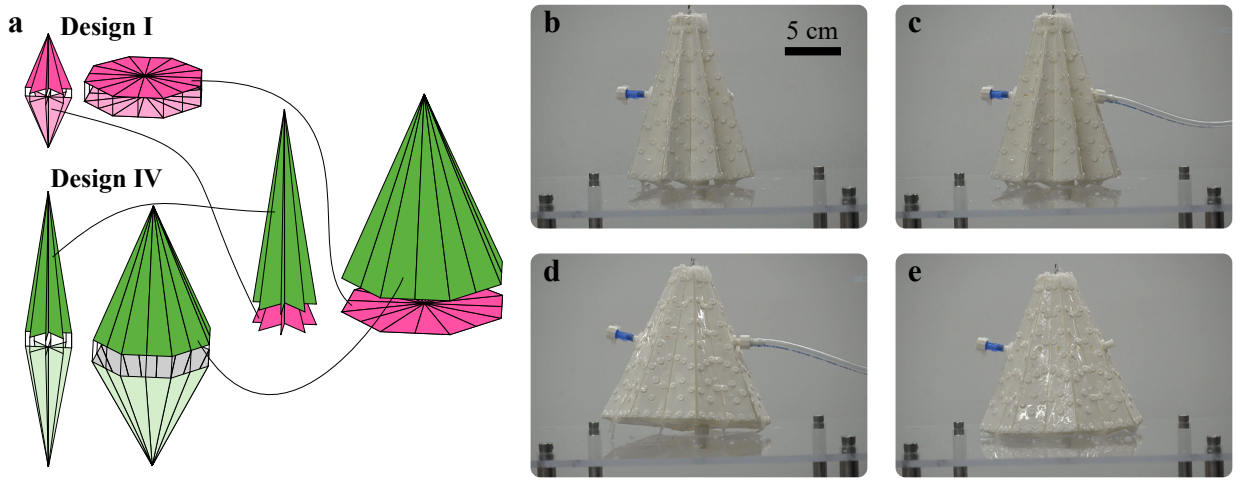

Figure A.24: Inflatable tent-like design. **(a)** By combining one layer of a Design I with $(\alpha_{\mathrm{I}}^{(1)}, \beta_{\mathrm{I}}^{(1)}) = (45°, 45°)$ and $(\alpha_{\mathrm{I}}^{(2)}, \beta_{\mathrm{I}}^{(2)}) = (45°, 45°)$ with another one of a Design IV with $(\alpha_{\mathrm{IV}}^{(1)}, \beta_{\mathrm{IV}}^{(1)}) = (10°, 80°)$ and $(\alpha_{xy}^{i}, \beta_{xy}^{i}) = (45°, 45°)$, we can create an inflatable tent-like cavity. **(b)** Centimeter-scale prototype with near zero volume in the initial stable state. Note that due to the finite thickness of the material, the initial state is not completely flat foldable. **(c)** We connect the prototype to a pressure supply. **(d)** Upon inflation, the tent-like design snaps into the deployed position. **(e)** Even after releasing the pressure, because of its bistability, the tent-like design remains in the deployed position.

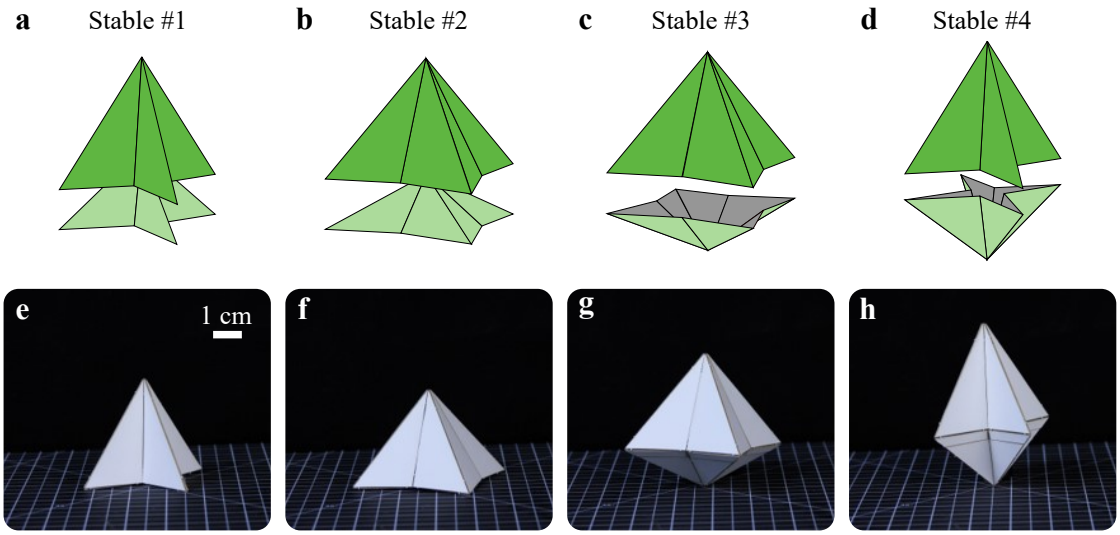

Figure A.25: Multistable origami shapes. Our design methodology can be used to realize origami shapes with more than two stable states. **(a-d)** By merging a layer of a Design IV unit with $(\alpha_{\mathrm{IV}}^{(1)}, \beta_{\mathrm{IV}}^{(1)}) = (29°, 56°)$ and $(\alpha_{xy}^{i}, \beta_{xy}^{i}) = (45°, 35°)$ with another one of a different Design IV unit with $(\alpha_{\mathrm{IV}}^{(1)}, \beta_{\mathrm{IV}}^{(1)}) = (40°, 42°)$ and $(\alpha_{xy}^{i}, \beta_{xy}^{i}) = (45°, 35°)$, we can obtain an origami shape with four stable states. **(e-h)** The four stable states of a fabricated centimeter-scale prototype.

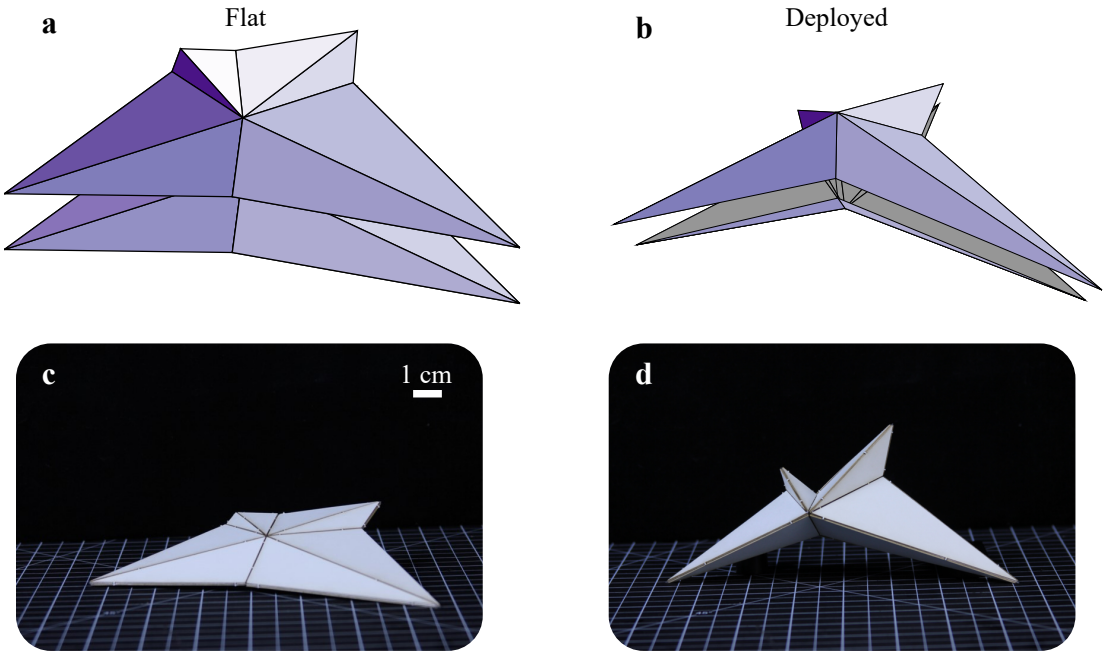

Figure A.26: Closed origami structure comprising eight different triangles. We can further increase our design space by connecting more than two different triangles. **(a-b)** Flat and deployed compatible states of an origami design comprising eight different triangles with $(\alpha^{(k)}, \beta^{(k)}) = (55°, 30°)$, $(21°, 40°)$, $(48°, 24°)$, $(68°, 17°)$, $(64°, 21°)$, $(57°, 22°)$, $(57°, 22°)$, $(15°, 52°)$, and $(32°, 49°)$ for $k = 1, \ldots, 8$. **(c-d)** Flat and deployed stable states of a fabricated centimeter-scale prototype.

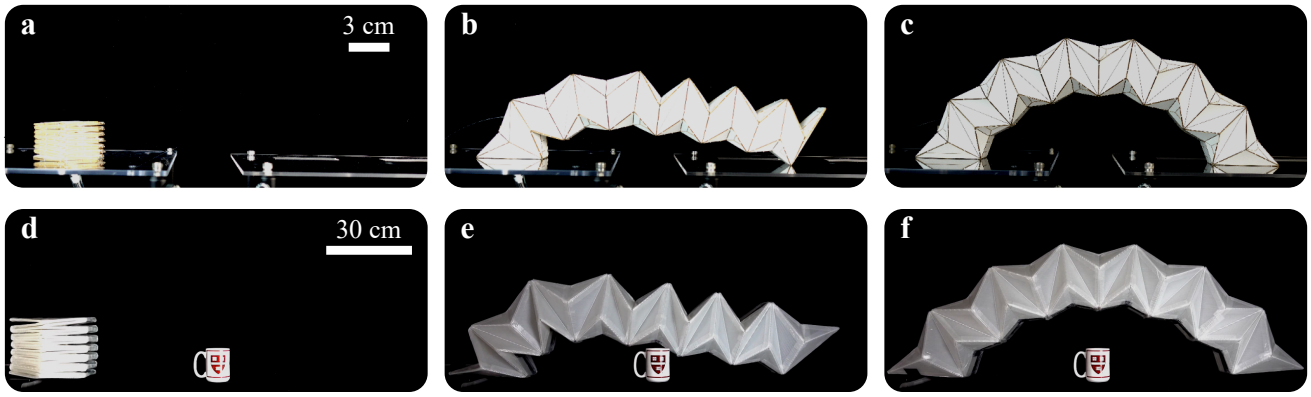

Figure A.27: Deployment of centimeter and meter-scale arches. The deployment of centimeter-scale (**a-c**) and meter-scale (**d-f**) arches is qualitatively similar.

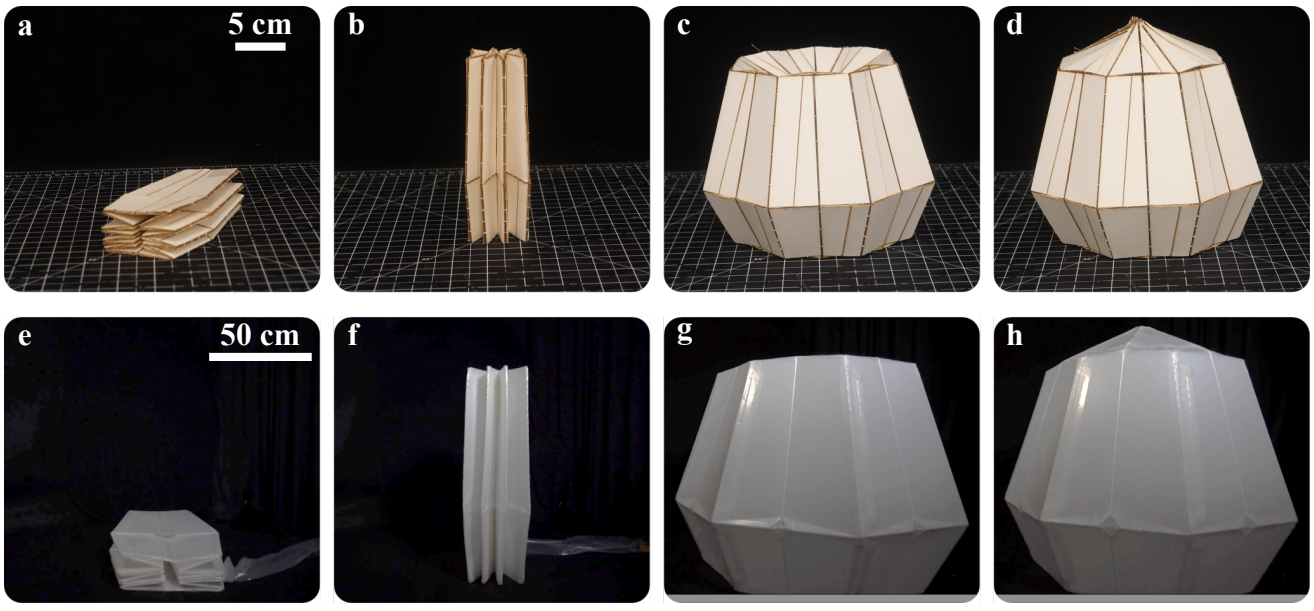

Figure A.28: Deployment of centimeter and meter-scale shelters. The deployment of centimeter-scale (**a-d**) and meter-scale (**e-h**) shelters is qualitatively similar.

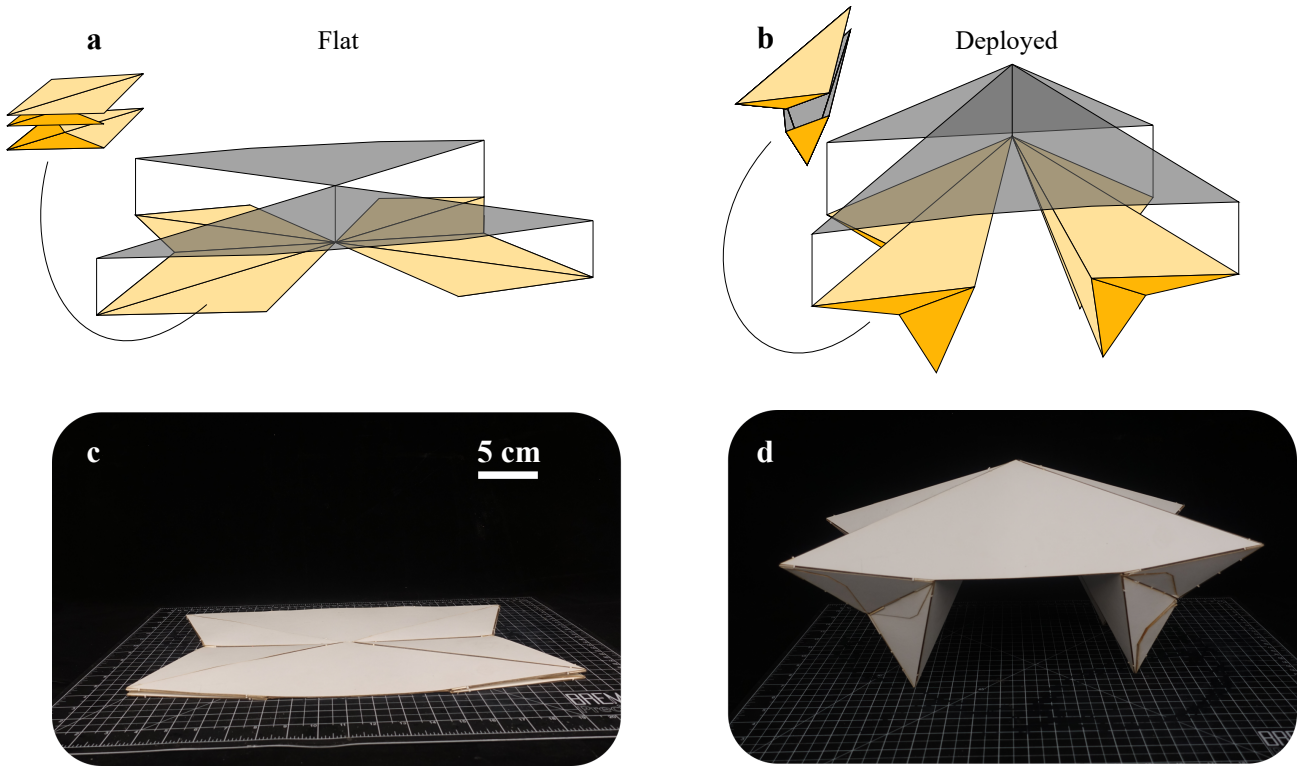

Figure A.29: A deployable pagoda-like structure. By assembling four identical Design III units, we can obtain a deployable pagoda-like structure. **(a-b)** Flat and deployed states of an origami design comprising four identical Design III units with $(\alpha_{III}^{(1)}, \beta_{III}^{(1)}) = (37°, 30°)$ and $(\alpha_{III}^{(2)}, \beta_{III}^{(2)}) = (37°, 40°)$. Note that the grey panels in **(a-b)** are added both for aesthetic reasons and to provide additional support. **(c-d)** Flat and deployed stable states of a fabricated centimeter-scale prototype.

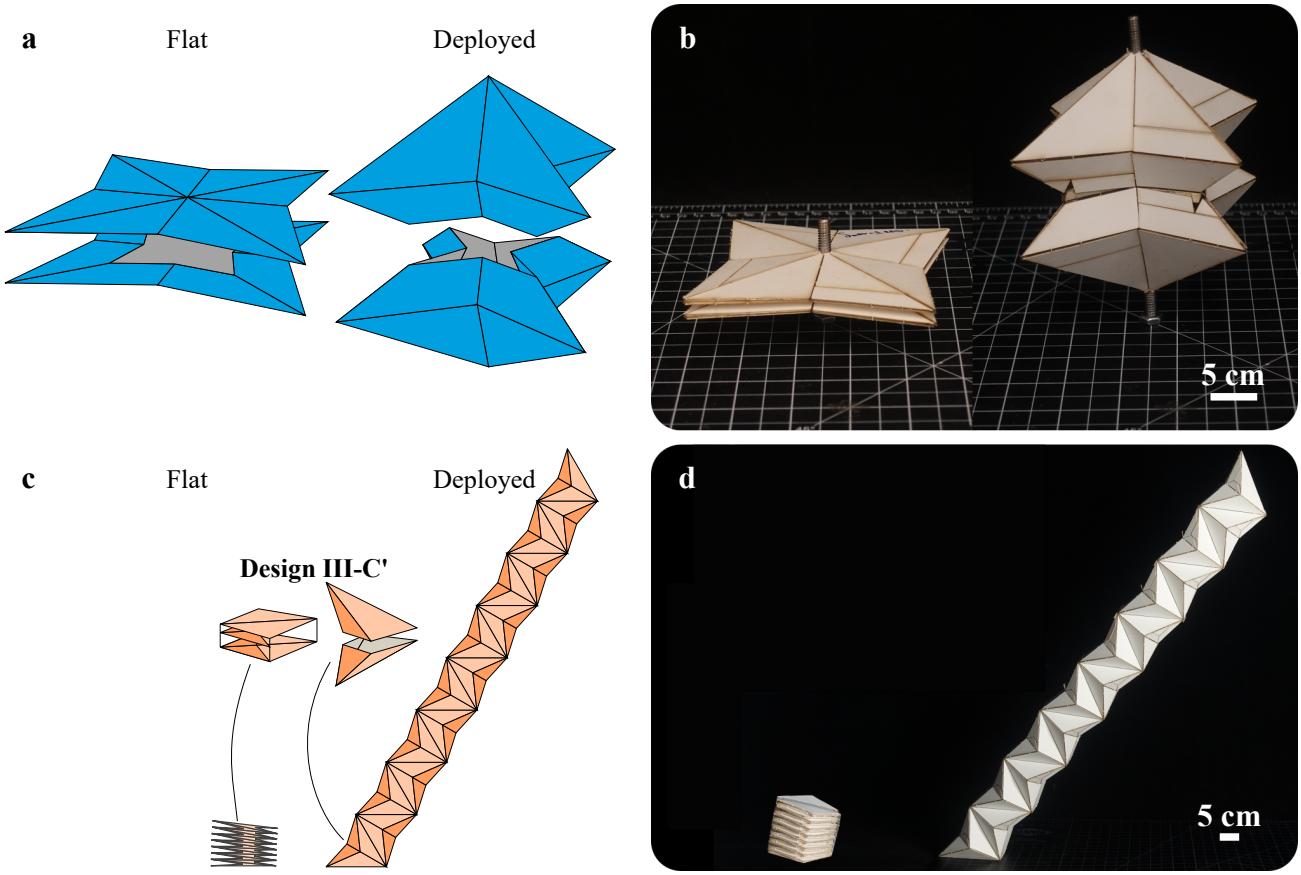

Figure A.30: Deployable booms. **(a-b)** By stacking Design I units, we can obtain a deployable boom. **(a)** Flat and deployed states of an origami boom design realized by connecting two Design I units with $(\alpha_I^{(1)}, \beta_I^{(1)}) = (\alpha_I^{(2)}, \beta_I^{(2)}) = (45°, 32°)$. Note that to avoid single point contact during assembly, we cut the units at 25 % of their deployed height and connect them with the tabs and pockets system described in Section A.2. **(b)** Flat and deployed stable states of a fabricated centimeter-scale prototype. **(c-d)** By assembling Design III units, we can obtain a bistable and inflatable boom. **(c)** Flat and deployed states of an origami boom comprising 15 identical Design III units with parameters ($\alpha_{\text{III-C}'}^{(1)}$, $\beta_{\text{III-C}'}^{(1)}$, $\alpha_{\text{III-C}'}^{(2)}$, $\beta_{\text{III-C}'}^{(2)}$) = (30°, 37°, 30°, and 51°). **(d)** Flat and deployed stable states of a fabricated centimeter-scale prototype.

B

Supplementary Information: MuA-Ori: Multimodal Actuated Origami

By: Antonio Elia Forte*, David Melancon*, Leon M. Kamp, Benjamin Gorissen, and Katia Bertoldi.
MuA-Ori: Multimodal Actuated Origami. arXiv:2112.01366.

B.1 Fabrication

The actuators tested in this study are constructed by connecting 3D-printed origami modules. This section gives details on the design and fabrication of the 3D-printed modules as well as their assembly to create multi-unit actuators and robots.

B.1.1 Design of the 3D-printed origami units

Each origami module is 3D-printed using a commercially available multi-material printer (Ultimaker 3). To account for geometric incompatibility during inflation, we print the 1-mm thick triangular facets out of compliant thermoplastic polyurethane (Ultimaker TPU 95A with tensile modulus $E = 26$ MPa). The thickness decreases to 0.4 mm at the junction of the triangular facets (hinges), to allow more compliance. This value is the lowest possible thickness our printer is able to print with a 0.4 mm print core. Further, to enable rigid connection of different units and increase bistability, we print the end caps as well as the four triangular facets of the bistable cell out of stiff polyactic acid (Ultimaker PLA with tensile modulus $E = 2.3$ GPa). As shown in Fig B.1, the single module consists of two hexagonal caps with edges of length $l = 30$ mm, separated by a distance $h = 24$ mm, and rotated by an angle $\alpha = 30°$ with respect to each other. To enable coupling of different units, we print a screw and a threaded hole on the top and bottom surfaces with length $w = 6$ mm an thread size $d_T = 24$ mm.

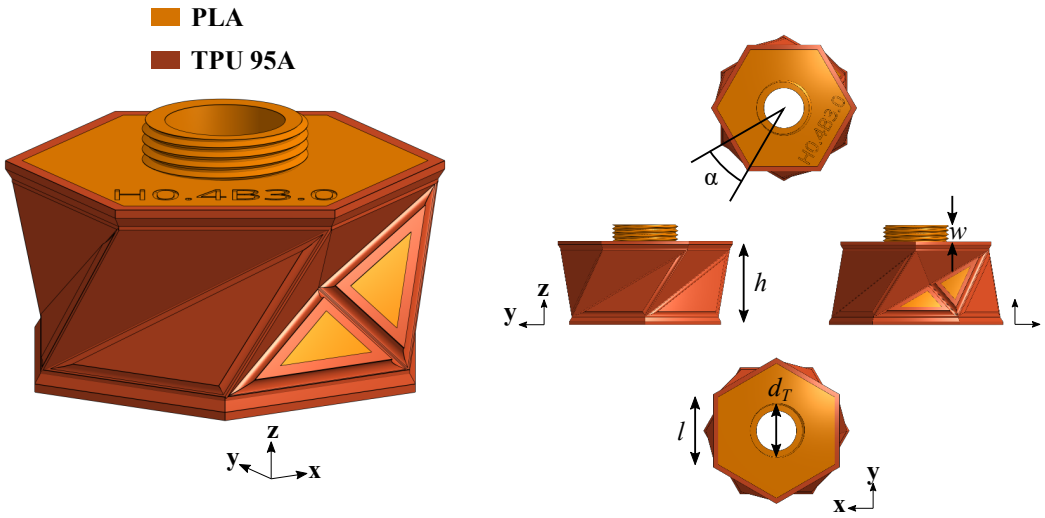

Figure B.1: 3D-printed origami modules. Isometric and projected views of the origami module.

B.1.2 Assembly of an inflatable multi-unit actuator

Below are the eight steps needed to fabricate and assemble an inflatable origami actuator sample made of multiple modules (see Figure B.2):

- **Step 1:** we 3D-print (Ultimaker 3) each origami unit out of polyactic acid (Ultimaker PLA) and thermoplastic polyurethane (Ultimaker TPU 95A), using 0.4 mm print cores with the *fine* default setting.
- **Step 2:** we cut the 3D-printed adhesion skirt with scissors.
- **Step 3:** we remove the 3D-printed support material inside of the origami unit with pliers.
- **Step 4:** we insert a toric joint on the connection screw to make the unit airtight (see **Steps 5-8**).
- **Step 5:** we assemble multiple units together through the connection screws ensuring a tight assembly through the toric joints inserted in **Step 4**.
- **Step 6:** we coat the sample with a 0.5 mm layer of polydimethylsiloxane (PDMS) and let it cure for 24 hours.
- **Step 7:** we fit end caps, making sure to have a tight assembly through the toric joints inserted in **Step 4**, to create an airtight cavity. Note that one of the end caps has an inlet for fluidic actuation.
- **Step 8:** we test the origami actuator by connecting it to a fluidic supply.

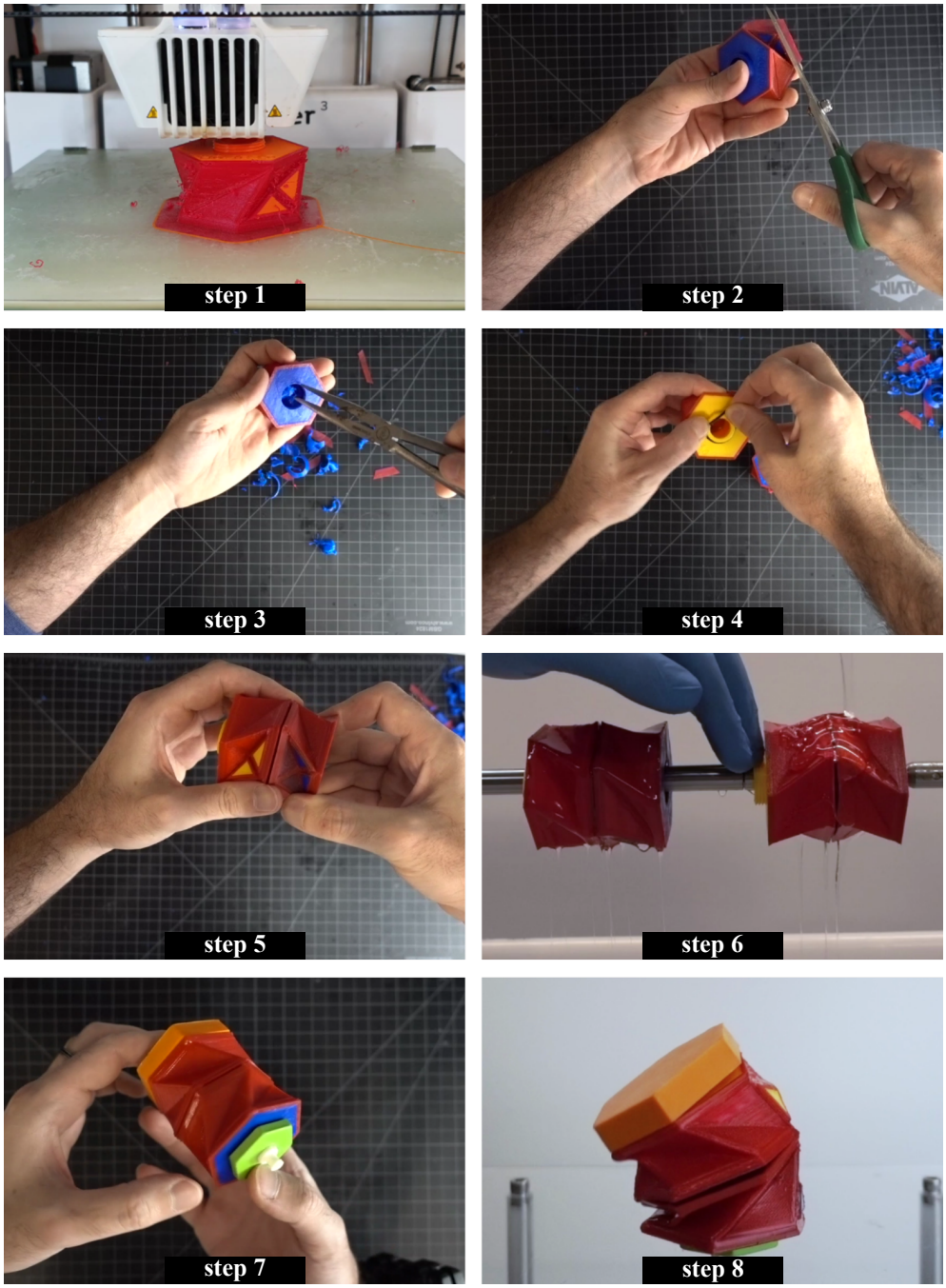

Figure B.2: Multi-unit actuator fabrication and assembly. Snapshots of the eight steps required to fabricate and assemble inflatable multi-unit origami actuators.

B.1.3 Design of the single pressure input origami robot

The origami robot is constructed by mounting two multi-unit actuators (each one acting as a crawling arm) on a wheeled chassis made of LEGO bricks (see Figures B.3a and b). To create a single airtight cavity, we connect the two multi-unit actuators through a fluidic line (1/16" soft plastic tubing and luer lock connectors) and a coupler (1/16" acrylic plate fixed on the chassis). Finally, we glue 10 cm-long amplifiers (1/4" acrylic plate) on the top caps of the actuators to accentuate the stroke during inflation and deflation. Note that we add a patch of silicon rubber on the amplifiers' tip (ecoflex 5 from Smooth-on) to increase the friction coefficient when in contact with the ground.

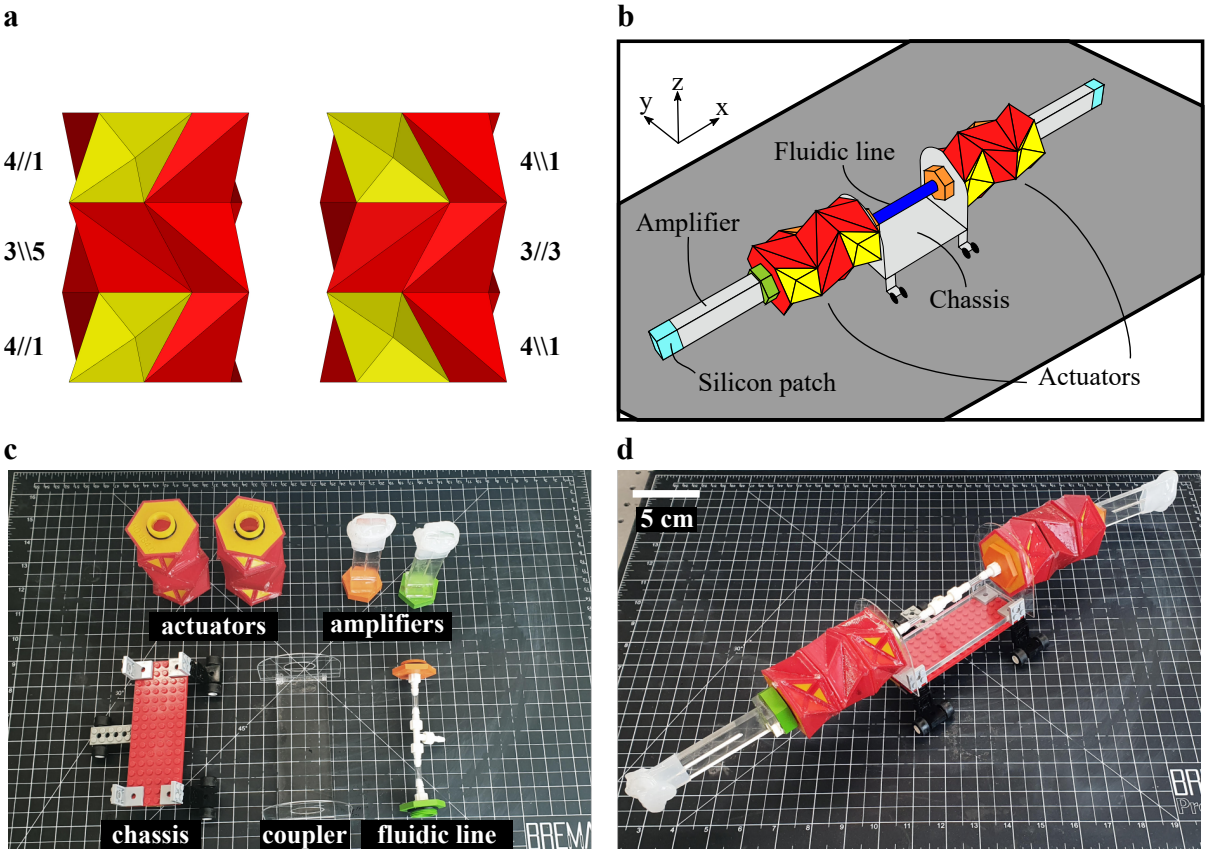

Figure B.3: Single pressure input origami robot. **(a)** The two identical actuators forming the arms of the robot. **(b)** Schematics of the origami robot. **(c)** Components of the origami robot. **(d)** Assembled origami robot.

B.2 Testing

To characterize the experimental response of the fabricated origami building blocks, we inflate them with water— to eliminate the influence of air compressibility— and measure their internal pressure while tracking their height and bending angle. As shown in Figure B.4, we use a syringe pump (Pump 33DS, Harvard Apparatus) to displace water into the origami unit at 10 mL/min, measure the pressure using a pressure sensor (ASDXRRX015PDAA5 with a measurement range of ± 15 psi by Honeywell), and track the height, bending angle, and twist angle of the upper cap using two digital cameras (front and top view with two SONY RX100 V). Note that we submerge the entire unit in a water tank to eliminate the influence of gravity while eliminating air from all supply tubes and calibrate the pressure sensor to atmospheric pressure before each measurement cycle.

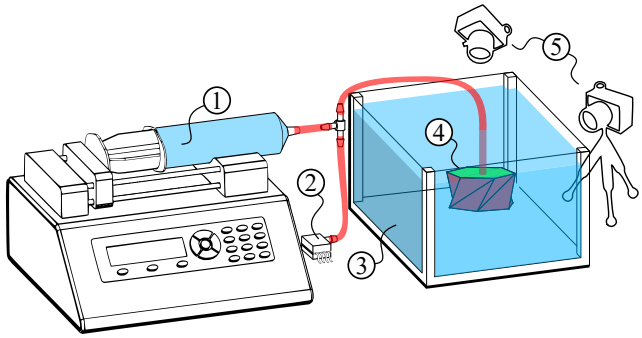

Figure B.4: Experimental setup of the inflation with water. Schematic of the test setup used to characterize the bending angle vs./ pressure and height vs./ pressure curves of the origami units with (1) syringe pump, (2) pressure sensor, (3) water tank, (4) origami unit, and (5) digital cameras.

We report in Figure B.5 the experimentally measured pressure, p, as a function of the end caps displacement, u_z, and the bending angle, θ, for the module with $\Delta = 3$mm. Further, we highlight on the curves the pressure thresholds, p_3^+ and p_3^-, as well as the maximum displacement, $u_z^{max,\pm}$, and bending angle, $\theta_{max,\pm}$, at snap-through for both the inflation and deflation regime.

We summarize all experimental results in Figure B.6 and plot the pressure, displacement, and bending angle of each design tested in this study as a function of normalized time, T, for both the inflation and deflation regime. To validate repeatability, we test for each design three specimens and report the mean (solid lines) and standard deviation (shaded region). We find that the classic Kresling module as well as the modified-panel module with $\Delta = 0$ mm do not show any snap-through instability. Modules with $\Delta = 1$ mm show a snapping transition during inflation, but bend marginally when later deflated. Modules with $\Delta = 2, 3, 4$ mm are bistable as they exhibit discontinuity in their $p - T$, $u_z - T$, and $\theta - T$ curves, and show substantial bending when deflated from the snapped configuration. Modules with $\Delta = 5$ mm break during the inflation before the panel snaps outward.

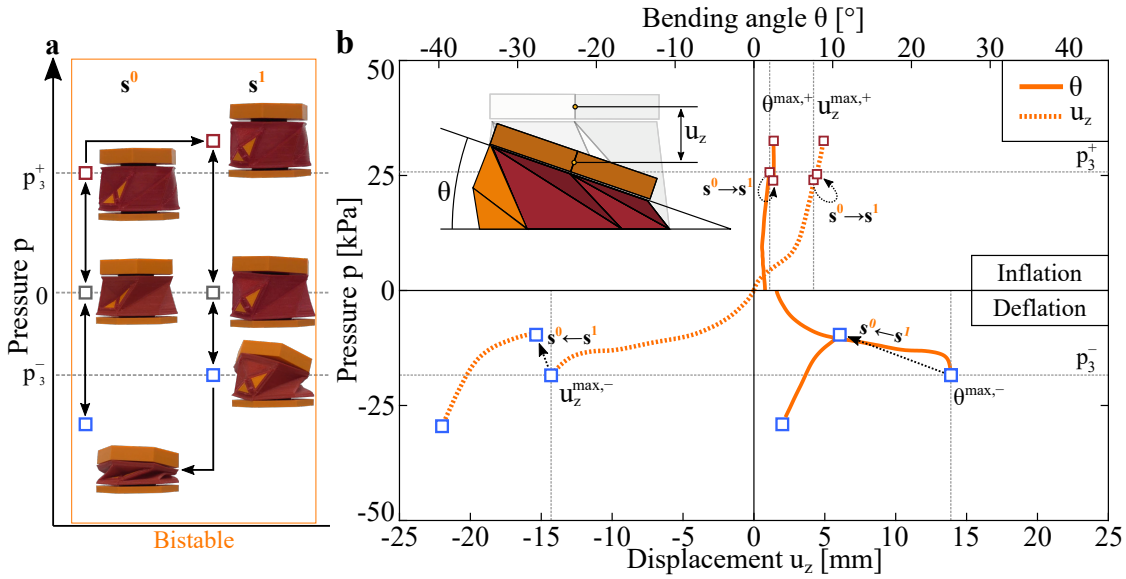

Figure B.5: Experimentally measured response of the $\Delta = 3$ mm module. (a) State diagram of the pressurized origami module. (b) Experimentally measured pressure, p, as a function both end caps' displacement, u_z, and bending angle, θ for the origami module with $\Delta = 3$ mm. In the plot, we highlight the pressure thresholds, p_3^+ and p_3^-, as well as the maximum displacement, $u_z^{max,\pm}$, and bending angle, $\theta_{max,\pm}$, at snap-through for both inflation and deflation.

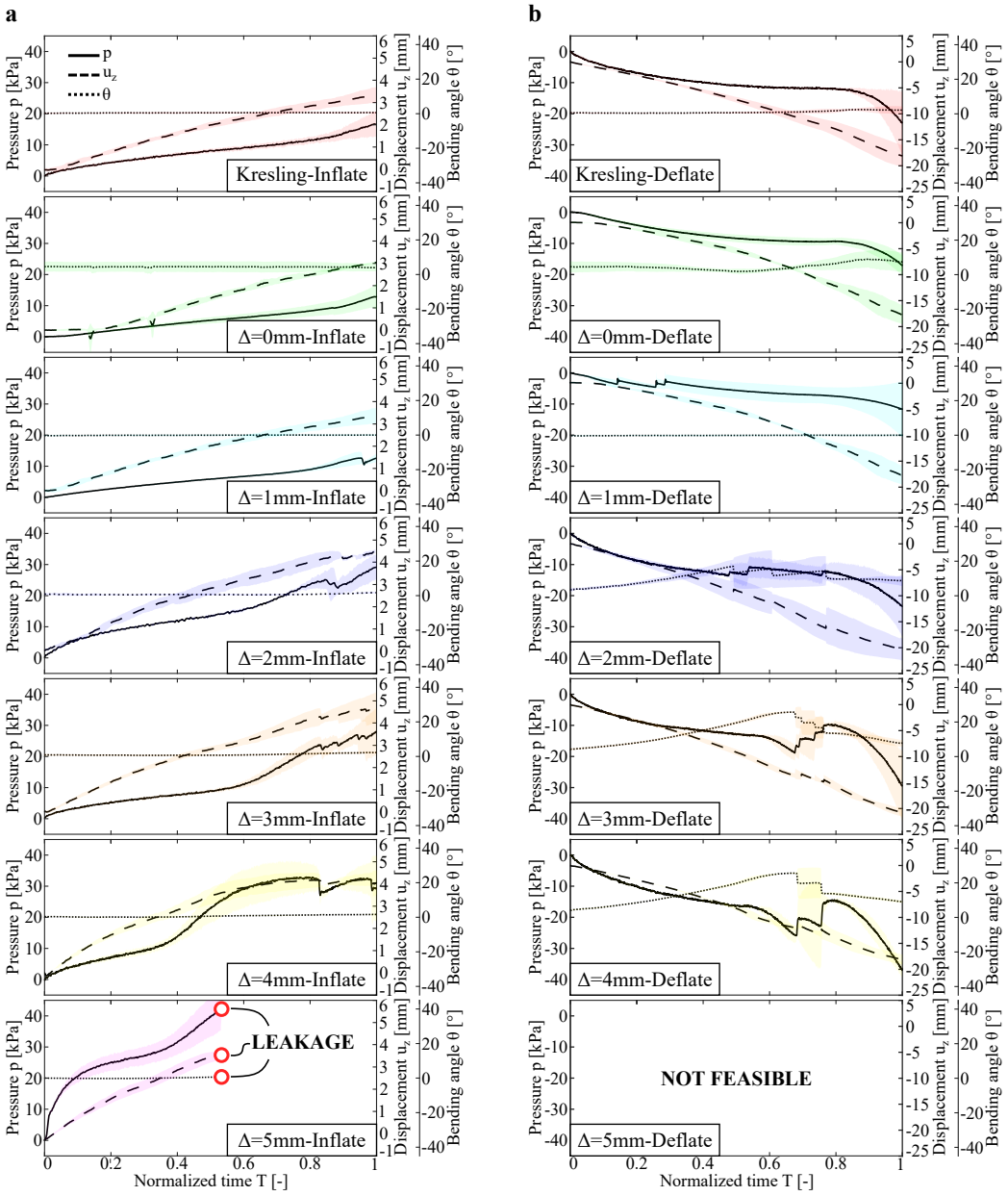

Figure B.6: Experimental pressure, displacement, and bending angle curves of our origami modules. Experimentally measured pressure (left vertical axis), end caps displacement (right vertical axis), and bending angle (right vertical axis) of each design tested in this study as a function of normalized time, $T = t/t_{end}$ (where t is real time and t_{end} the duration of the test), for both (a) inflation and (b) deflation. To validate repeatability, we test for each design three specimens and report the mean (solid lines) and standard deviation (shaded region). We find that the classic Kresling module as well as the modified-panel module with $\Delta = 0$ mm do not show any snap-through instability. Modules with $\Delta = 1$ mm show a snapping transition during inflation, but bend marginally when later deflated. Modules with $\Delta = 2, 3, 4$ mm are bistable as they exhibit discontinuity in their $p - T$, $u_z - T$, and $\theta - T$ curves, and show substantial bending when deflated from the snapped configuration. Modules with $\Delta = 5$ mm break during the inflation before the panel snaps outward.

From the experimental curves, we can extract the pressure thresholds at which the modified panel snaps outward during inflation, p_Δ^+ and inward during deflation, p_Δ^-. We summarize the mean and standard deviation of these pressure thresholds in Figure B.7 for the bistable modules with $\Delta = 2$, 3, and 4 mm. We also report in Figure B.7, the displacement and the bending angle at snap-through, $u_z^{max,\pm}$ and $\theta_{max,\pm}$ for both the inflation and deflation regime.

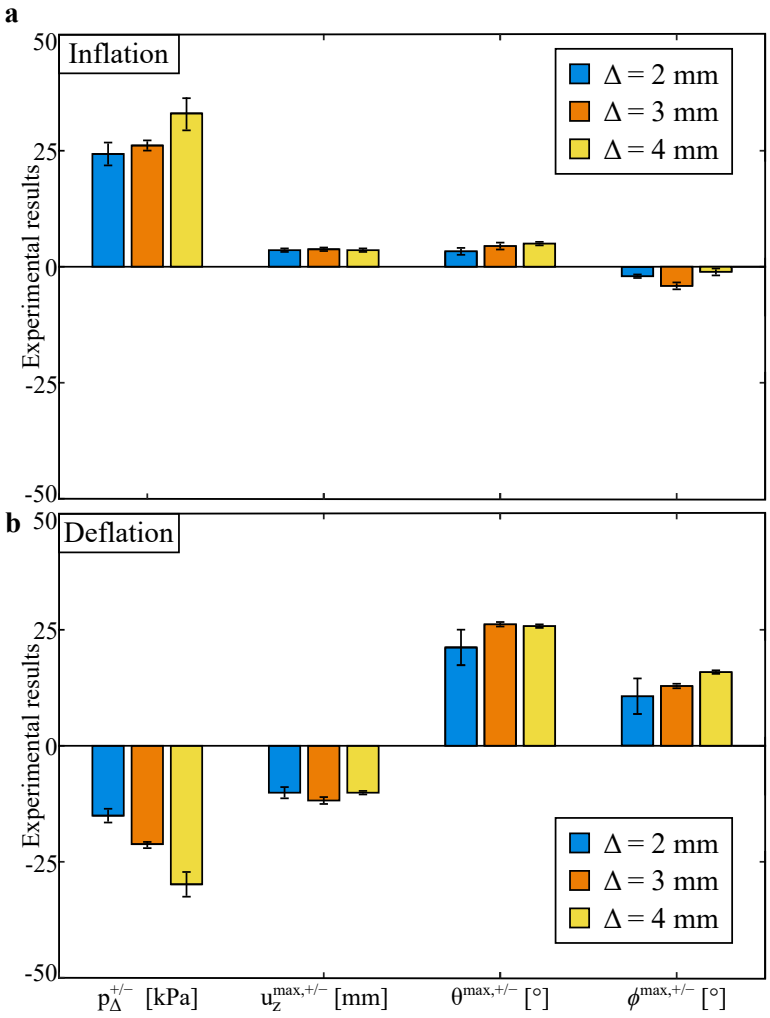

Figure B.7: Effects of Δ. Bar chart of the experimentally measured pressure thresholds, $p_\Delta^\pm$, end caps displacement, $u_z^{max,\pm}$, bending angle, $\theta^{max,\pm}$, and twist angle, $\varphi^{max,\pm}$, at snap-through during both inflation **(a)** and deflation **(b)** The values for $p_\Delta^\pm$, $u_z^{max,\pm}$, and $\theta^{max,\pm}$ are extracted from the curves shown in Figure B.6. The values for $\varphi^{max,\pm}$ were obtained measuring the twist angle at each stable configuration and snapping transition during the experiments.

B.3 Model

B.3.1 Origami module

We start by using the geometric quantities that we track in our experiments (shown in Figure B.7) to reconstruct the configuration of the origami module just before and just after each snapping transition (see Figure B.8).

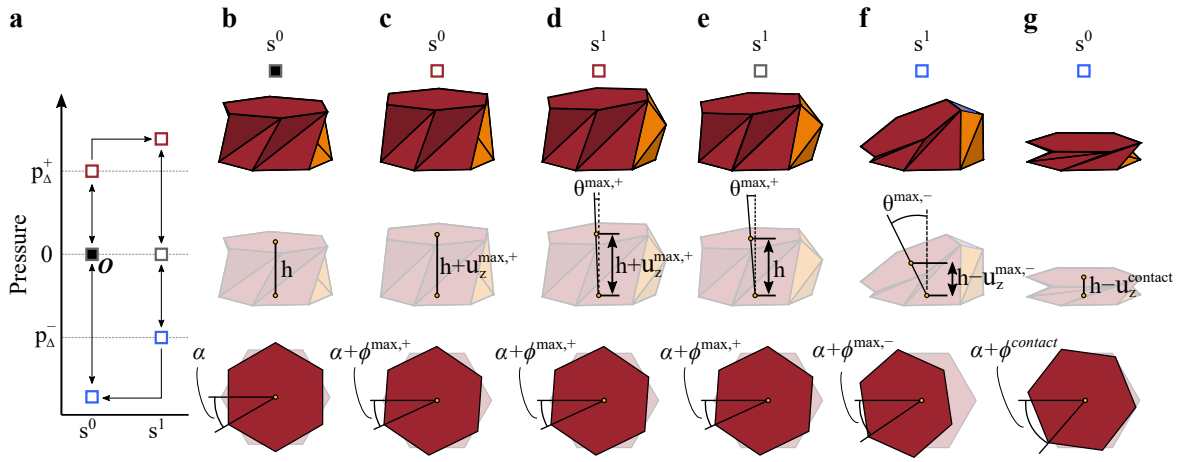

Figure B.8: Modeling the stable states and snapping transitions of our origami modules. (a) Typical state diagram for a origami module with a modified panel of depth Δ. The unit can transition between two stable states: state s^0 when the modified panel is folded inward, and state s^1 when the panel is popped outward and stays in that position even when the input pressure is removed **(b-g)** Reconstructed geometry of the origami module at each stable state and before and after each snapping transition.

B.3.2 Actuator comprising n modules

We can create actuator made of n units by simply combining the different stable states and snapping transitions found for the single unit model described in Figure B.8. Note that we impose that any n-units actuator forms a closed, inflatable cavity (i.e. they are all subjected to the same internal pressure). By combining n modules, we can construct $(3 \times 2 \times 6 + 1 \times 2)^n$ different actuators since for each module k we can select (*i*) either a regular Kresling module or a unit comprising a modified panel with depth $\Delta^k \in \{2, 3, 4\}$ mm; (*ii*) the upper cap to be rotated clockwise or anticlockwise with respect to the bottom one, $c^k \in \{//, \backslash\backslash\}$, and (*iii*) the side on which the modified panel is located, $f^k \in \{1, \ldots, 6\}$ (see Figure B.9).

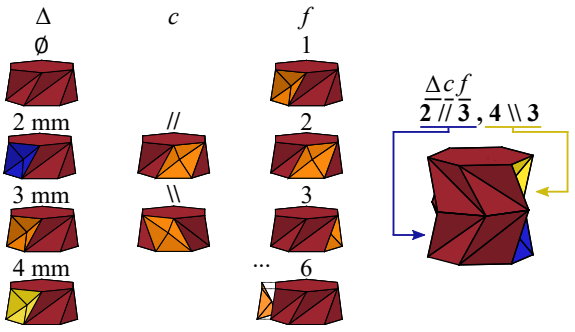

Figure B.9: Actuator's parameters. Our reconfigurable actuators are defined by the modified panel's depth, Δ^k, the initial rotation of the upper cap, c^k, and the position of the modified panel, f^k, of each their k unit.

For an actuator made of n units, the number of stable states is equal to 2^{n_Δ}, where n_Δ is the number of unique modified panel depths Δ. Note that we assume all units with the same Δ snap synchronously at the pressure thresholds, p^+_Δ and p^-_Δ. Since in this study, we consider only the discrete set $\Delta \in \{2, 3, 4\}$ mm, all our actuators have either $n_\Delta = 0$, 1, 2, or 3. For each different n_Δ, we report the corresponding state diagram in Figure B.10.

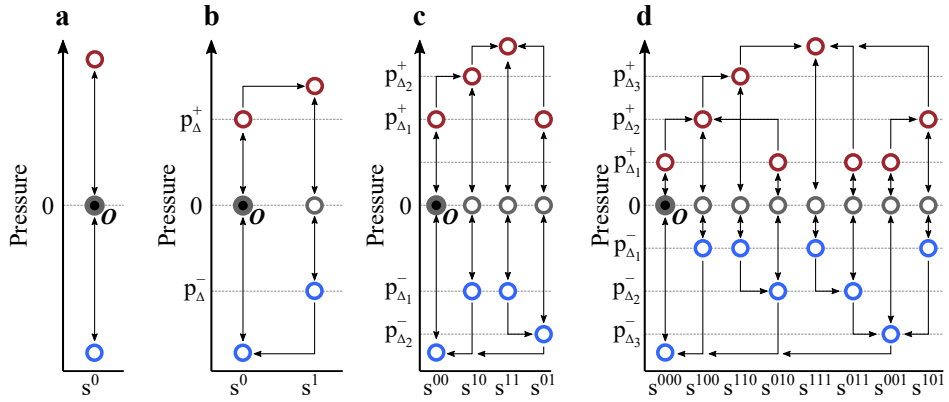

Figure B.10: State diagrams. (a) State diagram for any n-units actuator made only of Kresling modules. **(b-d)** State diagram for any n-units actuator made with 1, 2, and 3 unique modified panel's depth, i.e. $n_\Delta = 1$, 2, and 3, respectively.

In Figure B.11a we show the state diagram of an actuators comprising two modules characterized by $[\Delta^1 c^1 f^1; \Delta^2 c^2 f^2] = [2//3; 4\backslash\backslash 3]$ and compare the outputs from the geometric model to the experiments done on a physical prototype. Further, for each of the stable states and snapping transitions in the state diagram, we record the vector connecting the caps' centroids, $\mathbf{d}$. In Figure B.11b, we report the normalized deployment, $||\mathbf{d}||/h$, and angle, θ_{act} for each stable state and snapping transition of the actuator characterized by $[\Delta^1 c^1 f^1; \Delta^2 c^2 f^2] = [2//3; 4\backslash\backslash 3]$. Further, in Figure B.12 we report $||\mathbf{d}||/h$ and θ_{act} for each stable state and snapping transition of every actuator design with $n \in 1, 2, 3, 4$.

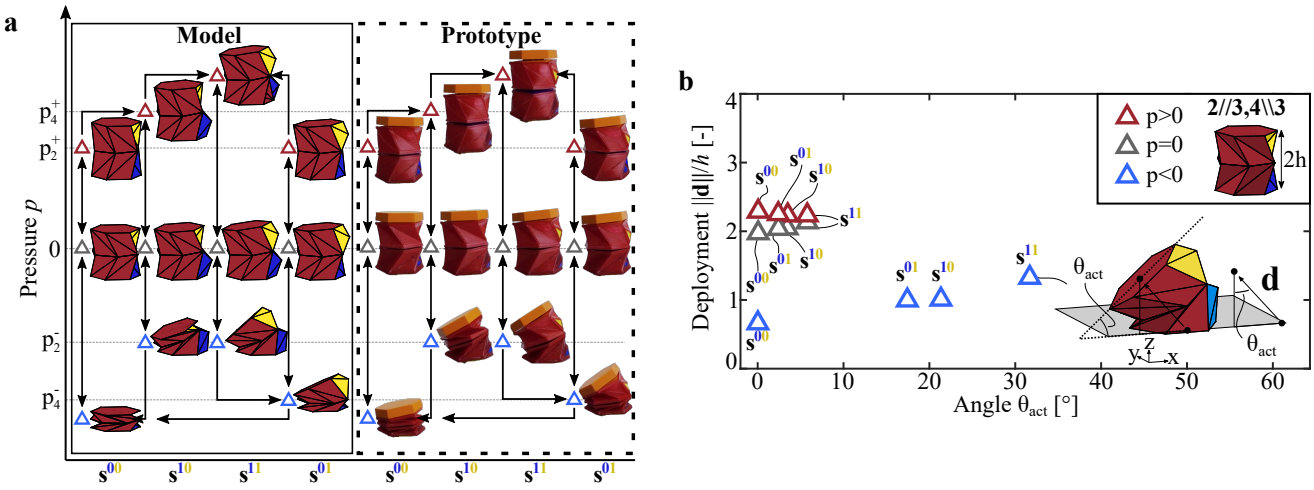

Figure B.11: **A 2-units actuator characterized by** $[\Delta^1 c^1 f^1; \Delta^2 c^2 f^2] = [2//3; 4\backslash\backslash 3]$. **(a)** State diagram for a 2-units actuator characterized by $[\Delta^1 c^1 f^1; \Delta^2 c^2 f^2] = [2//3; 4\backslash\backslash 3]$: geometrical model prediction on the left, experimental snapshots on the right. **(b)** Normalized deployment, $||\mathbf{d}||/h$, as a function of the bending angle θ_{act}, for every stable state and snapping transition.

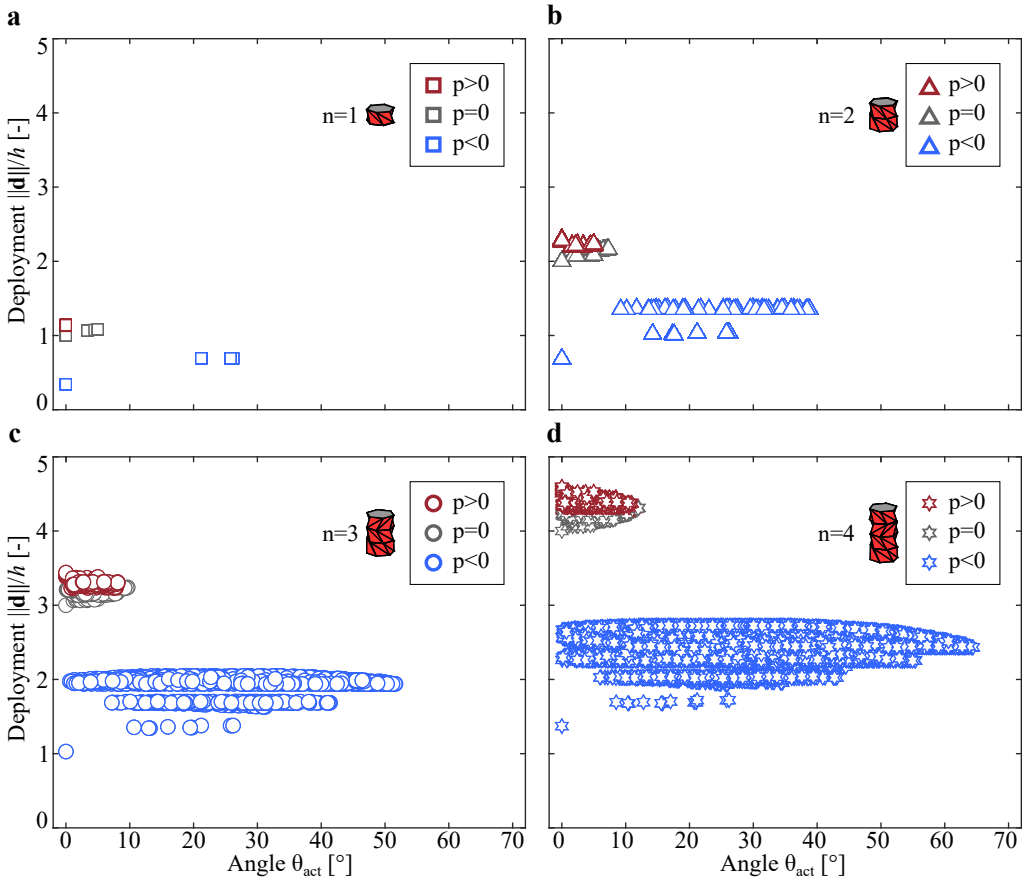

Figure B.12: **Design space for actuators with** $n \in \{1, 2, 3, 4\}$. Normalized deployment, $||\mathbf{d}||/h$, and bending angle, θ_{act}, for all possible 1-unit **(a)**, 2-unit **(b)**, 3-unit **(c)**, and 4-unit **(d)** constructed by combining our library of modules.

B.4 Optimization

To identify actuators capable of achieving target deformation modes, we solve the following discrete optimization problem

$$\begin{aligned} \min_{\Delta^k, c^k, f^k} \quad & \Psi\left(\Delta^k, c^k, f^k; n\right) \\ \text{s.t.} \quad & \Delta^k \in \{2,3,4\}\text{mm} \\ & c^k \in \{//, \backslash\backslash\} \\ & f^k \in \{1,2,3,4,5,6\} \\ & k \in \{1,2,\ldots,n\} \\ & n \in \mathcal{Z}^+, \end{aligned} \tag{B.1}$$

where Ψ is the cost function, n is the number of units making the actuator and Δ^k, c^k, and f^k are are the modified panel depth, the orientation of the upper cap with respect to the bottom one, and the side on which the modified panel is located for the k-unit in the array. Note that all design variables (i.e. Δ^k, c^k, and f^k) are constrained to be integer value and, for the sake of simplicity, we solve the optimization problem multiple times for fixed number of units $n \in [1, 15]$.

In the main text we use the optimization algorithm to identify actuators whose tip can approach a desired set of target points and therefore define the cost function as

$$\Psi = \frac{1}{n_{targets} \cdot h} \sum_{m=1}^{n_{targets}} \min ||\mathbf{d} - \mathbf{T}_m||, \tag{B.2}$$

where $n_{targets}$ is the number of targets, and $\mathbf{T}_m$ is the vector connecting the m-th target with the origin. Here, we also consider two additional optimization problems and use the algorithm to identify actuators that

- maximize the angle θ_{act} between the vector connecting the cap's centroids, $\mathbf{d}$, and the z-axis. For this case we define the cost function as

$$\Psi\left(\Delta^k, c^k, f^k; n\right) = -\theta_{act}. \tag{B.3}$$

- maximize the deployment height $||\mathbf{d}||/h$. For this case we define the cost function as

$$\Psi\left(\Delta^k, c^k, f^k; n\right) = -||\mathbf{d}||/h, \tag{B.4}$$

B.4.1 Optimization algorithms

There are many algorithms able to solve an optimization problem with integer constraints such as the one presented in Eq. B.1. In this study, we used three classic algorithms: (*i*) the genetic algorithm with integer constraints[110]; (*ii*) the integer optimization via a surrogate model[111]; and (*iii*) the greedy algorithm based on best-first search[109]. Note that given the high-dimensionality and complexity of this optimization problem, there is no guarantee that these algorithms will lead to a unique global minimum.

Genetic algorithm with integer constraints

We started by using the genetic algorithm with integer constraints[110], which attempts to minimize a penalty function that depends on the fitness (value of the cost function Ψ) and feasibility (design variables are integer) of an individual. For this study, we used the Matlab implementation of the algorithm (Matlab function `ga`) and imposed the constraint that all design variables, i.e. Δ^k, c^k, and f^k must have integer values with upper and lower bounds reported in Eq. B.1. We ran the function `ga` multiple times, each time considering a fixed value of $n \in [1, 15]$, using a population size of 200, a max stall generations (i.e. the consecutive number of generations with no change to the cost function value) of 500 and a maximum number of generations of 1000.

Integer optimization via a surrogate model

Next, we used the surrogate model optimization, which is a derivative-free method that replaces the complex and non-smooth objective function by a surrogate (i.e. an approximation of that function), which is created by sampling the objective function. For this study we used the Matlab implementation of the algorithm (Matlab function `surrogateopt`) and imposed the constraint that all design variables, i.e. Δ^k, c^k, and f^k, must have integer values with upper and lower bounds reported in Eq. B.1. We ran the algorithm for fixed values of n with a maximum number of function evaluations of $20,000$.

Greedy algorithm based on best-first search

For the greedy algorithm, we developed and in-house Matlab code based on the best-first search method that creates an actuator with n units out of n_s super-cells, each super-cell made of n_u modules (so that $n = n_u \cdot n_s$). At the first iteration, the algorithm selects the super-cell design that minimizes Ψ and stores it in memory. Then, in the second iteration, we identify a second super-cell that, when connected to the first one, minimizes Ψ. The first two super-cells are then stored in memory and the algorithm advances to the next iteration (see Figure B.13 and Algorithm 1 below).

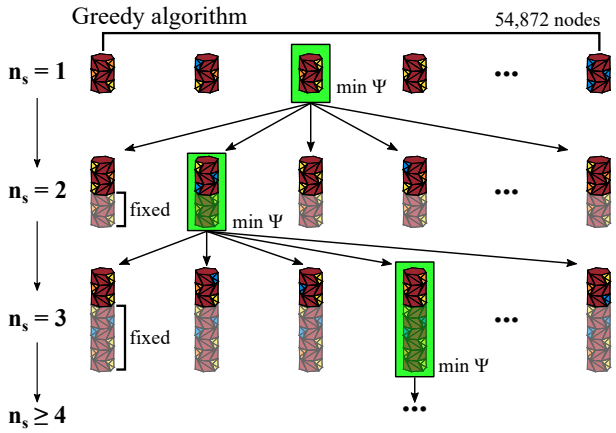

Figure B.13: Greedy algorithm. Schematic of the greedy algorithm with $n_u = 3$. At each iteration, the algorithm selects the actuator super-cell design that minimizes Ψ.

Algorithm 1 Greedy algorithm based on best-first search

Set n_{max};

Set n_u;

Set $n_s = 0$;

While $n_s \cdot n_u \leq n_{max}$

$n_s = n_s + 1$;

if $n_s = 1$ **then**

· Calculate Ψ for each actuator design with (Δ^k, c^k, f^k), $k = 1 : n_s \cdot n_u$;

· Find the actuator that minimizes Ψ and set its design variables to $(\Delta^{k^*}, c^{k^*}, f^{k^*})$

else

· Calculate Ψ for each actuator design with (Δ^k, c^k, f^k), where the set of variables from $k = 1 : (n_s - 1) \cdot n_u$ are coming from the previous iteration of $(\Delta^{k^*}, c^{k^*}, f^{k^*})$ and $k = (n_s - 1) \cdot n_u + 1 : n_s \cdot n_u$ are free.

· Find the actuator that minimizes Ψ and set its design variables to $(\Delta^{k^*}, c^{k^*}, f^{k^*})$

B.4.2 Results

In the following we first compare the performance of the three algorithms and then present additional results obtained using the greedy algorithm.

Comparison between the three algorithms

To test and compare the three algorithms, we considered the set of three targets (T_1, T_2, T_3) shown in Figure 3.3 and minimized the cost function given in Eq. B.2. In Figure B.14, we report the cost function value with respect to the number of generations/function evaluations as obtained using the three algorithms. We find that for all considered values of n both the genetic algorithm with integer constraints and the surrogate model stall quickly, with a minimum value of the cost function of 1.04 and 1.12 reached for $n = 15$, respectively. Further, we find that the greedy algorithm with $n_u = 3$ outperforms the genetic algorithm and the surrogate model optimization as it identifies an actuator design that leads to $\Psi = 0.729$ for $n = 12$. Note that, for $n_u = 3$, the greedy algorithm requires about 2.75×10^5 evaluations of Ψ to identify the optimal design, whereas the surrogate model takes about 1×10^5 evaluations of Ψ (the genetic algorithms requires about 8×10^5 evaluations of Ψ with a population size of 200). However, the greedy algorithm does not require any other operation apart from a simple computation of Ψ during each iteration. Differently, the surrogate algorithm has to update the underlying model. The simplicity of the greedy algorithm leads to a CPU time of 850 s (parallelized on 24 cores) to solve the algorithm compared to $2,500$ s and $4,000$ s for the genetic algorithm and the surrogate model, respectively. We therefore use the greedy algorithm to identify optimal configurations for our actuators.

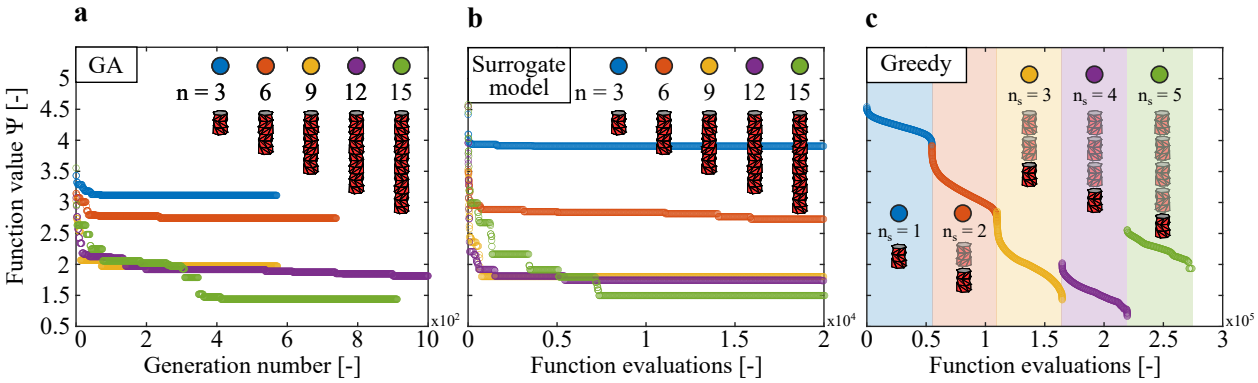

Figure B.14: Comparison between optimization algorithms with integer constraints. Comparison of the **(a)** generic algorithm, **(b)** surrogate model, and **(c)** greedy algorithm based on best-first search to solve the integer optimization problem of minimizing the targets error Ψ.

Additional results generated by the greedy algorithm

In Figure B.15 we present results obtained when the greedy algorithm is programmed to maximize θ_{act} (Figure B.15a-c) and $||\mathbf{d}||/h$ (Figure B.15d-f). Note that we present present results for three different values of n_u (i.e. $n_u = 1$, 2 and 3).

Next, in Figure B.16, we consider a set of three targets $(T1, T2, T3)$ different from that included in the main text and present the results for the optimal design identified by the greedy algorithm. Next, in Figure B.17 we show the inverse design of an actuator reaching the same set of three targets considered in Figure 3.3, but with the additional constraint that the targets much be reached successively by decreasing pressure.

Finally, in Figure B.18 we show how the minimum value of Ψ found by the greedy algorithm varies with the number of targets, $n_{targets}$, and the units forming a super-cell, n_u, and in Figure B.19 how the target radius (i.e. the radius of the sphere fitted with the targets) influences the optimal number of units of the actuator.

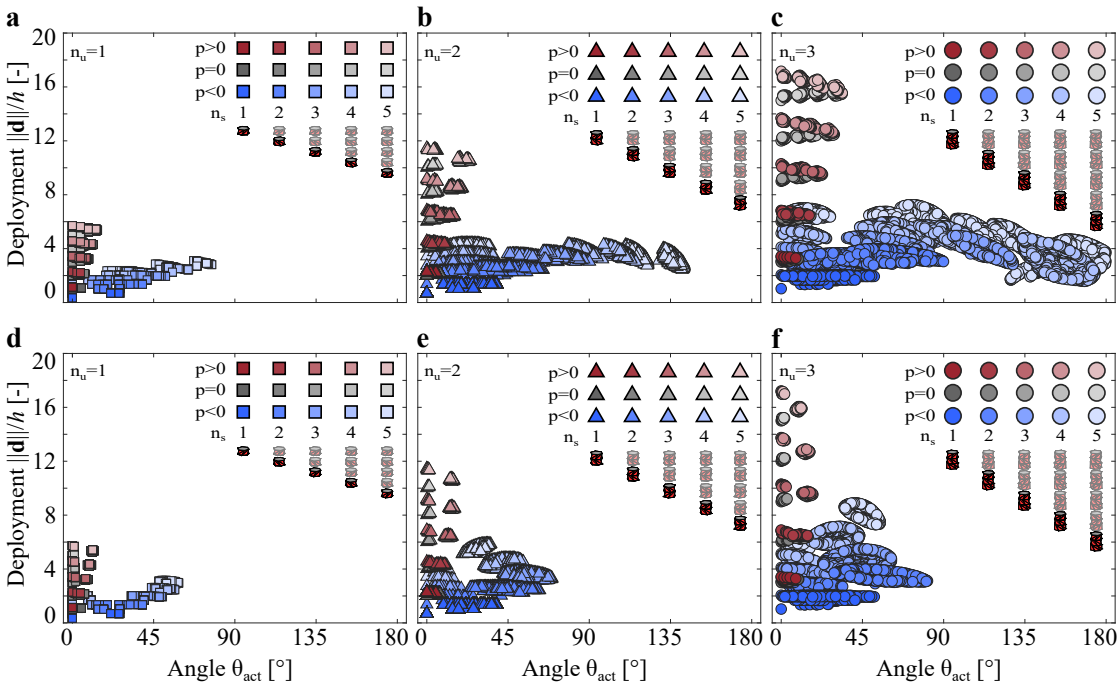

Figure B.15: Greedy algorithm results. Normalized deployment, $||\mathbf{d}||/h$, and bending angle, θ_{act}, for actuators with $n_s \in \{1, 2, 3, 4, 5\}$ and $n_u \in \{1, 2, 3\}$. **(a-c)** The greedy algorithm is programmed to maximize θ_{act} at each increment of n_s. **(d-f)** The greedy algorithm is programmed to maximize $||\mathbf{d}||/h$ at each increment of n_s.

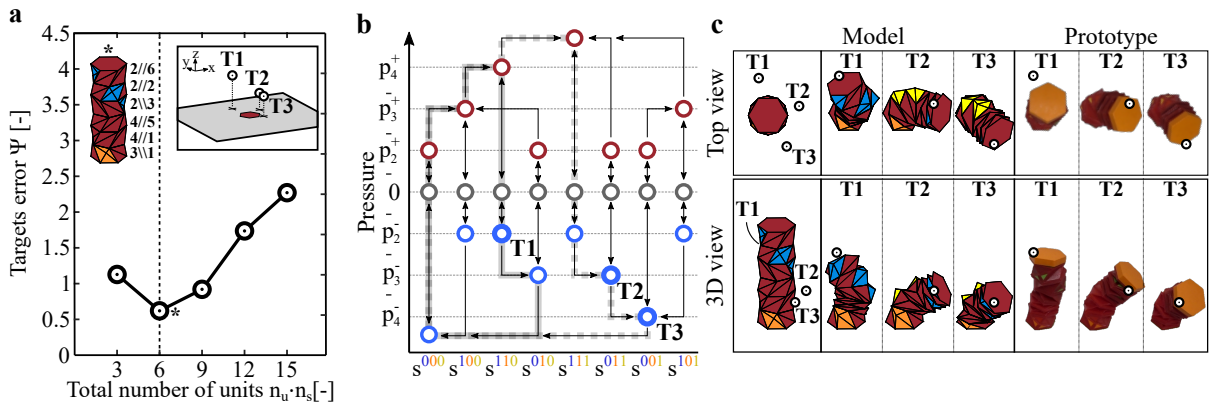

Figure B.16: A 6-units actuator reaching three targets. For a specific set of three targets, we use the greedy algorithm to find the actuator design that minimizes Ψ, i.e the error between the targets and the top cap's centroid. Note that we fix $n_u = 3$ and consider $n_s \in \{1, 2, 3, 4, 5\}$. **(a)** Targets error Ψ as a function of total number of units: the optimal actuator produced by the greedy algorithm for the three targets is reported as (*), along with the respective parameters for each module. The considered set of targets is shown in the inset. **(b)** State diagram for the 6-units actuator (*) with targets $T1$, $T2$, and $T3$ highlighted. **(c)** Top and 3D view of the model and the experimental prototype for the 6-units actuator reaching the targets.

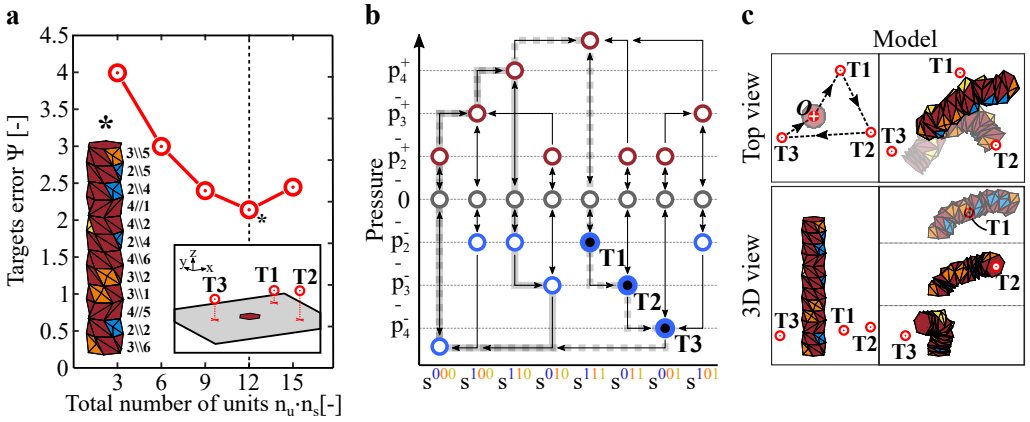

Figure B.17: The 12-units actuator with additional constraint. We focus on the same set of three targets considered in Figure 3.3 and further impose that each targets much be reached successively by decreasing pressure. **(a)** Targets error Ψ as a function of total number of units: the optimal actuator produced by the greedy algorithm for the three targets is reported as (*), along with the respective parameters for each module. **(b)** State diagram for the optimal 12-units actuator (*) with targets $T1$, $T2$, and $T3$ highlighted. **(c)** Top and 3D view of the model for the 12-units actuator reaching the targets.

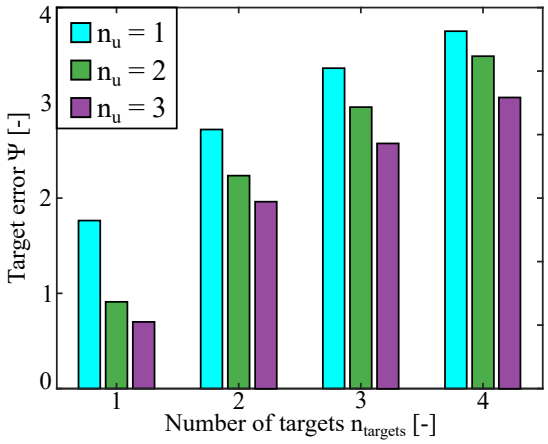

Figure B.18: Random targets error. For a random set of $n_{targets}$, we use the greedy algorithm to find the actuator design that minimizes the target error Ψ. Note that each target is bounded by a cubic domain centered with the actuator and norm equal to $1/2(n_u \cdot n_s)$ to ensure that it is within reach. We report the average error based 1000 simulations with $n_{targets} \in \{1,2,3,4\}$ and $n_u \in \{1,2,3\}$. Note that for each set of targets, we fix n_u and choose the n_s (with the constraint that $n = n_u \cdot n_s \leq 15$) that minimizes the error.

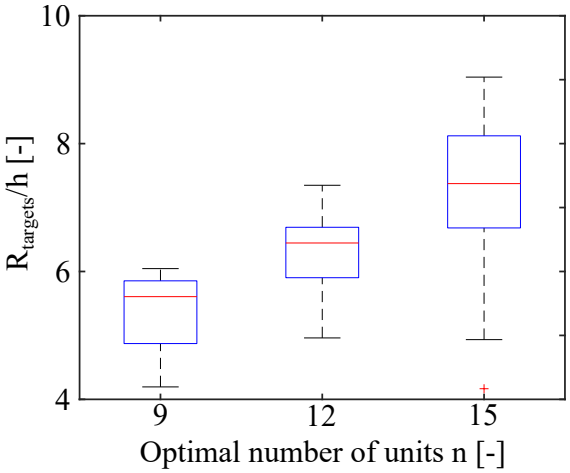

Figure B.19: Optimal number of units as a function of the target radius. For 100 random sets of $n_{targets} = 3$, we measure the target radius, $R_{targets}$, i.e. the radius of the sphere fitted with the targets, and we use the greedy algorithm to find the number of units that minimizes the error between the target and the top cap's centroid. We report here the target radius normalized by the module height, $R_{targets}/h$, as a function of the optimal number of units n found by the greedy algorithm. We find that the average target radius increases with the number of units to minimize the error Ψ.

C

Supplementary Information: Inflatable soft jumper inspired by shell snapping

By: Benjamin Gorissen*, David Melancon*, Nikolaos Vasios, Mehdi Torbati, and Katia Bertoldi.
Published in *Science Robotics* on May 20th, 2020. **doi:10.1126/scirobotics.abb1967**

C.1 Design

Our fluidic actuators are made out of two spherical caps: an inner cap that buckles under internal positive pressure and an outer cap that stretches under the same internal positive pressure. In this section, we first describe the ideal design in which the two caps are connected through a single line contact and then detail the modifications introduced to facilitate their fabrication. Note that throughout this manuscript, we will use the subscripts i and o to indicate the inner and outer caps, respectively.

C.1.1 Ideal design

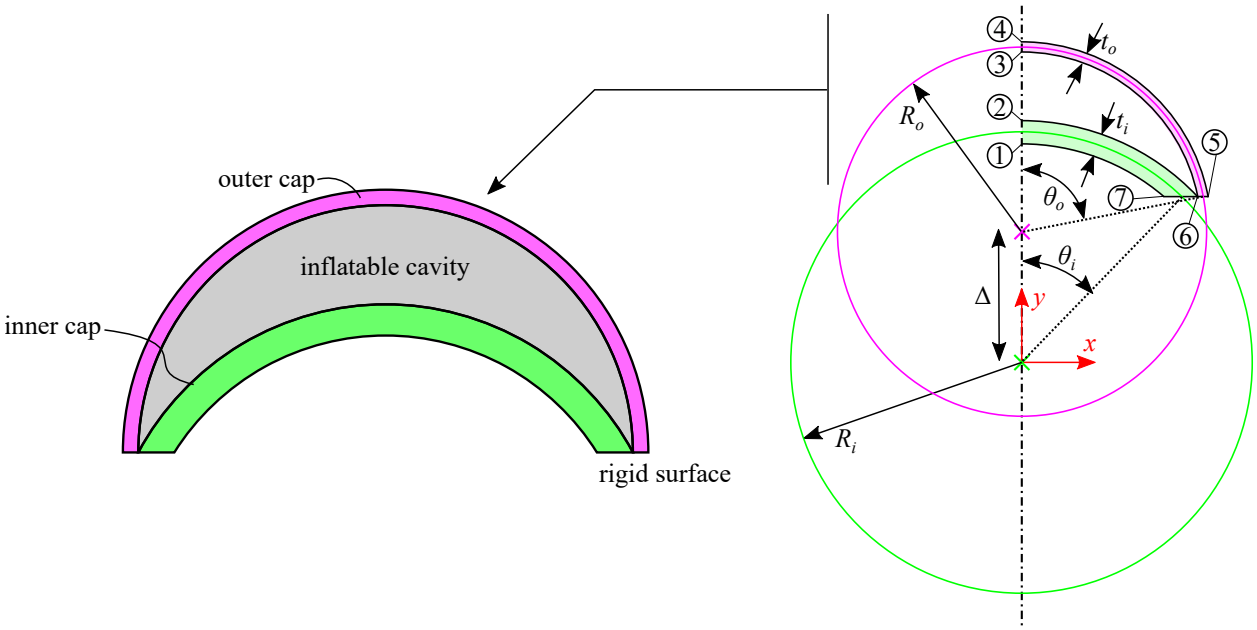

Figure C.1: Ideal design of the inflatable actuators. Schematics of the ideal design highlighting the seven points of the axisymmetric cross-section.

As shown in Figure C.1, our actuators consist of two axisymmetric spherical caps. As such, their geometry is fully defined by the opening angles θ_i and θ_o, the radii of the spheres R_i and R_o, the cap thicknesses t_i and t_o, and the center-to-center distance between the two spheres, Δ. More specifically, the coordinates of the seven points indicated in Figure C.1, which define the cross section of the actuator are given by

$$(x_1, y_1) = \left(0, R_i\left(1 - \frac{1}{2\eta_i}\right)\right) \tag{C.1a}$$

$$(x_2, y_2) = \left(0, R_i\left(1 + \frac{1}{2\eta_i}\right)\right) \tag{C.1b}$$

$$(x_3, y_3) = \left(0, R_o\left(1 - \frac{1}{2\eta_o}\right) + \Delta\right) \tag{C.1c}$$

$$(x_4, y_4) = \left(0, R_o\left(1 + \frac{1}{2\eta_o}\right) + \Delta\right) \tag{C.1d}$$

$$(x_5, y_5) = \left(R_o\sqrt{\left(1 + \frac{1}{2\eta_o}\right)^2 - \cos^2(\theta_o)}, R_i\cos(\theta_i)\right) \tag{C.1e}$$

$$(x_6^i, y_6^i) = \left(R_i\sqrt{\left(1 + \frac{1}{2\eta_i}\right)^2 - \cos^2(\theta_i)}, R_i\cos(\theta_i)\right) \tag{C.1f}$$

$$(x_6^o, y_6^o) = \left(R_o\sqrt{\left(1 - \frac{1}{2\eta_o}\right)^2 - \cos^2(\theta_o)}, R_o\cos(\theta_o) + \Delta\right) \tag{C.1g}$$

$$(x_7, y_7) = \left(R_i\sqrt{\left(1 - \frac{1}{2\eta_i}\right)^2 - \cos^2(\theta_i)}, R_i\cos(\theta_i)\right), \tag{C.1h}$$

(C.1i)

where $\eta_i = R_i/t_i$ and $\eta_o = R_o/t_o$ are the normalized radii, and (x_6^i, y_6^i) and (x_6^o, y_6^o) are the coordinates of point 6 expressed in terms of the inner cap and outer cap, respectively. However, an inflatable cavity is formed only if

$$x_6^i = x_6^o, \quad \text{and} \quad y_6^i = y_6^o \tag{C.2}$$

and we solve these two equations by substituting equations [C.1f] and [C.1g] to express the radius of the outer cap, R_o, and the center-to-center distance between the spheres, Δ, as a function of the other parameters:

$$R_o = R_i \sqrt{\frac{\left(1+\frac{1}{2\eta_i}\right)^2 - \cos^2(\theta_i)}{\left(1-\frac{1}{2\eta_o}\right)^2 - \cos^2(\theta_o)}}, \tag{C.3a}$$

$$\Delta = R_i \left(\cos(\theta_i) - \cos(\theta_o) \sqrt{\frac{\left(1+\frac{1}{2\eta_i}\right)^2 - \cos^2(\theta_i)}{\left(1-\frac{1}{2\eta_o}\right)^2 - \cos^2(\theta_o)}} \right). \tag{C.3b}$$

It follows that the geometry of the actuators is fully defined by 4 dimensionless and independent parameters:

$$\theta_i, \quad \theta_o, \quad \eta_i = \frac{R_i}{t_i}, \quad \eta_o = \frac{R_o}{t_o}. \tag{C.4}$$

Further, in order for the two caps to not intersect, we need to respect the following inequality constraints:

$$\begin{aligned} \theta_i &< \theta_o, \\ y_2 &< y_3. \end{aligned} \tag{C.5}$$

C.1.2 Modifications to facilitate fabrication

As shown in Figure C.1, the inner and outer caps are only connected through a line contact, which provides no structural integrity. To this end, we modify the geometry to enhance the robustness of the actuator, but also facilitate its fabrication. In particular, we extend the inner cap by introducing a ring around its base with thickness t_{ring} and width w_{ring} (see Figure **??**). As such, the base of the inner cap's cross section is defined by the three vertices:

$$(x_8, y_8) = \left(R_i \sqrt{\left(1-\frac{1}{2\eta_i}\right)^2 - \cos^2(\theta_i)}, R_i \left(\cos(\theta_i) - \frac{1}{\bar{t}_{ring}} \right) \right) \tag{C.6a}$$

$$(x_9, y_9) = \left(R_i \left(\sqrt{\left(1+\frac{1}{2\eta_i}\right)^2 - \cos^2(\theta_i)} + \frac{1}{\bar{w}_{ring}} \right), R_i \left(\cos(\theta_i) - \frac{1}{\bar{t}_{ring}} \right) \right) \tag{C.6b}$$

$$(x_{10}, y_{10}) = \left(R_i \left(\sqrt{\left(1+\frac{1}{2\eta_i}\right)^2 - \cos^2(\theta_i)} + \frac{1}{\bar{w}_{ring}} \right), R_i \cos(\theta_i) \right), \tag{C.6c}$$

(C.6d)

where $\bar{t}_{ring} = R_i/t_{ring}$ and $\bar{w}_{ring} = R_i/w_{ring}$.

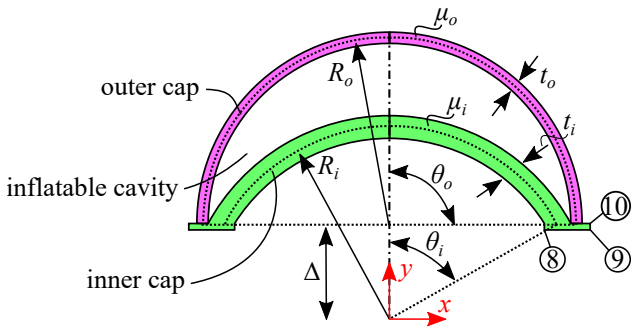

C.2 Fabrication

The actuators tested in this study are made of nearly incompressible silicone rubbers. Specifically, we use both Elite Double 32 from Zhermack (with green color and initial shear modulus $\mu = 0.35$ MPa) and Elite Double 8 from Zhermack (with purple color and initial shear modulus $\mu = 0.06$ MPa). The two caps are casted with a two-part mold, which is designed using NX 12 (Siemens) and 3d printed in VeroClear with a Connex3 Objet500 printer (Stratasys). The inner cap and outer cap are molded separately and combined afterwards to form an enclosed, inflatable cavity. Specifically, our actuators are fabricated using the following 12 steps (see Figure C.2):

- **Step 1:** we coat all inner mold surfaces with a release agent (Ease Release 200 spray, Mann Release Technologies) to facilitate demolding in a later step.
- **Step 2:** we fill the bottom halves of the molds with uncured polymer. In the case shown in Figure C.2, we use Elite Double 32 (Zhermack) for the inner cap and Elite Double 8 (Zhermack) for the outer cap.
- **Step 3:** we close both molds with pressure clamps to ensure accurate layer thickness and wait 15 minutes for the polymer to cure.
- **Step 4:** we remove both cured caps from the molds.
- **Step 5:** we puncture the outer cap to create an access hole for a tube.
- **Step 6:** we insert the tube in the outer cap.
- **Step 7:** we apply glue (Sil-Poxy Silicone Adhesive) around the edges of the top surface of the ring at the base of the inner cap.
- **Step 8:** we connect the outer cap to the inner cap and wait 15 minutes for the glue to cure.
- **Step 9:** we apply glue (Sil-Poxy Silicone Adhesive) to fix the tube to the outer cap.
- **Step 10:** we wait 15 minutes for the glue to cure.
- **Step 11:** we connect the actuator to a syringe pump.
- **Step 12:** we inflate the actuator to make sure there are no leaks.

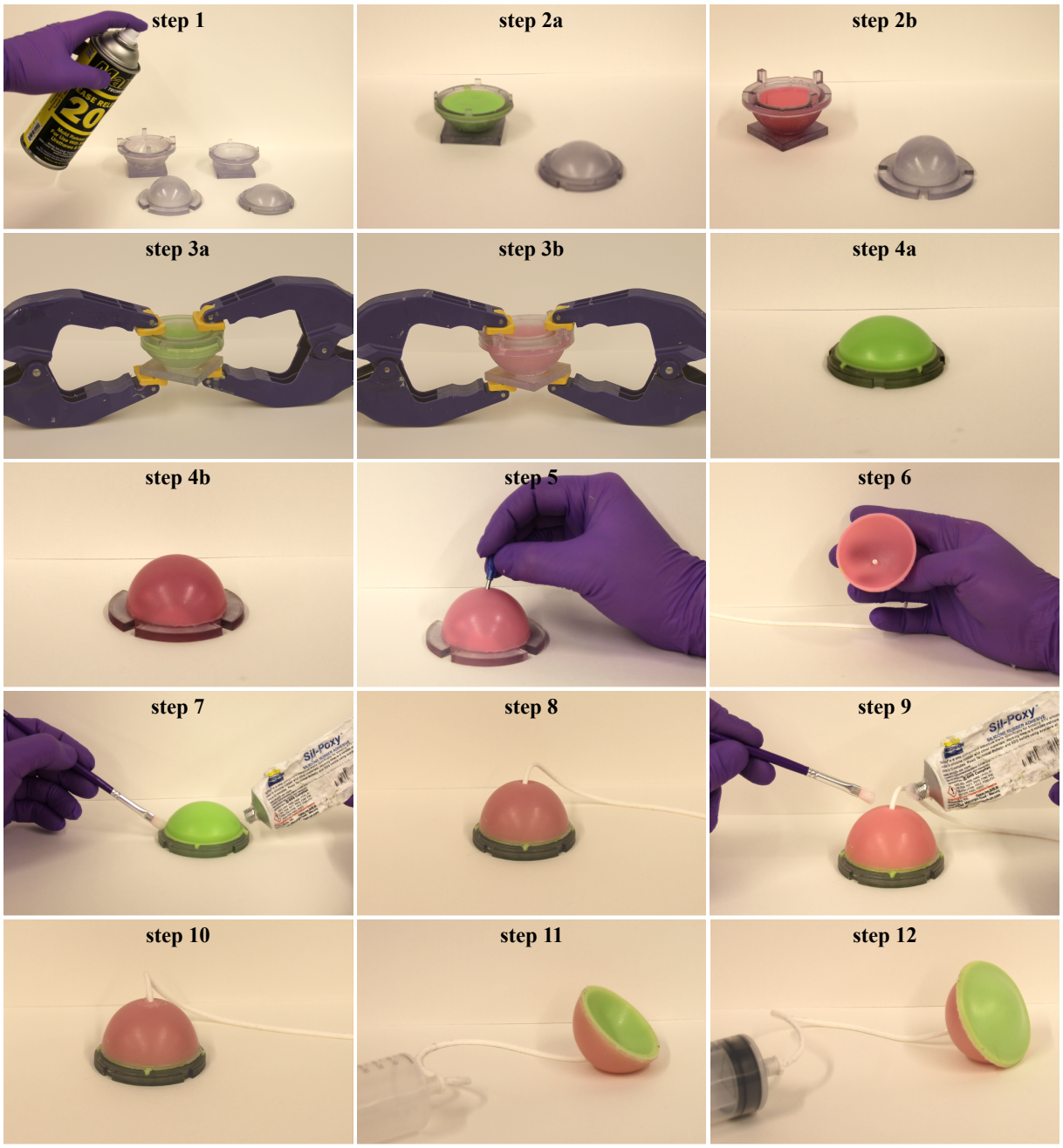

Figure C.2: Fabrication of the inflatable actuators. Snapshots of the 12 steps required to fabricate our actuators

As part of this study, we fabricate four prototypes, all with $R_i = 30\text{mm}$, $\bar{t}_{ring} = \frac{R_i}{t_{ring}} = 30$, $\bar{w}_{ring} = \frac{R_i}{w_{ring}} = 10$, and (see Figure C.3)

- *Design A:* $\eta_i = 30$, $\eta_o = 16.5$, $\theta_i = 60°$, $\theta_o = 90°$ and $\mu_i/\mu_o = 1$;
- *Design B:* $\eta_i = 8.5$, $\eta_o = 16.5$, $\theta_i = 60°$, $\theta_o = 90°$ and $\mu_i/\mu_o = 1$;
- *Design C:* $\eta_i = 8.5$, $\eta_o = 16.5$, $\theta_i = 60°$, $\theta_o = 90°$ and $\mu_i/\mu_o = 5.8$;
- *Design D:* $\eta_i = 6.2$, $\eta_o = 12.1$, $\theta_i = 80°$, $\theta_o = 82°$ and $\mu_i/\mu_o = 5.8$;

where μ_i/μ_o is the ratio between the initial shear modulus of the rubber used to fabricate the inner and outer caps, respectively.

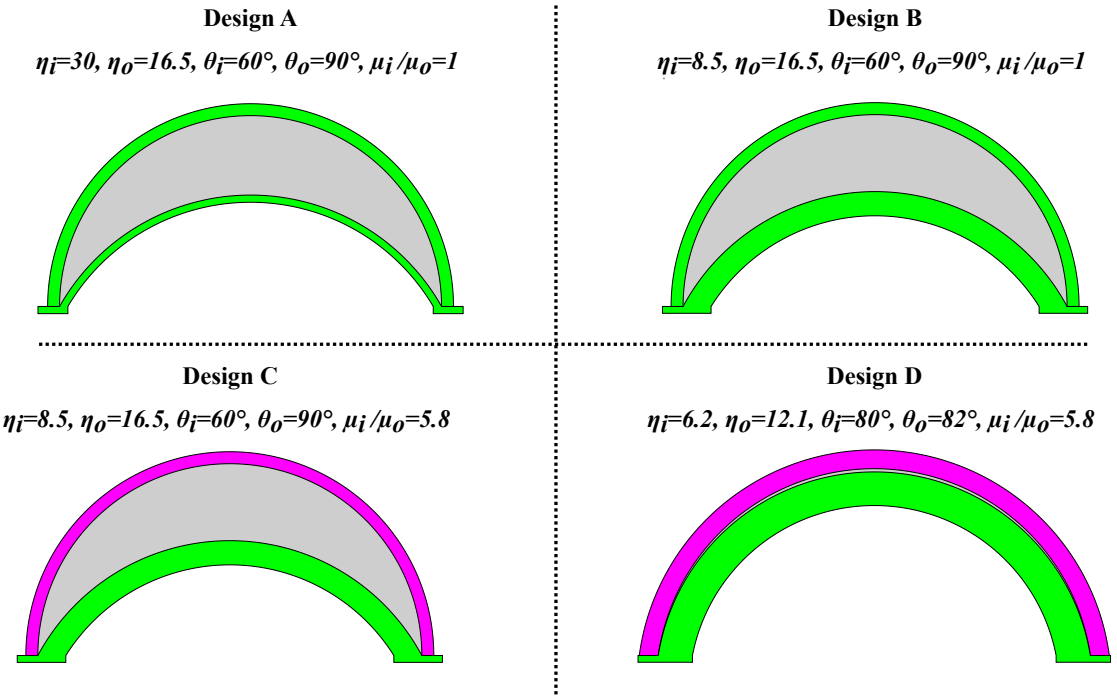

Figure C.3: Baseline designs of the inflatable actuators. Schematics of the four designs fabricated as part of this study.

C.3 Testing

In order to fully characterize the response of the fabricated actuators under quasi-static inflation, we first inflate them with water to measure their pressure-volume relation and then with air to assess their ability to jump.

C.3.1 Inflation with water

First, to decouple the effect of the geometry of the actuators from that of the compressibility of the fluid, we determine the pressure-volume curve by inflating the actuators with water. As depicted in Figure C.4, we use a syringe pump (Pump 33DS, Harvard Apparatus) to displace water into the actuator at 10 mL/min and measure the pressure using a pressure sensor (MPXV7002DP with a measurement range of ±2 kPa and MPXV7025DP with a measurement range of ±25 kPa, both by NXP USA). Note that to eliminate the influence of gravity, we submerge the entire actuator in a water tank. Moreover, to accurately determine the pressure-volume relation, air is eliminated from all supply tubes and the pressure is calibrated to atmospheric pressure before each measurement cycle.

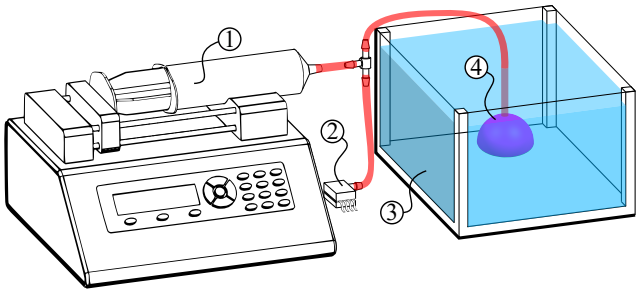

Figure C.4: Experimental setup of the inflation with water. Schematic of the test setup used to characterize the pressure-volume characteristic of the prototype actuators. (1) Syringe pump. (2) Pressure sensor. (3) Water tank. (4) Actuator.

In Figure C.5, we report the experimentally measured pressure-volume curves for Designs A-D, with the blue lines corresponding to inflation and the red ones to deflation. To make sure the response is repeatable, for each design we test three specimens across three inflation-deflation cycles. The continuous lines correspond to the mean of the responses recorded in all tests and the shaded region to the standard deviation.

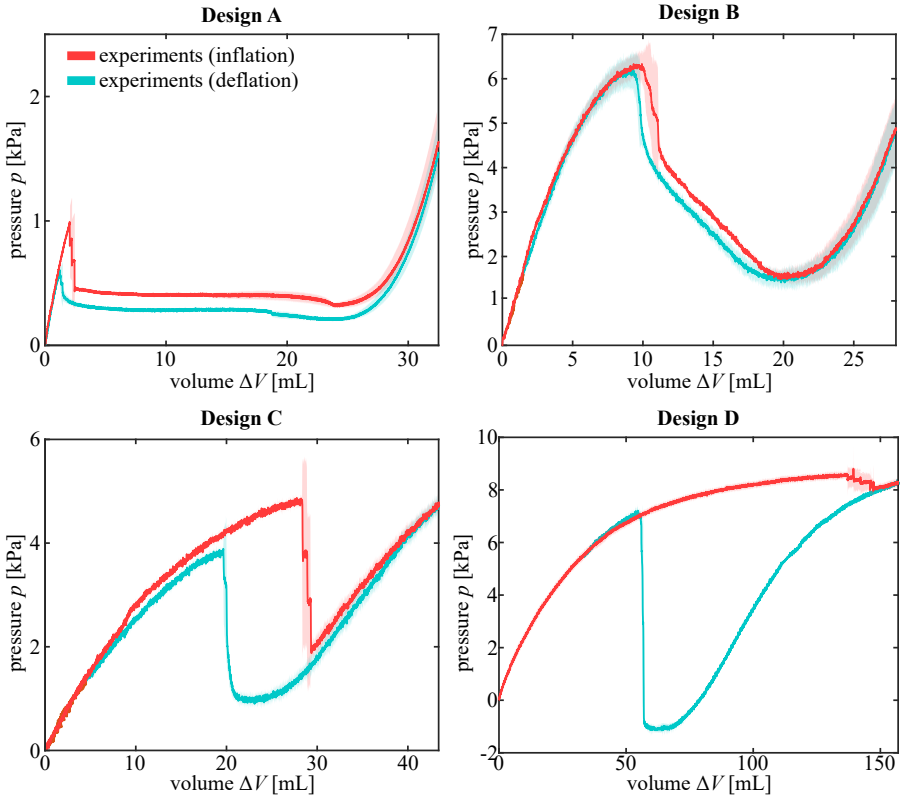

Figure C.5: Experimental pressure-volume curves of the inflatable actuators. Pressure vs. volume relationships measured for Designs A-D. The shaded region represents the standard deviation obtained from testing three specimens for each geometry.

C.3.2 Inflation with air

To investigate how snapping can be exploited to make our actuators jump even when inflated at a slow rate, we position them on a flat surface (to minimize the effect of viscous forces) and slowly inflate them with air (to minimize the effect of gravity). Specifically, we inflate them with air at 10 mL/min using a syringe pump (Pump 33DS, Harvard Apparatus), while capturing their deformation with a high speed camera (SONY RX100 V) recording at 240 frames per second (see Figure C.6). The jump height, y_{jump}, is defined as the distance between the flat surface and the lowest point of the inner cap measured when the actuator reaches its highest point (see Figure C.8). In Figure C.7, we show frames extracted from the recorded movies for the four different designs that we fabricated as part of this study. We find that only Designs C and D are able to jump and that $y_{jump} = 42.9$ mm and 283 mm for Design C and Design D, respectively.

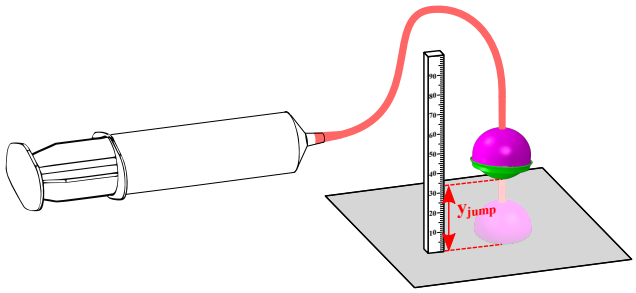

Figure C.6: Experimental setup of the inflation with air. Schematic of the test setup used to characterize the ability of the actuators to jump.

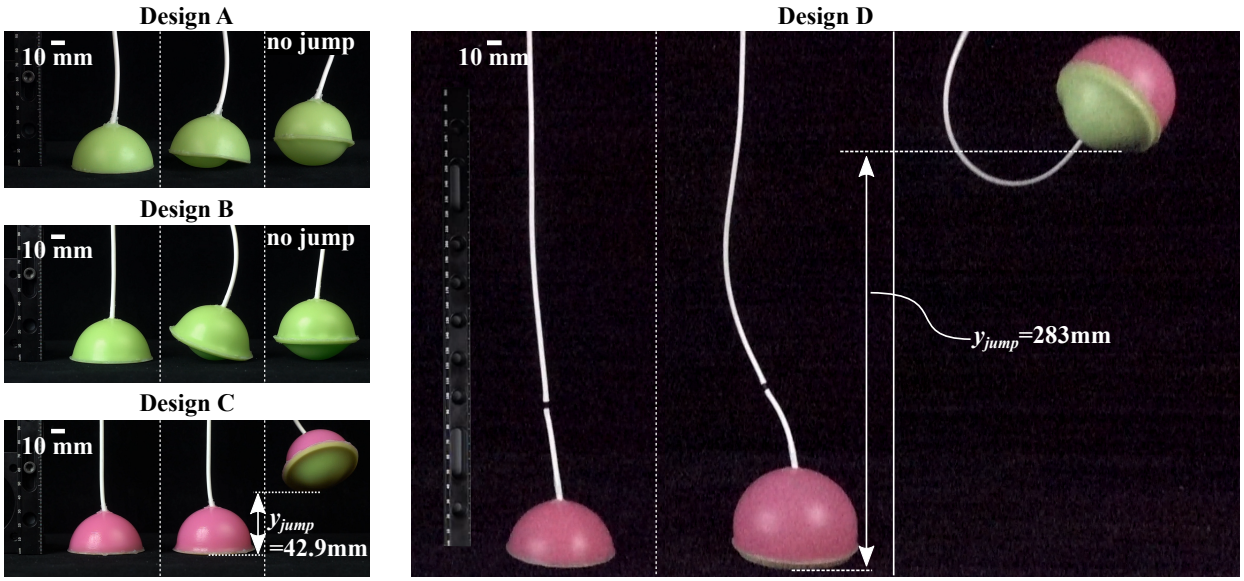

Figure C.7: Jumping tests of the inflatable actuators. Snapshots of the actuators before inflation, just before snapping of the inner cap, and at their highest point.

Finally, we note that, although this last set of test was conducted using a compressible fluid (air), the effect of fluid compressibility on the response of the system energy release is negligible. To demonstrate this important point, we also measure the pressure-volume curve of Design C while inflating with air at 10 mL/min and taking into account its compressibility to measure the volume inside the actuator. Specifically, the current volume of the system (which comprises the actuator, syringe, and connecting tube), V, at a given pressure p can be expressed as,

$$V = V_0^{sys} + \Delta V - \Delta V^{\text{syringe}}, \tag{C.7}$$

where V_0^{sys} is the initial pressure and volume of the system (which comprises the actuator, syringe, and connecting tube), ΔV is the change in volume of the actuator and $\Delta V^{\text{syringe}}$ is the amount of

volume dispense by the syringe. Since our system is a closed one

$$p_0 V_0^{sys} = pV, \tag{C.8}$$

which we combine with Eq. C.7 to obtain

$$\Delta V = \Delta V^{\text{syringe}} - \left(\frac{p - p_0}{p}\right) V_0^{sys}. \tag{C.9}$$

where p_0 is the initial pressure of the system. Given the fast time-scale of snapping, we can assume that during the instability $\Delta V^{\text{syringe}}$ is constant. Then, it follows that the change in volume of the actuator during snapping is

$$\Delta V^+ - \Delta V^- = \left(\frac{p^+ - p_0}{p^+} - \frac{p^- - p_0}{p^-}\right) V_0^{sys} = \frac{p_0(p^+ - p^-)}{p^+ p^-} V_0^{sys}, \tag{C.10}$$

where the superscripts $-$ and $+$ are used to indicate quantities evaluated immediately before and after snapping, respectively. Eq. C.10 reveals that the drop in pressure that accompanies snapping results in a change in the volume of the actuator that scales with the initial volume V_0^{sys}.

In Figure C.8 we report the pressure-volume curves for Design C as measured in three different tests in which we vary the initial volume of air in the syringe (so that V_0^{sys}=40, 45 and 100 ml). We find that in all three cases the response of the actuator is close to that measured when inflating with air.

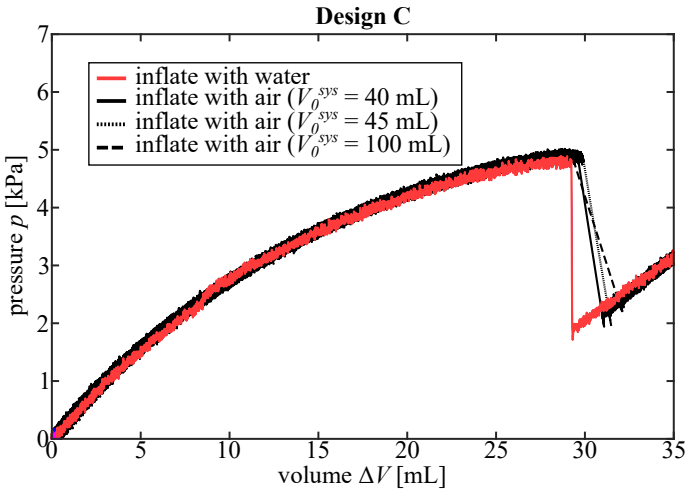

Figure C.8: Effect of air compressibility. Pressure vs. volume relationships measured for Design C inflated with water and air for three different tests in which we vary V_0^{sys} by controlling the initial volume of air in the syringe.

C.4 Finite element simulations

To gain a deeper understanding of the mechanical response of the inflatable actuators and calculate their release of energy and pole displacement during snapping, we perform Finite Element (FE) simulations using the commercial package ABAQUS 2018/Standard. In all our analyses, the response of the silicone rubber used to fabricate the caps (Elite Double 32 and Elite Double 8 from Zhermack) is modeled using an incompressible Gent material model[20] with strain energy density function W given by

$$W = -\frac{\mu J_{lim}}{2} \ln\left(1 - \frac{I_1 - 3}{J_{lim}}\right), \tag{C.11}$$

where μ and J_{lim} represent the small strain shear modulus and a material parameter related to the limiting stretch, respectively, and $I_1 = \mathrm{tr}(\mathbf{F}^T\mathbf{F})$, $\mathbf{F}$ being the deformation gradient. We find that the response of the pink Elite Double 8 and the green Elite Double 32 is accurately captured using $(\mu, J_m) = (0.06 \text{ MPa}, 24)$ and $(0.35 \text{ MPa}, 24)$, respectively. Note that these values are obtained by minimizing the error between experiments and simulations for Design C and that the obtained values for the shear modulus are within the range previously reported in the literature[? ?]. An in-house ABAQUS user subroutine (UHYPER) is used to define the hyperelastic material behavior given by Eq. C.11 in the FE simulations.

In the following, we present the different types of simulations used to determine the behavior off the actuator upon quasi-satic inflation.

C.4.1 3D simulations

We start by conducting full 3D FE simulations of the actuators. To this end, we create 3D models and discretize them using a non-structured mesh of 4-node linear tetrahedron elements (ABAQUS element type: C3D4H), with mesh size adapted to ensure that at least four elements are used to discretize the thickness of the thinnest cap.

To remove rigid body translations and rotations, we impose a no vertical displacement boundary condition ($u_y = 0$) at the nodes located on the line of contact between the two caps (defined by point 6 in Figure C.1). All models are inflated via a fluid cavity interaction with an hydraulic fluid (of density $\rho = 1000$ kg/m^3 and bulk modulus $B = 2000$ MPa). The volume-controlled inflation is driven by a fictitious thermal expansion of the hydraulic fluid, relating to the change in volume ΔV in the cavity through,

$$\frac{\Delta V}{V_0^{cav}} = 3\alpha_T \Delta T, \tag{C.12}$$

where ΔT is the change in temperature, α_T is the coefficient of thermal expansion of the fluid and V_0^{cav} is the initial volume of the cavity. In the simulations, we set $\alpha_T = 1$ m/(m$\cdot$ K) and gradually

increase the temperature ΔT until the isochoric snap-through is reached. We simulate the inflation using the dynamic implicit solver (using a density of $\rho = 1000$ kg/m^3 for the silicone rubber) and ensure quasi-static conditions by monitoring the kinetic energy of the model (note that quasi-static conditions are achieved by using a time period of 1 second, minimum increment size of 1e$-$10 s, maximum increment size of 0.01 s, and 10, 000 maximum number of increments).

In Figures C.9, C.10, and C.11 we report the pressure vs. volume curves, pole displacement vs. volume relations, and numerical snapshots of the deformed configurations for Designs A-D. First, in Figure C.9, we find very good agreement between the pressure-volume curve measured in experiments and predicted by our simulations, with the numerical analyses that correctly capture the isochoric snap-through instability. Second, in in Figure C.10, the numerical predictions for the evolution of the pole displacement of Designs C and D suggest that the snap-through instability is accompanied by a sudden and large change in the displacement of the pole, which ultimately enables these Designs to jump. Finally, by looking at the deformation experienced by the actuators during inflation and deflation (Figure C.11), we find that Designs C and D maintain an axisymmetric configurations also during the isochoric snap-through.

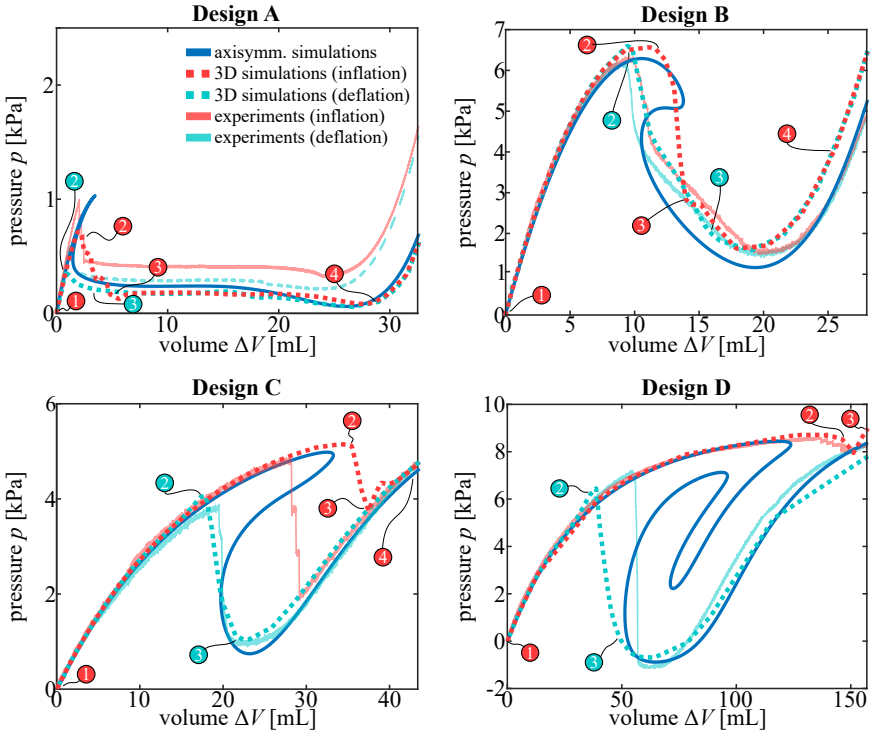

Figure C.9: Numerical and experimental pressure-volume curves of the inflatable actuators. Pressure-volume relations for Designs A-D as predicted by our 3D (blue dashed lines for inflation and orange dashed lines for deflation) and axisymmetric (black line) simulations and measured in experiments (blue solid lines for inflation and orange solid lines for deflation). The numbers on the plots indicate the deformation states shown in Figure C10.

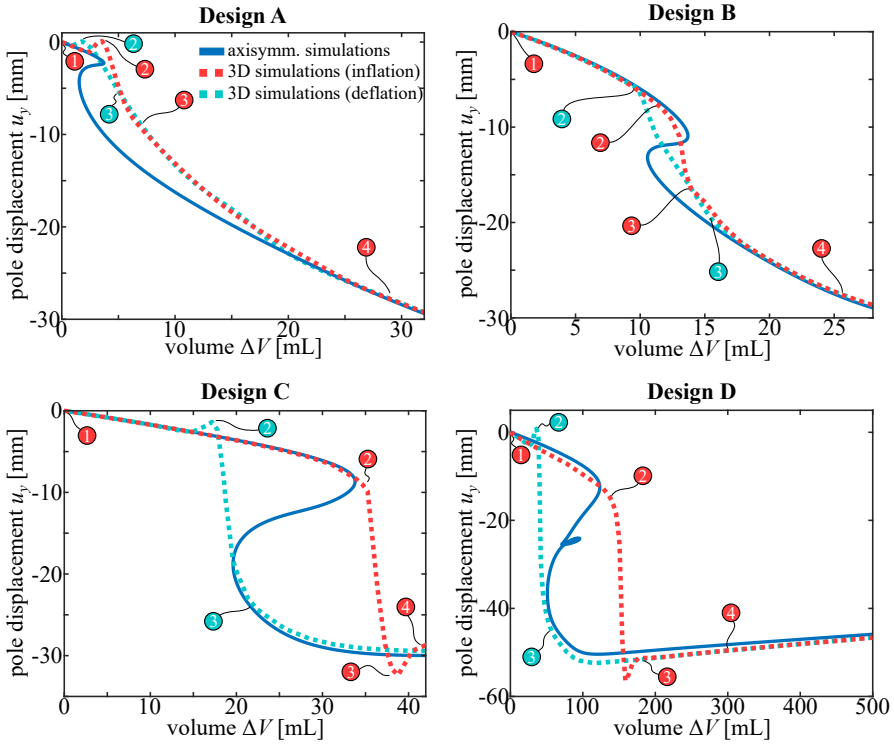

Figure C.10: Pole displacement of the inflatable actuators. Pole displacement vs. volume curves for Designs A-D as predicted by our 3D (blue dashed lines for inflation and orange dashed lines for deflation) and axisymmetric (black line) simulations. The numbers on the plots indicate the deformation states shown in Figure C.10.

C.4.2 Axisymmetric simulations

While our 3D FE simulations accurately capture and predict the response of our actuators, their high computational cost prohibits their use for efficient exploration of the design space. To this end, we assume that the deformation of the actuators is axisymmetric and discretize the models using using 4-node bilinear axisymmetric solid elements (ABAQUS element type: CAX4H), with the mesh size adapted to make sure the thinnest cap has at least four elements through thickness. To predict the energy released during the isochoric snap-through, we determine the full pressure-volume relation using the modified Riks algorithm[115,116] as implemented in Abaqus. As for the 3D simulations, the axisymmetric models are inflated via a fluid cavity interaction with an hydraulic fluid (of density $\rho = 1000$ kg/m^3 and bulk modulus $B = 2000$ MPa) and we stop inflating when the pressure p is equal to

$$p = 1.5\, p_c, \tag{C.13}$$

where p_c is the critical pressure for a thin spherical shell and the factor 1.5 is introduced to account for the fact that most of the caps we are simulating are not thin (i.e. $R/t < 25$). For a spherical shell

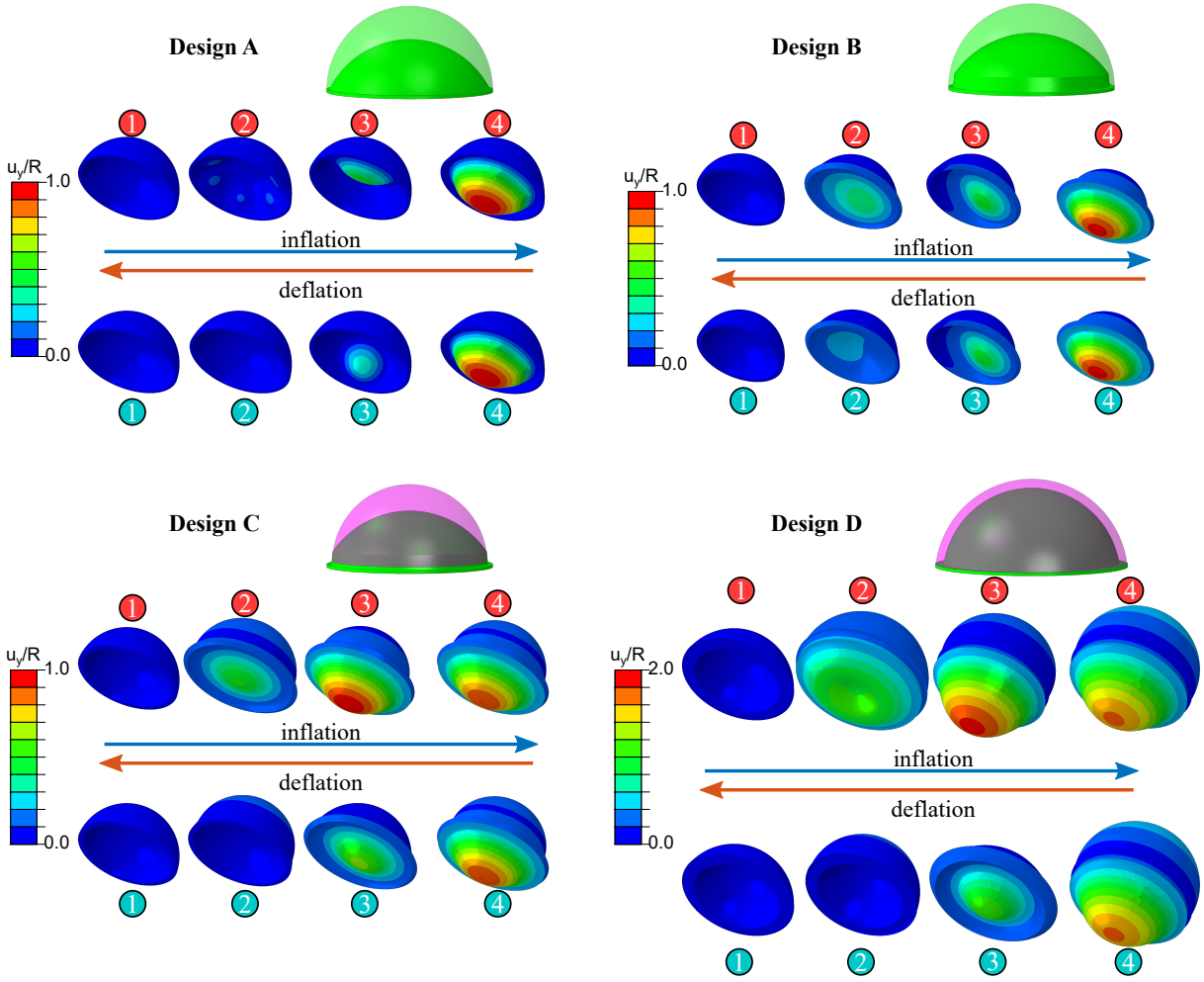

Figure C.11: 3D simulations of the inflatable actuators. Numerical snapshots showing the deformation of Designs A-D as predicted by our 3D FE simulations for inflation and deflation. The numbers next to the snapshots correspond to the numbers indicated in Figures C.10 and C.11.

of radius R and thickness t, such critical pressure can be estimated as[119]

$$p_c = \frac{2E}{\sqrt{3(1-\nu^2)}} \left(\frac{t}{R}\right)^2, \tag{C.14}$$

where E and ν are the Young's modulus and Poisson's ratio, respectively (for the considered incompressible hyperelastic material $E = 3\mu$ and $\nu = 0.5$).

Full actuators. To simulate the response of the actuators, we impose roller boundary conditions ($u_x = 0$) on the rotational axis of symmetry. Moreover, to eliminate rigid-body translations and rotations, we impose a no vertical displacement boundary condition at the point of contact between

the two caps (Figure C.12A). In Figure C.12, we focus on Design C and report numerical snapshots at different levels of inflation (Figure C.12B), the pressure-volume curve (Figure C.12C), the evolution of the strain energy as a function of volume (Figure C.12D), and the evolution of the pole displacement as a function of volume (Figure C.12E) as predicted by our axisymmetric simulations. Since the Riks analyses is able to trace the entire pressure-volume curve, we can direcly extract the energy released ΔE during the isochoric snap-through (see highlighted area in blue in Figure C.12C and step-by-step method in Figure C.13). Moreover, in Figures C.10 and C.12 we compare the numerical predictions of our axisymmetric analyses with those of the 3D simulations. The good agreement between the two sets of data validates the axisymmetric analyses.

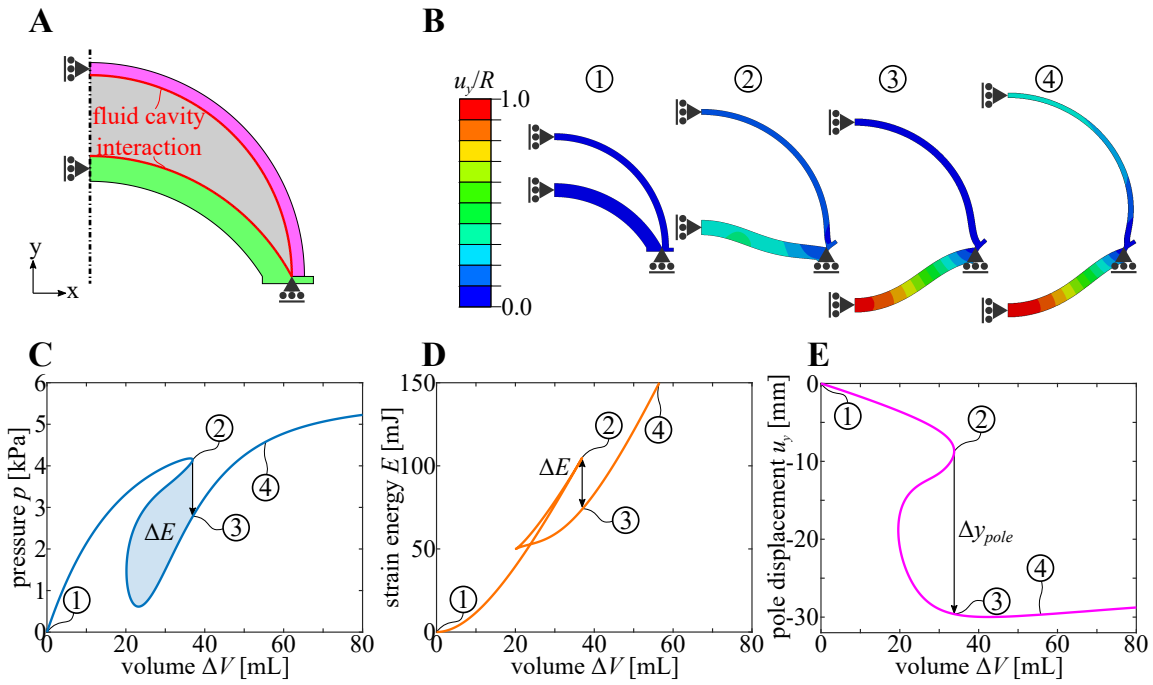

Figure C.12: Axisymmetric simulations of the inflatable actuators. **(a)** Schematic of the axisymmetric model. **(b)** Numerical snapshots of Design C at (1) rest, (2) before snapping, (3) after snapping, and (4) upon further inflation. **(c)** Pressure vs. volume relation as predicted by our axisymmetric simulations for Design C. **(d)** Strain energy vs. volume relation as predicted by our axisymmetric simulations for Design C. **(e)** Pole displacement vs. volume relation as predicted by our axisymmetric simulations for Design C.

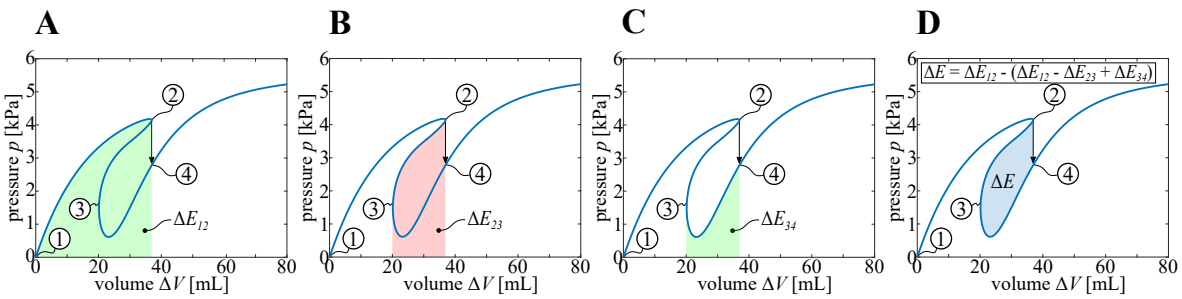

Figure C.13: Extracting ΔE from the numerical pressure-volume curves of the full actuators. **(a)** Highlighted green region represents the strain energy stored in the system when inflated up to the snapping point (i.e. when inflated from state (1) to state (2)). **(b)** Highlighted red region represents the strain energy released from the system when it moves from state (2) to state (3). **(c)** Highlighted green region represents the strain energy stored in the system between when it moves from state (3) to state (4). **(d)** Highlighted blue region represents the energy released from the system during the isochoric snap-through.

Separate inner and outer caps. To gain further insights into the response of our actuators, we investigate separately the inner and the outer caps via axisymmetric simulations for a wide range of geometric parameters (i.e. $40° \leq \theta_i \leq 80°$, $5 \leq \eta_i \leq 12.5$, $40° \leq \theta_o \leq 90°$, $5 \leq \eta_o \leq 20$). Similarly to the actuator, the models in these cases are discretized with 4-node bilinear axisymmetric solid elements (CAX4H element type) with mesh size adapted to ensure at least four elements through thickness. For both inner and outer caps, we capture the materials response using the Gent model in Eq. C.11 and impose $u_x = 0$ on the rotational axis of symmetry. Moreover, for the inner cap we impose $u_y = 0$ at the connection between the base of the cap and the angular ring (inset in Figure C.14F), whereas for the outer cap we assume that the base is completely fixed (Figure C.16B).

Focusing on the inner cap, the numerical results summarized in Figure C.14A-B indicate that by varying the polar angle θ_i and the radius to thickness ratio η_i, the response of the cap undergoes several transitions. For low values of θ_i and η_i (i.e. for thick and shallow caps), the inner cap does not exhibit the snap-through behavior (see light grey region in Figure C.14B-C). By increasing θ_i at constant η_i, a snap-through instability is eventually triggered upon inflation, which results in a sudden release of energy and fast cap's pole displacement. Within this domain, ΔE_i and Δy_{pole} both increase monotonically as a function of θ_i (see Figure C.14C). Finally, for high values of θ_i and η_i (i.e. for thin and deep caps) the pressure-volume curves become self-crossing (see dark grey region in Figure C.14-B). By comparing the results of axisymmetric and 3D simulations we find that a highly complex, self-crossing pressure-volume response indicates the existence of a more favorable asymmetric deformation path with low energy release upon snapping (Figure C.15).

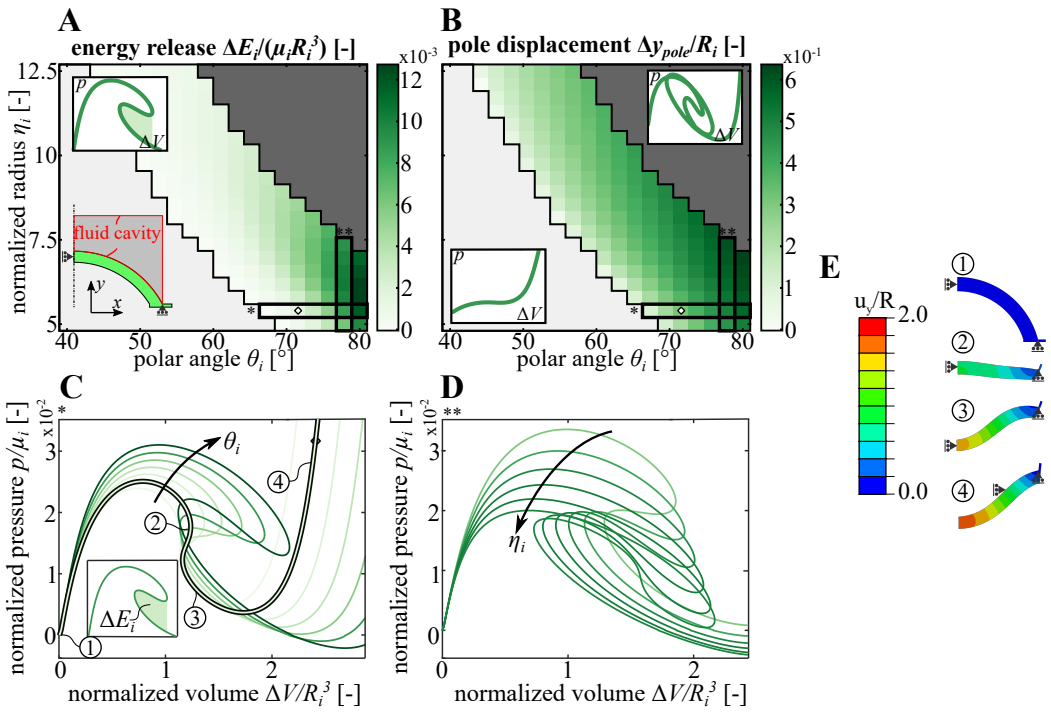

Figure C.14: Axisymmetric simulations of the inner cap. **(a-b)** Evolution of the (a) normalized energy released and (b) pole displacement as a function of the normalized radius, η_i, and the polar angle, θ_i. **(c-d)** Pressure-volume curves of the inner cap for (c) varying polar angle and (d) normalized radius. **(e)** Numerical snapshots of an inner cap characterized by $\eta_i = 5.4$ and $\theta_i = 74°$ at (1) rest, (2) before snapping, (3) after snapping, and (4) upon further inflation.

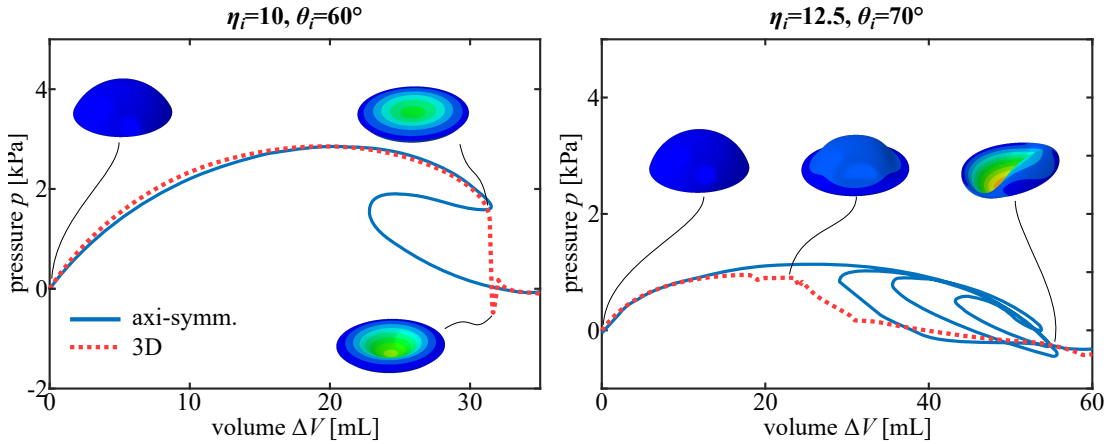

Figure C.15: Asymmetric deformation emerges in designs with self-crossing pressure-volume curves. Pressure-volume curve for an inner cap with $(\eta_i, \theta_i) = (10, 60°)$ (left) and $(12.5, 70°)$ (right) as predicted by our axisymmetric (back solid lines) and 3D (dashed blue lines) simulations. We find that caps for which the axisymmetric simulations predict a self crossing pressure-volume curve typically deform asymmetrically.

Finally, in Figure C.16 we present results for the outer cap. More specifically, in Figure C.16A we show the evolution of the stored energy at $p_o/\mu_o = 0.5$, E_0, as a function of the polar angle θ_o and the normalized radius η_o. The energy increases monotonically with increasing θ_o, almost irrespective of η_o.

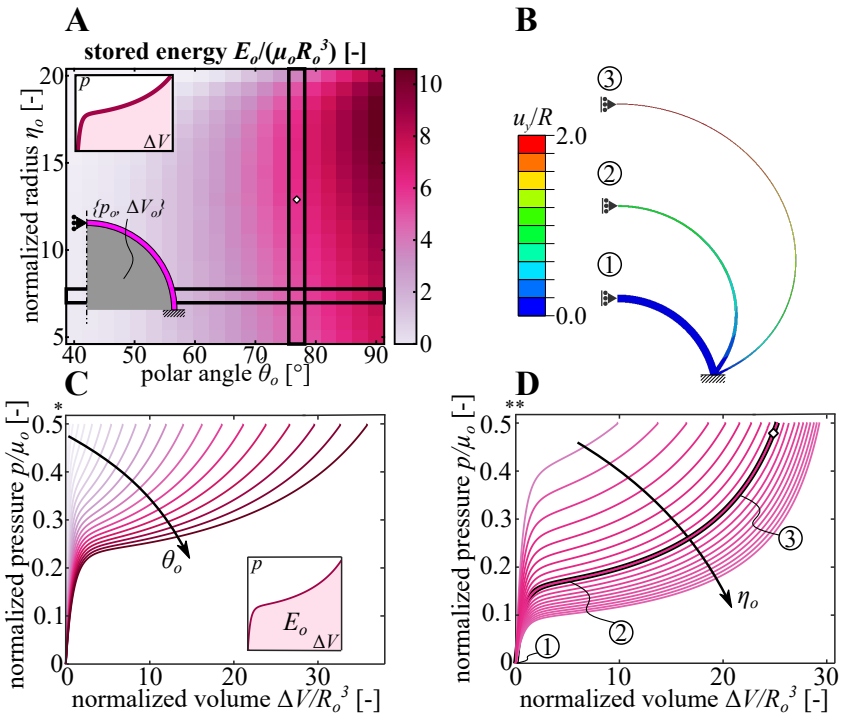

Figure C.16: Axisymmetric simulations of the outer cap (a) Evolution of the normalized stored energy at $p/\mu_o = 0.5$, $E_o/(\mu_o R_o^3)$, as a function of the normalized radius η_o and the polar angle θ_o. **(b)** Numerical snapshots of an outer cap characterized by $\eta_i = 12.9$ and $\theta_i = 77°$ at different levels of inflation. **(c-d)** Normalized pressure-volume curves for varying (c) θ_o and (d) η_o.

C.5 Mass-spring model to predict the jump height

Our quasi-static FE simulations allow us to efficiently explore the design space and calculate ΔE and Δy_{pole} for a large number of designs. However, since they do not account for dynamic effects, they cannot be used to directly characterize the ability of the actuators to jump. To overcome this limitation, as described in the main text we establish a simple mass-spring model (see Figure C.17) that takes the FE results as input and predicts the jump height.

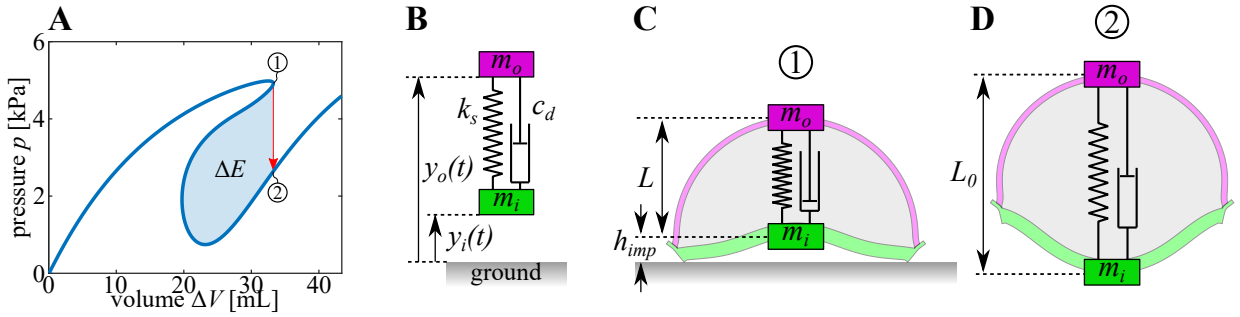

Figure C.17: Mass-spring model to predict jump height. **(a)** Pressure-volume curve for Design C as predicted by our FE simulations. **(b)** Our spring-mass model comprise two rigid masses, m_i and m_o, constrained to move vertically. We choose m_i and m_o to be equal to the mass of the inner and outer cap, respectively, and to be located at their corresponding poles. **(c)** We assume that the mechanical system stores an amount of energy equal to ΔE in the numerically predicted configuration immediately before snapping. **(d)** We assume that the mechanical system is stress-free in the numerically predicted configuration immediately after snapping.

Specifically, to solve for the jumping height of the actuator we determine the position of the individual masses, $y_i(t)$ and $y_o(t)$ as a function of time. The differential equations describing the motion of the model are

$$\begin{bmatrix} m_i & 0 \\ 0 & m_o \end{bmatrix} \begin{bmatrix} \ddot{y}_i \\ \ddot{y}_o \end{bmatrix} + \begin{bmatrix} c_d & -c_d \\ -c_d & c_d \end{bmatrix} \begin{bmatrix} \dot{y}_i \\ \dot{y}_o \end{bmatrix} + \begin{bmatrix} k_s & -k_s \\ -k_s & k_s \end{bmatrix} \begin{bmatrix} y_i \\ y_o \end{bmatrix} = \begin{bmatrix} -m_i g - k_s L_0 \\ -m_o g + k_s L_0 \end{bmatrix}, \tag{C.15}$$

where g is the gravitational acceleration ($g = 9.81$ m/s^2). To determine $y_i(t)$ and $y_o(t)$, we define $v_i = \dot{y}_i$ and $v_o = \dot{y}_o$ and transform Eqs. [C.15] into a first-order ODE system of the type

$$\dot{\mathbf{Y}} = \mathbf{A}\mathbf{Y} + \mathbf{B}, \tag{C.16}$$

where

$$\mathbf{Y} = \begin{bmatrix} y_i \\ y_o \\ v_i \\ v_o \end{bmatrix}, \quad \mathbf{A} = \begin{bmatrix} 0 & 0 & 1 & 0 \\ 0 & 0 & 0 & 1 \\ \frac{-k_s}{m_i} & \frac{k_s}{m_i} & \frac{-c_d}{m_i} & \frac{c_d}{m_i} \\ \frac{k_s}{m_o} & \frac{-k_s}{m_o} & \frac{c_d}{m_o} & \frac{-c_d}{m_o} \end{bmatrix}, \quad \mathbf{B} = \begin{bmatrix} 0 \\ 0 \\ -g - \frac{k_s L_0}{m_i} \\ -g + \frac{k_s L_0}{m_o} \end{bmatrix}. \tag{C.17}$$

We then write the solution for the homogeneous system $\dot{\mathbf{Y}} = \mathbf{A}\mathbf{Y}$ as

$$\mathbf{Y}_h = a\mathbf{P}_1 + b\left[\mathbf{P}_1 t + \mathbf{P}_2\right] + c\mathbf{P}_3 e^{\lambda_3 t} + d\mathbf{P}_4 e^{\lambda_4 t}, \tag{C.18}$$

where λ_i are the eigenvalues obtained by solving the characteristic equation $\det(\mathbf{A} - \lambda\mathbf{I}) = 0$

$$\begin{aligned}
\lambda_1 &= \lambda_2 = 0, \\
\lambda_3 &= \frac{-c_d m_i - c_d m_o - \sqrt{m_i + m_o}\sqrt{c_d^2 m_i + c_d^2 m_o - 4k_s m_i m_o}}{2m_i m_o}, \\
\lambda_4 &= \frac{-c_d m_i - c_d m_o - \sqrt{m_i + m_o}\sqrt{c_d^2 m_i + c_d^2 m_o - 4k_s m_i m_o}}{2m_i m_o},
\end{aligned} \tag{C.19}$$

and $\mathbf{P}_i$ are the corresponding eigenvectors

$$\begin{aligned}
\mathbf{P}_1 &= \begin{bmatrix} 1 & 1 & 0 & 0 \end{bmatrix}^T, \\
\mathbf{P}_2 &= \begin{bmatrix} 0 & 0 & 1 & 1 \end{bmatrix}^T, \\
\mathbf{P}_3 &= \begin{bmatrix} \frac{2m_o^2}{c_d m_i + c_d m_o + \sqrt{m_i+m_o}\sqrt{c_d^2 m_i + c_d^2 m_o - 4k_s m_i m_o}} & \frac{2m_i m_o}{c_d m_i + c_d m_o + \sqrt{m_i+m_o}\sqrt{c_d^2 m_i + c_d^2 m_o - 4k_s m_i m_o}} & -\frac{m_o}{m_i} & 1 \end{bmatrix}^T, \\
\mathbf{P}_4 &= \begin{bmatrix} \frac{2m_o^2}{c_d m_i + c_d m_o - \sqrt{m_i+m_o}\sqrt{c_d^2 m_i + c_d^2 m_o - 4k_s m_i m_o}} & \frac{2m_i m_o}{c_d m_i + c_d m_o - \sqrt{m_i+m_o}\sqrt{c_d^2 m_i + c_d^2 m_o - 4k_s m_i m_o}} & -\frac{m_o}{m_i} & 1 \end{bmatrix}^T.
\end{aligned} \tag{C.20}$$

Moreover, a, b, c, d are constants of integration. Next, we determine the particular solution $\mathbf{Y}_p$ of the system of ODE through the method of variation of parameters as

$$\mathbf{Y}_p = \mathbf{\Phi}(t) \int \Phi^{-1}(t) B \mathrm{d}t, \tag{C.21}$$

where $\mathbf{\Phi}(t)$ is the fundamental matrix of the system

$$\mathbf{\Phi}(t) = \begin{bmatrix} \mathbf{P}_1 & \mathbf{P}_1 t + \mathbf{P}_2 & \mathbf{P}_3 e^{\lambda_3 t} & \mathbf{P}_4 e^{\lambda_4 t} \end{bmatrix}. \tag{C.22}$$

We then write the general solution of the system of ODE as

$$\mathbf{Y} = \mathbf{Y}_h + \mathbf{Y}_p \tag{C.23}$$

and determine the constants of integration by applying the initial condition

$$\mathbf{Y}^0 = \begin{bmatrix} y_i^0 & y_o^0 & v_i^0 & v_o^0 \end{bmatrix}^T = \begin{bmatrix} h_{imp} & h_{imp} + L & 0 & 0 \end{bmatrix}^T. \tag{C.24}$$

In all our analyses, we release the system at $t = 0$ and account for the collision between m_i and

the ground by resetting the variables when a negative height $y_i(t)$ is calculated:

$$\text{if} \quad y_i(t_i) < 0 : \begin{cases} y_i(t_i) = 0 \\ v_i(t_i) = -\alpha \cdot v_i(t_{i-1}) \end{cases} , \tag{C.25}$$

where α is the coefficient of restitution. Note that $\alpha = 0$ is equivalent to a fully plastic collision and $\alpha = 1$ corresponds to a fully elastic collision with conservation of linear momentum. In all our analyses we use $\alpha = 0.5$, as we find that this gives good agreement between the predicted and experimentally measured jumping height.

In Figure C.18 we show the evolution of both y_i and y_o as predicted by the spring-mass model for Designs C and D. In the plots, we also compare the analytical solution to that obtained by integrating Eqs. (C.17) with the numerical solver `ODE45` of Matlab and, as expected, find perfect agreement between the two.

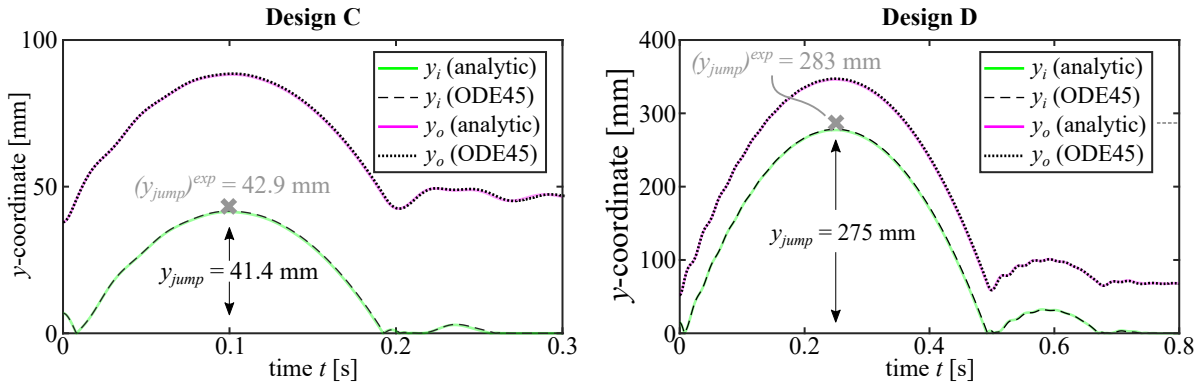

Figure C.18: Jump height prediction of the inflatable actuators. Evolution of both y_i and y_o as predicted by solving Eq. C.17 analytically (continuous lines) and numerically via `ODE45` of Matlab (dashed lines) for Designs C and D.

C.6 Additional results

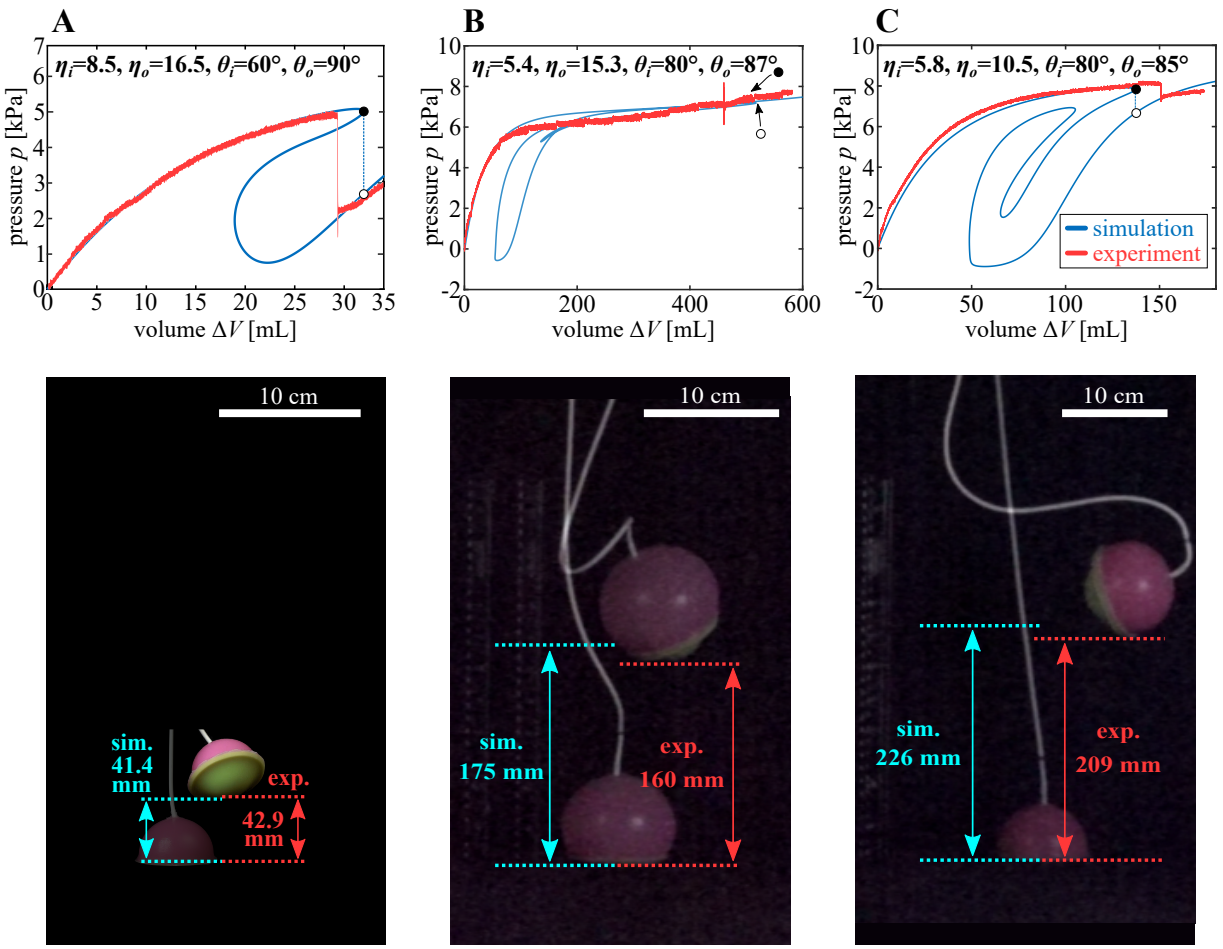

Figure C.19: Validation of the spring-mass model. To verify the validity of our simple mass-spring model, we focus on three designs with **(a)** (η_i, θ_i, η_o, θ_o, μ_i/μ_o)= (8.5, 60°, 16.5, 90°, 5.8) (Design C), **(b)** (5.4, 80°, 15.3, 87°, 5.8), and **(c)** (5.8, 80°, 10.5, 85°, 5.8) and compare the experimentally measured jump heights (h_{jump} = 42.9 mm, 160 mm, and 209 mm, respectively) to the predicted ones (h_{jump} = 41.4 mm, 175 mm, and 226 mm, respectively). On the top, for each actuator we show the numerical (blue lines) and experimental (red lines) pressure-volume relations. On the bottom, we show experimental snapshots of the actuators before ischoric snap-through and at the highest point after jump. The good agreement between numerical and experimental results for all designs confirms the validity of our analyses.

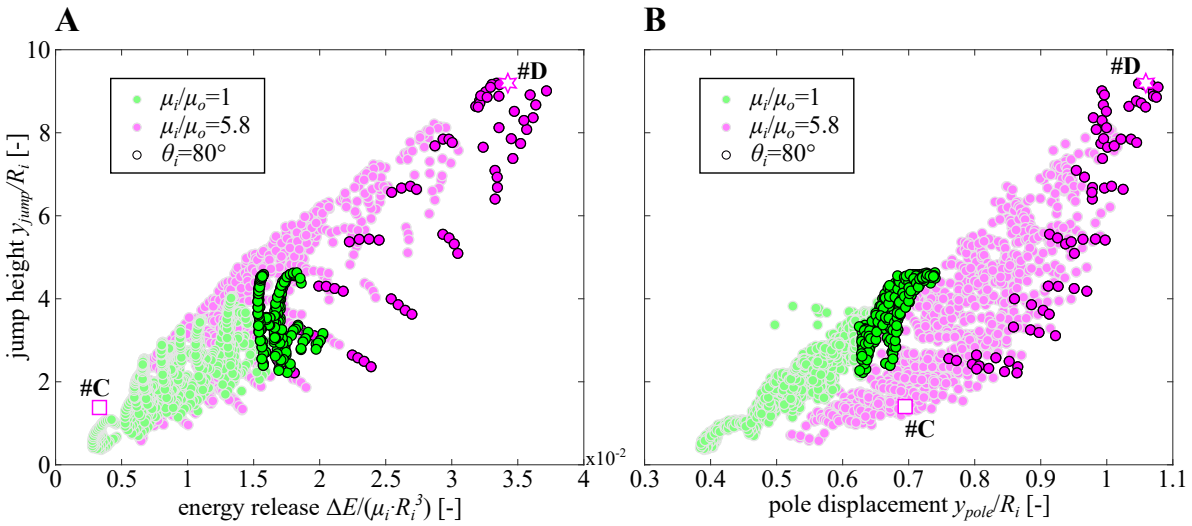

Figure C.20: Improving the performance our soft fluidic actuators through a grid search. Jump height vs. energy released (**a**) and jump height vs. pole displacement (**b**) as predicted by our analyses for 4800 actuators with $\theta_i \geq 70°$, $\eta_i \leq 8$, and $\theta_o \geq 76°$.

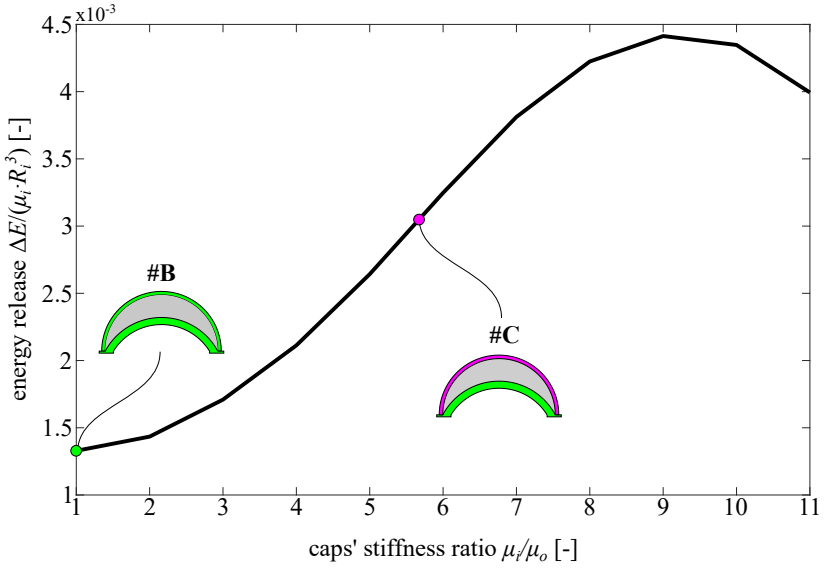

Figure C.21: Influence of the outer cap stiffness on the actuators' response. Energy release vs. ratio of the caps' stiffness for an actuator with $(\eta_i, \theta_i, \eta_o, \theta_o) = (8.5, 60°, 16.5, 90°)$. Note that for $\mu_i/\mu_o = 1$ and 5.8 the actuator corresponds to Designs B and C, respectively. We find that for this geometry, there exists a stiffness ratio ($\mu_i/\mu_o \sim 9$) for which the energy released by the system during snapping is maximized.

References

[1] Pellegrino, S. (2014). *Deployable Structures in Engineering*. Springer-Verlag Wien GmbH.

[2] You, Z. and Pellegrino, S. (1997). Foldable bar structures. *International Journal of Solids and Structures*, 34(15):1825 – 1847.

[3] Liu, Y., Du, H., Liu, L., and Leng, J. (2014). Shape memory polymers and their composites in aerospace applications: a review. *Smart Materials and Structures*, 23(2).

[4] Puig, L., Barton, A., and Rando, N. (2010). A review on large deployable structures for astrophysics missions. *Acta Astronautica*, 67(1-2):12–26.

[5] Rus, D. and Tolley, M. T. (2015). Design, fabrication and control of soft robots. *Nature*, 521(7553):467.

[6] Majidi, C. (2014). Soft robotics: a perspective—current trends and prospects for the future. *Soft Robotics*, 1(1):5–11.

[7] Trivedi, D., Rahn, C. D., Kier, W. M., and Walker, I. D. (2008). Soft robotics: Biological inspiration, state of the art, and future research. *Applied bionics and biomechanics*, 5(3):99–117.

[8] Litteken, D. A. (2019). Inflatable technology: using flexible materials to make large structures. In *Electroactive Polymer Actuators and Devices (EAPAD) XXI*, volume 10966 of *Proceedings of SPIE*.

[9] MSF (2010). Inflatable hospitals: A fast and effective surgical response. *The Frontline*.

[10] Mosadegh, B., Polygerinos, P., Keplinger, C., Wennstedt, S., Shepherd, R. F., Gupta, U., Shim, J., Bertoldi, K., Walsh, C. J., and Whitesides, G. M. (2014). Pneumatic networks for soft robotics that actuate rapidly. *Advanced Functional Materials*, 24(15):2163–2170.

[11] Martinez, R. V., Branch, J. L., Fish, C. R., Jin, L., Shepherd, R. F., Nunes, R. M. D., Suo, Z., and Whitesides, G. M. (2013). Robotic Tentacles with Three-Dimensional Mobility Based on Flexible Elastomers. *Advanced Materials*, 25(2):205–212.

[12] Sinatra, N. R., Teeple, C. B., Vogt, D. M., Parker, K. K., Gruber, D. F., and Wood, R. J. (2019). Ultragentle manipulation of delicate structures using a soft robotic gripper. *Science Robotics*, 4(33):eaax5425.

[13] Shepherd, R. F., Ilievski, F., Choi, W., Morin, S. A., Stokes, A. A., Mazzeo, A. D., Chen, X., Wang, M., and Whitesides, G. M. (2011). Multigait soft robot. *Proceedings of the National Academy of Sciences of the United States of America*, 108(51):20400–20403.

[14] Rafsanjani, A., Zhang, Y., Liu, B., Rubinstein, S. M., and Bertoldi, K. (2018). Kirigami skins make a simple soft actuator crawl. *Science Robotics*, 3(15).

[15] Marchese, A. D., Onal, C. D., and Rus, D. (2014). Autonomous Soft Robotic Fish Capable of Escape Maneuvers Using Fluidic Elastomer Actuators. *Soft Robotics*, 1(1):75–87. PMID: 27625912.

[16] Hu, W., Lum, G. Z., Mastrangeli, M., and Sitti, M. (2018). Small-scale soft-bodied robot with multimodal locomotion. *Nature*, 554(7690):81–85.

[17] Shepherd, R. F., Stokes, A. A., Freake, J., Barber, J., Snyder, P. W., Mazzeo, A. D., Cademartiri, L., Morin, S. A., and Whitesides, G. M. (2013). Using explosions to power a soft robot. *Angewandte Chemie International Edition*, 52(10):2892–2896.

[18] Bartlett, N. W., Tolley, M. T., Overvelde, J. T. B., Weaver, J. C., Mosadegh, B., Bertoldi, K., Whitesides, G. M., and Wood, R. J. (2015). A 3D-printed, functionally graded soft robot powered by combustion. *Science*, 349:161–165.

[19] Wehner., M., Truby, R., Fitzgerald, D., Mosadegh, B., Whitesides, G., Lewis, J., and Wood, R. (2016). An integrated design and fabrication strategy for entirely soft, autonomous robots. *Nature*, 536(7617):451–455.

[20] Gent, A. (1996). A new constitutive relation for rubber. *Rubber Chemistry Tech.*, 69:59–61.

[21] Dudte, L. H., Vouga, E., Tachi, T., and Mahadevan, L. (2016). Programming curvature using origami tessellations. *Nature Materials*, 15:583–588.

[22] Lang, R. J. (1996). A Computational Algorithm for Origami Design. *Proc. of the 12th Annual ACM Symposium on Computational Geometry*, pages 98–105.

[23] Demaine, E. D. and Mitchell, J. S. B. (2001). Reaching Folded States of a Rectangular Piece of Paper. In *Proceedings of the 13th Canadian Conference on Computational Geometry (CCCG 2001)*, pages 73–75, Waterloo, Ontario, Canada.

[24] Demaine, E. D. and Tachi, T. (2017). Origamizer: A Practical Algorithm for Folding Any Polyhedron. In *Proceedings of the 33rd International Symposium on Computational Geometry (SoCG 2017)*, pages 34:1–34:15, Brisbane, Australia.

[25] Silverberg, J. L., Evans, A. A., McLeod, L., Hayward, R. C., Hull, T., Santangelo, C. D., and Cohen, I. (2014). Using origami design principles to fold reprogrammable mechanical metamaterials. *Science*, 345(6197):647–650.

[26] Santangelo, C. D. (2017). Extreme Mechanics: Self-Folding Origami. *Annual Review of Condensed Matter Physics*, 8(1):165–183.

[27] Felton, S., Tolley, M., Demaine, E., Rus, D., and Wood, R. (2014). A method for building self-folding machines. *Science*, 345(6197):644–646.

[28] Martinez, R. V., Fish, C. R., Chen, X., and Whitesides, G. M. (2012). Elastomeric Origami: Programmable Paper-Elastomer Composites as Pneumatic Actuators. *Advanced Functional Materials*, 22(7):1376–1384.

[29] Li, S., Vogt, D. M., Rus, D., and Wood, R. J. (2017). Fluid-driven origami-inspired artificial muscles. *Proceedings of the National Academy of Sciences*, 114(50):13132–13137.

[30] Kim, W., Byun, J., Kim, J.-K., Choi, W.-Y., Jakobsen, K., Jakobsen, J., Lee, D.-Y., and Cho, K.-J. (2019). Bioinspired dual-morphing stretchable origami. *Science Robotics*, 4(36).

[31] Kamrava, S., Mousanezhad, D., Ebrahimi, H., Ghosh, R., and Vaziri, A. (2017). Origami-based cellular metamaterial with auxetic, bistable, and self-locking properties. *Scientific Reports*, 7(1).

[32] Hanna, B., Lund, J., Lang, R., Magleby, S., and Howell, L. (2014). Waterbomb base: A symmetric single-vertex bistable origami mechanism. *Smart Materials and Structures*, 23:094009.

[33] Jianguo, C., Xiaowei, D., Ya, Z., Jian, F., and Yongming, T. (2015). Bistable Behavior of the Cylindrical Origami Structure With Kresling Pattern. *Journal of Mechanical Design*, 137(6). 061406.

[34] Silverberg, J. L., Na, J.-H., Evans, A. A., Liu, B., Hull, T. C., Santangelo, C., Lang, R. J., Hayward, R. C., and Cohen, I. (2015). Origami structures with a critical transition to bistability arising from hidden degrees of freedom. *Nature Materials*, 14:389–393.

[35] Waitukaitis, S., Menaut, R., Chen, B. G.-g., and van Hecke, M. (2015). Origami Multistability: From Single Vertices to Metasheets. *Physical Review Letters*, 114(5).

[36] Yasuda, H. and Yang, J. (2015). Reentrant Origami-Based Metamaterials with Negative Poisson's Ratio and Bistability. *Physical Review Letters*, 114:185502.

[37] Reid, A., Lechenault, F., Rica, S., and Adda-Bedia, M. (2017). Geometry and design of origami bellows with tunable response. *Physical Review E*, 95:013002.

[38] Faber, J. A., Arrieta, A. F., and Studart, A. R. (2018). Bioinspired spring origami. *Science*, 359(6382):1386–1391.

[39] Zirbel, S., Wilson, M., Magleby, S., and Howell, L. (2013). An Origami-Inspired Self-Deployable Array. In *ASME 2013 Conference on Smart Materials, Adaptive Structures and Intelligent Systems, SMASIS 2013*, volume 1.

[40] Kidambi, N. and Wang, K. W. (2020). Dynamics of Kresling origami deployment. *Physical Review E*, 101:063003.

[41] Overvelde, J. T., Kloek, T., D'haen, J. J., and Bertoldi, K. (2015). Amplifying the response of soft actuators by harnessing snap-through instabilities. *Proceedings of the National Academy of Sciences*, 112(35):10863–10868.

[42] Rothemund, P., Ainla, A., Belding, L., Preston, D. J., Kurihara, S., Suo, Z., and Whitesides, G. M. (2018). A soft, bistable valve for autonomous control of soft actuators. *Science Robotics*, 3(16):eaar7986.

[43] Forterre, Y., Skotheim, J. M., Dumais, J., and Mahadevan, L. (2005). How the Venus flytrap snaps. *Nature*, 433(7024):421.

[44] Pandey, A., Moulton, D. E., Vella, D., and Holmes, D. P. (2014). Dynamics of snapping beams and jumping poppers. *EPL (Europhysics Letters)*, 105(2):24001.

[45] Vella, D. (2019). Buffering by buckling as a route for elastic deformation. *Nature Reviews Physics*, page 1.

[46] Rafsanjani, A., Akbarzadeh, A., and Pasini, D. (2015). Snapping Mechanical Metamaterials under Tension. *Advanced Materials*, 27(39):5931–5935.

[47] Zhao, J.-S., Chu, F., and Feng, Z.-J. (2009). The mechanism theory and application of deployable structures based on SLE. *Mechanism and Machine Theory*, 44(2):324–335.

[48] Mira, L. A., Thrall, A. P., and Temmerman, N. D. (2014). Deployable scissor arch for transitional shelters. *Automation in Construction*, 43:123 – 131.

[49] Thrall, A., Adriaenssens, S., Paya-Zaforteza, I., and Zoli, T. (2012). Linkage-based movable bridges: Design methodology and three novel forms. *Engineering Structures*, 37:214 – 223.

[50] Arnouts, L., Massart, T., De Temmerman, N., and Berke, P. (2019). Structural optimisation of a bistable deployable scissor module. In Lázaro, C., Bletzinger, K.-U., and Oñate, E., editors, *Proceedings of the IASS Annual Symposium 2019 – Structural Membranes 2019*.

[51] García-Mora, C. J. and Sánchez-Sánchez, J. (2020). Geometric method to design bistable and non - bistable deployable structures of straight scissors based on the convergence surface. *Mechanism and Machine Theory*, 146:103720.

[52] Cadogan, D., Stein, J., and Grahne, M. (1999). Inflatable composite habitat structures for lunar and Mars exploration. *Acta Astronautica*, 44(7-12, SI):399–406.

[53] Block, J., Straubel, M., and Wiedemann, M. (2011). Ultralight deployable booms for solar sails and other large gossamer structures in space. *Acta Astronautica*, 68(7-8):984–992. 60th International Astronautical Congress, Daejeon, SOUTH KOREA, OCT 12-16, 2009.

[54] Siéfert, E., Reyssat, E., Bico, J., and Roman, B. (2020). Programming stiff inflatable shells from planar patterned fabrics. *Soft Matter*, 16:7898–7903.

[55] Siéfert, E., Reyssat, E., Bico, J., and Roman, B. (2019). Bio-inspired pneumatic shape-morphing elastomers. *Nature Materials*, 18(1):16692–16696.

[56] Usevitch, N. S., Hammond, Z. M., Schwager, M., Okamura, A. M., Hawkes, E. W., and Follmer, S. (2020). An untethered isoperimetric soft robot. *Science Robotics*, 5(40).

[57] Skouras, M., Thomaszewski, B., Kaufmann, P., Garg, A., Bickel, B., Grinspun, E., and Gross, M. (2014). Designing Inflatable Structures. *ACM Trans. Graph.*, 33(4).

[58] Rus, D. and Tolley, M. T. (2018). Design, fabrication and control of origami robots. *Nature Reviews Materials*, 3(6):101–112.

[59] Onal, C. D., Wood, R. J., and Rus, D. (2013). An Origami-Inspired Approach to Worm Robots. *IEEE/ASME Transactions on Mechatronics*, 18(2):430–438.

[60] Onal, C. D., Tolley, M. T., Wood, R. J., and Rus, D. (2015). Origami-Inspired Printed Robots. *IEEE/ASME Transactions on Mechatronics*, 20(5):2214–2221.

[61] Li, S., Stampfli, J. J., Xu, H. J., Malkin, E., Diaz, E. V., Rus, D., and Wood, R. J. (2019). A Vacuum-driven Origami "Magic-ball" Soft Gripper. In *2019 International Conference on Robotics and Automation (ICRA)*, pages 7401–7408.

[62] Miskin, M. Z., Dorsey, K. J., Bircan, B., Han, Y., Muller, D. A., McEuen, P. L., and Cohen, I. (2018). Graphene-based bimorphs for micron-sized, autonomous origami machines. *Proceedings of the National Academy of Sciences*, 115(3):466–470.

[63] Filipov, E. T., Tachi, T., and Paulino, G. H. (2015). Origami tubes assembled into stiff, yet reconfigurable structures and metamaterials. *Proceedings of the National Academy of Sciences*, 112(40):12321–12326.

[64] Rational design of reconfigurable prismatic architected materials. Overvelde, J., Weaver, J. C., Hoberman, C., and Bertoldi, K. (2017). Rational design of reconfigurable prismatic architected materials. *Nature*, 541:347–352.

[65] Iniguez-Rabago, A., Li, Y., and Overvelde, J. T. B. (2019). Exploring multistability in prismatic metamaterials through local actuation. *Nature Communications*, 10.

[66] Seymour, K., Burrow, D., Avila, A., Bateman, T., Morgan, D., Magleby, S., and Howell, L. (2018). Origami-Based Deployable Ballistic Barrier. In *Proceedings of the 7th International Meeting on Origami in Science*, pages 763–778, Oxford, UK.

[67] Del Grosso, A. and Basso, P. (2010). Adaptive building skin structures. *Smart Materials and Structures*, 19:124011.

[68] Tachi, T. (2011). Rigid-Foldable Thick Origami. *Origami 5*, 5:12.

[69] Zirbel, S. A., Lang, R. J., Thomson, M. W., Sigel, D. A., Walkemeyer, P. E., Trease, B. P., Magleby, S. P., and Howell, L. L. (2013). Accommodating Thickness in Origami-Based Deployable Arrays. *Journal of Mechanical Design*, 135(11, SI).

[70] Dolciani, M. P., Donnelly, A. J., and Jurgensen, R. C. (1963). *Modern Geometry, Structure and Method*. Houghton Mifflin Company.

[71] Connelly, R. (1979). The Rigidity of Polyhedral Surfaces. *Mathematics Magazine*, 52(5):275–283.

[72] Connelly, R., Sabitov, I., and Walz, A. (1997). The Bellows Conjecture. *Contrib. Algebra Geom.*, 38:1–10.

[73] Mackenzie, D. (1998). Polyhedra Can Bend But Not Breathe. *Science*, 279(5357):1637–1637.

[74] Chen, Y., Feng, H., Ma, J., Peng, R., and You, Z. (2016). Symmetric waterbomb origami. *Proceedings of the Royal Society A: Mathematical, Physical and Engineering Sciences*, 472(2190).

[75] Paulino, G. and Liu, K. (2017). Nonlinear mechanics of non-rigid origami: an efficient computational approach. *Proceedings of the Royal Society A: Mathematical, Physical and Engineering Sciences*, 473:20170348.

[76] Rus, D. and Tolley, M. (2015). Design, fabrication and control of soft robots. *Nature*, 521:467–475.

[77] Hawkes, E. W., Blumenschein, L. H., Greer, J. D., and Okamura, A. M. (2017). A soft robot that navigates its environment through growth. *Science Robotics*, 2(8).

[78] Pikul, J. H., Li, S., Bai, H., Hanlon, R. T., Cohen, I., and Shepherd, R. F. (2017). Stretchable surfaces with programmable 3D texture morphing for synthetic camouflaging skins. *Science*, 358(6360):210–214.

[79] Konaković-Luković, M., Panetta, J., Crane, K., and Pauly, M. (2018). Rapid Deployment of Curved Surfaces via Programmable Auxetics. *ACM Trans. Graph.*, 37(4).

[80] Jin, L., Forte, A. E., Deng, B., Rafsanjani, A., and Bertoldi, K. (2020). Kirigami-Inspired Inflatables with Programmable Shapes. *Advanced Materials*, page 2001863.

[81] Runciman, M., Darzi, A., and Mylonas, G. P. (2019). Soft Robotics in Minimally Invasive Surgery. *Soft Robotics*, 6(4):423–443.

[82] Polygerinos, P., Wang, Z., Galloway, K. C., Wood, R. J., and Walsh, C. J. (2015). Soft robotic glove for combined assistance and at-home rehabilitation. *Robotics and Autonomous Systems*, 73:135–143.

[83] Barreiros, J., Claure, H., Peele, B., Shapira, O., Spjut, J., Luebke, D., Jung, M., and Shepherd, R. (2019). Fluidic Elastomer Actuators for Haptic Interactions in Virtual Reality. *IEEE Robotics and Automation Letters*, 4(2):277–284.

[84] Gorissen, B., Milana, E., Baeyens, A., Broeders, E., Christiaens, J., Collin, K., Reynaerts, D., and De Volder, M. (2019). Hardware sequencing of inflatable nonlinear actuators for autonomous soft robots. *Advanced Materials*, 31(3):1804598.

[85] Vasios, N., Gross, A., Soifer, S., Overvelde, J., and Bertoldi, K. (2019). Harnessing Viscous Flow to Simplify the Actuation of Fluidic Soft Robots. *Soft Robotics*, 7(1):1–9.

[86] Robertson, M. A. and Paik, J. (2017). New soft robots really suck: Vacuum-powered systems empower diverse capabilities. *Science Robotics*, 2(9).

[87] Booth, J. W., Shah, D., Case, J. C., White, E. L., Yuen, M. C., Cyr-Choiniere, O., and Kramer-Bottiglio, R. (2018). OmniSkins: Robotic skins that turn inanimate objects into multifunctional robots. *Science Robotics*, 3(22).

[88] Paez, L., Agarwal, G., and Paik, J. (2016). Design and Analysis of a Soft Pneumatic Actuator with Origami Shell Reinforcement. *Soft Robotics*, 3(3):109–119.

[89] Marchese, A. D., Onal, C. D., and Rus, D. (2014). Autonomous Soft Robotic Fish Capable of Escape Maneuvers Using Fluidic Elastomer Actuators. *Soft Robotics*, 1(1):75–87. PMID: 27625912.

[90] Ellis, D. R., Venter, M. P., and Venter, G. (2021). Soft Pneumatic Actuator with Bimodal Bending Response Using a Single Pressure Source. *Soft Robotics*, 8(4):478–484. PMID: 32846112.

[91] Wakimoto, S., Suzumori, K., and Ogura, K. (2011). Miniature Pneumatic Curling Rubber Actuator Generating Bidirectional Motion with One Air-Supply Tube. *Advanced Robotics*, 25(9-10):1311–1330.

[92] Zentner, L., Böhm, V., and Minchenya, V. (2009). On the new reversal effect in monolithic compliant bending mechanisms with fluid driven actuators. *Mechanism and Machine Theory*, 44(5):1009 – 1018.

[93] Hawkes, E., An, B., Benbernou, N. M., Tanaka, H., Kim, S., Demaine, E. D., Rus, D., and Wood, R. J. (2010). Programmable matter by folding. *Proceedings of the National Academy of Sciences*, 107(28):12441–12445.

[94] Zhao, Z., Kuang, X., Wu, J., Zhang, Q., Paulino, G. H., Qi, H. J., and Fang, D. (2018). 3D printing of complex origami assemblages for reconfigurable structures. *Soft Matter*, 14:8051–8059.

[95] Lin, Z., Novelino, L. S., Wei, H., Alderete, N. A., Paulino, G. H., Espinosa, H. D., and Krishnaswamy, S. (2020). Folding at the Microscale: Enabling Multifunctional 3D Origami-Architected Metamaterials. *Small*, 16(35):2002229.

[96] Jianguo, C., Xiaowei, D., Ya, Z., Jian, F., and Yongming, T. (2015). Bistable Behavior of the Cylindrical Origami Structure With Kresling Pattern. *Journal of Mechanical Design*, 137(6). 061406.

[97] Novelino, L. S., Ze, Q., Wu, S., Paulino, G. H., and Zhao, R. (2020). Untethered control of functional origami microrobots with distributed actuation. *Proceedings of the National Academy of Sciences*, 117(39):24096–24101.

[98] Liu, K., Tachi, T., and Paulino, G. (2019). Invariant and smooth limit of discrete geometry folded from bistable origami leading to multistable metasurfaces. *Nature Communications*, 10:1–10.

[99] Mintchev, S., Shintake, J., and Floreano, D. (2018). Bioinspired dual-stiffness origami. *Science Robotics*, 3(20).

[100] Treml, B., Gillman, A., Buskohl, P., and Vaia, R. (2018). Origami mechanologic. *Proceedings of the National Academy of Sciences*, 115(27):6916–6921.

[101] Sadeghi, S. and Li, S. (2020). Dynamic folding of origami by exploiting asymmetric bistability. *Extreme Mechanics Letters*, 40:100958.

[102] Kresling, B. (2002). Folded tubes as compared to Kikko ("Tortoise-Shell") bamboo. In Hull, T, editor, *ORIGAMI3*, pages 197–207. 3rd International Meeting of Origami Science, Mathematics, and Education, PACIFIC GROVE, CA, 2001.

[103] Bhovad, P., Kaufmann, J., and Li, S. (2019). Peristaltic locomotion without digital controllers: Exploiting multi-stability in origami to coordinate robotic motion. *Extreme Mechanics Letters*, 32:100552.

[104] Pagano, A., Yan, T., Chien, B., Wissa, A., and Tawfick, S. (2017). A crawling robot driven by multi-stable origami. *Smart Materials and Structures*, 26(9):094007.

[105] Kaufmann, J., Bhovad, P., and Li, S. (2021). Harnessing the Multistability of Kresling Origami for Reconfigurable Articulation in Soft Robotic Arms. *Soft Robotics*, 00(00).

[106] Yasuda, H., Tachi, T., Lee, M., and Yang, J. (2017). Origami-based tunable truss structures for non-volatile mechanical memory operation. *Nature Communications*, 8.

[107] Fang, H., Li, S., Ji, H., and Wang, K. W. (2016). Uncovering the deformation mechanisms of origami metamaterials by introducing generic degree-four vertices. *Physical Review E*, 94:043002.

[108] Curtis, S. (2003). The classification of greedy algorithms. *Science of Computer Programming*, 49(1):125–157.

[109] Vidal, V. (2004). A Lookahead Strategy for Heuristic Search Planning. pages 150–160.

[110] Deep, K., Singh, K., Kansal, M., and Mohan, C. (2009). A real coded genetic algorithm for solving integer and mixed integer optimization problems. *Applied Mathematics and Computation*, 212:505–518.

[111] Müller, J., Shoemaker, C. A., and Piché, R. (2014). SO-I: a surrogate model algorithm for expensive nonlinear integer programming problems including global optimization applications. *Journal of Global Optimization*, 59(4):865–889.

[112] Gorissen, B., Reynaerts, D., Konishi, S., Yoshida, K., Kim, J.-W., and De Volder, M. (2017). Elastic inflatable actuators for soft robotic applications. *Advanced Materials*, 29(43):1604977.

[113] Brown, E., Rodenberg, N., Amend, J., Mozeika, A., Steltz, E., Zakin, M. R., Lipson, H., and Jaeger, H. M. (2010). Universal robotic gripper based on the jamming of granular material. *Proceedings of the National Academy of Sciences*, 107(44):18809–18814.

[114] Lee, H., Xia, C., and Fang, N. X. (2010). First jump of microgel; actuation speed enhancement by elastic instability. *Soft Matter*, 6(18):4342–4345.

[115] Riks, E. (1979). An incremental approach to the solution of buckling and snapping problems. *International Journal of Solids and Structures*, 15:524–551.

[116] Crisfield, M. (1983). A fast incremental/iterative solution procedure that handles snap-through. *Computers and Structures*, 13:55–62.

[117] Hutchinson, J. W. (2016). Buckling of spherical shells revisited. *Proceedings of the Royal Society A: Mathematical, Physical and Engineering Sciences*, 472(2195):20160577.

[118] Lee, A., Jiménez, F. L., Marthelot, J., Hutchinson, J. W., and Reis, P. M. (2016). The geometric role of precisely engineered imperfections on the critical buckling load of spherical elastic shells. *Journal of Applied Mechanics*, 83(11):111005.

[119] Zoelly, R. (1915). *Ueber ein knickungsproblem an der kugelschale*. PhD thesis, ETH Zurich.

[120] Florijn, B., Coulais, C., and van Hecke, M. (2014). Programmable Mechanical Metamaterials. *Physical Review Letters*, 113:175503.

[121] Stein-Montalvo, L., Costa, P., Pezzulla, M., and Holmes, D. P. (2019). Buckling of geometrically confined shells. *Soft Matter*, 15:1215–1222.

[122] Overvelde, J. T. B., Dykstra, D. M. J., de Rooij, R., Weaver, J., and Bertoldi, K. (2016). Tensile Instability in a Thick Elastic Body. *Physical Review Letters*, 117:094301.

[123] Needleman, A. (1977). Inflation of spherical rubber balloons. *International Journal of Solids and Structures*, 13(5):409–421.

[124] Müller, I. and Strehlow, P. (2004). *Rubber and rubber balloons: paradigms of thermodynamics*, volume 637. Springer Science & Business Media.

[125] Gomez, M., Moulton, D. E., and Vella, D. (2019). Dynamics of viscoelastic snap-through. *Journal of the Mechanics and Physics of Solids*, 124:781 – 813.

[126] D. Karagiozova, X.-W. Zhang, T.-X. Y. (2012). Static and dynamic snap-through behaviour of an elastic spherical shell. *Acta Mechanica Sinica*, 28(3):695.

[127] Hines, L., Petersen, K., and Sitti, M. (2016). Inflated soft actuators with reversible stable deformations. *Advanced Materials*, 28(19):3690–3696.

[128] Ben-Haim, E., Salem, L., Or, Y., and Gat, A. D. (2020). Single-Input Control of Multiple Fluid-Driven Elastic Actuators via Interaction Between Bistability and Viscosity. *Soft Robotics*, 7(2):259–265. PMID: 31891525.

[129] Mahajan, S. (2014). *The art of insight in science and engineering: mastering complexity*. MIT Press.

[130] Tolley, M. T., Shepherd, R. F., Mosadegh, B., Galloway, K. C., Wehner, M., Karpelson, M., Wood, R. J., and Whitesides, G. M. (2014). A Resilient, Untethered Soft Robot. *Soft Robotics*, 1(3):213–223.

[131] Neville, R. M., Groh, R. M., Pirrera, A., and Schenk, M. (2018). Shape control for experimental continuation. *Physical Review Letters*, 120(25):254101.

[132] Bende, N. P., Evans, A. A., Innes-Gold, S., Marin, L. A., Cohen, I., Hayward, R. C., and Santangelo, C. D. (2015). Geometrically controlled snapping transitions in shells with curved creases. *Proceedings of the National Academy of Sciences*, 112(36):11175–11180.

[133] Raney, J. R., Nadkarni, N., Daraio, C., Kochmann, D. M., Lewis, J. A., and Bertoldi, K. (2016). Stable propagation of mechanical signals in soft media using stored elastic energy. *Proceedings of the National Academy of Sciences*, 113(35):9722–9727.

[134] Nadkarni, N., Arrieta, A. F., Chong, C., Kochmann, D. M., and Daraio, C. (2016). Unidirectional transition waves in bistable lattices. *Physical Review Letters*, 116(24):244501.

[135] Shan, S., Kang, S. H., Raney, J. R., Wang, P., Fang, L., Candido, F., Lewis, J. A., and Bertoldi, K. (2015). Multistable architected materials for trapping elastic strain energy. *Advanced Materials*, 27(29):4296–4301.

[136] Chen, T., Bilal, O. R., Shea, K., and Daraio, C. (2018). Harnessing bistability for directional propulsion of soft, untethered robots. *Proceedings of the National Academy of Sciences*, 115(22):5698–5702.

[137] Chen, T., Pauly, M., and Reis, P. M. (2021). A reprogrammable mechanical metamaterial with stable memory. *Nature*, 589:386–390.

[138] Xue, T., Beatson, A., Chiaramonte, M., Roeder, G., Ash, J. T., Menguc, Y., Adriaenssens, S., Adams, R. P., and Mao, S. (2020). A data-driven computational scheme for the nonlinear mechanical properties of cellular mechanical metamaterials under large deformation. *Soft Matter*, 16:7524–7534.

[139] Mao, Y., He, Q., and Zhao, X. (2020). Designing complex architectured materials with generative adversarial networks. *Science Advances*, 6(17).

[140] Choi, G., Dudte, L., and Mahadevan, L. (2019). Programming shape using kirigami tessellations. *Nature Materials*, 18:999–1004.

[141] Bertoldi, K., Vitelli, V., Christensen, J., and van Hecke, M. (2017). Flexible mechanical metamaterials. *Nature Reviews Materials*, 2:17066.

[142] Forte*, A. E., Melancon*, D., Kamp, L. M., Gorissen, B., and Bertoldi, K. (In preparation). MuA-Ori: Multimodal Actuated Origami.

[143] Gibson, L. (2013). The elastic and plastic behaviour of cellular materials.

[144] Tang, P. and Sirignano, W. (1973). Theory of a generalized Helmholtz resonator. *Journal of Sound and Vibration*, 26(2):247–262.

[145] Melancon, D., Gorissen, B., Garcia-Mora, C. J., Hoberman, C., and Bertoldi, K. (2021). Multistable inflatable origami structures at the metre scale. *Nature*, 592:545–550.

List of Ph.D. publications

Peer Reviewed Journals

1. B. Gorissen*, **D. Melancon***, N. Vasios, M. Torbati, K. Bertoldi, Inflatable soft jumper inspired by shell snapping. *Science Robotics*. 5, eabb1967(2020). **doi:10.1126/scirobotics.abb1967**

2. **D. Melancon**, B. Gorissen, C.J. Garcia Mora, C. Hoberman, K. Bertoldi, Multistable inflatable origami structures at the metre scale. *Nature*. 592, 545–550 (2021). **doi:10.1038/s41586-021-03407-4**

3. S. Mhatre, E. Boatti, **D. Melancon**, A. Zareei, M. Dupont, M. Bechthold, K. Bertoldi, Deployable structures based on buckling of curved beams upon a rotational input. *Advanced Functional Materials*. 2101144 (2021). **doi:10.1002/adfm.202101144**

4. A.E. Forte*, **D. Melancon***, L. Kamp, B. Gorissen, K. Bertoldi, MuA-Ori: Multimodal Actuated Origami. arXiv:2112.01366.

5. **D. Melancon**, M. Zanati, M. De Giorgi, A.E. Forte†, K. Bertoldi†, Optical Metamaterials. (2021). *In preparation*.